

Quantum Chemical Investigation of Electronic and Structural Properties of Crystalline Bismuth and Lanthanide Triborates

Inaugural - Dissertation

Zur

Erlangung des Doktorgrades
der Mathematisch-Naturwissenschaftlichen Fakultät
der Universität zu Köln

vorgelegt von

JUN YANG
aus Chongqing, China

Köln 2007

Berichtersteller:

Prof. Dr. M. Dolg

Prof. Dr. L. Bohatý

Prof. Dr. H. Stoll

Tag der mündlichen Prüfung: 19.04.2007

Acknowledgements

“There are no knowns. There are known unknowns. But there are also unknown unknowns”, once said by Donald Rumsfeld, the former U.S. Defense Secretary. But that is the universal truth in the world. Yes, doing a PhD is quite an apprehensively challenging work, going through the three and a half years with unease and tension to find out “known unknowns”. It is highly unlikely to be approaching the end of this period and to accomplish a thesis unless one is working in a collaborative team that is always supportive, liberal, encouraging and friendly. This is exactly where I stay. I thereby sincerely devote all the thanks and gratitude to my colleagues who have spent time on assisting, talking, discussing and even arguing sometimes in the scientific interests and beyond.

Foremost, I would like to thank my supervisor, Prof. Dr. Michael Dolg, for providing me the opportunity in this fascinating area. His support and guidance have made the completion of my PhD thesis possible. He has been actively interested in my work and been always available to advise me in making progress with additional insightful efforts in reviewing and correcting my papers and thesis. His careful patience, achievement motivation, academic enthusiasm, profound knowledge, and day-by-day diligence have led himself not only an example for us as an excellent scientist but also a great mentor in science and a close friend in life to his students.

I am grateful to Prof. Dr. Ladislav Bohatý and Priv. Doz. Dr. Petra Becker in the Institut für Kristallographie and Dipl. Phys. Wolf-Dieter Stein in the Physikalisches Institut for the valuable discussions and for sharing their knowledge and data.

Work has been financially supported by Deutsche Forschungsgemeinschaft via the project Graduiertenkolleg 549, "Azentrische Kristalle" at the Universität zu Köln. I also thank the computer center at the Universität zu Köln (RRZK) for providing me the access to the high performance computing CLIO Sun-Opteron cluster.

My work has indispensably benefited from the professional expertise of Dr. Michael Hanrath in many ways and he was there to help me out whenever I had difficulties with the computer system. I felt immensely instructive, as well, in his informative lectures about the coupled cluster theory and programming techniques although they are too advanced for me to quite yet get them though.

I feel very lucky thanks to Frau Birgitt Börsch-Pulm, who has also helped me with computer systems especially my laptop system which collapsed and needed reinstallation more often than usual. It is her swift assistance to have my posters printed out with good qualities that makes the poster presentations possible in the conferences.

Dr. Xiaoyan Cao is my Chinese colleague. The talk and discussion with her in the mother tongue is one of my most unforgettable experiences in Köln. I also thank Dr. Cao for the invitation to be part of her family dinner. The hospitalities of her and her husband offered me a chance to get used to my new and totally different way of life as easy as possible.

I should not forget our dear secretary Herr Martin Böhler, who assisted me to make all the administrative issues. He is an accommodating person and has always patiently interpreted me the university regulations and German documents in detail.

I must express the most particular acknowledgement to my other group members for sharing every moment, which is happening in our institute every day, with Herr Mark Burkatzki, Frau Rebecca Fondermann, Herr Sombat Ketrat, Herr Joachim Friedrich, Herr Alexander Schnurpfeil, Herr Jonas Wiebke, Frau Anna Moritz and Frau Anna Engels-Putzka. Especially thanks to Herr Joachim Friedrich, my office-mate, our talking at the non-scientific side has provided me one of the sources that I understand the European and German society. It is due to their contributions and involvements that I am working in an atmosphere filled with a team spirit. The thanks are addressed as well to the former members, i.e., Dr. Atashi Basu Mukhopadhyay and Dr. Johannes Weber.

I would like to acknowledge Priv. Doz. Dr. Beate Paulus in the Max-Planck-Institut für Physik komplexer Systeme and Priv. Doz. Dr. Timo Fleig in the Institute of Theoretical and Computational Chemistry at the University of Düsseldorf who kindly invited me to give presentations. I thank all the people who have had me in their scientific discussions and who I have learned a lot from, including those in all the conferences I have attended.

I am very much indebted to my wife, Ms. Yu Wang. She is always supportive to my work, and has collated the complete sheets for all copies of the thesis overnight and sent them for binding the next morning. It was unfeasible to meet the deadline for handing in thesis without her assistance.

Finally, I am totally responsible for, if any, all the layout errors, theoretical mistakes, computational deficiencies, misleading arguments and controversial conclusions throughout this thesis.

Thank you very much indeed!

Jun Yang

December, 2006

Köln, Deutschland

Kurzzusammenfassung

Die Ursachen der optischen Effekte und der chemischen Stabilität von BiB_3O_6 wurden mit der gradienten-korrigierten hybrid B3PW-Methode der Dichtefunktionaltheorie im Rahmen eines Gauß-orbital-basierten CO-LCAO Schemas untersucht. Bei Einschluß der Spin-Bahn-Kopplung liefert das B3PW Hybrid-Funktional für die indirekte Bandlücke Näherungswerte von 4.29~4.99 eV, die näher am experimentellen Wert von 4.3 eV liegen als die HF, LDA oder GGA Ergebnisse. Mit Hilfe einer Populationsanalyse der Kristallorbitale wurde eine detaillierte auf first-principles Berechnungen beruhende Analyse der Bindungsverhältnisse durchgeführt. Es wurde festgestellt, daß die Bi 6s und O 2p Orbitale in einer primären Wechselwirkung koppeln, woraus bindende und antibindende Zustände unterhalb der Fermi-Energie entstehen. Die Bi 6p Orbitale sind an einer sekundären Wechselwirkung mit den gefüllten antibindenden Bi 6s-O 2p Orbitalen beteiligt. Die stereochemische Aktivität des freien Elektronenpaares auf Bi entsteht im wesentlichen durch die primäre Wechselwirkung in den besetzten antibindenden Bi 6s-O 2p Orbitalen. Es wurde gefunden, daß die Bi 6p Orbitale nicht wesentlich für die nicht-sphärische Form des freien Elektronenpaares auf Bi verantwortlich sind. Die Dichten der optischen Absorption des gesamten BiB_3O_6 Kristalls sowie der $[\text{BiO}_4]^{5-}$, $[\text{BO}_3]^{3-}$ und $[\text{BO}_4]^{5-}$ Einheiten wurden individuell berechnet. Es ergab sich, daß die $[\text{BiO}_4]^{5-}$ Einheiten hauptsächlich für die optischen Eigenschaften von BiB_3O_6 im Bereich langer Wellenlängen verantwortlich sind. Der Grund hierfür ist, daß die kovalenten Bi-O Bindungen zu starken räumlichen Überlappungen führen und so den Elektronentransfer von den besetzten O 2p in die unbesetzten Bi 6p Orbitale ermöglichen. Relativistischen Korrekturen und Korrelationskorrekturen führen zu fundamentalen Unterschieden in den Bindungsverhältnissen, der Bandstruktur und den optischen Eigenschaften von BiB_3O_6 im Vergleich zu nichtrelativistischen und unkorrelierten Berechnungen. Die harmonischen Frequenzen von BiB_3O_6 wurden mit einer numerischen Methode zur Ermittlung des Hesse-Matrix berechnet. Alle 13 A und 14 B Schwingungsmoden wurden zugeordnet, graphisch dargestellt und nach ihren Bi-O und B-O Bewegungen klassifiziert. Der Vergleich mit vorherigen experimentellen Arbeiten wird eingehend diskutiert.

Für Elektronenstrukturberechnungen an Festkörpern geeignete primitive (4s4p3d), (5s5p4d) und (6s6p5d) Gauß-Valenzbasissätze wurden für die Stuttgart-Köln 4f-im-Rumpf-Pseudopotentiale der Lanthanoiden optimiert. Diese sind für Berechnungen von Kristallen geeignet, die dreiwertige Lanthanoidionen enthalten, insbesondere für die in dieser Arbeit untersuchte Frage der relativen Stabilität der C2 und I2 Phasen von LnB_3O_6 . Unterschiedliche segmentierte Kontraktionsmuster wurden in Berechnungen an A-typ Pm_2O_3 kalibriert. Die Anwendung in Geometrieoptimierungen anderer A-typ Ln_2O_3 (Ln=La-Nd) ergibt zufriedenstellende Übereinstimmung mit experimentellen Daten für (6s6p5d)/[4s4p4d] Valenzbasissätze der Lanthanoiden. Die Kohäsionsenergie von A-typ Ln_2O_3 wurde mit der konventionellen Kohn-Sham DFT und der a posteriori-HF

Korrelations-DFT mit um diffuse Funktionen erweiterten (8s7p6d)/[6s5p5d] Valenzbasissätzen für die freien Lanthanoidatome berechnet. Beurteilt nach den berechneten energetischen Daten sowie einer Bindungsanalyse sind die I2 Phasen von LaB_3O_6 und GdB_3O_6 stabiler als die C2 Phasen. Dieser Befund stimmt mit den experimentellen Ergebnissen überein.

Ein neues Verfahren zur Berechnung der optischen Eigenschaften großer Systeme wurde auf Basis des Inkrementenschemas für Wellenfunktions-basierte Korrelationsmethoden entwickelt. Das Konvergenzverhalten der Polarisierbarkeiten erster und zweiter Ordnung bezüglich der Wahl der Domänen und der Ordnung der inkrementellen Entwicklung wurde für das Testsystem $\text{Ga}_4\text{As}_4\text{H}_{18}$ untersucht und diskutiert.

Abstract

The origins of the optical effects and the chemical stability of BiB_3O_6 are studied by gradient-corrected hybrid B3PW density functional theory within the Gaussian-orbital-based CO-LCAO scheme. Including spin-orbit coupling, B3PW yields an estimate of the indirect band gap of 4.29~4.99 eV which is closer to the experimental value of 4.3 eV than the HF, LDA or GGA results. The crystal orbital overlap population is carried out to give a detailed first-principles analysis of chemical bonding. It is found that the Bi 6s couples with the O 2p in the primary interaction, which eventually forms both bonding and antibonding orbitals below the Fermi level. The Bi 6p is further involved in the secondary interaction with the filled Bi 6s-O 2p antibonding orbitals. The stereochemical activity of the Bi lone-pairs mainly originates from the primary interaction for the occupied Bi 6s-O 2p antibonding orbitals. It is found that the Bi 6p orbitals are not critically responsible for the non-spherical shape of the Bi lone-pairs. The densities of optical absorptions for the total BiB_3O_6 crystal, $[\text{BiO}_4]^{5-}$ and $[\text{BO}_3]^{3-}$ and $[\text{BO}_4]^{5-}$ subunits are individually calculated by convoluting the total occupied density of states and the virtual densities of states of the corresponding unit. It is found that the $[\text{BiO}_4]^{5-}$ units are mainly responsible for the optics of BiB_3O_6 in the long wavelength region. The reason is that the Bi-O covalent bonds lead to large spatial orbital overlappings and thus favor the electronic transfer from the occupied O 2p to the empty Bi 6p orbitals. The relativistic and correlation effects lead to fundamental differences of the band structure, chemical bonds and optical effects for BiB_3O_6 compared with non-relativistic and uncorrelated calculations. The harmonic frequencies of BiB_3O_6 are calculated by applying the numerical-difference technique. The complete 13 A and 14 B vibrational modes are assigned, graphically visualized and classified according to the Bi-O and B-O motions. Comparisons with previous experimental reports are discussed in detail.

Crystal orbital adapted Gaussian (4s4p3d), (5s5p4d) and (6s6p5d) valence primitive basis sets are derived, in line with relativistic energy-consistent 4f-in-core lanthanide pseudopotentials of the Stuttgart-Köln variety, for calculating periodic bulk materials containing trivalent lanthanide ions, particularly in this thesis for the investigation of the relative stability of C2 and I2 phases of LnB_3O_6 . Different segmented contraction schemes are calibrated on A-type Pm_2O_3 studying the basis set size effects. Further applications to the geometry optimization of other A-type Ln_2O_3 ($\text{Ln}=\text{La-Nd}$) show a satisfactory agreement with experimental data using the lanthanide valence basis sets (6s6p5d)/[4s4p4d]. The cohesive energies of A- Ln_2O_3 within both conventional Kohn-Sham DFT and the a posteriori-HF correlation DFT schemes are evaluated by using the corresponding augmented sets (8s7p6d)/[6s5p5d] with additional diffuse functions for the atomic energies of free lanthanide atoms. The I2 phases of LaB_3O_6 and GdB_3O_6 crystals are more stable than C2 phases according to both of the calculated energetic data and first-principles bond analysis. This is in agreement with the experimental results.

A new method is developed to calculate the optical properties for large systems based on available wavefunction correlation approaches in the framework of the incremental scheme. The convergence behaviors of first- and second-order polarizabilities with respect to the domain distances and incremental expansion orders are examined and discussed for the model system $\text{Ga}_4\text{As}_4\text{H}_{18}$.

Publications

1. Jun Yang, Michael Dolg

Valence basis sets for lanthanide 4f-in-core pseudopotential adapted for crystal orbital ab initio calculations

Theo. Chem. Acc. **113**, 212-224 (2005)

2. Jun Yang, Michael Dolg

First-principles electronic structure study of the monoclinic crystal bismuth triborate BiB_3O_6

J. Phys. Chem. B **110**, 19254-19263 (2006)

3. Jun Yang, Michael Dolg

Computational investigation of the Bi lone-pairs in monoclinic bismuth triborate BiB_3O_6

Phys. Chem. Chem. Phys. **9**, 2094 (2007)

4. Jun Yang, Michael Dolg

First-principles calculation of vibrational frequencies for monoclinic bismuth triborate BiB_3O_6

Z. Kristallographie (in press)

5. Jun Yang, Michael Dolg

Wavefunction-based correlation method to evaluate optical tensors for large systems in the incremental scheme

J. Chem. Phys. (accepted)

6. Jun Yang, Michael Dolg

Energetics and chemical bonds on the phase stabilities between $C2$ and $I2/c$ monoclinic oxoborates of LaB_3O_6 and GdB_3O_6 derived from first-principles calculations

J. Solid State Chem. (submitted)

Lectures

Invited:

1. *Do we really understand chemical bonds inside BiB_3O_6 and LnB_3O_6 ?*

Max-Planck-Institut für Physik komplexer Systeme

June 2006 **Dresden**, Germany

2. *Quantum chemical simulations of metal triborates containing Bi and lanthanides*

Institute of Theoretical and Computational Chemistry, Universität Düsseldorf

January 2007, **Düsseldorf**, Germany

Contributed:

Density Functional Investigation of Monoclinic BiB_3O_6 within a LCAO Scheme: the Bi lone pair and its role in electronic structure and vibrational modes

9th National Conference on Theoretical Chemistry

October 2005, **Guilin**, China

Posters

1. Jun Yang, Michael Dolg

Valence basis sets for lanthanide 4f-in-core pseudopotential adapted for crystal orbital Hartree-Fock calculations

Ab initio Modeling in Solid State Chemistry

September 2004, **London**, United Kingdom

2. Jun Yang, Michael Dolg

Density Functional Investigation of Monoclinic BiB_3O_6 within a LCAO Scheme: the Bi lone pair and its role in electronic structure and vibrational modes

41st Symposium on Theoretical Chemistry

September 2005, **Innsbruck**, Austria

3. Jun Yang, Michael Dolg

First-principle electronic structure study of the monoclinic crystal BiB_3O_6

42nd Symposium on Theoretical Chemistry

September 2006, **Berlin**, Germany

4. Jun Yang, Michael Dolg

Valence basis sets for lanthanide 4f-in-core pseudopotentials adapted for crystal orbital calculations

42nd Symposium on Theoretical Chemistry

September 2006, **Berlin**, Germany

5. Jun Yang, Michael Dolg

Wave function-based correlation methods to calculate optical tensors for large systems

42nd Symposium on Theoretical Chemistry

September 2006, **Berlin**, Germany

Erklärung

Ich versichere, dass ich die von mir vorgelegte Dissertation selbständig angefertigt, die benutzten Quellen und Hilfsmittel vollständig angegeben und die Stellen der Arbeit – einschließlich Tabellen, Karten und Abbildungen -, die anderen Werken im Wortlaut oder dem Sinn nach entnommen sind, in jedem Einzelfall als Entlehnung kenntlich gemacht habe; dass diese Dissertation noch keiner anderen Fakultät oder Universität zur Prüfung vorgelegen hat; dass sie – abgesehen von unten angegebenen Teilpublikationen – noch nicht veröffentlicht worden ist sowie, dass ich eine solche Veröffentlichung vor Abschluss des Promotionsverfahrens nicht vornehmen werde. Die Bestimmungen der Promotionsordnung sind mir bekannt. Die von mir vorgelegte Dissertation ist von Prof. Dr. M. Dolg betreut worden.

Köln, den 02.02.2007

Contents

INTRODUCTION	1
Considering solid state calculations	1
Bismuth- and lanthanide-containing borates	2
Borate crystals	2
BiB ₃ O ₆	3
LnB ₃ O ₆	4
About this thesis	5
CHAPTER 1 PERIODICITY IN PERFECT CRYSTALS	11
1.1 Crystal lattice in direct space	11
1.2 Crystal electronic states in reciprocal space	13
CHAPTER 2 DERIVING BAND STRUCTURES	20
2.1 Setting up one-electron Bloch orbitals	21
2.2 Setting up the one-electron Hamiltonian	23
2.3 Tight-binding approximation (CO-LCAO)	25
2.3.1 Gaussian basis sets	26
2.3.2 Self-consistent procedure	28
2.3.3 Coulomb and exchange integrals criteria	30
2.4 Plane-waves (PW)	31
2.4.1 Orthogonalized plane-waves (OPW)	31
2.4.2 Pseudopotentials (PP)	32
2.5 Superposition of GTO+PW	33
2.5.1 Augmented plane-waves (APW)	33
2.5.2 Korringa-Kohn-Rostoker (KKR)	35
2.5.3 Linearized augmented plane-waves (LAPW) and APW+lo method	36
2.6 k·p method	38
2.7 Electronic correlation methods for solids	39
2.7.1 Density functional theory (DFT)	39
2.7.1.1 LDA	42
2.7.1.2 GGA	43
2.7.1.3 Hybrid functionals	44
2.7.2 Incremental scheme	44

CHAPTER 3 RELATIVISTIC CORRECTIONS.....	49
3.1 The fully-relativistic Schrödinger equation	49
3.2 All-electron approach	51
3.2.1 Foldy-Wouthuysen Hamiltonian	51
3.2.2 Douglas-Kroll-Hess Hamiltonian	51
3.2.3 Wood-Boring Hamiltonian.....	52
3.3 Effective core potential (ECP).....	53
3.3.1 Frozen core approximation.....	53
3.3.2 Model potentials (MP).....	54
3.3.3 Pseudopotentials (PP).....	55
3.3.3.1 Shape-consistent PPs	56
3.3.3.2 Energy-consistent PPs.....	57
CHAPTER 4 BONDS AND BANDS IN CRYSTALS	58
4.1 Bonding and antibonding interactions	58
4.1.1 s orbitals	58
4.1.2 p orbitals.....	59
4.1.3 s-p _z orbital interactions.....	59
4.2 Energy band.....	59
4.3 Density of states (DOS)	60
CHAPTER 5 HARMONIC PHONON FREQUENCIES	65
5.1 Harmonic approximations.....	65
5.2 Lattice summation and collective displacements.....	68
5.2.1 Frozen phonon approach	68
5.2.2 Supercell approach	69
5.3 Implementing the Γ frequencies in the CO-LCAO approach	71
CHAPTER 6 ELECTRONIC STRUCTURE OF BIBO	75
6.1 Computational details.....	75
6.2 Accuracies of HF, LDA, GGA and hybrid functionals	76
6.3 Energy band.....	78
6.4 Electronic state distribution	78
6.5 Spin-orbit coupling.....	79
CHAPTER 7 ORBITAL INTERACTIONS AND BONDS IN BIBO.....	84
7.1 Origin of chemical stabilities.....	84

7.1.1	Crystal orbital overlap population	84
7.1.2	Quantifying chemical bonds in BiBO	85
7.2	Origin of optical effects.....	86
7.3	Scalar-relativistic and correlation effects.....	87
CHAPTER 8 ASYMMETRIC BI LONE-PAIR ELECTRONS IN BIBO		95
8.1	Advances for electronic lone-pairs.....	95
8.2	Modeling orbital interactions for Bi 6s, Bi 6p and O 2p	96
8.3	Origin of asymmetric Bi lone-pair electrons.....	98
CHAPTER 9 HARMONIC VIBRATIONAL MODES OF BIBO.....		107
9.1	Introduction.....	107
9.2	Computing dynamic matrix	108
9.3	Method calibration study for cubic MgO.....	110
9.4	Vibrational modes of BiBO	111
CHAPTER 10 PHASE STABILITIES OF MONOCLINIC LNBO		121
10.1	Crystal orbital adapted valence basis sets for lanthanide 4f-in-core pseudopotentials.....	121
10.1.1	Introduction	121
10.1.2	Computational methods.....	122
10.1.3	Valence basis sets derived from atomic calculations.....	126
10.1.4	Calibration calculations of crystalline A-Ln ₂ O ₃	128
10.1.4.1	Geometry	128
	HF scheme.....	128
	DFT scheme	129
10.1.4.2	Charge distribution	131
10.1.4.3	Cohesive energy.....	132
10.2	Phase stabilities of LaBO and GdBO	142
10.2.1	Computational details	142
10.2.2	Optimized geometric structures	143
10.2.3	Electronic structures	144
10.2.4	Energetics and stabilities	144
10.2.5	Chemical bonds and stabilities	145
CHAPTER 11 INCREMENTAL SCHEME FOR OPTICAL TENSORS.....		155
11.1	Advances of the calculations for crystal NLO coefficients.....	155
11.2	Exact incremental expansion of optical tensors.....	157
11.3	Tentative application for Ga₄As₄H₁₈ model system.....	161

CONCLUSIONS	166
INDEX OF FIGURES	170
INDEX OF TABLES.....	172
CURRICULUM VITAE	173
BIBLIOGRAPHY	174

Introduction

Considering solid state calculations

Crystals can be viewed in two different ways. The simplest way is to regard a crystal as, probably inspired by the finite appearance of a large mineralogical specimen in the museum, a huge macroscopic molecule consisting of about as many as Avogadro's number of atoms, ions or molecules. In line with this philosophy and by noting the unattainable computational problem of treating the complete huge molecule, a crystalline electronic structure and properties may be represented by a properly truncated cluster within a crystal usually under the constraint of macroscopic point group symmetry. Theories and methods successfully invented for molecules can be applied to deal with this kind of calculation. However, such a cluster model indeed suffers the slow convergence of crystalline electronic structure and properties with respect to the cluster size related to the non-local potential in crystals as well as the boundary effects originating from surface dangling bonds cleaved from the surrounding atoms or ions. The second insightful understanding of a crystal structure, large enough on the microscopic scale to implement an additional translation symmetry besides the point group symmetry, remedies the above difficulties by realizing that the atoms or ions in a perfect crystal do not arrange themselves into a superficial massive collection, but rather, in a very periodic array where an identical motif is repeated throughout the crystal, known as a crystal lattice.

The solid state calculations can be traced back to the empirical models of treating metals. The first attempt was suggested by Drude, three years after the discovery of the electron by J. J. Thomson, to apply the kinetic theory of gases to metals, i.e., the free independent electron gas. Later on, in view of the revolutionary development of quantum mechanics, there was an unprecedented rise to describe the microscopic world within the frame work of quantum theory rather than Newton motions, which leads to the so-called Sommerfeld theory, replacing the classical theory of the free independent electron gas by the quantum theory of the free independent electron gas. Although the Sommerfeld theory is probably one of the earliest quantum theoretical insights of solids, it does not take into account the periodicity of crystals. The first method to incorporate the periodic lattice potential of crystals is the independent electron model, more similar to the modern HF (Hartree-Fock) approach for crystals.

Nowadays, electronic structures of crystals are predominantly calculated with two major approaches, either the plane-wave scheme or the local orbital scheme (i.e., ***crystal orbital linear combinations of atomic orbitals, CO-LCAO***, cf. Table 1). Here only a brief comparison between some available periodic codes is given in Table 1 in terms of basis set types. It is clear that the plane-wave codes are prevailing against the local orbital ones. What remains common for the two different approaches is that the electron-electron correlation interactions are considered within the density functional theory. Several

Introduction

advantages of local orbitals motivated us to apply the local orbital scheme besides the plane-wave approaches. First of all, a relatively small number of Gaussian orbitals is sufficient for an accurate description of the periodic system, and makes the approach attractive in terms of the computational cost. Due to the closely packed nature of atoms in cells, the most diffuse functions of standard basis sets can be eliminated or replaced by tighter orbitals which significantly shorten the computational time of integral evaluation without significant loss of accuracy. Second, in the framework of density functional theory (DFT) some popular hybrid functionals such as B3PW and B3LYP well established for molecules to be a crucial improvement in terms of accuracy over pure LDA (Local Density Approximation) and GGA (Generalized Gradient Approximation) functionals can be used since local orbitals like Gaussian type orbitals (GTO) enable the CO-LCAO scheme to evaluate the HF exchange interactions analytically. It is worthwhile pointing out that by following the HF calculation within CO-LCAO one is in principle able to include the dynamic correlation energy beyond DFT by some highly correlating post-HF method such as the recent reports on linear scaling local MP2 [1] or even more advanced FCI (Full Configuration Interaction) and CCSD (Coupled Cluster Single and Double Excitations) in an incremental scheme at the controlled accuracy of several kcal/mol per unit cell [2, 3, 4].

Bismuth- and lanthanide-containing borates

Borate crystals

The Borate crystal chemistry has kept on obtaining fruitful achievements and has been recently reviewed in the reference [5], since the first two classifications of borate structural formulas proposed by Hermans [6] and Menzel [7] in the 1920's based on the general chemical principles. The earliest borate crystal structure investigations were carried out first by Zachariassen in 1931 [8] and later on by Goldschmidt, Hauptmann [9] and Fang [10], etc. The isolated $[\text{BO}_3]^{3-}$ triangular units were first found in the crystal structure of $\text{Be}_2\text{BO}_3(\text{OH})$ [8]. The $[\text{BO}_4]^{5-}$ tetrahedral units were first found in coexistence with $[\text{BO}_3]^{3-}$ triangular units, forming the pentaborate, in the structure of $\text{KH}_2(\text{H}_3\text{O})_2\text{B}_5\text{O}_{10}$ [11]. Up to now, almost one thousand borate crystal structures have been resolved. In general, a borate structure was usually regarded as polymerized clusters of corner-sharing-only $[\text{BO}_3]^{3-}$ triangular and $[\text{BO}_4]^{5-}$ tetrahedral units, until the first oxoborate with edge-sharing $[\text{BO}_4]^{5-}$ tetrahedrons was determined for the high-pressure structure of $\text{Dy}_4\text{B}_6\text{O}_{15}$ in 2002. These units occur as discrete polyanions to form larger clusters, chains, sheets or frameworks [12]. The excess charge of the array of borate polyhedrons is balanced by the presence of low-valence interstitial cations.

Among all these structures, there is a special type of oxoborates that come into the focus of scientific interests. This is called acentric crystal, which owns the non-centrosymmetry in its structure and consequently exhibits excellent nonlinear optical (NLO) properties in aspects of frequency conversion as well as self-frequency-doubling. The first well described NLO borate crystal is probably $\text{KB}_3\text{O}_8 \cdot 4\text{H}_2\text{O}$ (KB5) [13] in 1975. Additionally,

Introduction

the borate crystals with well-defined NLO properties, according to the review by Becker [14], are β -BaB₂O₄ (BBO) [15, 16], LiB₃O₅ (LBO) [17], CsB₃O₅ (CBO) [18], CsLiB₆O₁₀ (CLBO) [19, 20], Li₂B₄O₇ [21], KBe₂BO₃F₂ (KBBF) [22, 23], Sr₂Be₂B₂O₇ (SBBO) [24], YCa₄(BO₃)₃O (YCOB) [25, 26] and GdCa₄O(BO₃)₃ (GdCOB) [27].

BiB₃O₆

During the past two decades, a polar monoclinic bismuth triborate BiB₃O₆ (BiBO) [28, 29, 30] has stood out along with increasing scientific interests focusing on its crystalline growth [28, 31, 32, 33, 34] and excellent physical properties. Numerous reports have confirmed that BiBO is an outstanding NLO material [35, 36, 37, 38, 39, 40] due to its large effective SHG (Second Harmonic Generation) coefficient, which is higher than that of other borate-based NLO materials like LBO and BBO. BiBO is more advantageous than other borates in terms of several aspects such as a wider transparency range, a short ultraviolet absorption wedge, a lower laser threshold, a higher damage threshold, a small beam convergence and a larger angular acceptance [41, 42].

The three-dimensional structure of BiBO consists of *c* direction-alternating layers of [B₃O₆]³⁻ rings forming sheets of corner-sharing distorted [BO₃]³⁻ triangles and [BO₄]⁵⁻ tetrahedra (Figure 1). These are linked by six-fold coordinated Bi (III) cations forming [BiO₆]⁹⁻ units in which four oxygen atoms at the same side of Bi (III) are the nearest neighbours (2.390 Å off O4 and O5, 2.086 Å off O6 and O7) and other two oxygens at the other side of Bi (III) remain relatively far away (2.632 Å off O6' and O7') (Figure 2). Nevertheless, the two Bi-O6' (Bi-O7') bonds are too long to be accepted as a chemical bond in the usual sense. Obviously O6' and O7' are else coordinated to the next translated Bi along the *b* lattice vector as the shortest Bi-O6-like bonds. Therefore, in this thesis Bi is considered to be four-fold coordinated in [BiO₄]⁵⁻ units.

While the optical properties of BiBO have been widely investigated experimentally, its electronic structure has not been examined in great detail partly because of the tremendously demanding computational complexity of the first-principles calculations for a crystal with low symmetry such as BiBO. Only a few theoretical reports focusing on the evaluation of the optical tensors of BiBO based on different semi-empirical models appeared so far [43, 44, 45]. In general it is simply assumed that the central Bi cation holds a +3 charge by transferring the 6p³ electrons to the polyanionic [B₃O₆]³⁻ rings. The remaining 6s² electrons form on Bi the so-called “inert lone-pairs” which are said to stay nonbonding. The 6s² lone-pair electrons at Bi (III) have been suggested to point along the *b* lattice vector in the opposite direction against the four nearest oxygens around Bi (III) according to the distorted square pyramidal structure of [BiO₄]⁵⁻ units. Without knowing the reasons of the optical properties resulting from electronic structure in detail, the large NLO effects of BiBO are usually explained by the main contributions from the Bi 6s lone-pair electrons which are suggested to have more pronounced effects than the [BO₃]³⁻ and [BO₄]⁵⁻ units.

Introduction

Beyond the optical studies for BiBO, several other contributions have attempted to explore the topological rules for the structure stability of polyborate anion type compounds via a statistical analysis of existing structural data [46, 47, 48, 49]. The $[\text{BO}_4]^{5-}$ tetrahedrons have been considered as favored units in polyborates under high pressures. Unfortunately BiBO turns out to fall into the type for which the structure occurrence rules are least reliable. Therefore a detailed depiction of the electronic structure of BiBO would bring us important insights, as one example of polyborates, to understand the electronic origins of both the structure stability and optical properties by employing quantum chemical calculations.

We intend to answer the following basic questions in this thesis:

1. How do the $[\text{BiO}_4]^{5-}$, $[\text{BO}_3]^{3-}$ triangles and $[\text{BO}_4]^{5-}$ tetrahedrons contribute to the structural stability of BiBO?
2. How are the correlation and relativistic effects involved in the electronic structure of BiBO?
3. Where do the asymmetric Bi lone-pairs originate?
4. Where does the optical effect of BiBO originate from the ground-state electronic structure point of view?

LnB_3O_6

Among the series of metal-containing triborates MB_3O_6 , only BiBO crystallizes in the monoclinic space group C2 without inversion centers in the asymmetric crystallographic cells. The other important monoclinic low-pressure phases of triborates that have been structurally resolved are the binary lanthanide oxoborates of general composition LnB_3O_6 (LnBO) in the space group of I2/c with inversion centers. The starting of the monoclinic I2/c series is marked by LaBO and terminated at TbBO [50, 51, 52, 53, 54]. TbBO is the starting point of another orthorhombic series for LnBO containing the smaller lanthanides from Tb to Lu [55, 56]. In this thesis, only the monoclinic structures are investigated since the calculation of orthorhombic phase demands unaffordable computational efforts which can be hardly achieved within the period of PhD work.

The monoclinic LnBO crystal structures are shown in Figure 3 and Figure 4. Such a structure contains infinite chains of $[\text{B}_6\text{O}_{12}]^{6-}$ running along the c axis. Each tetrahedral unit $[\text{BO}_4]^{5-}$ is linked via two triangular units $[\text{BO}_3]^{3-}$ on both sides, and vice versa (cf. Figure 4). One O atom connecting $[\text{BO}_4]^{5-}$ and $[\text{BO}_3]^{3-}$ belongs to the coordination polyhedron of one Ln, and each of the non-bridging O atoms of $[\text{BO}_3]^{3-}$ units coordinates to two Ln. The central Ln is irregularly coordinated by ten O atoms and the resultant $[\text{LnO}_{10}]^{17-}$ infinite chains run along the c axis. Concerning another kind of monoclinic asymmetric C2 phase which is found only for BiBO, one question is therefore open for discussion that whether or not, at least theoretically, it is possible to realize the isostructural LnBO with respect to BiBO, without inversion centers in monoclinic C2 space due to the similar ionic radii and electronegativities for Ln(III) and Bi(III). To this

Introduction

end, we would rather take LaBO and GdBO as two examples which contain the lanthanide elements with the similar ground state electronic configurations $5s^25p^65d^16s^2$ and $4f^75s^25p^65d^16s^2$, respectively, to seek the possible answer to this question without the loss of general features, than go through the entire series.

About this thesis

The work included in this thesis is subject to the project Graduiertenkolleg 549, “Azentrische Kristalle” at the University of Cologne, with the support of the Deutsche Forschungsgemeinschaft.

This thesis is divided into two parts. In the part I, the related theoretical background is introduced. These theoretical methods have been applied to the computational study of BiBO and LnBO. In Chapter 1, the periodicity of perfect crystals is outlined and crystal electronic states are generally classified in the reciprocal space. Chapter 2 proceeds to describe the most available non-relativistic first-principles methods for deriving the band structures of crystals in association with the translation symmetry. The relativistic corrections are given for both all-electron and pseudopotential methods from the scalar-relativistic effects through spin-orbit corrections to a full-relativistic scheme in Chapter 3. In Chapter 4, it is exhibited how to depict chemical bonds through the entire infinite crystals by exploiting the one-dimensional mono-atomic chain and the formal concepts of energy band and density of states are also given. Chapter 5 intends to discuss the harmonic approximation for lattice dynamics of crystals, and the evident distinctions from molecules in this area are shown.

In the part II, we focus on understanding the mechanism of metal-oxygen orbital interactions (also known as covalent bonds in classic chemistry) and its consequence on the electronic structure, optical effects and chemical stabilities within the first-principles DFT scheme for metal-containing triborates, i.e., BiBO and LnBO. First of all, the first-principles electronic structure of BiBO is discussed in Chapter 6. Subsequently, in Chapter 7 and 8, we invoke the insightful relation between the ground state electronic structure and the chemical stabilities by quantitating the chemical bonds within BiBO, the origin of asymmetric Bi lone-pairs by studying the Bi-O interactions, and the factors for the optical responses by examining the contributions of individual structural components, respectively. The correlation and relativistic effect originating from Bi cations are also discussed. Chapter 9 contributes to talk about the harmonic normal modes of BiBO under the investigation and the comparison with available experimental measurements.

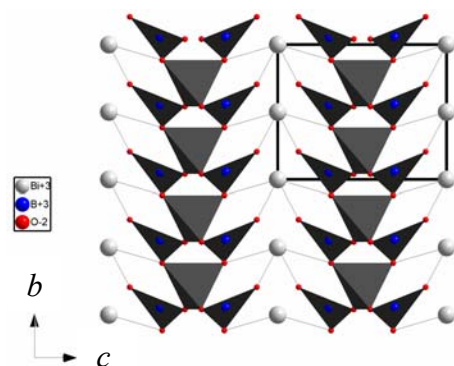
In Chapter 10, we aim at the investigation of the structures and stabilities of LnBO using first-principles DFT calculations by comparing the calculated geometries, enthalpies and chemical bonds for two monoclinic phases, $I2/c$ and $C2$ space group. To this end, first of all, new energy-consistent valence Gaussian basis sets of lanthanide elements have been generated for the adaptation to crystal orbitals, in connection with the effective core pseudopotentials method for heavy lanthanide metals to reduce the computational costs and to include the necessary scalar-relativistic effects. Second, the BiBO-like $C2$ phases

Introduction

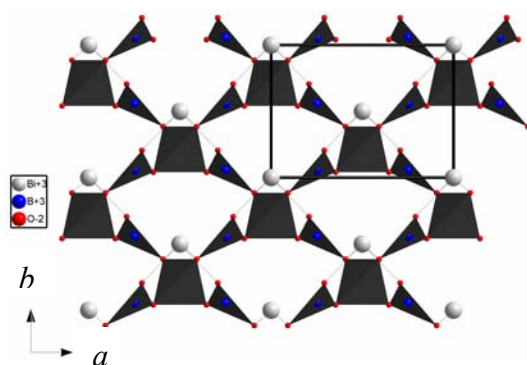
of LnBO containing La and Gd elements were assumed and optimized, as two examples for the LnBO series. Discussions of phase stabilities rely upon the calculated correlation between enthalpies and external pressures as well as the quantitative description of chemical bonds.

In the last Chapter 11, the wavefunction-based highly correlating method has been primarily developed, in association with the incremental scheme, to calculate optical tensors of large systems. The long-term goal of this method is to incorporate these sophisticated molecular correlation methods (e.g., CCSD), in an affordable way in terms of computational expenses, into the accurate wavefunction calculation of the optical properties for NLO crystals like BiBO. However, in this thesis, it is currently not possible to treat the BiBO crystal in this new method due to its large primitive unit cell and its low symmetry. Instead, we focus on the discussion of general formulas and application to a model system.

Introduction



(a) View of the b-c plane



(b) View of the b-a plane

Figure 1 The asymmetric crystallographic cell of monoclinic BiBO (C2 space group) with the lattice parameters of $a=7.116 \text{ \AA}$, $b=4.993 \text{ \AA}$, $c=6.508 \text{ \AA}$, and $\beta=105.62^\circ$. The polyhedral $[\text{B}_3\text{O}_6]^{3-}$ sheet (dark grey areas) along c direction contains triangular $[\text{BO}_3]^{3-}$ (Δ) and tetrahedral $[\text{BO}_4]^{5-}$ (T) units with a ratio $2\Delta:1\text{T}$.

Introduction

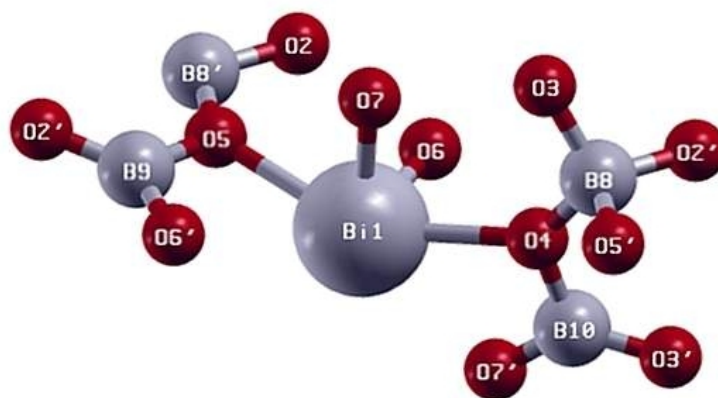


Figure 2 The experimental six-fold coordination of Bi (III) in monoclinic BiBO. Bismuth is indicated by the sequence number 1. Six-fold oxygens are numbered by 4, 5, 6, 7, 6' and 7'. Borons in the centers of tetrahedral units $[\text{BO}_4]^{5-}$ are labeled by 8 (8') and those in triangular units $[\text{BO}_3]^{3-}$ labeled by 9 and 10. Translationally identical atoms are indicated by the same number with a prime as the atoms in the reference primitive cell. The bond distances of Bi-O6' (Bi-O7'), Bi-O4 (Bi-O5) and Bi-O6 (Bi-O7) are 2.632 Å, 2.390 Å and 2.087 Å.

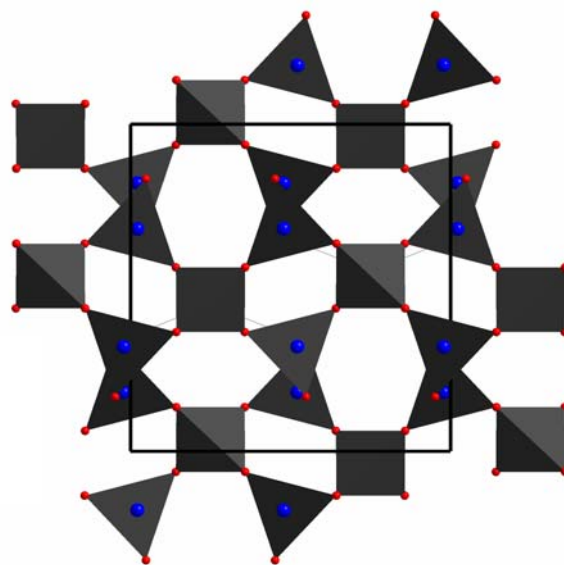


Figure 3 The projection of the LnBO (Ln=La~Tb) monoclinic $I2/c$ centric structure along $[100]$.

Introduction

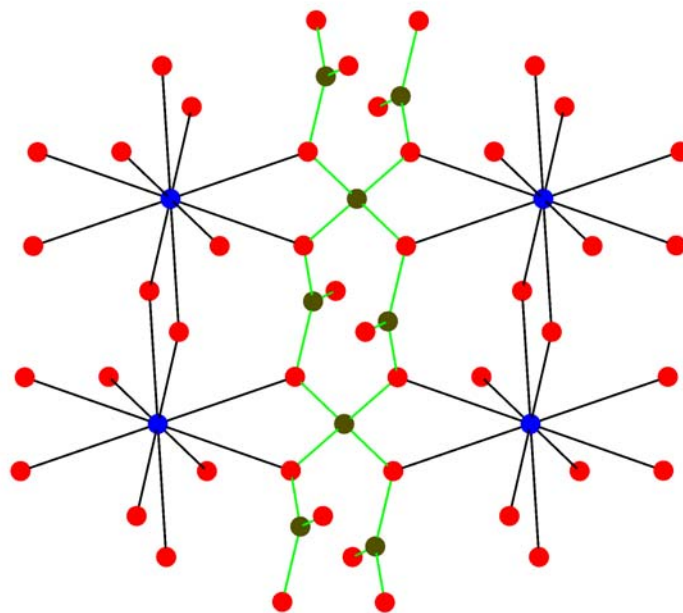


Figure 4 The constituent borate anions and Ln tenfold coordination for the LnBO (Ln=La~Tb) monoclinic I2/c centric structure. The lanthanides are shown in blue, oxygens in red and borons in dark green.

Table 1 The comparison between the plane-wave and local orbital methods.

Approaches	Plane-Wave	CO-LCAO (STO ^a /GTO ^b)	NTO ^c
Periodic codes	Abinit, Castep, CPMD, Dacapo, DoD, Fhi98md, Paratec, PWSCF, Vasp, CP-PAW, PW-PAW, CP2K, LmtART, Fleur, WIEN2K	ADF2002 (BAND) (STO) Gaussian03 (GTO) Crystal03 (GTO)	Siesta DMol
Basis sets size	~1000 PW functions most PP	DZ/TZ-quality, AE, PP too diffuse functions eliminated	small
HF	no	yes	no
DFT	LDA, GGA	LDA, GGA hybrid functionals	LDA, GGA
post-HF	no	local MP2, FCI, CC (incremental scheme)	no

a: Slater-Type Orbital;

b: Gaussian-Type-Orbital;

c: Numerical-Type-Orbital

Part I

Theoretical Methods

Chapter 1 Periodicity in Perfect Crystals

1.1 Crystal lattice in direct space

The abstract concept of the *Bravais lattice* has been widely used to specify a periodic structure in the crystallographer's view of a crystal [57]. A crystal structure is determined by one particular abstract Bravais lattice plus the physical basis structure at each abstract Bravais lattice point at which the maximum possible point symmetry of the basis structure is retained. A three-dimensional Bravais lattice point \mathbf{R} is defined by any three basis vectors \mathbf{a}_1 , \mathbf{a}_2 and \mathbf{a}_3 along non-coplanar directions with three corresponding coefficients n_1 , n_2 and n_3 ranging through all integers with respect to one chosen origin:

$$\mathbf{R} = n_1\mathbf{a}_1 + n_2\mathbf{a}_2 + n_3\mathbf{a}_3 \quad (1-1)$$

The *translation symmetry* is of the highest importance in solid state theory of crystalline systems, and is defined by the translation operation \mathbf{T} for the lattice point \mathbf{R} :

$$\mathbf{TR} = \mathbf{R} + \mathbf{t} = (n_1 + t_1)\mathbf{a}_1 + (n_2 + t_2)\mathbf{a}_2 + (n_3 + t_3)\mathbf{a}_3 \quad (1-2)$$

The three lattice basis vectors \mathbf{a}_1 , \mathbf{a}_2 and \mathbf{a}_3 can also be called the *basis translation vectors*. Point and translational symmetry operations combine to form a *space group*. Each space group refers to only one particular Bravais lattice. Let us consider an operation α acting on a lattice point \mathbf{R} :

$$\alpha\mathbf{R} = \mathbf{R}' = n'_1\mathbf{a}_1 + n'_2\mathbf{a}_2 + n'_3\mathbf{a}_3 \quad (1-3)$$

The resulting new lattice point \mathbf{R}' should also be one of the Bravais lattice points with integer coefficients n'_1 , n'_2 and n'_3 . Due to the restriction of (1-3), there are only 7 distinct finite point groups, the so-called 7 *crystal systems*, being the subsets of only 14 distinct space groups, the so-called 14 *Bravais lattices*. The hierarchy of the symmetries among the 7 crystal systems can be explored via the matrix \mathbf{G} :

$$\mathbf{G} = \mathbf{A} \cdot \tilde{\mathbf{A}} = \begin{bmatrix} \mathbf{a}_1 \cdot \mathbf{a}_1 & \mathbf{a}_1 \cdot \mathbf{a}_2 & \mathbf{a}_1 \cdot \mathbf{a}_3 \\ \mathbf{a}_2 \cdot \mathbf{a}_1 & \mathbf{a}_2 \cdot \mathbf{a}_2 & \mathbf{a}_2 \cdot \mathbf{a}_3 \\ \mathbf{a}_3 \cdot \mathbf{a}_1 & \mathbf{a}_3 \cdot \mathbf{a}_2 & \mathbf{a}_3 \cdot \mathbf{a}_3 \end{bmatrix} = \begin{bmatrix} g_{11} & g_{12} & g_{13} \\ g_{21} & g_{22} & g_{23} \\ g_{31} & g_{32} & g_{33} \end{bmatrix} \quad (1-4)$$

where the basis matrix \mathbf{A} and its transpose $\tilde{\mathbf{A}}$ are defined as:

$$\mathbf{A} = \begin{bmatrix} \mathbf{a}_1 \\ \mathbf{a}_2 \\ \mathbf{a}_3 \end{bmatrix}, \quad \tilde{\mathbf{A}} = [\mathbf{a}_1 \quad \mathbf{a}_2 \quad \mathbf{a}_3] \quad (1-5)$$

For example, the matrix \mathbf{G} with all the non-zero elements g_{ij} and the non-equal diagonal elements determines a *triclinic lattice*; the *monoclinic lattice* can be reached with g_{13} , g_{23} , g_{31} and g_{32} equal to zero; the *orthorhombic lattice* possesses with all null non-diagonal elements; further more, the *tetragonal lattice* requires $g_{11}=g_{22} \neq g_{33}$; finally, the *cubic lattice* demands $g_{11}=g_{22}=g_{33}$.

Periodicity in Perfect Crystals

In the Bravais lattice, the three vectors $[n_1a_1, 0, 0]$, $[0, n_2a_2, 0]$ and $[0, 0, n_3a_3]$ form a parallelepiped unit cell. Although the definition of a unit cell is arbitrary, a unit cell can be topologically classified into two different types, i.e., the *primitive cell* containing only one Bravais lattice point with all integers being units and the *conventional cell* containing more than one Bravais lattice point with at least one integer being non-unit. Nevertheless, the transformation between the primitive cell and conventional cell for a particular Bravais lattice is straightforward. For example, the transformation from a primitive cell P to a C-face centered conventional cell C is given by equation (1-6):

$$\mathbf{A}(C) = \mathbf{A}(P) \begin{bmatrix} 1 & 1 & 0 \\ -1 & 1 & 0 \\ 0 & 0 & 1 \end{bmatrix} \quad (1-6)$$

Although the crystallographer usually describes a crystal and determines its structure with the conventional cell, the conventional cell is not a good choice for solid state theoreticians to derive its electronic quantum states. The reason is that the conventional cell brings a redundant amount of one- and two-electron integrals to be evaluated, which is unnecessary except that one needs to handle defects or impurities in crystals. On the other hand, the primitive cell is advantageous to reduce the computational cost as further as possible due to the translational invariance of these integrals. However, the cost that one has to pay by choosing a general primitive cell is likely the loss of some point symmetries of the Bravais lattice. In 1933, Wigner and Seitz came up with a special unit cell, i.e., the *Wigner-Seitz cell* [58] for the first serious attempt to calculate a first-principles band structure of metallic sodium. The Wigner-Seitz cell is constructed by drawing lines connecting a point to all nearby others in the Bravais lattice, bisecting each line with a plane, and taking the smallest polyhedron containing the point bounded by these planes. Therefore a Wigner-Seitz cell spans the entire Bravais lattice with neither overlapping nor leaving any gaps or holes in between. By far, the price of losing symmetries for the primitive cell has been paid off by a Wigner-Seitz cell since it contains the complete symmetry operations of the Bravais lattice but only one lattice point. Thus it is still the most common choice even today.

Besides the type of Bravais lattice, the crystal structure also depends on the physical basis with real objects at each lattice point. Therefore, there may be more than one atom, ion or molecule even in a primitive cell with only one lattice point. By taking into account the basis structure with a certain arbitrary symmetry, there are 32 crystallographic point groups and 230 space groups, which equivalently correspond to the 7 crystal systems and 14 Bravais lattices for abstract lattice points with spherical symmetry at each point. In a unit cell (either primitive cell or conventional cell), not all sites that atoms, ions or molecules are occupying are unrelated to each other, i.e., some sites are invariant to one or more symmetry operations. The minimum set of atoms, ions or molecules that generates the complete unit cell after the application of all space group symmetry operations is referred to an *asymmetric unit*. That is the reason why in the ICSD

Periodicity in Perfect Crystals

(Inorganic Crystal Structure Database) only the coordinates of atoms in the asymmetric unit are given. Unlike the lattice point with integer coordinates, neither like the Cartesian coordinates for molecules, the position \mathbf{r} of an atom within an asymmetric unit is expressed in terms of fractional coordinates x_1, x_2 and x_3 ranging between 0 and 1:

$$\mathbf{r} = x_1 \mathbf{a}_1 + x_2 \mathbf{a}_2 + x_3 \mathbf{a}_3 \quad (1-7)$$

1.2 Crystal electronic states in reciprocal space

Let us examine the matrix \mathbf{G} in (1-4) again. If the \mathbf{G} is set up between the basis vector \mathbf{A} and another set of basis vector \mathbf{B} , and let \mathbf{G} equal to the unit matrix normalized by a factor 2π , we come to:

$$\mathbf{G} = \mathbf{A} \cdot \tilde{\mathbf{B}} = \begin{bmatrix} \mathbf{a}_1 \cdot \mathbf{b}_1 & \mathbf{a}_1 \cdot \mathbf{b}_2 & \mathbf{a}_1 \cdot \mathbf{b}_3 \\ \mathbf{a}_2 \cdot \mathbf{b}_1 & \mathbf{a}_2 \cdot \mathbf{b}_2 & \mathbf{a}_2 \cdot \mathbf{b}_3 \\ \mathbf{a}_3 \cdot \mathbf{b}_1 & \mathbf{a}_3 \cdot \mathbf{b}_2 & \mathbf{a}_3 \cdot \mathbf{b}_3 \end{bmatrix} = 2\pi \begin{bmatrix} 1 & 0 & 0 \\ 0 & 1 & 0 \\ 0 & 0 & 1 \end{bmatrix} \quad (1-8)$$

where we end up with a new space \mathbf{B} which is determined by the reciprocal of space \mathbf{A} with $\tilde{\mathbf{B}} = 2\pi \mathbf{A}^{-1}$. Therefore \mathbf{B} is called the *reciprocal space*¹ relative to the *direct space* \mathbf{A} . The basis vectors in the two spaces are transformed to each other following the important orthogonal rule:

$$\mathbf{a}_i \cdot \mathbf{b}_j = 2\pi \delta_{ij} \quad (1-9)$$

The basis vectors $\mathbf{b}_1, \mathbf{b}_2$ and \mathbf{b}_3 enclose a reciprocal lattice cell. Any reciprocal vector \mathbf{K} can be expressed as:

$$\mathbf{K} = q_1 \mathbf{b}_1 + q_2 \mathbf{b}_2 + q_3 \mathbf{b}_3 \quad (1-10)$$

If a crystal is composed of N_1, N_2 and N_3 cells along $\mathbf{a}_1, \mathbf{a}_2$ and \mathbf{a}_3 lattice direction, there are $N_1 \times N_2 \times N_3$ number of \mathbf{k} points in every reciprocal lattice cell, each of which can be written as:

$$\mathbf{k} = \frac{k_1}{N_1} \mathbf{b}_1 + \frac{k_2}{N_2} \mathbf{b}_2 + \frac{k_3}{N_3} \mathbf{b}_3 \quad (1-11)$$

Here the integer k_i follows $0 \leq k_i < N_i$. Therefore the number of \mathbf{k} points in each reciprocal cell is almost infinite and the coordinates of \mathbf{k} points can be regarded as continuous since N_i goes almost to the infinity. This is essentially where the continuous band structure of a crystal originates, as discussed in the following.

The wavefunction $\Psi_i(\mathbf{r})$ for the i -th crystal orbital should not only meet the Schrödinger equation (1-12), but also need to fulfill an additional eigenequation (1-13) due to the periodic condition as well as the translation operator \mathbf{T}_R commuting with the Hamiltonian $H(\mathbf{r})$:

¹ In the crystallographic community, the reciprocal space is defined without the factor 2π . In the present thesis, however, we prefer this factor since it simplifies the notation of describing the crystal wavefunctions.

Periodicity in Perfect Crystals

$$H(\mathbf{r})\Psi_i(\mathbf{r}) = \varepsilon_i\Psi_i(\mathbf{r}) \quad (1-12)$$

$$\mathbf{T}_{\mathbf{R}}\Psi_i(\mathbf{r}) = \Psi_i(\mathbf{r} + \mathbf{R}) = \lambda\Psi_i(\mathbf{r}) \quad (1-13)$$

where the eigenvalue λ in the second equation can be proven [59, 60, 61] to be a plane-wave factor $e^{i\mathbf{k}\cdot\mathbf{R}}$ with the wave-vector \mathbf{k} and the direct lattice vector \mathbf{R} defined in (1-11) and (1-2), respectively. It turns out that the crystal wavefunction $\Psi_i(\mathbf{r})$ and orbital energy ε_i should also be functions of the continuous \mathbf{k} points in the reciprocal space, as shown in (1-14) and (1-15). Here the latter is known as the **Bloch theorem** [62] and $\Psi_i(\mathbf{r}; \mathbf{k})$ is called a **Bloch function**, or **crystalline orbital** (CO) associated with the Hamiltonian $H(\mathbf{r})$:

$$H(\mathbf{r})\Psi_i(\mathbf{r}; \mathbf{k}) = \varepsilon_i(\mathbf{k})\Psi_i(\mathbf{r}; \mathbf{k}) \quad (1-14)$$

$$\Psi_i(\mathbf{r} + \mathbf{R}; \mathbf{k}) = e^{i\mathbf{k}\cdot\mathbf{R}}\Psi_i(\mathbf{r}; \mathbf{k}) \quad (1-15)$$

If the eigenenergy $\varepsilon_i(\mathbf{k})$ for the i -th crystal orbital is plotted against the \mathbf{k} points, one ends up with a continuous curve. A family of such curves with respect to all the orbital levels forms a **band structure**, where the orbital level index i is referred to the **band index**. This infinite and continuous electronic state distribution in crystals essentially results from the periodicity condition (i.e., the translation symmetry), which marks the crucial difference from molecules whose electronic states are finitely separated.

On the other hand, a complete energy band structure demonstrates the translation invariance by a reciprocal lattice vector \mathbf{K} in (1-16), due to the factor $e^{i\mathbf{K}\cdot\mathbf{R}} = 1$, the rotation invariance by a rotation operation β in (1-17) as well as the time-reversal invariance in (1-18):

$$\varepsilon_i(\mathbf{k}) = \varepsilon_i(\mathbf{k} + \mathbf{K}) \quad (1-16)$$

$$\varepsilon_i(\mathbf{k}) = \varepsilon_i(\beta\mathbf{k}) \quad (1-17)$$

$$\varepsilon_i(\mathbf{k}) = \varepsilon_i(-\mathbf{k}) \quad (1-18)$$

Thanks to (1-16), (1-17) and (1-18), it is not necessary to explore the entire reciprocal space to derive the crystal electronic state. The most common solution for this problem is to construct a Wigner-Seitz primitive cell in the reciprocal space, termed only for the \mathbf{k} -space cell as the *first Brillouin zone*, where all the possible crystal electronic states can be sorted out. The Brillouin zone is important not only to the solid state electronic states but also to the lattice dynamics as will be discussed in Chapter 5. Therefore, following the first Brillouin zone these \mathbf{k} points range as:

$$-\frac{\mathbf{b}_i}{2} \leq \mathbf{k} < \frac{\mathbf{b}_i}{2} \quad (1-19)$$

where the corresponding integers k_i in (1-11) should meet:

$$-\frac{N_i}{2} \leq k_i < \frac{N_i}{2} \quad (1-20)$$

Periodicity in Perfect Crystals

For the practical solid state calculation, as handling the infinite number of \mathbf{k} points is totally beyond the ken of mortal, the finite \mathbf{k} -mesh is produced following the suggestion by Monkhorst and Pack [63], as being implemented in many codes like the CRYSTAL03 [64] package. In the Monkhorst net, the N_1 , N_2 and N_3 in (1-11) are replaced by the shrinking factors S_1 , S_2 and S_3 with the common factor of 2 or 3 that is required by the available point symmetry operations. The shrinking factors generate a finite commensurate grid which specifies that only $S_1 \times S_2 \times S_3$ number of \mathbf{k} points is taken along each direction of \mathbf{b}_1 , \mathbf{b}_2 and \mathbf{b}_3 inside one reciprocal lattice cell. However, the actual need for those inequivalent \mathbf{k} points in the irreducible part (i.e., the asymmetric unit in reciprocal space) of the first Brillouin zone is much less than the total $S_1 \times S_2 \times S_3$ number of \mathbf{k} points, which is approximately given by $\frac{S_1 \times S_2 \times S_3}{h}$, where h is the order of the point group.

The Bloch theorem (1-15) states that the crystal wavefunction $\Psi_i(\mathbf{r}; \mathbf{k})$ is not invariant with respect to a general direct lattice vector \mathbf{R} defined in (1-1), since the plane-wave factor $e^{i\mathbf{k} \cdot \mathbf{R}}$ leads to a phase variation of a wavefunction. However, such a periodicity is preserved if the crystal is regarded as a three-dimensional infinite $m \times m \times m$ array of identical and continuous crystals each of which consists of $N_1 \times N_2 \times N_3$ number of cells closed by the three lattice basis vectors \mathbf{a}_1 , \mathbf{a}_2 and \mathbf{a}_3 :

$$\mathbf{R}_{mN} = mN_1 \mathbf{a}_1 + mN_2 \mathbf{a}_2 + mN_3 \mathbf{a}_3 \quad (1-21)$$

Consequently we come to the ***Born-von Karman boundary condition*** in (1-22) by combining (1-9), (1-11), (1-15) and (1-21):

$$\begin{aligned} \Psi_i(\mathbf{r} + \mathbf{R}_{mN}; \mathbf{k}) &= e^{i(\frac{k_1}{N_1} \mathbf{b}_1 + \frac{k_2}{N_2} \mathbf{b}_2 + \frac{k_3}{N_3} \mathbf{b}_3) \cdot (mN_1 \mathbf{a}_1 + mN_2 \mathbf{a}_2 + mN_3 \mathbf{a}_3)} \Psi_i(\mathbf{r}; \mathbf{k}) \\ &= e^{im(k_1 \mathbf{b}_1 \cdot \mathbf{a}_1 + k_2 \mathbf{b}_2 \cdot \mathbf{a}_2 + k_3 \mathbf{b}_3 \cdot \mathbf{a}_3)} \Psi_i(\mathbf{r}; \mathbf{k}) \\ &= e^{i2\pi m(k_1 + k_2 + k_3)} \Psi_i(\mathbf{r}; \mathbf{k}) \\ &= \Psi_i(\mathbf{r}; \mathbf{k}) \end{aligned} \quad (1-22)$$

However, the crystal wavefunction $\Psi_i(\mathbf{r}; \mathbf{k})$ is periodic and invariant with respect a reciprocal lattice vector \mathbf{K} defined in (1-10):

$$\Psi_i(\mathbf{r}; \mathbf{k} + \mathbf{K}) = \Psi_i(\mathbf{r}; \mathbf{k}) \quad (1-23)$$

The Bloch theorem (1-15) and the periodicity of (1-23) in the reciprocal space can be schematically represented in Figure 1-1 for the two-dimensional lattice.

Before we proceed to the next chapter on the first-principles methods of calculating crystals, some general features of Bloch functions and corresponding integrals rooting upon the translation symmetry need to be stressed, irrelevant to what kinds of basis sets and potentials are applied. Let us consider a periodic potential function $U(\mathbf{r})$ with the same periodicity and symmetry of the direct Bravais lattice. From the textbook

Periodicity in Perfect Crystals

mathematics, a continuous derivative periodic function can be expanded by a Fourier series over a discrete variable. Therefore both the crystal Bloch function $\Psi_i(\mathbf{r}; \mathbf{k})$ and the potential function $U(\mathbf{r})$ can be written as:

$$\Psi_i(\mathbf{r}; \mathbf{k}) = \sum_{\mathbf{K}} c_{i,\mathbf{K}} e^{i(\mathbf{k}+\mathbf{K})\cdot\mathbf{r}} \quad (1-24)$$

$$U(\mathbf{r}) = \sum_{\mathbf{K}} u_{\mathbf{K}} e^{i\mathbf{K}\cdot\mathbf{r}} \quad (1-25)$$

The following integral spanning the entire crystal space thus has the form:

$$\begin{aligned} U_{ij}(\mathbf{k}, \mathbf{k}') &= \langle \Psi_i(\mathbf{r}; \mathbf{k}) | U(\mathbf{r}) | \Psi_j(\mathbf{r}; \mathbf{k}') \rangle \\ &= \sum_{\mathbf{K}} \sum_{\mathbf{K}'} \sum_{\mathbf{K}''} c_{i,\mathbf{K}} c_{j,\mathbf{K}'} u_{\mathbf{K}''} \langle e^{i(\mathbf{k}+\mathbf{K})\cdot\mathbf{r}} | e^{i\mathbf{K}''\cdot\mathbf{r}} | e^{i(\mathbf{k}'+\mathbf{K}')\cdot\mathbf{r}} \rangle \\ &= \sum_{\mathbf{K}} \sum_{\mathbf{K}'} \sum_{\mathbf{K}''} c_{i,\mathbf{K}} c_{j,\mathbf{K}'} u_{\mathbf{K}''} \int e^{i[(\mathbf{k}'+\mathbf{K}'+\mathbf{K}'')-(\mathbf{k}+\mathbf{K})]\cdot\mathbf{r}} d\mathbf{r} \\ &= \sum_{\mathbf{K}} \sum_{\mathbf{K}'} \sum_{\mathbf{K}''} c_{i,\mathbf{K}} c_{j,\mathbf{K}'} u_{\mathbf{K}''} \delta[(\mathbf{k}'+\mathbf{K}'+\mathbf{K}'')-(\mathbf{k}+\mathbf{K})] \end{aligned} \quad (1-26)$$

The last equality is due to the Fourier transform of a δ -function. It turns out that the integral is non-zero only if:

$$\mathbf{k}'+\mathbf{K}'+\mathbf{K}'' = \mathbf{k} + \mathbf{K} \quad (1-27)$$

In view of the definitions of \mathbf{K} in (1-10) and \mathbf{k} in (1-11), the above equality (1-27) should be fulfilled for any reciprocal lattice vector \mathbf{K} , \mathbf{K}' and \mathbf{K}'' only if:

$$\mathbf{k}' = \mathbf{k} \quad (1-28)$$

It turns out that all integrals that need to be evaluated for solving the Schrödinger equation (1-14) should be zero between two different reciprocal lattice \mathbf{k} points, since all the potential functions including the kinetic energy term adding up to $H(\mathbf{r})$ are periodic as the Bravais lattice. It means that the Hamiltonian matrix (e.g., the kinetic energy matrix, the electron-electron potential matrix and the electron-nuclear potential matrix) is block-diagonal with each block referring to one particular point \mathbf{k} in the reciprocal space, given that the Bloch basis is applied to construct the crystal wavefunctions. The number of these \mathbf{k} -blocks is infinite since it is exactly given by the number of infinite \mathbf{k} points. That is to say, the translation symmetry transforms a problem of an infinite size into an infinite number of problems with a finite size. The finite size of every \mathbf{k} -block is identical and determined by the size of the basis sets. Fortunately, as we have discussed above, the finite delicate \mathbf{k} points with high symmetries can be sampled in the first Brillouin zone to solve (1-14) with high accuracies. All these \mathbf{k} -blocks are virtually independent to each other since each \mathbf{k} -block belongs to one irreducible representation for a translation group², labeled as \mathbf{k} . Such an advantage has been implemented in most solid state codes by using the powerful parallel technique that all \mathbf{k} points are distributed onto different computer

² The translation group is an invariant subgroup of the space group for a particular Bravais lattice with only the translation operations. The character for each irreducible representation \mathbf{k} of a translation group is $e^{i\mathbf{k}\cdot\mathbf{R}}$.

Periodicity in Perfect Crystals

nodes and thus these \mathbf{k} -blocks can be simultaneously calculated independently. However, it is not necessary to calculate all these finite \mathbf{k} -points since the eigenvectors of any two \mathbf{k} -blocks can be transformed to each other and their eigenvalues essentially coincide as long as one \mathbf{k} point is moved to the other \mathbf{k} point by the point group operations of the space group. This is why the Schrödinger equation (1-14) is only solved at those inequivalent \mathbf{k} points in the irreducible region of the first Brillouin zone, as we mentioned above.

Besides the translation symmetry, the point group symmetry is significant to one particular \mathbf{k} -block within which the reducible structure is composed of block-diagonal irreducible blocks (**IR**-blocks) which are sorted by the point group symmetry. One special reciprocal point is the origin in the first Brillouin zone, which is called Γ point with the full point symmetry of the Bravais lattice. All the other \mathbf{k} points belong to the subgroups of Γ point group. The diagonalization of every **IR**-block needs to be performed only for one particular operation and all other eigenvectors of this **IR**-block are readily available by corresponding transformations of this known eigenvector. This is effective when the dimensionality of an **IR**-block is high³.

Summing up, the dimensionality of each Hamiltonian matrix $D_{\mathbf{H}}$ is given by the following formula:

$$D_{\mathbf{H}} = \sum_{\mathbf{k}} n_{\mathbf{k}} D_{\mathbf{k}} \quad (1-29)$$

where $n_{\mathbf{k}}$ is the number of the equivalent \mathbf{k} points, and the sum runs over all inequivalent \mathbf{k} point. $D_{\mathbf{k}}$ is the dimensionality of each \mathbf{k} -block, i.e., the constant size of basis sets:

$$D_{\mathbf{k}} = \sum_{\mathbf{IR}} D_{\mathbf{IR}} n_{\mathbf{IR}} \quad (1-30)$$

where $D_{\mathbf{IR}}$ is the dimensionality of each **IR**-block and $n_{\mathbf{IR}}$ is the number of those blocks belonging to the same **IR**.

³ In the reciprocal space, the dimensionality of an **IR**-block for some certain \mathbf{k} points can be far more than three, which is obviously the maximum in the direct space. For example, there are 6-dimensional **IR**-blocks at H point according to the cubic space group $Ia3d$.

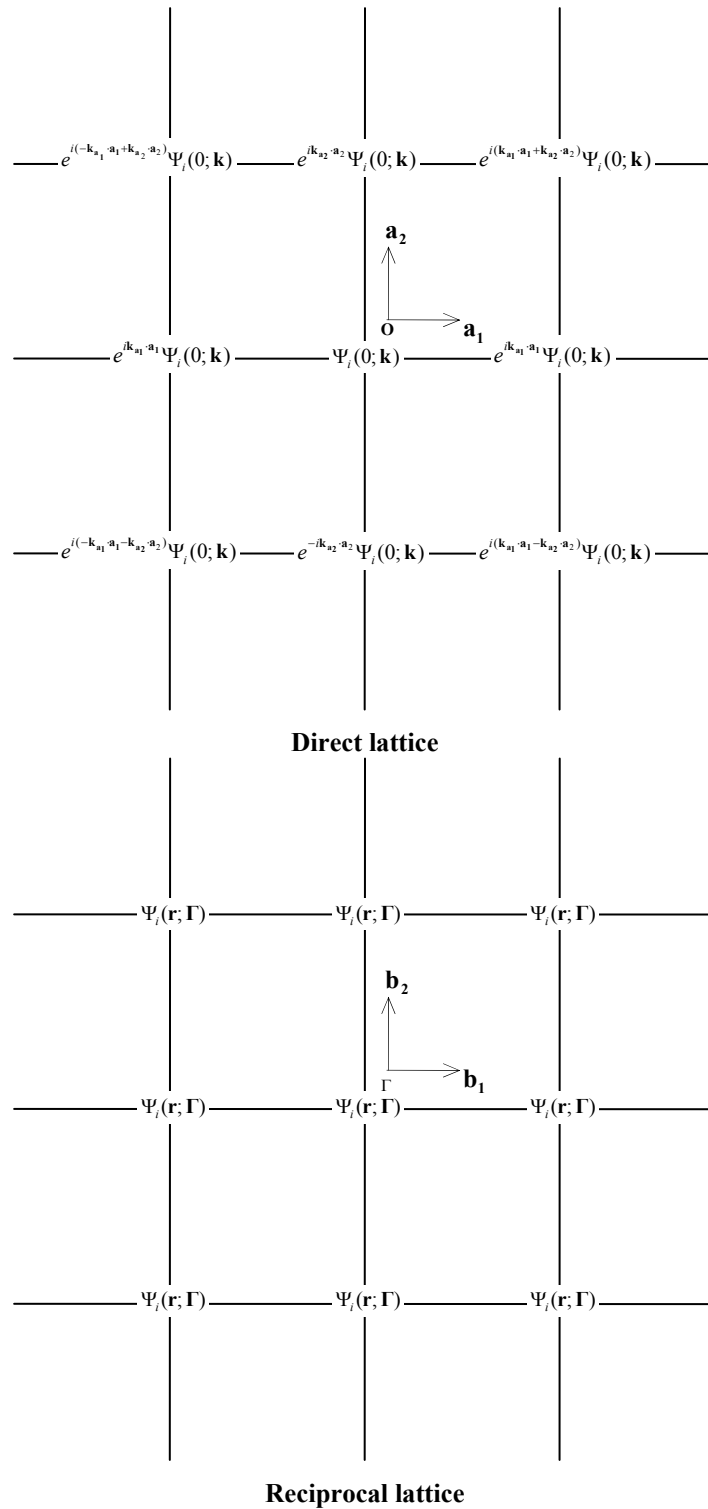


Figure 1-1 The schematic illustration of crystal wavefunctions at different two-dimensional lattice points in both direct space (top) and reciprocal space (bottom).

Chapter 2 Deriving Band Structures

The general features of crystal wavefunctions depicted in Chapter 1 are actually derived with only the assumptions of the *Born-Oppenheimer* approximation and the translation invariance. Generally, we can write down the Schrödinger equation in (2-1) which is the eigen-equation of the total crystal wavefunction $\Psi_0(\mathbf{r}_1\sigma_1, \mathbf{r}_2\sigma_2, \dots, \mathbf{r}_N\sigma_N; \mathbf{k})$ for an N -electron crystal:

$$\left(-\frac{1}{2}\sum_i^N \nabla^2(\mathbf{r}_i) + U\right)\Psi_0(\mathbf{r}_1\sigma_1, \mathbf{r}_2\sigma_2, \dots, \mathbf{r}_N\sigma_N; \mathbf{k}) = E_0(\mathbf{k})\Psi_0(\mathbf{r}_1\sigma_1, \mathbf{r}_2\sigma_2, \dots, \mathbf{r}_N\sigma_N; \mathbf{k}) \quad (2-1)$$

where U is the real non-relativistic potential⁴ with the same periodicity as the Bravais lattice expressed in (2-2), and $E_0(\mathbf{k})$ is the total ground state energy at a particular \mathbf{k} point.

$$U = -\sum_i^N \sum_A \frac{Z_A}{|\mathbf{r}_i - \mathbf{r}_A|} + \frac{1}{2} \sum_i^N \sum_{j \neq i}^N \frac{1}{|\mathbf{r}_i - \mathbf{r}_j|} \quad (2-2)$$

However, the Schrödinger equation (2-1) is too complicated to be solvable due to the difficulty of treating the actual inter-electronic interactions in a many-electron problem. One approach is to simplify the many-electron wavefunction into antisymmetrized products of one-electron wavefunctions (i.e., the single-determinant approximation) while the potential U retains the exact form as in (2-2). Most of the available methods for solid state calculations are based on this simplification. Due to the one-electron approximation with the potential (2-2), a moving electron is sensing a mean-potential which is created by the other $N-1$ electrons. This is called *mean-field approximation*, which essentially gives the birth to *Hartree-Fock* (HF) theory. Such a simplification is, although qualitatively good for most systems staying close to their equilibrium ground states, not sufficient for accurate calculations except for systems containing one electron or at most only few electrons, since a considerable part of electron-electron correlations has not been accounted for. Although many sophisticated schemes have been invented to consider the correlation effects in molecules with high accuracy, for solids such treatments are still at an earlier stage and only the *density functional theory* (DFT) approach seems to be prevailing in the solid state community. DFT essentially modifies the one-electron Fock operator by adding an additional exchange-correlation potential to the classic electron-electron Coulomb repulsion and thus in its Kohn-Sham formulation attempts to map the many-electron problem to an efficient one-electron problem. Besides the DFT approach, the highly correlating wavefunction methods have also been suggested to be applicable to periodic systems in association with the *incremental scheme* (cf. the section 2.7.2).

⁴ The relativistic corrections will be considered in Chapter 3.

2.1 Setting up one-electron Bloch orbitals

The total crystal wavefunction $\Psi_0(\mathbf{r}_1\sigma_1, \mathbf{r}_2\sigma_2, \dots, \mathbf{r}_N\sigma_N; \mathbf{k})$ at \mathbf{k} is constructed by the following *Slater determinant* for an N -electron system according to the antisymmetry principle demanded by the Pauli exclusion rule:

$$\Psi_0(\mathbf{r}_1\sigma_1, \mathbf{r}_2\sigma_2, \dots, \mathbf{r}_N\sigma_N; \mathbf{k}) = \frac{1}{\sqrt{N!}} \begin{vmatrix} \Psi_1(\mathbf{r}_1; \mathbf{k})\omega_1 & \Psi_2(\mathbf{r}_1; \mathbf{k})\omega_1 & \cdots & \Psi_N(\mathbf{r}_1; \mathbf{k})\omega_1 \\ \Psi_1(\mathbf{r}_2; \mathbf{k})\omega_2 & \Psi_2(\mathbf{r}_2; \mathbf{k})\omega_2 & \cdots & \Psi_N(\mathbf{r}_2; \mathbf{k})\omega_2 \\ \vdots & \vdots & & \vdots \\ \Psi_1(\mathbf{r}_N; \mathbf{k})\omega_N & \Psi_2(\mathbf{r}_N; \mathbf{k})\omega_N & \cdots & \Psi_N(\mathbf{r}_N; \mathbf{k})\omega_N \end{vmatrix} \quad (2-3)$$

where σ_i is the spin coordinate of the i -th electron at the spin function ω_i with either spin-up or spin-down. $\Psi_i(\mathbf{r}; \mathbf{k})$ is the one-electron crystal partial orbital, usually represented by different basis functions, i.e., either the local atomic orbitals, or the plane-waves, or even the superposition of both. All of them would be equivalent to derive the crystal electronic states, only if that an infinite number of basis functions was considered. However, they are not equivalent in the practical calculation and their accuracies depend on the implementation of the corresponding methods.

In the history of developing methods to derive the one-electron crystal orbitals, there have been two completely contradictory philosophies regarding the potential experienced by electrons in crystals, i.e., the *tight-binding approximation* and the weak periodic potential approximation, both of which end up having the practical utilities and surprising reconciliation.

The tight-binding approximation considers a solid as a collection of weakly interacting neutral atoms with their local electrons moving tightly around the nuclei on the lattice sites. In other words, the tight-binding approximation deals with the case in which the overlap of atomic wavefunctions is enough to require corrections to the picture of isolated atoms, but not so much as to render the atomic description completely irrelevant [59]. Therefore the wavefunctions of isolated atoms with the modified or even abandoned tail regions are good approximations to the Bloch orbitals. This strategy is similar in many aspects to molecular cases based on the scheme of MO-LCAO, and provides a language familiar by the chemical community, particular suitable to describe the chemical bonds. The one-electron crystal orbital $\Psi_i(\mathbf{r}; \mathbf{k})$ is written as the linear combination of the translation-symmetrized atomic orbitals, i.e., the local Bloch orbitals $\Phi_j(\mathbf{r}; \mathbf{k})$, used as the one-electron basis set:

$$\Psi_i(\mathbf{r}; \mathbf{k}) = \sum_j^{J \geq N} c_{ji}(\mathbf{k}) \Phi_j(\mathbf{r}; \mathbf{k}) \quad (2-4)$$

That is to say, the Bloch orbital $\Phi_j(\mathbf{r}; \mathbf{k})$ is the real basis set to solve the one-electron Schrödinger equation unlike in the molecular case where the local Gaussian or Slater orbitals are directly applied as the basis sets. The number J determines the size of Bloch

Deriving Band Structures

basis sets. However, this method especially with the addition of diffuse functions often leads to enormous numerical instabilities due to the linear dependence problem, caused by the non-orthogonality in the CO-LCAO approach, on the description of free or nearly free electrons in conductors and metals. One possible reason is that the translational invariance in crystals requires that the tails of atomic orbitals in one unit cell should not spatially overlap with the function in the next neighbor unit cell (see Figure 2-1).

On the contrary, the weak periodic potential approximation regards solids the other way round that the electrons are only weakly perturbed by the periodic potential of the atoms or ions. Accordingly the periodic Bloch orbitals are represented by the plane-waves expansion in (1-24). The plane-wave methods are more suitable to the description of delocalized electrons in systems such as metals and other conductors. As a matter of fact, it was the fever of exploiting the constitution of metals by quantum mechanics that has motivated the plane-wave methods since 1930's which in turn were found most successful for the band structures of several specific metals. However, the plane-wave expansion in (1-24) has proven in practice to be very slowly convergent for the major reason that the plane-waves approximate well the fluctuation of real wavefunctions and potentials in the vicinity of nuclei only if the number of plane-waves is large enough along with the large wave vectors \mathbf{k} . Several efforts have been made to tackle this problem by replacing the plane-wave factors $e^{i(\mathbf{k}+\mathbf{K})\cdot\mathbf{r}}$ by other plane-wave-like functions $\Phi(\mathbf{r};\mathbf{k}+\mathbf{K}_j)$ in (2-5).

$$\Psi_i(\mathbf{r};\mathbf{k}) = \sum_j^{J \geq N} c_i(\mathbf{K}_j) \Phi(\mathbf{r};\mathbf{k}+\mathbf{K}_j) \quad (2-5)$$

Several attempts have been put to establish $\Phi(\mathbf{r};\mathbf{k}+\mathbf{K}_j)$. Herring developed *orthogonalized plane-waves* (OPW) method in 1940 [65] by demanding the orthogonality between $\Phi(\mathbf{r};\mathbf{k}+\mathbf{K}_j)$ and the core orbitals, followed by the extension of OPW with the *pseudopotential* method by Phillips and Kleinman in 1959 [66] by completely eliminating the core wavefunctions. There are other attempts, by using the *Muffin-Tin potential*, associated with the superposition of local functions with a more rapid oscillatory atomic behavior for the core electrons sensing a spherical potential and the finite number of plane-waves for the interstitial valence electrons sensing a constant potential. For example, Slater proposed the *augmented plane-waves* (APW) method in 1937 [67] and 1953 [68, 69]; Korringa in 1947 [70], Kohn and Rostoker in 1954 [71] alternatively provided a so-called *KKR* approach based on the Green's function, general and exact for the Muffin-Tin potential. In 2001, Schwarz et al. [72] further developed an efficient *Full-potential* method called the *linearized augmented plane-waves* (LAPW) method and the new APW+lo, based on the linear method of band theory by Anderson [73] and the energy derivative of the radial solution for APW by Arbman et al. [74] in 1975.

Deriving Band Structures

All the above methods are designed to calculate the dispersion relation $\varepsilon_i(\mathbf{k})$ with respect to \mathbf{k} points for energy bands in crystals. There is another scheme called $\mathbf{k}\cdot\mathbf{p}$ method, however, which enables knowledge of the $\varepsilon_i(\mathbf{k})$ relation at some given point \mathbf{k}_0 to be extended into the vicinity of this point, without further numerical solution of the Schrödinger equation. This method is essentially based on the perturbation theory in the momentum space associated with momentum eigenfunctions.

2.2 Setting up the one-electron Hamiltonian

In this part, we discuss the HF theory for solids, where in principle either CO-LCAO or plane-waves⁵ can be applied. The total electronic energy $E_0(\mathbf{k})$ at \mathbf{k} is the expectation value of the Hamiltonian $H(\mathbf{r})$:

$$E_0(\mathbf{k}) = \langle \Psi_0(\mathbf{k}) | H(\mathbf{r}) | \Psi_0(\mathbf{k}) \rangle \quad (2-6)$$

By applying the Slater determinant (2-3) in (2-6) and minimizing $E_0(\mathbf{k})$ with respect to a trial crystal orbital $\Psi_i^0(\mathbf{r}; \mathbf{k})$ according to the variational principle:

$$\Psi_i^0(\mathbf{r}; \mathbf{k}) \rightarrow \Psi_i^0(\mathbf{r}; \mathbf{k}) + \delta\Psi_i^0(\mathbf{r}; \mathbf{k}) \quad (2-7)$$

one gets a one-electron canonical HF equation, similar to the one for molecules:

$$f(\mathbf{r}; \mathbf{k})\Psi_i(\mathbf{r}; \mathbf{k}) = \varepsilon_i(\mathbf{k})\Psi_i(\mathbf{r}; \mathbf{k}) \quad (2-8)$$

Here the one-electron Fock operator $f(\mathbf{r})$ is:

$$f(\mathbf{r}; \mathbf{k}) = -\frac{1}{2}\nabla^2(\mathbf{r}) - \sum_A \frac{Z_A}{|\mathbf{r} - \mathbf{r}_A|} + \sum_j^N J_j(\mathbf{r}; \mathbf{k}) - \sum_j^N K_j(\mathbf{r}; \mathbf{k}) \quad (2-9)$$

with the Coulomb and Exchange operators defined by their effects on the crystal orbital $\Psi_i(\mathbf{r}; \mathbf{k})$, respectively:

Coulomb operator:

$$J_j(\mathbf{r}; \mathbf{k})\Psi_i(\mathbf{r}; \mathbf{k}) = \left[\int \Psi_j^*(\mathbf{r}'; \mathbf{k}) \frac{1}{|\mathbf{r} - \mathbf{r}'|} \Psi_j(\mathbf{r}'; \mathbf{k}) d\mathbf{r}' \right] \Psi_i(\mathbf{r}; \mathbf{k}) \quad (2-10)$$

Exchange operator:

$$K_j(\mathbf{r}; \mathbf{k})\Psi_i(\mathbf{r}; \mathbf{k}) = \left[\int \Psi_j^*(\mathbf{r}'; \mathbf{k}) \frac{1}{|\mathbf{r} - \mathbf{r}'|} \Psi_i(\mathbf{r}'; \mathbf{k}) d\mathbf{r}' \right] \Psi_j(\mathbf{r}; \mathbf{k}) \quad (2-11)$$

The equation (2-8) can be written as an equivalent matrix representation, for example, by combining (2-4) for CO-LCAO⁶, for solids at each \mathbf{k} point in the reciprocal space, similar to the procedure of molecular HF calculations, known as ***Roothaan-Hall equation***:

⁵ However, for the technical difficulty of treating HF exchange integrals, the HF plane-waves have not yet been implemented into most solid state programs.

⁶ All equations derived in this section can be directly applied to the plane-waves methods as long as $\Phi_i(\mathbf{r}; \mathbf{k})$ is replaced by $\Phi(\mathbf{r}; \mathbf{k} + \mathbf{K}_i)$ and $c_{ij}(\mathbf{k})$ by $c_{ij}(\mathbf{K}_i)$.

Deriving Band Structures

$$\mathbf{F}(\mathbf{k})\mathbf{C}(\mathbf{k}) = \mathbf{S}(\mathbf{k})\mathbf{C}(\mathbf{k})\boldsymbol{\varepsilon}(\mathbf{k}) \quad (2-12)$$

with the orthonormalization condition (\mathbf{I} is the $J \times J$ identity matrix):

$$\mathbf{C}(\mathbf{k})\mathbf{S}(\mathbf{k})\mathbf{C}^T(\mathbf{k}) = \mathbf{I} \quad (2-13)$$

All these $J \times J$ matrices in (2-12) are read as:

Fock matrix $\mathbf{F}(\mathbf{k})$:

$$\mathbf{F}(\mathbf{k}) = \begin{pmatrix} \langle \Phi_1(\mathbf{r}; \mathbf{k}) | f(\mathbf{r}) | \Phi_1(\mathbf{r}; \mathbf{k}) \rangle & \langle \Phi_1(\mathbf{r}; \mathbf{k}) | f(\mathbf{r}) | \Phi_2(\mathbf{r}; \mathbf{k}) \rangle & \cdots & \langle \Phi_1(\mathbf{r}; \mathbf{k}) | f(\mathbf{r}) | \Phi_J(\mathbf{r}; \mathbf{k}) \rangle \\ \langle \Phi_2(\mathbf{r}; \mathbf{k}) | f(\mathbf{r}) | \Phi_1(\mathbf{r}; \mathbf{k}) \rangle & \langle \Phi_2(\mathbf{r}; \mathbf{k}) | f(\mathbf{r}) | \Phi_2(\mathbf{r}; \mathbf{k}) \rangle & \cdots & \langle \Phi_2(\mathbf{r}; \mathbf{k}) | f(\mathbf{r}) | \Phi_J(\mathbf{r}; \mathbf{k}) \rangle \\ \vdots & \vdots & \ddots & \vdots \\ \langle \Phi_J(\mathbf{r}; \mathbf{k}) | f(\mathbf{r}) | \Phi_1(\mathbf{r}; \mathbf{k}) \rangle & \langle \Phi_J(\mathbf{r}; \mathbf{k}) | f(\mathbf{r}) | \Phi_2(\mathbf{r}; \mathbf{k}) \rangle & \cdots & \langle \Phi_J(\mathbf{r}; \mathbf{k}) | f(\mathbf{r}) | \Phi_J(\mathbf{r}; \mathbf{k}) \rangle \end{pmatrix} \quad (2-14)$$

Coefficient matrix $\mathbf{C}(\mathbf{k})$:

$$\mathbf{C}(\mathbf{k}) = \begin{pmatrix} c_{11}(\mathbf{k}) & c_{12}(\mathbf{k}) & \cdots & c_{1J}(\mathbf{k}) \\ c_{21}(\mathbf{k}) & c_{22}(\mathbf{k}) & \cdots & c_{2J}(\mathbf{k}) \\ \vdots & \vdots & \ddots & \vdots \\ c_{J1}(\mathbf{k}) & c_{J2}(\mathbf{k}) & \cdots & c_{JJ}(\mathbf{k}) \end{pmatrix} \quad (2-15)$$

Overlap matrix $\mathbf{S}(\mathbf{k})$:

$$\mathbf{S}(\mathbf{k}) = \begin{pmatrix} \langle \Phi_1(\mathbf{r}; \mathbf{k}) | \Phi_1(\mathbf{r}; \mathbf{k}) \rangle & \langle \Phi_1(\mathbf{r}; \mathbf{k}) | \Phi_2(\mathbf{r}; \mathbf{k}) \rangle & \cdots & \langle \Phi_1(\mathbf{r}; \mathbf{k}) | \Phi_J(\mathbf{r}; \mathbf{k}) \rangle \\ \langle \Phi_2(\mathbf{r}; \mathbf{k}) | \Phi_1(\mathbf{r}; \mathbf{k}) \rangle & \langle \Phi_2(\mathbf{r}; \mathbf{k}) | \Phi_2(\mathbf{r}; \mathbf{k}) \rangle & \cdots & \langle \Phi_2(\mathbf{r}; \mathbf{k}) | \Phi_J(\mathbf{r}; \mathbf{k}) \rangle \\ \vdots & \vdots & \ddots & \vdots \\ \langle \Phi_J(\mathbf{r}; \mathbf{k}) | \Phi_1(\mathbf{r}; \mathbf{k}) \rangle & \langle \Phi_J(\mathbf{r}; \mathbf{k}) | \Phi_2(\mathbf{r}; \mathbf{k}) \rangle & \cdots & \langle \Phi_J(\mathbf{r}; \mathbf{k}) | \Phi_J(\mathbf{r}; \mathbf{k}) \rangle \end{pmatrix} \quad (2-16)$$

Diagonal energy matrix $\boldsymbol{\varepsilon}(\mathbf{k})$:

$$\boldsymbol{\varepsilon}(\mathbf{k}) = \begin{pmatrix} \varepsilon_1(\mathbf{k}) & 0 & \cdots & 0 \\ 0 & \varepsilon_2(\mathbf{k}) & \cdots & 0 \\ \vdots & \vdots & \ddots & \vdots \\ 0 & 0 & \cdots & \varepsilon_J(\mathbf{k}) \end{pmatrix} \quad (2-17)$$

The ij -th element of the Fock matrix $\mathbf{F}(\mathbf{k})$ is formulated in the basis of Bloch orbital $\Phi_j(\mathbf{r}; \mathbf{k})$:

$$\begin{aligned} F_{ij}(\mathbf{k}) &= \langle \Phi_i(\mathbf{r}; \mathbf{k}) | f(\mathbf{r}) | \Phi_j(\mathbf{r}; \mathbf{k}) \rangle \\ &= T_{ij}(\mathbf{k}) + Z_{ij}(\mathbf{k}) + \sum_k \sum_l P_{kl}(\mathbf{k}) \left[J_{ijkl}(\mathbf{k}) - \frac{1}{2} K_{ilkj}(\mathbf{k}) \right] \end{aligned} \quad (2-18)$$

where the first and second terms result from the one-electron Fock operators, which refer to the kinetic energy and the electron-nuclear attraction energy at \mathbf{k} , respectively. The last

Deriving Band Structures

two terms are the contributions of two-electron Fock operators, namely the Coulomb integral $J(\mathbf{k})$ and the exchange integral $K(\mathbf{k})$ at \mathbf{k} .

$$T_{ij}(\mathbf{k}) = \langle \Phi_i(\mathbf{r}; \mathbf{k}) | -\frac{1}{2} \nabla^2 | \Phi_j(\mathbf{r}; \mathbf{k}) \rangle \quad (2-19)$$

$$Z_{ij}(\mathbf{k}) = \langle \Phi_i(\mathbf{r}; \mathbf{k}) | -\sum_A \frac{Z_A}{|\mathbf{r} - \mathbf{r}_A|} | \Phi_j(\mathbf{r}; \mathbf{k}) \rangle \quad (2-20)$$

$$J_{ijkl}(\mathbf{k}) = \int \Phi_i^*(\mathbf{r}_1; \mathbf{k}) \Phi_j(\mathbf{r}_1; \mathbf{k}) \frac{1}{|\mathbf{r}_1 - \mathbf{r}_2|} \Phi_k^*(\mathbf{r}_2; \mathbf{k}) \Phi_l(\mathbf{r}_2; \mathbf{k}) d\mathbf{r}_1 d\mathbf{r}_2 \quad (2-21)$$

$$K_{ilkj}(\mathbf{k}) = \int \Phi_i^*(\mathbf{r}_1; \mathbf{k}) \Phi_l(\mathbf{r}_1; \mathbf{k}) \frac{1}{|\mathbf{r}_1 - \mathbf{r}_2|} \Phi_k^*(\mathbf{r}_2; \mathbf{k}) \Phi_j(\mathbf{r}_2; \mathbf{k}) d\mathbf{r}_1 d\mathbf{r}_2 \quad (2-22)$$

The density matrix element $P_{kl}(\mathbf{k})$ are expressed in the reciprocal space as:

$$P_{kl}(\mathbf{k}) = \sum_a^J c_{ka}^*(\mathbf{k}) c_{la}(\mathbf{k}) H(E_{\text{Fermi}} - \varepsilon_a(\mathbf{k})) \quad (2-23)$$

In order to deal with the intercrossed feature of band structures for some periodic solids (cf. Figure 2-2), the Heaviside step function H has to be introduced to build up the density matrix below the Fermi energy level E_{Fermi} ⁷. This cannot be achieved by the usual simple truncation of the sum in terms of indices of occupied orbitals. This marks the major difference from molecular cases.

The total electronic energy $E_0(\mathbf{k})$ at \mathbf{k} is given by:

$$E_0(\mathbf{k}) = \frac{1}{2} \sum_i^J \sum_j^J P_{ij}(\mathbf{k}) [T_{ij}(\mathbf{k}) + Z_{ij}(\mathbf{k}) + F_{ij}(\mathbf{k})] \quad (2-24)$$

The total ground state energy per unit cell is obtained by transforming (2-24) to the direct space with the addition of nuclear-nuclear energies E_{nn} :

$$E_0 = E_{nn} + \frac{1}{V_{BZ}} \int_{BZ} E_0(\mathbf{k}) d\mathbf{k} \quad (2-25)$$

where the integral is performed within the first Brillouin zone with the volume of V_{BZ} .

2.3 Tight-binding approximation (CO-LCAO)

The most important property of a Bloch orbital $\Phi_j(\mathbf{r}; \mathbf{k})$ is its periodicity. Therefore in CO-LCAO, the first step for solving (2-12) is to generate the Bloch

⁷ The Fermi level $E_{\text{Fermi}}(\mathbf{k})$ is essentially available for each \mathbf{k} point, which separates the highest occupied and lowest empty states at a specific \mathbf{k} point. The plot of $E_{\text{Fermi}}(\mathbf{k})$ against \mathbf{k} coordinates is a multi-dimensional hypersurface, called **Fermi surface**, within which all the Bloch electrons are generated. In this thesis, we pick the highest occupied level among all states of a crystal available in a given \mathbf{k} -mesh as E_{Fermi} .

Deriving Band Structures

function $\Phi_j(\mathbf{r}; \mathbf{k})$ based on a non-periodic local atomic orbital $\chi_j(\mathbf{r} - \mathbf{R} - \mathbf{A}_j)$ by requiring the following transformation for an N -electron crystal:

$$\Phi_j(\mathbf{r}; \mathbf{k}) = \frac{1}{\sqrt{N}} \sum_{\mathbf{R}} e^{i\mathbf{k} \cdot \mathbf{R}} \chi_j(\mathbf{r} - \mathbf{R} - \mathbf{A}_j) \quad (2-26)$$

where \mathbf{A}_j is the coordinate of the nucleus in the 0-cell (reference cell) on which the j -th atomic orbital $\chi_j(\mathbf{r} - \mathbf{R} - \mathbf{A}_j)$ is centered, and the sum runs over the set of all lattice vectors \mathbf{R} (cf. Figure 2-3). The Bloch basis $\Phi_j(\mathbf{r}; \mathbf{k})$ comes thereby as a complex function in contrary to the real basis for molecules, which may lead to more severe numerical problems.

2.3.1 Gaussian basis sets

The Gaussian type orbitals (GTO) are by far the most common choice to expand the atomic orbitals $\chi_j(\mathbf{r} - \mathbf{R} - \mathbf{A}_j)$ in the same LCAO approach for molecules. $\chi_j(\mathbf{r} - \mathbf{R} - \mathbf{A}_j)$ is approximated by a linear combination of a finite number of GTOs at the same center as $G(\zeta_\mu; \mathbf{r} - \mathbf{R} - \mathbf{A}_j)$ times the spherical harmonics $Y_{lm}(\theta, \phi)$ describing the orbital shape:

$$\chi_j(\mathbf{r} - \mathbf{R} - \mathbf{A}_j) = \sum_{\mu}^{n_G} g_{\mu} G(\zeta_{\mu}; \mathbf{r} - \mathbf{R} - \mathbf{A}_j) Y_{lm}(\theta, \phi) \quad (2-27)$$

Some detailed reviews of GTO are available for molecules in references [75, 76, 77]. The equation (2-27) is called a **contraction** of the n_G **primitive Gaussians** $G(\zeta_{\mu}; \mathbf{r} - \mathbf{R} - \mathbf{A}_j)$ with predefined exponents ζ_{μ} , weighed by the contraction coefficient g_{μ} . Usually these exponents of primitive Gaussians are optimized independently for atoms at the HF level, and some diffuse exponents need to be modified or even eliminated when they are applied to solids.

There are two basic forms of contractions, namely **segmented contraction** and **general contraction**. The segmented contractions are disjointed, i.e., given primitive Gaussians appear only in one contraction. The general contractions, on the contrary, allow each of the primitives to appear in each basis function (contraction). The segmented contractions are far more popular for solid state calculations and will be applied in this thesis.

The **minimal basis sets** provide only one single contraction which includes only one primitive Gaussian for each j -th atomic orbital. The quality of larger basis sets is denoted by double- ζ , triple- ζ , quadruple- ζ , quintuple- ζ , ..., where the number of “ ζ ”s originally referred to the number of contractions assigned to each atomic orbital. Nowadays the number of “ ζ ”s indicates the number of contractions only for valence atomic orbitals. These kinds of basis sets are termed **split-valence basis sets**. Sometimes it is necessary to augment the original basis sets with one additional Gaussian primitive, called **polarization function**, of an angular momentum that is typically higher by one than the

Deriving Band Structures

highest angular momentum in the remaining basis sets. Too diffuse Gaussian primitives with low exponents often cause a numerical catastrophe due to the non-orthogonality in the HF CO-LCAO approach and should be thus avoided in the solid state calculations in order to remove the linear- or quasi-linear-dependence problems.

Each primitive Gaussian is virtually an approximation of the eigenfunction of the Hamiltonian for a one-electron system with a spherical potential. So far there are two types of GTOs, the **Spherical GTO** (SGTO) denoted in (2-26) and the **Cartesian GTO** (CGTO) in (2-28).

For SGTO:

$$G(\zeta_\mu; \mathbf{r} - \mathbf{R} - \mathbf{A}_j) = C(\zeta_\mu, n)(r - R - A_j)^{n-1} e^{-\zeta_\mu(r-R-A_j)^2} \quad (2-28)$$

with the normalization factor $C(\zeta_\mu, n)$:

$$C(\zeta_\mu, n) = \sqrt{\frac{2^{2n}(n-1)!}{2n-1}} \sqrt{\frac{(2\zeta_\mu)^{2n+1}}{\pi}} \quad (2-29)$$

For CGTO:

$$G(\zeta_\mu; \mathbf{r} - \mathbf{R} - \mathbf{A}_j) = N(\zeta_\mu, n)(x_r - x_R - x_{A_j})^{n_x} (y_r - y_R - y_{A_j})^{n_y} (z_r - z_R - z_{A_j})^{n_z} e^{-\zeta_\mu(r-R-A_j)^2} \quad (2-30)$$

with the normalization factor $N(\zeta_\mu, n)$:

$$N(\zeta_\mu, n) = \left[\left(\frac{2}{\pi} \right)^{\frac{3}{4}} \frac{2^n \zeta_\mu^{\frac{2n+3}{4}}}{\sqrt{(2n_x-1)!(2n_y-1)!(2n_z-1)!}} \right] \quad n = n_x + n_y + n_z \quad (2-31)$$

The CGTO leads to redundant functions for the Gaussians with the angular momentum higher than one. For example, the CGTO with $n_x + n_y + n_z = 2$ gives six Cartesian Gaussians due to the six possible sets of sums for n , whereas there are only five linearly independent and orthogonal d orbitals. In addition to the five 3d functions one 3s function is generated. Similarly for $n_x + n_y + n_z = 3$ ten f -type Cartesian Gaussians for only seven linearly independent and orthogonal f orbitals are generated. In addition to these seven 4f functions three 4p functions result. These redundant functions are not independent and thus may cause the linear dependence problems due to the non-orthogonality of basis sets in the CO-LCAO approach. It is indeed even more problematic and computationally inefficient for the integral evaluations as the quantum numbers are further increased. Therefore only SGTOs have been implemented in the CO-LCAO approach and applied in this thesis.

The segmented contractions belonging to a given atom are grouped in shells corresponding to the same value of principal and angular quantum numbers, e.g., the 1s-

Deriving Band Structures

shell is a collection of 1s-type GTOs with $n=1$, 2p-shell is a collection of 2p-type GTOs with $n=2$, 3d-shell is a collection of 3d-type GTOs with $n=3$, and so on. In some codes like CRYSTAL03 [64], the *sp-shell constraint* is also one option to share the same number of contractions and exponents of corresponding Gaussian primitives for all atomic orbitals with the same principal quantum number, which considerably speeds up the calculation by reducing the cost of integral evaluations.

2.3.2 Self-consistent procedure

Inserting (2-24) into (2-25), the total ground state energy per unit cell E_0 is eventually written as:

$$E_0 = E_{nn} + \frac{1}{2} \sum_i^J \sum_j^J \sum_{\mathbf{R}} P_{ij}^{\mathbf{R}} [T_{ij}^{\mathbf{R}} + Z_{ij}^{\mathbf{R}} + F_{ij}^{\mathbf{R}}] \quad (2-32)$$

where $P_{ij}^{\mathbf{R}}$ is the density matrix element in the direct space, which is determined by the inverse Fourier transform from the reciprocal to the direct space:

$$P_{ij}^{\mathbf{R}} = \frac{1}{V_{BZ}} \int_{BZ} P_{ij}(\mathbf{k}) e^{i\mathbf{k}\cdot\mathbf{R}} d\mathbf{k} \quad (2-33)$$

The Fock matrix element $F_{ij}(\mathbf{k})$, kinetic energy matrix element $T_{ij}(\mathbf{k})$ and electron-nuclear attraction matrix element $Z_{ij}(\mathbf{k})$ in the Bloch basis can be written as the Fourier-transforms from the direct to the reciprocal space in the atomic orbitals (local basis sets) $\chi_i(\mathbf{r} - \mathbf{A}_i)$ in the 0-cell and $\chi_j(\mathbf{r} - \mathbf{R} - \mathbf{A}_j)$ in the \mathbf{R} -cell:

$$F_{ij}(\mathbf{k}) = \sum_{\mathbf{R}} F_{ij}^{\mathbf{R}} e^{i\mathbf{k}\cdot\mathbf{R}} \quad (2-34)$$

$$T_{ij}(\mathbf{k}) = \sum_{\mathbf{R}} T_{ij}^{\mathbf{R}} e^{i\mathbf{k}\cdot\mathbf{R}} \quad (2-35)$$

$$Z_{ij}(\mathbf{k}) = \sum_{\mathbf{R}} Z_{ij}^{\mathbf{R}} e^{i\mathbf{k}\cdot\mathbf{R}} \quad (2-36)$$

The corresponding coefficients in the direct space are:

$$\begin{aligned} F_{ij}^{\mathbf{R}} &= \langle \chi_i(\mathbf{r} - \mathbf{A}_i) | f(\mathbf{r}) | \chi_j(\mathbf{r} - \mathbf{R} - \mathbf{A}_j) \rangle \\ &= T_{ij}^{\mathbf{R}} + Z_{ij}^{\mathbf{R}} + \sum_k^J \sum_l^J \sum_{\mathbf{G}} P_{kl}^{\mathbf{G}} \sum_{\mathbf{H}} \left[J_{ijkl}^{\mathbf{0},\mathbf{R},\mathbf{H},\mathbf{H}+\mathbf{G}} - \frac{1}{2} K_{ilkj}^{\mathbf{0},\mathbf{H}+\mathbf{G},\mathbf{H},\mathbf{R}} \right] \end{aligned} \quad (2-37)$$

$$T_{ij}^{\mathbf{R}} = \langle \chi_i(\mathbf{r} - \mathbf{A}_i) | -\frac{1}{2} \nabla^2 | \chi_j(\mathbf{r} - \mathbf{R} - \mathbf{A}_j) \rangle \quad (2-38)$$

$$Z_{ij}^{\mathbf{R}} = \langle \chi_i(\mathbf{r} - \mathbf{A}_i) | -\sum_A \frac{Z_A}{|\mathbf{r} - \mathbf{r}_A|} | \chi_j(\mathbf{r} - \mathbf{R} - \mathbf{A}_j) \rangle \quad (2-39)$$

where in (2-37) the Coulomb and exchange integrals in the atomic orbitals are:

Deriving Band Structures

$$J_{ijkl}^{0,\mathbf{R},\mathbf{H},\mathbf{H}+\mathbf{G}} = \int \chi_i^*(\mathbf{r}_1 - \mathbf{A}_i) \chi_j(\mathbf{r}_1 - \mathbf{R} - \mathbf{A}_j) \frac{1}{|\mathbf{r}_1 - \mathbf{r}_2|} \chi_k^*(\mathbf{r}_2 - \mathbf{H} - \mathbf{A}_k) \chi_l(\mathbf{r}_2 - \mathbf{H} - \mathbf{G} - \mathbf{A}_l) d\mathbf{r}_1 d\mathbf{r}_2 \quad (2-40)$$

$$K_{ilkj}^{0,\mathbf{H}+\mathbf{G},\mathbf{H},\mathbf{R}} = \int \chi_i^*(\mathbf{r}_1 - \mathbf{A}_i) \chi_l(\mathbf{r}_1 - \mathbf{H} - \mathbf{G} - \mathbf{A}_l) \frac{1}{|\mathbf{r}_1 - \mathbf{r}_2|} \chi_k^*(\mathbf{r}_2 - \mathbf{H} - \mathbf{A}_k) \chi_j(\mathbf{r}_2 - \mathbf{R} - \mathbf{A}_j) d\mathbf{r}_1 d\mathbf{r}_2 \quad (2-41)$$

The overlap matrix element $S_{ij}^{\mathbf{R}}$ in the atomic orbitals (local basis sets) is:

$$S_{ij}(\mathbf{k}) = \sum_{\mathbf{R}} S_{ij}^{\mathbf{R}} e^{i\mathbf{k}\cdot\mathbf{R}} \quad (2-42)$$

$$S_{ij}^{\mathbf{R}} = \langle \chi_i(\mathbf{r} - \mathbf{A}_i) | \chi_j(\mathbf{r} - \mathbf{R} - \mathbf{A}_j) \rangle \quad (2-43)$$

The total energy of an infinite crystal is obviously infinite and has no physical meaning, but the total energy per unit cell, more specifically for the 0-cell in this case, which includes the interaction of the nuclei and electrons in the 0-cell with all nuclei and electrons in the entire crystal, is finite. In this total energy expression (2-32), the major difference compared to that of molecular cases is that a new sum over the infinite direct lattice vectors \mathbf{R} takes place.

It is possible to compare the self-consistent steps of solid calculations implemented in the CRYSTAL03 [64] program with the main steps, e.g., suggested by Szabo and Ostlund in [78], for molecules.

1. Specify a crystal with fractional atomic coordinates in an asymmetric unit, lattice constants, atomic numbers and space group;
2. Specify Gaussian primitives $G(\zeta_\mu; \mathbf{r} - \mathbf{R} - \mathbf{A}_j)$ with adjusted exponents and form the contractions times angular functions for atomic orbitals $\chi_j(\mathbf{r} - \mathbf{R} - \mathbf{A}_j)$ as a local basis set with contraction coefficients following (2-27); Express the Bloch basis $\Phi_j(\mathbf{r}; \mathbf{k})$ according to (2-26);
3. Evaluate the matrix elements $S_{ij}^{\mathbf{R}}$, $T_{ij}^{\mathbf{R}}$, $Z_{ij}^{\mathbf{R}}$, $J_{ijkl}^{0\mathbf{R}\mathbf{H}\mathbf{G}}$ and $K_{ilkj}^{0\mathbf{G}\mathbf{H}\mathbf{R}}$ in the atomic orbitals according to (2-43), (2-38), (2-39), (2-40) and (2-41), respectively ⁸;
4. Guess initial density matrix elements $P_{ij}(\mathbf{k})$;

⁸ In the conventional approach, these integrals are stored in memory or on disk and replicated to the next self-consistent cycle without being calculated again, suitable for small systems; the alternative direct approach for large systems is to recalculate these integrals in each self-consistent cycle, which on the other hand dramatically increases the computational time.

Deriving Band Structures

5. Perform the inverse Fourier transform of $P_{ij}(\mathbf{k})$ in the reciprocal space to form the density matrix elements $P_{ij}^{\mathbf{R}}$ in the direct space by (2-33);
6. Evaluate the Fock matrix elements $F_{ij}^{\mathbf{R}}$ based on the results of step 3 and 5 according to (2-37);
7. Perform the Fourier transform of $S_{ij}^{\mathbf{R}}$ and $F_{ij}^{\mathbf{R}}$ in the direct space to form the corresponding matrix elements $S_{ij}(\mathbf{k})$ and $F_{ij}(\mathbf{k})$ in the reciprocal space according to (2-42) and (2-34);
8. Solve the Roothaan-Hall equation (2-12) with the condition (2-13) at every \mathbf{k} point of the sampling net;
9. Determine the Fermi energy E_{Fermi} , which is the highest energy value $\varepsilon_i(\mathbf{k}_j)$ of an occupied state in the system inside the first Brillouin zone;
10. Check whether the procedure has converged in terms of the difference between the new density matrix of step 8 and the previous density matrix within a specified criterion. If not, repeat steps 5 to 10 to find the new density matrix elements $P_{ij}(\mathbf{k})$;
11. Calculate the total energy per unit cell by (2-32);

2.3.3 Coulomb and exchange integrals criteria

The detailed discussion on Coulomb and exchange integral calculations in the local basis sets associated with the role of symmetry is available in the paper by Dovesi [79]. It has to be manifested that the equations (2-32), (2-34)~(2-37) and (2-42) are totally useless unless one indicates an economical, reasonably precise, asymptotically exact procedure to handle the three indices \mathbf{R} , \mathbf{G} , and \mathbf{H} direct lattice infinite sum. It must also be stressed that the individual sum of Coulomb and exchange integrals in (2-35) diverges and that the convergence is obtained by a delicate balance between the two different contributions. In the presentation of the CRYSTAL03 package [64], the truncation criteria have been proposed for both Coulomb [80] and exchange series [81]. The main points are summarized as follows:

1. The one-electron integrals $T_{ij}^{\mathbf{R}}$ and $Z_{ij}^{\mathbf{R}}$ as well as the two-electron Coulomb integral J_{ijkl}^{ORHG} are disregarded by truncating the \mathbf{R} sum in (2-32) or the \mathbf{G} sum in (2-37), when, either the overlap distribution $Q_1 = \langle \chi_i(\mathbf{r}_1 - \mathbf{A}_i) | \chi_j(\mathbf{r}_1 - \mathbf{R} - \mathbf{A}_j) \rangle$ with respect to \mathbf{R} or $Q_2 = \langle \chi_k(\mathbf{r}_2 - \mathbf{H} - \mathbf{A}_k) | \chi_l(\mathbf{r}_2 - \mathbf{H} - \mathbf{G} - \mathbf{A}_l) \rangle$ with respect to \mathbf{G} , is smaller than an “overlap” threshold, also-called **Coulomb overlap threshold ITOL1** in the CRYSTAL03 package.
2. The truncation of the \mathbf{H} sum in (2-37) is more delicate since it indicates the distance between the two contributions Q_1 and Q_2 . The so-called **Coulomb penetration threshold**

Deriving Band Structures

ITOL2 is applied to tell the attribution of the interaction between Q_1 and Q_2 is evaluated whether exactly or approximately. If Q_1 and Q_2 do not penetrate each other due to a large $|\mathbf{H}|$ value, where the charge Q_2 in the cell \mathbf{H} belongs to the “monoelectronic zone” of Q_1 , the Coulomb integral $\langle Q_1 | Q_2 \rangle$ is evaluated by a multipolar expansion truncated at some given L value termed **POLEORDER**; otherwise, when the penetration between Q_1 and Q_2 is larger than **ITOL2**, where the charge Q_2 in the cell \mathbf{H} belongs to the “bielectronic zone” of Q_1 , the Coulomb integral $\langle Q_1 | Q_2 \rangle$ is evaluated exactly. Consequently, by setting **ITOL2** to an extremely low level, all the two-electron integrals are calculated exactly.

3. For the exchange integral $K_{ilkj}^{0,\mathbf{H}+\mathbf{G},\mathbf{H},\mathbf{R}}$ similar to the case 1, the \mathbf{H} sum is truncated, when either the overlap distribution $\langle \chi_i(\mathbf{r}_1 - \mathbf{A}_i) | \chi_l(\mathbf{r}_1 - \mathbf{H} - \mathbf{G} - \mathbf{A}_l) \rangle$ or $\langle \chi_k(\mathbf{r}_2 - \mathbf{H} - \mathbf{A}_k) | \chi_j(\mathbf{r}_2 - \mathbf{R} - \mathbf{A}_j) \rangle$ is smaller than an **Exchange overlap threshold ITOL3**.

4. The situation is more complicated when the sums of \mathbf{R} and \mathbf{G} are concerned. Therefore two arbitrary **exchange pseudoverlap thresholds ITOL4** and **ITOL5** are suggested for $\langle \chi_i(\mathbf{r}_1 - \mathbf{A}_i) | \chi_j(\mathbf{r}_2 - \mathbf{R} - \mathbf{A}_j) \rangle$ and $\langle \chi_k(\mathbf{r}_2 - \mathbf{H} - \mathbf{A}_k) | \chi_l(\mathbf{r}_1 - \mathbf{H} - \mathbf{G} - \mathbf{A}_l) \rangle$ for exchange integrals. Both of \mathbf{R} and \mathbf{G} sum are special since they concern not only the exchange integral but also the density matrix elements. It has been further suggested [82] that the truncation of \mathbf{G} sum should be much more severe than that of \mathbf{R} sum by three to eight orders of magnitude to remove the distortion of the exchange potential and thus to achieve a stable self-consistent behavior in most cases.

2.4 Plane-waves (PW)

2.4.1 Orthogonalized plane-waves (OPW)

An alternative method for the one-electron crystal orbital $\Psi_i(\mathbf{r}; \mathbf{k})$ in (2-5) is to set up proper Bloch functions $\Phi(\mathbf{r}; \mathbf{k} + \mathbf{K}_j)$ which combine rapid oscillations in the core region with plane-wave-like behaviors interstitially, namely the orthogonalized plane-waves suggested by Herring [65]. In this method, no special potentials are required for the following methods where the crystal potentials have been simplified along with the adaptation of orbitals. By distinguishing $\Psi_i(\mathbf{r}; \mathbf{k})$ between the valence electrons and core electrons, $\Psi_i(\mathbf{r}; \mathbf{k})$ is expanded by remaining the plane-wave factor $e^{i(\mathbf{k}+\mathbf{K})\cdot\mathbf{r}}$ in (1-24) but with the addition of the linear combination of core orbitals $\Psi_c(\mathbf{r}; \mathbf{k})$:

$$\Phi(\mathbf{r}; \mathbf{k} + \mathbf{K}_j) = e^{i(\mathbf{k}+\mathbf{K}_j)\cdot\mathbf{r}} + \sum_{c \in \text{core}} b_c(\mathbf{k} + \mathbf{K}_j) \Psi_c(\mathbf{r}; \mathbf{k}) \quad (2-44)$$

where the sum in (2-44) is over only all core levels for the Bloch wave-vector \mathbf{k} . The core

Deriving Band Structures

orbitals $\Psi_c(\mathbf{r}; \mathbf{k})$ are taken to be the tight-binding linear combination of atomic core orbitals $\chi_c(\mathbf{r} - \mathbf{R} - \mathbf{A}_j)$ similar to (2-26).

$$\Psi_c(\mathbf{r}; \mathbf{k}) = \frac{1}{\sqrt{N}} \sum_{\mathbf{R}} e^{i\mathbf{k}\cdot\mathbf{R}} \chi_c(\mathbf{r} - \mathbf{R} - \mathbf{A}_j) \quad (2-45)$$

By requiring $\Phi(\mathbf{r}; \mathbf{k} + \mathbf{K}_j)$ being orthogonal to every core level $\Psi_c(\mathbf{r}; \mathbf{k})$ ⁹:

$$\int \Psi_c^*(\mathbf{r}; \mathbf{k}) \Phi(\mathbf{r}; \mathbf{k} + \mathbf{K}_j) d\mathbf{r} = 0 \quad (2-46)$$

and by assuming the condition that:

$$\int \Psi_c^*(\mathbf{r}; \mathbf{k}) \Psi_{c'}(\mathbf{r}; \mathbf{k}) d\mathbf{r} = \delta_{cc'} \quad (2-47)$$

the coefficient $b_c(\mathbf{k} + \mathbf{K}_j)$ can be readily shown as:

$$b_c(\mathbf{k} + \mathbf{K}_j) = - \int \Psi_c^*(\mathbf{r}; \mathbf{k}) e^{i(\mathbf{k} + \mathbf{K}_j)\cdot\mathbf{r}} d\mathbf{r} \quad (2-48)$$

The faster convergence compared to that of pure plane-waves is a consequence of the fact that the Fock matrix element $F_{ij}^{\text{OPW}}(\mathbf{k})$ for OPW turns out to be much smaller than $F_{ij}^{\text{PW}}(\mathbf{k})$ for pure plane-waves.

2.4.2 Pseudopotentials (PP)

Let us look at another face of the OPW method, called the Pseudopotential method, which is formally transformed from OPW. The one-electron crystal state $\Psi_i(\mathbf{r}; \mathbf{k})$ formed in terms of equation (2-44) and (2-5) actually corresponds to the exact valence wavefunction $\Psi_v(\mathbf{r}; \mathbf{k})$,

$$\Psi_v(\mathbf{r}; \mathbf{k}) = \phi_v(\mathbf{r}; \mathbf{k}) - \sum_{c \in \text{core}} \left(\int \Psi_c^*(\mathbf{r}; \mathbf{k}) \phi_v(\mathbf{r}; \mathbf{k}) d\mathbf{r} \right) \Psi_c(\mathbf{r}; \mathbf{k}) \quad (2-49)$$

where the plane-wave part is written as:

$$\phi_v(\mathbf{r}; \mathbf{k}) = \sum_j c_v(\mathbf{K}_j) e^{i(\mathbf{k} + \mathbf{K}_j)\cdot\mathbf{r}} \quad (2-50)$$

Both the exact valence and core orbitals $\Psi_c(\mathbf{r}; \mathbf{k})$ and $\Psi_v(\mathbf{r}; \mathbf{k})$ satisfy the Schrödinger equation with the eigenvalue $\varepsilon_v(\mathbf{k})$ and $\varepsilon_c(\mathbf{k})$, respectively:

$$H(\mathbf{r})\Psi_v(\mathbf{r}; \mathbf{k}) = \varepsilon_v(\mathbf{k})\Psi_v(\mathbf{r}; \mathbf{k}) \quad (2-51)$$

$$H(\mathbf{r})\Psi_c(\mathbf{r}; \mathbf{k}) = \varepsilon_c(\mathbf{k})\Psi_c(\mathbf{r}; \mathbf{k}) \quad (2-52)$$

⁹ Note that $\Phi(\mathbf{r}; \mathbf{k} + \mathbf{K})$ is also automatically orthogonal to $\Psi_c(\mathbf{r}; \mathbf{k}')$ when $\mathbf{k}' \neq \mathbf{k}$ due to the Bloch condition.

Deriving Band Structures

Combining equations from (2-49) to (2-52), one goes to an interesting so-called effective Schrödinger equation for which the plane-wave part $\phi_v(\mathbf{r}; \mathbf{k})$ turns out to be solved in this eigenfunction:

$$[T(\mathbf{r}) + U_{Pseudo}] \phi_v(\mathbf{r}; \mathbf{k}) = \varepsilon_v(\mathbf{k}) \phi_v(\mathbf{r}; \mathbf{k}) \quad (2-53)$$

where the **pseudopotential** U_{Pseudo} is defined to be the sum of the actual periodic potential $U(\mathbf{r})$ and U_R :

$$U_{Pseudo} = U(\mathbf{r}) + U_R \quad (2-54)$$

where the complicated nonlocal operator U_R has the property of transformation:

$$U_R \phi_v(\mathbf{r}; \mathbf{k}) = \sum_{c \in core} [\varepsilon_v(\mathbf{k}) - \varepsilon_c(\mathbf{k})] \left(\int \Psi_c^*(\mathbf{r}; \mathbf{k}) \phi_v(\mathbf{r}; \mathbf{k}) d\tau \right) \Psi_c(\mathbf{r}; \mathbf{k}) \quad (2-55)$$

Since the effective Schrödinger equation (2-53) provides a **pseudo wavefunction** $\phi_v(\mathbf{r}; \mathbf{k})$ as the eigenfunction, formed by the linear combination of plane-wave, it is helpful to find the pseudopotential, U_{Pseudo} , small enough that the Bloch electrons in crystals can be treated as nearly free electrons. This is actually true according to (2-55) which takes a positive U_R and partially cancels the actual potential $U(\mathbf{r})$, since the valence orbital energies lie above the core energies. There appears to be many ways other than (2-55) to define U_R such that the equation (2-53) has the same valence eigenvalues as the actual crystal Hamiltonian $H(\mathbf{r})$ [83].

2.5 Superposition of GTO+PW

In the following methods, the approximation of a special periodic potential, i.e., Muffin-Tin potential for APW and KKR or Full-potential for LAPW, is demanded for the superposition of local orbitals and plane-waves.

2.5.1 Augmented plane-waves (APW)

In order to make the Schrödinger equation more easily solvable, Slater in 1937 first simplified the real crystal potential to a Muffin-Tin (M-T) potential for the core in each Wigner-Seitz cell [67]:

$$U_{M-T}(\mathbf{r}) = \begin{cases} V(\mathbf{r} - \mathbf{R} - \mathbf{A}_{r_c}), & \text{for } |\mathbf{r} - \mathbf{R} - \mathbf{A}_{r_c}| < r_c \\ 0, & \text{for } |\mathbf{r} - \mathbf{R} - \mathbf{A}_{r_c}| \geq r_c \end{cases} \quad (2-56)$$

Here \mathbf{A}_{r_c} is the coordinate for a nucleus in the \mathbf{R} -cell with the specified critical radius r_c .

Therefore the total periodic M-T potential can be simply written down as:

$$U_{M-T}(\mathbf{r}) = \sum_{\mathbf{R}} V(\mathbf{r} - \mathbf{R} - \mathbf{A}_{r_c}) \quad (2-57)$$

Deriving Band Structures

The M-T potential indicates that the potential $U_{M-T}(\mathbf{r})$ is a sphere within a spherical core of radius r_c around each atom or ion, and taken to be a constant (usually zero) in the interstitial region between two cores. The r_c is taken to be less than half of the nearest-neighbor distance so that the spheres do not overlap. Usually, for each type of nucleus with the critical radius r_c , there exists a spherical potential $V(\mathbf{r} - \mathbf{R} - \mathbf{A}_{r_c})$ for it.

Correspondingly, the $\Phi(\mathbf{r}; \mathbf{k})$ in (2-5) can be achieved as a plane-wave in the flat interstitial region, while forcing $\Phi(\mathbf{r}; \mathbf{k})$ to have a more rapid oscillatory atomic behavior in the core region [68]:

$$\begin{aligned} \Phi(\mathbf{r}; \mathbf{k}) = & H(|\mathbf{r} - \mathbf{R} - \mathbf{A}_{r_c}| - r_c) e^{i\mathbf{k}\cdot\mathbf{r}} + \\ & H(r_c - |\mathbf{r} - \mathbf{R} - \mathbf{A}_{r_c}|) \sum_{lm} a_{lm}(\mathbf{k}) R_{nl}(\varepsilon_{nl}, |\mathbf{r} - \mathbf{R} - \mathbf{A}_{r_c}|) Y_{lm}(\theta, \phi) \end{aligned} \quad (2-58)$$

where H is the Heaviside function. The coefficient $a_{lm}(\mathbf{k})$ is determined by the continuity condition of $\Phi(\mathbf{r}; \mathbf{k})$ at the boundary between atomic and interstitial regions:

$$a_{lm}(\mathbf{k}) = 4\pi^l Y_{lm}^*(\theta, \phi) \frac{j_l(\mathbf{k}, r_c)}{R_{nl}[\varepsilon_{nl}, |\mathbf{r} - \mathbf{R} - \mathbf{A}_{r_c}|]} \quad (2-59)$$

where $j_l(\mathbf{k}, r_c)$ is the Bessel function.

In the atomic region, $\Phi(\mathbf{r}; \mathbf{k})$ meets the atomic Schrödinger equation for the atom with r_c :

$$\left(-\frac{1}{2} \nabla^2 + V(\mathbf{r} - \mathbf{R} - \mathbf{A}_{r_c}) \right) \Phi(\mathbf{r}; \mathbf{k}) = \varepsilon_{nl} \Phi(\mathbf{r}; \mathbf{k}) \quad (2-60)$$

which eventually leads to the radial differential equation:

$$-\frac{1}{r^2} \frac{d}{dr} \left(r^2 \frac{dR_{nl}}{dr} \right) + \left(\frac{l(l+1)}{r^2} + V(\mathbf{r} - \mathbf{R} - \mathbf{A}_{r_c}) \right) R_{nl} = \varepsilon_{nl} R_{nl} \quad (2-61)$$

However, in the flat interstitial region, it is easy to show that $\Phi(\mathbf{r}; \mathbf{k})$ does not satisfy the equation (2-60) but the Schrödinger equation for free electrons:

$$\left(-\frac{1}{2} \nabla^2 \right) \Phi(\mathbf{r}; \mathbf{k}) = \left(\frac{\mathbf{k}^2}{2} \right) \Phi(\mathbf{r}; \mathbf{k}) \quad (2-62)$$

The one-electron crystal wavefunction $\Psi_i(\mathbf{r}; \mathbf{k})$ follows (2-5), replicated here again:

$$\Psi_i(\mathbf{r}; \mathbf{k}) = \sum_j c_i(\mathbf{K}_j) \Phi(\mathbf{r}; \mathbf{k} + \mathbf{K}_j) \quad (2-63)$$

Although $\Phi(\mathbf{r}; \mathbf{k})$ is continuous at the boundary between the atomic and interstitial region exists, the derivative on the boundary is discontinuous, which leads to the δ -singularities there for the second-order derivative of $\Phi(\mathbf{r}; \mathbf{k})$. This difficulty, which is severe for the

Deriving Band Structures

kinetic energy, can be avoided, due to Green's theorem, by applying the variational principle to the following equation:

$$\varepsilon_i(\mathbf{k}) = \frac{\int \left(\frac{1}{2} |\nabla \Psi_i(\mathbf{r}; \mathbf{k})|^2 + U_{M-T}(\mathbf{r}) |\Psi_i(\mathbf{r}; \mathbf{k})|^2 \right) d\mathbf{r}}{\int |\Psi_i(\mathbf{r}; \mathbf{k})|^2 d\mathbf{r}} \quad (2-64)$$

The APW SCF procedure is presented in the flow chart in Figure 2-4.

2.5.2 Korringa-Kohn-Rostoker (KKR)

The KKR method was originally formulated [70, 71] by applying the multiple-scattering theory to seek the solution of the Schrödinger equation and to determine the electronic band structure for solids. Later on, the KKR method was further developed based on the Green's function [84, 85, 86]. The KKR method is applied not only to perfect crystals, but also useful to treat impurities [87] and even chemically disordered alloys [88]. To facilitate the KKR method, two significant points need to be independently addressed: The Muffin-Tin potential $U_{M-T}(\mathbf{r})$ expressed in (2-57) as well as the structure factor $G_{\varepsilon_i(\mathbf{k})}(\mathbf{r}-\mathbf{r}')$ associated with the lattice geometries. The **Green function** $G_{\varepsilon_i(\mathbf{k})}(\mathbf{r}-\mathbf{r}')$ is defined through:

$$\left(\frac{1}{2} \nabla^2 + \varepsilon_i(\mathbf{k}) \right) G_{\varepsilon_i(\mathbf{k})}(\mathbf{r}-\mathbf{r}') = \delta(\mathbf{r}-\mathbf{r}') \quad (2-65)$$

The one-electron Schrödinger equation can be written down in a similar form:

$$\left(\frac{1}{2} \nabla^2 + \varepsilon_i(\mathbf{k}) \right) \Psi_i(\mathbf{r}; \mathbf{k}) = U_{M-T}(\mathbf{r}) \Psi_i(\mathbf{r}; \mathbf{k}) \quad (2-66)$$

The one-electron crystal wavefunction which is a solution of both (2-65) and (2-66) provides:

$$\Psi_i(\mathbf{r}; \mathbf{k}) = \int G_{\varepsilon_i(\mathbf{k})}(\mathbf{r}-\mathbf{r}') U_{M-T}(\mathbf{r}') \Psi_i(\mathbf{r}'; \mathbf{k}) d\mathbf{r}' \quad (2-67)$$

By taking into account the Bloch condition (1-15) as well as the total periodic M-T potential (2-57), one comes to the result formally similar to (2-67):

$$\Psi_i(\mathbf{r}; \mathbf{k}) = \int g_{\varepsilon_i(\mathbf{k})}(\mathbf{r}-\mathbf{r}'; \mathbf{k}) V(\mathbf{r}'-\mathbf{A}_{r_c}) \Psi_i(\mathbf{r}'; \mathbf{k}) d\mathbf{r}' \quad (2-68)$$

where the **structure Green function** $g_{\varepsilon_i(\mathbf{k})}(\mathbf{r}-\mathbf{r}'; \mathbf{k})$ is calculated through:

$$g_{\varepsilon_i(\mathbf{k})}(\mathbf{r}-\mathbf{r}'; \mathbf{k}) = \sum_{\mathbf{R}} G_{\varepsilon_i(\mathbf{k})}(\mathbf{r}-\mathbf{r}'-\mathbf{R}) e^{i\mathbf{k}\cdot\mathbf{R}} \quad (2-69)$$

The factor $G_{\varepsilon_i(\mathbf{k})}(\mathbf{r}-\mathbf{r}'-\mathbf{R})$ is chosen to be a single-site scattering for the free electron reference system:

Deriving Band Structures

$$G_{\varepsilon_i(\mathbf{k})}(\mathbf{r} - \mathbf{r}' - \mathbf{R}) = -\frac{e^{iP(\mathbf{k})|\mathbf{r} - \mathbf{r}' - \mathbf{R}|}}{4\pi |\mathbf{r} - \mathbf{r}' - \mathbf{R}|} \quad (2-70)$$

with the momentum $P(\mathbf{k})$ to be:

$$P(\mathbf{k}) = \begin{cases} \sqrt{\varepsilon_i(\mathbf{k})} & \text{if } \varepsilon_i(\mathbf{k}) \geq 0 \\ i\sqrt{-\varepsilon_i(\mathbf{k})} & \text{if } \varepsilon_i(\mathbf{k}) < 0 \end{cases} \quad (2-71)$$

From (2-69), all the information depending on the wave-vector \mathbf{k} and the crystal structure is contained in the structure Green function $g_{\varepsilon_i(\mathbf{k})}(\mathbf{r} - \mathbf{r}'; \mathbf{k})$, which in turn can be calculated for a variety of crystal structures of specified values of ε and \mathbf{k} , once and for all.

2.5.3 Linearized augmented plane-waves (LAPW) and APW+lo method

The main drawback of the APW method is the energy dependence of the radial function R_{nl} in (2-58), i.e., inside the M-T sphere a crystal orbital $\Psi_i(\mathbf{r}; \mathbf{k})$ can be accurately described only if ε_{nl} is equal to the eigenenergy $\varepsilon_i(\mathbf{k})$ of $\Psi_i(\mathbf{r}; \mathbf{k})$ being sought. This directly leads to the nonlinear eigenvalue problem to go through a set of different energy dependent APW basis functions for each eigenenergy $\varepsilon_i(\mathbf{k})$, which is computationally very demanding (see Figure 2-4). The first successful solution to this problem was suggested by Anderson in 1975 [73] by giving an additional linearizing term to the radial part of APW basis functions:

$$\Phi(\mathbf{r}; \mathbf{k}) = \begin{cases} e^{i\mathbf{k}\cdot\mathbf{r}}, & \text{for } |\mathbf{r} - \mathbf{R} - \mathbf{A}_{r_c}| \geq r_c \\ \sum_{lm} \left[a_{lm}(\mathbf{k}) R_{nl}(\varepsilon_{nl}, |\mathbf{r} - \mathbf{R} - \mathbf{A}_{r_c}|) \right. \\ \left. + b_{lm}(\mathbf{k}) \dot{R}_{nl}(\varepsilon_{nl}, |\mathbf{r} - \mathbf{R} - \mathbf{A}_{r_c}|) \right] Y_{lm}(\theta, \phi), & \text{for } |\mathbf{r} - \mathbf{R} - \mathbf{A}_{r_c}| < r_c \end{cases} \quad (2-72)$$

Here R_{nl} is the regular solution of the radial Schrödinger equation (2-61) at a fixed energy ε_{nl} (usually chosen at the center of the corresponding energy band with l -like character), and \dot{R}_{nl} is energy derivative of R_{nl} at the same energy ε_{nl} . The coefficients $a_{lm}(\mathbf{k})$ and $b_{lm}(\mathbf{k})$ as functions of \mathbf{k} are determined by requiring that $\Phi(\mathbf{r}; \mathbf{k})$ is not only continuous itself as in the APW method but also continuously differentiable. This is called **linearized augmented plane-waves** (LAPW). It provides a sufficiently flexible basis to properly describe eigenfunctions with those eigenenergies all of which can be obtained by one single diagonalization for the energy ε_{nl} . It turns out that the nonlinear eigenvalue problems are converted into linear eigenvalue problems with much less computational costs. However, LAPW is suitable for treating neither states that stay far from the linearization energy ε_{nl} like semicore states with a principal quantum number one less than the corresponding valence state, nor broad valence bands whose partial waves show

Deriving Band Structures

large energy variations inside the M-T sphere like d or f states. Improvements were done by Singh in 1991 [89] by further augmenting the LAPW basis set (2-72) for certain l values with local orbitals (LO), expressed in (2-73). The three coefficients in (2-73) are determined by the requirements that the LO should have zero value and slope at the M-T sphere boundary and the normalization.

$$\phi_{lm}^{LO}(\mathbf{r}) = \begin{cases} 0, \text{ for } |\mathbf{r} - \mathbf{R} - \mathbf{A}_{r_c}| \geq r_c \\ \left[\begin{array}{l} a_{lm}^{LO} R_{nl}(\varepsilon_{nl}, |\mathbf{r} - \mathbf{R} - \mathbf{A}_{r_c}|) \\ + b_{lm}^{LO} \dot{R}_{nl}(\varepsilon_{nl}, |\mathbf{r} - \mathbf{R} - \mathbf{A}_{r_c}|) \\ + c_{lm}^{LO} R_{n+1l}(\varepsilon_{nl}, |\mathbf{r} - \mathbf{R} - \mathbf{A}_{r_c}|) \end{array} \right] Y_{lm}(\theta, \phi), \text{ for } |\mathbf{r} - \mathbf{R} - \mathbf{A}_{r_c}| < r_c \end{cases} \quad (2-73)$$

Recently, Sjöstedt et al. [90] have found that such a linearization of LAPW is not most efficient and suggested an important modification of LAPW, associated with the original APW basis set (2-58), called the $APW+lo$ method, where another type of local orbitals (denoted as lo to be distinguished from LO) is introduced in (2-74). The two coefficients are determined by the normalization and the condition that $\phi_{lm}^{lo}(r_c)$ has zero value but no requirement for the slope. Therefore this set of lo has more variational flexibility than LO and provides a more efficient linearization of APW.

$$\phi_{lm}^{lo}(\mathbf{r}) = \begin{cases} 0, \text{ for } |\mathbf{r} - \mathbf{R} - \mathbf{A}_{r_c}| \geq r_c \\ \left[\begin{array}{l} a_{lm}^{lo} R_{nl}(\varepsilon_{nl}, |\mathbf{r} - \mathbf{R} - \mathbf{A}_{r_c}|) \\ + b_{lm}^{lo} \dot{R}_{nl}(\varepsilon_{nl}, |\mathbf{r} - \mathbf{R} - \mathbf{A}_{r_c}|) \end{array} \right] Y_{lm}(\theta, \phi), \text{ for } |\mathbf{r} - \mathbf{R} - \mathbf{A}_{r_c}| < r_c \end{cases} \quad (2-74)$$

The LO in (2-73) and lo in (2-74) look quite similar. However, the difference is significant since LO is combined with the LAPW basis set engaging the energy derivative \dot{R}_{nl} in (2-72) and lo with APW engaging only the radial solution R_{nl} in (2-58). This leads to the fact that \dot{R}_{nl} for lo is \mathbf{k} -independent on the plane-waves in the interstitial region and thus can be included for the physically important l -quantum numbers.

The $APW+lo$ method shows more rapid convergence with about 50% reduced basis sets than LAPW. The program WIEN2K [91] actually provides a flexibly mixed LAPW and $APW+lo$ method to treat different atoms or different l -values for the same atom. $APW+lo$ can be applied to those atoms with small M-T sphere sizes or orbitals which require a large number of plane-waves and thus converge slowly, while the rest can be handled by LAPW.

Another advantage of the linearization of APW is, as shown by Koelling [74], that it facilitates the inclusion of a **full-potential**:

Deriving Band Structures

$$U(\mathbf{r}) = \begin{cases} \sum_{lm} V_{lm}(\mathbf{r}) Y_{lm}(\mathbf{r}) \text{ for } |\mathbf{r}| < r_c \\ \sum_{\mathbf{k}} V_{\mathbf{k}} e^{i\mathbf{k}\cdot\mathbf{r}} \text{ for } |\mathbf{r}| \geq r_c \end{cases} \quad (2-75)$$

The M-T potential is actually one special case of the full-potential with $l=0$ for a spherical potential in the core region and $\mathbf{K}=0$ for a constant potential in the interstitial region.

In the practical calculation by LAPW and APW+lo routines, one needs to handle the wavefunctions with distinguishable definitions of core, semicore and valence configurations¹⁰. According to the case implemented in WIEN2K [91], core states are those, whose electrons are entirely confined inside the corresponding M-T potential and deeply low in energy. Valence states remain at the energetically highest occupied levels with electrons outside the M-T potential. Semicore states stay higher in energy than core states, but lower than valence states, which leads to the electronic population both inside and outside the M-T potential. These different states are usually prescribed by a properly selected cut-off energy E_{cutoff} separating the core states and semicore-valence states, as well as the M-T radius determining non-overlap atomic spheres identical for the same type of atoms and so adapted to E_{cutoff} that there is no leakage of core states outside the atomic sphere.

The LAPW SCF procedure is presented in Figure 2-5.

2.6 *k*-p method

The methods discussed above aim at seeking the independent solutions at different \mathbf{k} points. However, the \mathbf{k} -p method employs a different philosophy that once a solution at a certain \mathbf{k}_0 is available, the solutions at other nearby \mathbf{k} points can be obtained directly based on the perturbation theory with respect to the \mathbf{k} coordinates.

The Bloch condition (1-15) can be equivalently rewritten in terms of a periodic function $u_i(\mathbf{r}; \mathbf{k})$ with the periodicity of the lattice:

$$\Psi_i(\mathbf{r}; \mathbf{k}) = e^{i\mathbf{k}\cdot\mathbf{r}} u_i(\mathbf{r}; \mathbf{k}) \quad (2-76)$$

where for a lattice vector \mathbf{R} :

$$u_i(\mathbf{r} + \mathbf{R}; \mathbf{k}) = u_i(\mathbf{r}; \mathbf{k}) \quad (2-77)$$

It can be derived that the one-electron Schrödinger equation is transformed to:

$$\left(-\frac{\nabla^2 - k^2}{2} + U(\mathbf{r}) - i\mathbf{k} \cdot \nabla \right) u_i(\mathbf{r}; \mathbf{k}) = \varepsilon_i(\mathbf{k}) u_i(\mathbf{r}; \mathbf{k}) \quad (2-78)$$

¹⁰ Such an attempt is, however, strictly speaking, against the basic law of quantum mechanics, that electrons are regarded as indistinguishable particles each of which has a certain probability to stroll away in the entire space.

Deriving Band Structures

If we know the solution of (2-78) at a certain point \mathbf{k}_0 , we can rewrite (2-78) at a point \mathbf{k} :

$$\left[-\frac{\nabla^2 - k_0^2}{2} + U(\mathbf{r}) - i\mathbf{k}_0 \cdot \nabla\right]u_i(\mathbf{r};\mathbf{k}) - i(\mathbf{k} - \mathbf{k}_0) \cdot \nabla u_i(\mathbf{r};\mathbf{k}) = \left[\varepsilon_i(\mathbf{k}) - \frac{k^2 - k_0^2}{2}\right]u_i(\mathbf{r};\mathbf{k}) \quad (2-79)$$

Therefore the term $-i(\mathbf{k} - \mathbf{k}_0) \cdot \nabla u_i(\mathbf{r};\mathbf{k})$ is regarded as a perturbation on the Hamiltonian for $u_i(\mathbf{r};\mathbf{k}_0)$. It can be further shown by the perturbation theory that the second order correction to the energy is as follows:

$$\varepsilon_i(\mathbf{k}) = \varepsilon_i(\mathbf{k}_0) + \frac{k^2}{2} + \sum_{\mu} \sum_{\nu} \sum_{j \neq i} \frac{\langle \Psi_i(\mathbf{r};\mathbf{k}_0) | p_{\mu} | \Psi_j(\mathbf{r};\mathbf{k}_0) \rangle \langle \Psi_j(\mathbf{r};\mathbf{k}_0) | p_{\nu} | \Psi_i(\mathbf{r};\mathbf{k}_0) \rangle k_{\mu} k_{\nu}}{\varepsilon_i(\mathbf{k}_0) - \varepsilon_j(\mathbf{k}_0)} \quad (2-80)$$

The corrected wavefunction to the first-order at \mathbf{k} is:

$$\Psi_i(\mathbf{r};\mathbf{k}) = e^{i\mathbf{k} \cdot \mathbf{r}} \left(\Psi_i(\mathbf{r};\mathbf{k}_0) + \sum_{j \neq i} \frac{\langle \Psi_j(\mathbf{r};\mathbf{k}_0) | \langle \Psi_j(\mathbf{r};\mathbf{k}_0) | \mathbf{k} \cdot \mathbf{p} | \Psi_i(\mathbf{r};\mathbf{k}_0) \rangle}{\varepsilon_i(\mathbf{k}_0) - \varepsilon_j(\mathbf{k}_0)} \right) \quad (2-81)$$

2.7 Electronic correlation methods for solids

2.7.1 Density functional theory (DFT)

The most widely used correlation method for solids is probably the density functional theory (DFT). As commented for molecular cases by Parr and Yang [92], DFT is “*a remarkable theory that allows one to replace the complicated N -electron wavefunction and the associated Schrödinger equation by the much simpler density and its associated calculational scheme. Remarkable indeed!*”. All modern DFT methods are based on two fundamental theorems, well known as first and second Hohenberg-Kohn theorem established in their landmark paper in 1964 [93].

The Hamiltonian $\hat{H}(\mathbf{r})$ can be expressed as the sum of kinetic operator $\hat{T}(\mathbf{r})$, external potential $\hat{V}_{ext}(\mathbf{r})$ (by the nucleus) and electron-electron interaction $\hat{V}_{ee}(\mathbf{r})$:

$$\hat{H}(\mathbf{r}) = \hat{T}(\mathbf{r}) + \hat{V}_{ext}(\mathbf{r}) + \hat{V}_{ee}(\mathbf{r}) \quad (2-82)$$

The **first Hohenberg-Kohn theorem** states that, quoting directly from the 1964 paper and using $\rho(\mathbf{r})$ to be the electronic density, “*the external potential $\hat{V}_{ext}(\mathbf{r})$ is (within a constant) a unique functional of $\rho(\mathbf{r})$; since, in turn, $\hat{V}_{ext}(\mathbf{r})$ fixes \hat{H} we see that the full many-particle ground state is a unique functional of $\rho(\mathbf{r})$* ”. Accordingly, the total energy $E[\rho(\mathbf{r})]$ is a unique functional of the density $\rho(\mathbf{r})$ and can be decomposed into the contributions from system dependent part and an independent part with the latter universal functional called **Hohenberg-Kohn functional** $F[\rho(\mathbf{r})]$:

Deriving Band Structures

$$E[\rho(\mathbf{r})] = \underbrace{\int V_{\text{ext}}[\rho(\mathbf{r})]\rho(\mathbf{r})d\mathbf{r}}_{\text{system dependent}} + \underbrace{F[\rho(\mathbf{r})]}_{\text{universal}} \quad (2-83)$$

Here the Hohenberg-Kohn functional, which is valid for any number of particles and any external potential, can be identified as:

$$F[\rho(\mathbf{r})] = T[\rho(\mathbf{r})] + V_{ee}[\rho(\mathbf{r})] \quad (2-84)$$

$V_{ee}[\rho(\mathbf{r})]$ has contributions of the classic Coulomb repulsion and nonclassic interactions:

$$\begin{aligned} V_{ee}[\rho(\mathbf{r})] &= J[\rho(\mathbf{r})] + V_{ncl}[\rho(\mathbf{r})] \\ &= \frac{1}{2} \int \int_{\mathbf{r}_1 \mathbf{r}_2} \frac{\rho(\mathbf{r}_1)\rho(\mathbf{r}_2)}{|\mathbf{r}_1 - \mathbf{r}_2|} d\mathbf{r}_1 d\mathbf{r}_2 + V_{ncl}[\rho(\mathbf{r})] \end{aligned} \quad (2-85)$$

The *second Hohenberg-Kohn theorem* says that a functional $F[\rho(\mathbf{r})]$ which delivers the ground state energy delivers the lowest energy if and only if the trial density $\rho(\mathbf{r})$ is the true ground state density $\rho_0(\mathbf{r})$ [94]. Obviously this is nothing new but the recapitulation of the variational principle in terms of the electronic density $\rho(\mathbf{r})$ instead of wavefunctions for an N -electron system:

$$\rho^0(\mathbf{r}) \rightarrow \rho^0(\mathbf{r}) + \delta\rho^0(\mathbf{r}) \quad \int \rho^0(\mathbf{r})d\mathbf{r} = N \quad (2-86)$$

$$E_0[\rho_0(\mathbf{r})] \leq E[\rho^0(\mathbf{r})] = \int V_{\text{ext}}[\rho^0(\mathbf{r})]\rho^0(\mathbf{r})d\mathbf{r} + F[\rho^0(\mathbf{r})] \quad (2-87)$$

with the equal sign when $\rho_0(\mathbf{r}) = \rho^0(\mathbf{r})$.

Combining (2-83), (2-84) and (2-85), the complete energy functional is obtained:

$$E[\rho(\mathbf{r})] = \underbrace{\int V_{\text{ext}}[\rho(\mathbf{r})]\rho(\mathbf{r})d\mathbf{r}}_{\text{known}} + \underbrace{\frac{1}{2} \int \int \frac{\rho(\mathbf{r})\rho(\mathbf{r}')}{|\mathbf{r} - \mathbf{r}'|} d\mathbf{r}d\mathbf{r}'}_{\text{known}} + \underbrace{T[\rho(\mathbf{r})]}_{\text{unknown}} + \underbrace{V_{ncl}[\rho(\mathbf{r})]}_{\text{unknown}} \quad (2-88)$$

The central task in the DFT scheme to determine the ground state energy and density in a given external potential is to seek the universal Hohenberg-Kohn functional, i.e., to seek the unknown terms of kinetic functional and nonclassic functional. That brings DFT much more complexities than what it looks like at its first glance. A genius work was done by Kohn and Sham [95], called *Kohn-Sham approach*, by formally splitting the unknown kinetic energy functional into two parts:

$$T[\rho(\mathbf{r})] = \underbrace{T_S[\rho(\mathbf{r})]}_{\text{known by HF method}} + \underbrace{T_C[\rho(\mathbf{r})]}_{\text{unknown}} \quad (2-89)$$

$T_S[\rho(\mathbf{r})]$ is the exact kinetic energy for a non-interacting system with the same density of a real interacting one. The residual part $T_C[\rho(\mathbf{r})]$ is still unknown and contains the difference between the real kinetic energy $T[\rho(\mathbf{r})]$ and the non-interacting part $T_S[\rho(\mathbf{r})]$. $T_S[\rho(\mathbf{r})]$ can be expressed as in the HF method:

Deriving Band Structures

$$T_s[\rho(\mathbf{r})] = -\frac{1}{2} \sum_i \langle \Psi_i(\mathbf{r}) | \nabla^2 | \Psi_i(\mathbf{r}) \rangle \quad (2-90)$$

However, $T_s[\rho(\mathbf{r})]$ is neither equal to the real kinetic energy of the interacting system, nor equal to the HF kinetic energy since $T_s[\rho(\mathbf{r})]$ is a functional of the exact density of the interacting system which is not the HF density of the non-interacting system.

One can write the total energy as

$$E[\rho(\mathbf{r})] = \left\{ \underbrace{\int V_{ext}[\rho(\mathbf{r})]\rho(\mathbf{r})d\mathbf{r} + J[\rho(\mathbf{r})] + T_s[\rho(\mathbf{r})]}_{\text{known}} \right\} + \left\{ \underbrace{T_c[\rho(\mathbf{r})] + V_{ncI}[\rho(\mathbf{r})]}_{\text{unknown}} \right\} \quad (2-91)$$

and treat the two unknown terms as *exchange-correlation energy* $E_{xc}[\rho(\mathbf{r})]$:

$$E_{xc}[\rho(\mathbf{r})] = T_c[\rho(\mathbf{r})] + V_{ncI}[\rho(\mathbf{r})] \quad (2-92)$$

The latter is, although still mysterious, a kind of junk box that exactly smuggles everything unknown, i.e., the self-interaction, exchange, correlation and a portion of the kinetic energy, into the ship of the exact energy functional.

Following what has been done within the HF method along with the variational principals, the so-called one-electron ***Kohn-Sham equation*** is produced in terms of a set of one-electron *Kohn-Sham orbitals* $\Psi_i(\mathbf{r}; \sigma)$ (σ is the spin coordinate):

$$f^{KS} \Psi_i(\mathbf{r}; \sigma) = \varepsilon_i \Psi_i(\mathbf{r}; \sigma) \quad (2-93)$$

Here f^{KS} is the ***Kohn-Sham operator***:

$$f^{KS} = -\frac{1}{2} \nabla^2 - \sum_A \frac{Z_A}{|\mathbf{r} - \mathbf{r}_A|} + \int \frac{\rho(\mathbf{r}')}{|\mathbf{r} - \mathbf{r}'|} d\mathbf{r}' + V_{xc}[\rho(\mathbf{r})] \quad (2-94)$$

with the ***exchange-correlation potential*** $V_{xc}[\rho(\mathbf{r})]$, a yet unknown functional derivative of $E_{xc}[\rho(\mathbf{r})]$ with respect to the density:

$$V_{xc}[\rho(\mathbf{r})] = \frac{\delta E_{xc}[\rho(\mathbf{r})]}{\delta \rho(\mathbf{r})} \quad (2-95)$$

The Kohn-Sham orbitals $\Psi_i(\mathbf{r}; \sigma)$ are required to produce the exact density of the interacting system:

$$\rho_0(\mathbf{r}) = \sum_{\sigma} \sum_i |\Psi_i(\mathbf{r}; \sigma)|^2 = \rho_0(\mathbf{r})|_{\text{spin-up}} + \rho_0(\mathbf{r})|_{\text{spin-down}} \quad (2-96)$$

The Kohn-Sham approach, exact in principle and involving the single exchange-correlation integral for the density on the scale of N -dimensionality, generally demands the less computational efforts than the HF method, with the latter involved in the non-local exchange integral for wavefunctions on the scale of $3N$ -dimensionality.

Deriving Band Structures

The unknown part $E_{xc}[\rho(\mathbf{r})]$ remains, although mysterious and uncomfortable, formally exact and completely open for being upgraded, as has been done in the past decades from the **Local Density Approximation** (LDA) through the **Generalized Gradient Approximation** (GGA) to the **Becke three-parameter hybrid functionals** (B3).

2.7.1.1 LDA

Generally the exchange-correlation energy $E_{xc}[\rho(\mathbf{r})]$ can be expanded in the following form:

$$E_{xc}[\rho(\mathbf{r})] = \int \rho(\mathbf{r})V_{xc}[\rho(\mathbf{r})]d\mathbf{r} + \int |\nabla\rho(\mathbf{r})|^2 V_{xc}^{(2)}[\rho(\mathbf{r})]d\mathbf{r} + \dots \quad (2-97)$$

where $V_{xc}^{(2)}[\rho(\mathbf{r})]$ is the second order correction to the exchange-correlation energy. Within the LDA approach, the N -electron system can be considered to have a slowly varying density, which leads to the neglect of the density gradient $|\nabla\rho(\mathbf{r})|^2$. This simplification turns out to determine the total energy with errors of the order $|\nabla\rho(\mathbf{r})|^2$, and even surprisingly the total density with a greater accuracy at the order $|\nabla\rho(\mathbf{r})|^4$. Therefore the exchange-correlation energy is expressed as:

$$E_{xc}^{LDA}[\rho(\mathbf{r})] \approx \int \rho(\mathbf{r})V_{xc}^{LDA}[\rho(\mathbf{r})]d\mathbf{r} \quad (2-98)$$

Here $V_{xc}^{LDA}[\rho(\mathbf{r})]$ can be further split into:

$$V_{xc}^{LDA}[\rho(\mathbf{r})] = V_x^{LDA}[\rho(\mathbf{r})] + V_c^{LDA}[\rho(\mathbf{r})] \quad (2-99)$$

$V_x^{LDA}[\rho(\mathbf{r})]$ and $V_c^{LDA}[\rho(\mathbf{r})]$ denote the exchange and correlation LDA potential, respectively.

$V_x^{LDA}[\rho(\mathbf{r})]$ has an exact form for a uniform electron gas with a particular density, an excellent model for a slowly varying density, called **Dirac-Slater exchange**¹¹ [96, 97]:

$$V_x^{DS}[\rho(\mathbf{r})] = -\frac{3}{4} \left(\frac{3}{\pi} \rho(\mathbf{r}) \right)^{\frac{1}{3}} \quad (2-100)$$

Another option of the exchange potential $V_x^{LDA}[\rho(\mathbf{r})]$ for the spin σ in a spin polarized case is called **Barth-Hedin exchange** [98] within the framework of the *local spin-density approximation* (LSDA):

$$V_x^{BH}[\rho(\mathbf{r})]_{|\sigma} = A[\rho(\mathbf{r})] \left(\frac{2\rho(\mathbf{r})_{|\sigma}}{\rho(\mathbf{r})} \right)^{\frac{1}{3}} + B[\rho(\mathbf{r})] \quad (2-101)$$

$$\rho(\mathbf{r}) = \rho(\mathbf{r})_{|\text{spin-up}} + \rho(\mathbf{r})_{|\text{spin-down}} \quad (2-102)$$

¹¹ Such a form of exchange potential $V_x[\rho(\mathbf{r})]$ for a uniform electron gas was found by Slater due to his approximation of HF exchange, but was originally derived by Dirac apart from the pre-factor.

Deriving Band Structures

Although the explicit expression of the correlation part $V_c[\rho(\mathbf{r})]$ is unknown, it can be calculated, however, with highly accurate numerical quantum Monte Carlo simulations of a uniform gas from the work of Ceperley and Alder in 1980 [99]. On the basis of these results, various authors have presented analytical expressions of $V_c[\rho(\mathbf{r})]$ based on sophisticated interpolation schemes. For example, the **VWN** correlation potential was proposed by Vosko, Wilk and Nusair in 1980 [100], **PZ** by Perdew and Zunger in 1981 [101] as well as the recent **PW** by Perdew and Wang in 1992 [102].

2.7.1.2 GGA

One significant improvement of the LDA approach is to take into account not only the density but also the density gradient. Those functionals which include the gradient of the electronic density and restore the exchange-correlation hole are referred to as GGA for both spinless and spin polarized systems, which have the following general form:

$$E_{XC}^{GGA}[\rho_\alpha(\mathbf{r}), \rho_\beta(\mathbf{r})] = \int f_{XC}[\rho_\alpha(\mathbf{r}), \rho_\beta(\mathbf{r}), \nabla\rho_\alpha(\mathbf{r}), \nabla\rho_\beta(\mathbf{r})] d\mathbf{r} \quad (2-103)$$

$E_{XC}^{GGA}[\rho_\alpha(\mathbf{r}), \rho_\beta(\mathbf{r})]$ can be written as the similar sum of two parts as for LDA:

$$E_{XC}^{GGA}[\rho_\alpha(\mathbf{r}), \rho_\beta(\mathbf{r})] = E_X^{GGA}[\rho_\alpha(\mathbf{r}), \rho_\beta(\mathbf{r})] + E_C^{GGA}[\rho_\alpha(\mathbf{r}), \rho_\beta(\mathbf{r})] \quad (2-104)$$

The GGA exchange functional $E_X^{GGA}[\rho_\alpha(\mathbf{r}), \rho_\beta(\mathbf{r})]$ is specified by the exchange LDA functional corrected with the addition of a gradient factor:

$$E_X^{GGA}[\rho_\alpha(\mathbf{r}), \rho_\beta(\mathbf{r})] = E_X^{LDA}[\rho_\alpha(\mathbf{r}), \rho_\beta(\mathbf{r})] - \sum_\sigma \int F(s_\sigma) \rho_\sigma^{4/3}(\mathbf{r}) d\mathbf{r} \quad (2-105)$$

where s_σ is a **reduced density gradient** for spin σ :

$$s_\sigma = \frac{|\nabla\rho_\sigma(\mathbf{r})|}{\rho_\sigma^{4/3}(\mathbf{r})} \quad (2-106)$$

Several GGA exchange functionals are available so far by defining different explicit forms of the function $F(s_\sigma)$, listed as follows for **Becke88** [103], **Perdew86** [104] and **PBE** [105].

$$F^{\text{Becke88}}(s_\sigma) = \frac{0.0042s_\sigma^2}{1 + 0.0252s_\sigma \sinh^{-1}(s_\sigma)} \quad (2-107)$$

$$F^{\text{Perdew86}}(s_\sigma) = \left[1 + 1.296 \left(\frac{s_\sigma}{\sqrt[3]{24\pi^2}} \right)^2 + 14 \left(\frac{s_\sigma}{\sqrt[3]{24\pi^2}} \right)^4 + 0.2 \left(\frac{s_\sigma}{\sqrt[3]{24\pi^2}} \right)^6 \right]^{1/15} \quad (2-108)$$

$$F^{\text{PBE}}(s_\sigma) = 1.804 - \frac{0.804}{1 + 0.273s_\sigma^2} \quad (2-109)$$

Deriving Band Structures

For the GGA correlation functionals $E_C^{GGA}[\rho_\alpha(\mathbf{r}), \rho_\beta(\mathbf{r})]$, they have more complicated analytical forms. One of the most often used GGA correlation functionals is Perdew86 [106], the counterpart of the Perdew86 exchange functional. Later on Perdew and Wang suggested **PW91** [102, 104, 107, 108]. Probably a more popular non-local correlation functional is due to Lee, Yang and Parr [109], called **LYP**. Another option was provided by **PBE**, the correlation counterpart of the PBE exchange functional.

2.7.1.3 Hybrid functionals

The basic idea behind the method of hybrid functionals is that some portion of the exact HF exchange functional is incorporated into the pure density functionals described above, all weighted by three semi-empirical coefficients, in the way of the adiabatic connection method proposed by Becke [110], such that the promisingly improved results would be produced by DFT. The most popular hybrid functionals are **B3PW91** and **B3LYP**, which can be generated by¹²:

$$E_{XC}^{B3} = (1-a)(E_X^{\text{Dirac-Slater}} + bE_X^{\text{Becke88}}) + aE_X^{\text{HF}} + (1-c)E_C^{\text{VWN}} + cE_C^{\text{nonlocal}} \quad (2-110)$$

where the three parameters a , b and c refer to the HF exchange percentage, weight of the nonlocal exchange and weight of the nonlocal correlation. The B3PW91 and B3LYP are achieved when the nonlocal correlation functional stands for PW91 and LYP, respectively.

2.7.2 Incremental scheme

For solids, the correlation effects are usually accounted for basically by DFT. Some sophisticated wavefunction-based correlation methods that have been successfully developed for molecules, such as Configuration Interaction (CI) and Coupled Cluster (CC), are not feasible so far in the way to consider the translation symmetry, with the only exception that solids are truncated properly to be treated in a cluster model. The Incremental Scheme [111, 112, 113] is a powerful approach for large and periodic systems to derive the correlation energies by using wavefunction-based correlation methods.

Given a group D of local domains i defined in the reference 0-cell which can be accurately derived from HF wavefunctions, the correlation energy per unit cell can be expanded in equation (2-111) as the sum of so-called n -body increments (e.g., one-, two-, three-, ... n -body):

$$E_{corr} = \sum_{i \in D} \varepsilon_i + \sum_{i < j \in D} \Delta \varepsilon_{ij} + \sum_{i < j < k \in D} \Delta \varepsilon_{ijk} \cdots \quad (2-111)$$

where

¹² This is how B3PW91 and B3LYP have been implemented in CRYSTAL03 program. For other codes, they may correspond to different parameters or even different components.

$$\begin{aligned}
\Delta\varepsilon_{ij} &= \varepsilon_{ij} - \varepsilon_i - \varepsilon_j \\
\Delta\varepsilon_{ijk} &= \varepsilon_{ijk} - \Delta\varepsilon_{ij} - \Delta\varepsilon_{jk} - \Delta\varepsilon_{ik} - \varepsilon_i - \varepsilon_j - \varepsilon_k \\
&\dots
\end{aligned}
\tag{2-112}$$

Those local domains denoted as j, k, \dots must be addressed in the entire crystal. The local domain i can be a set of different atomic/ionic sites in ionic systems or of different bonds in covalent systems or arise from other definitions. ε_i is the correlation energy, which is calculated by allowing the orbital excitation within each local domain i but entirely freezing others at the correlation level. For each $\Delta\varepsilon_{ij}$, ε_{ij} is obtained by exciting orbitals in both domains i and j but freezing orbitals in the other domains. The higher-order increments can be calculated in an analogous way.

The expansion (2-111) for correlations makes sense only if this series is ensured to have a fast convergence at a low order of increments. This can be achieved when the localized-orbital-centered domains are defined. Accuracies are controlled by truncating a fast-converging series at a certain n -body increment derived with properly defined local domains. On the other hand, besides the truncation of the series (2-111), a given order increment must also be truncated up to certain nearest neighbor unit cells. Therefore highly correlating methods used in connection with (2-111) are required to be size-consistent.

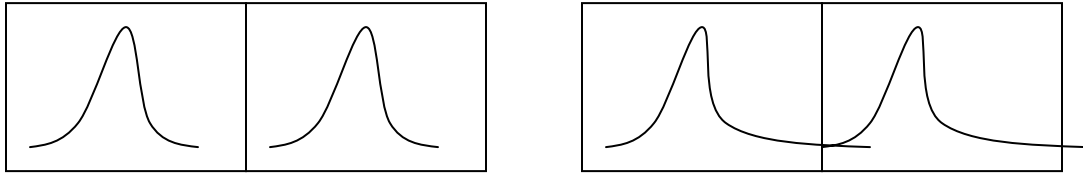


Figure 2-1 The schematic illustration of basis sets linear-dependence.

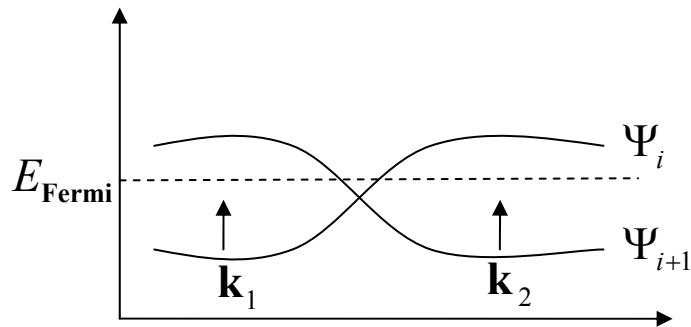


Figure 2-2 The schematic crossing of two bands Ψ_i and Ψ_{i+1} , both of which are only partially occupied. The Fermi level E_{Fermi} therefore stays within the energy interval ranging over more than one band when this partial occupation occurs.

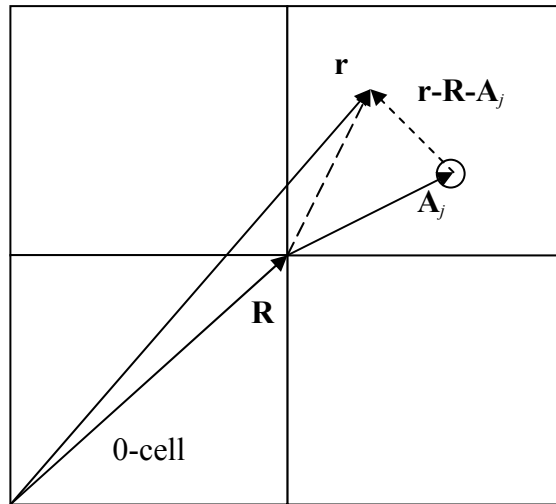


Figure 2-3 The nuclear center with respect to the lattice origin in the 0-cell.

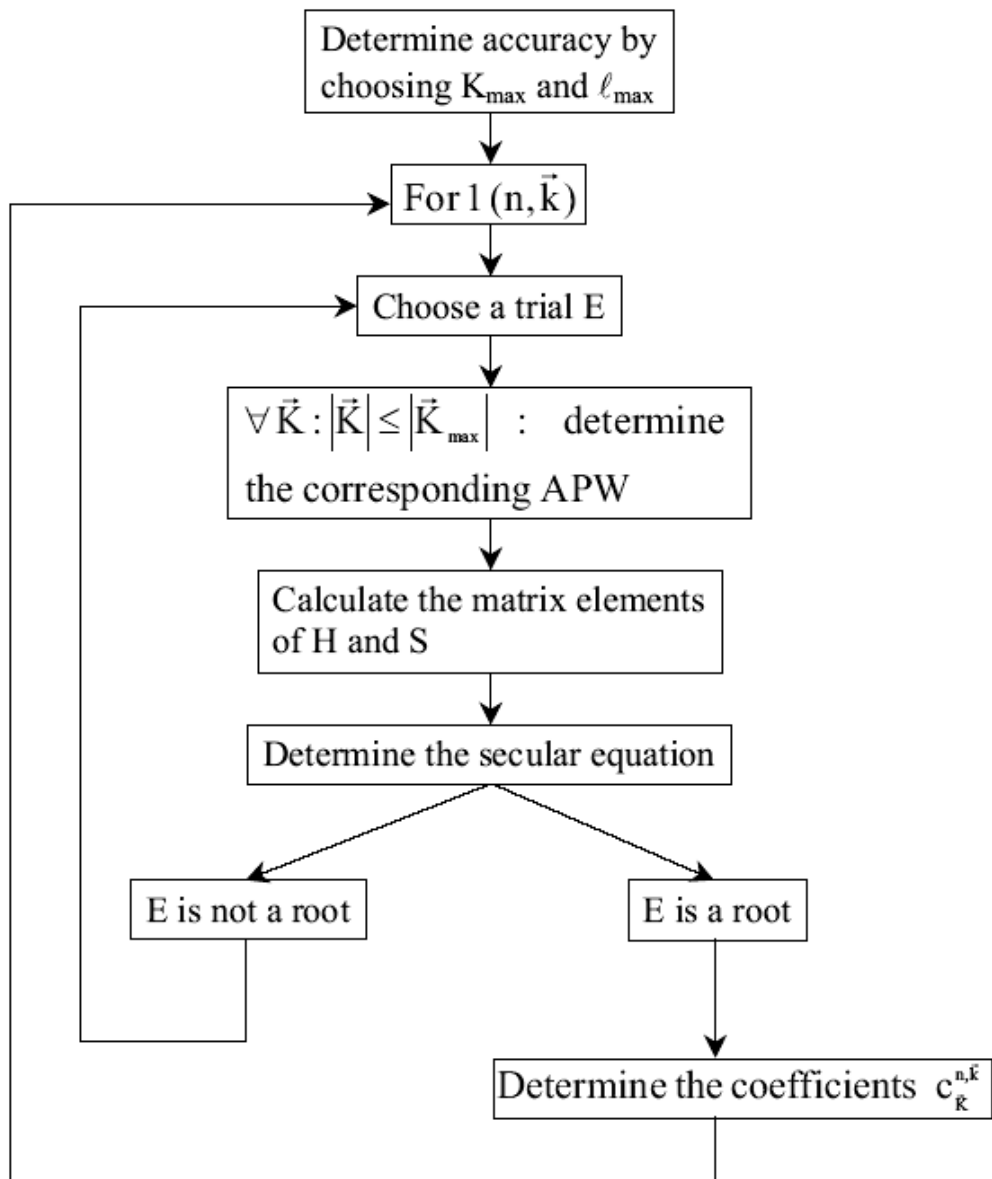


Figure 2-4 The flow chart for the APW SCF procedure.

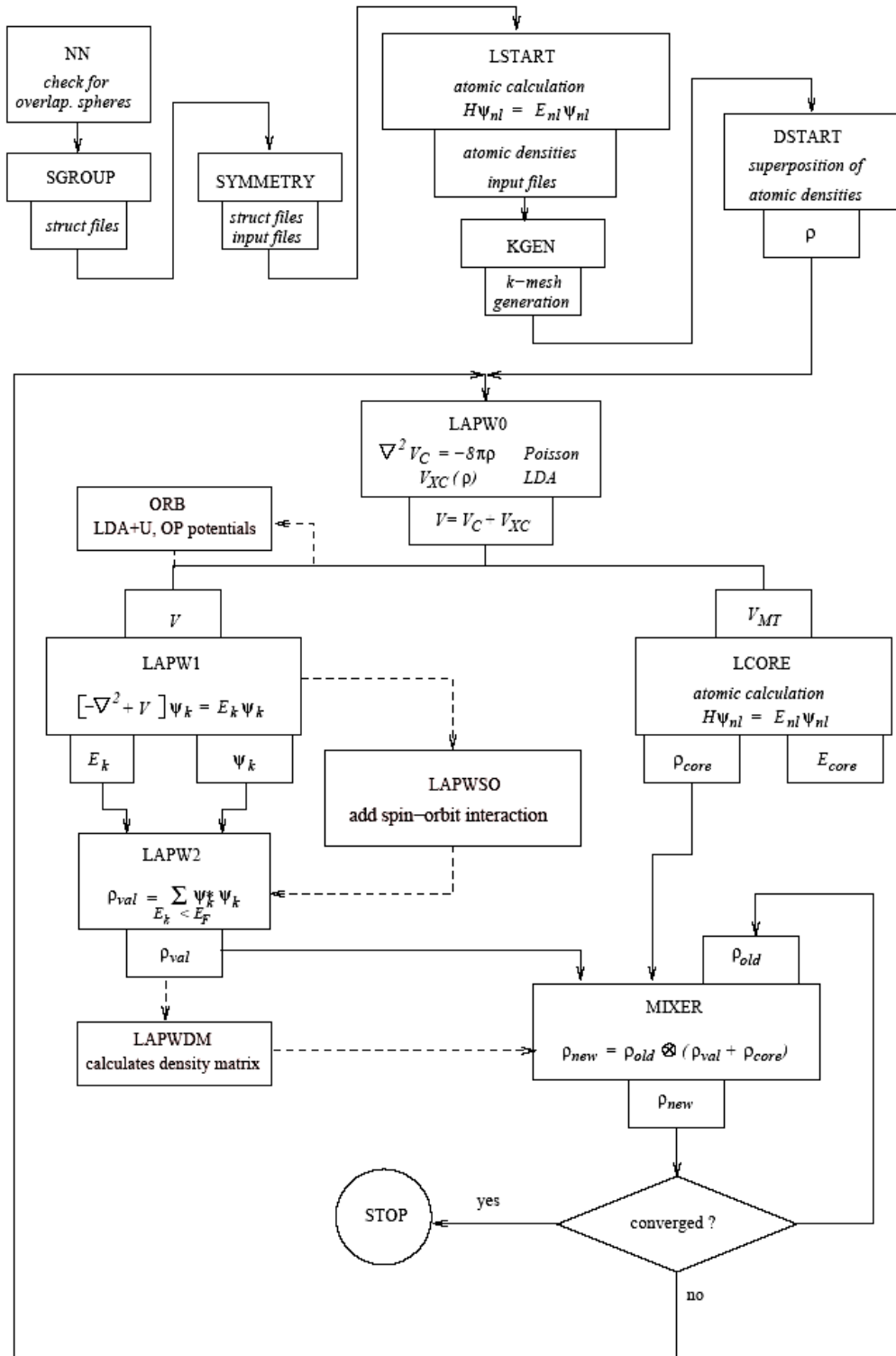


Figure 2-5 The flow chart for the LAPW SCF procedure implemented in WIEN2K [91].

Chapter 3 Relativistic Corrections

All that have been discussed so far is how to solve the Schrödinger equation for solids and derive the band structures within the framework of non-relativistic approximation. However, the relativistic effects can manifest themselves for solids through heavy elements contained in such functional materials as ferroelectric and ferromagnetic crystals.

Formally, the relativistic effects can be viewed as the difference between the results from a relativistic and a non-relativistic calculation. The relativistic correction is usually estimated to increase as $\sim \frac{Z^4}{c^2}$. The correction is thus significant only for heavy nuclei.

Generally, the relativistic corrections bring us two consequences, i.e., the dominating *direct relativistic effect* resulting in the contraction and stabilization of core-penetrating orbitals like s and p orbitals, as well as the dominating *indirect relativistic effect* resulting in the expansion and destabilization of non-core-penetrating orbitals like d and f orbitals.

3.1 The fully-relativistic Schrödinger equation

The relativistic corrections met in the theory of solid electronic states are basically the same as those encountered in the theory of atomic and molecular electronic states. In the non-relativistic treatment augmented by the experimentally obtained motion of electron spin, the wavefunction has two components for electronic states, i.e., the spin-up and spin-down components. In the relativistic case, however, we have four instead of two components, i.e., two *upper components* Φ mainly corresponding to electronic spinor states and two *lower components* \mathbf{X} mainly corresponding to positronic spinor states.

$$\Psi_{rel} = \begin{pmatrix} \Phi \\ \mathbf{X} \end{pmatrix} \quad (3-1)$$

with

$$\Phi = \begin{pmatrix} \psi_1 \\ \psi_2 \end{pmatrix}, \quad \mathbf{X} = \begin{pmatrix} \psi_3 \\ \psi_4 \end{pmatrix} \quad (3-2)$$

The corresponding relativistic Schrödinger equation associated with the four-component wavefunction is:

$$H\Psi_{rel} = E\Psi_{rel} \quad (3-3)$$

where the relativistic Hamiltonian for an N -electron system reads:

$$H = \boldsymbol{\alpha} \cdot \sum_i^N (c\mathbf{p}_i + \mathbf{M}_i) + (\boldsymbol{\beta} - \mathbf{I}_4)Nc^2 + \sum_i^N \sum_{i<j}^N \frac{1}{r_{ij}} + \sum_i^N V_i^{ext} \quad (3-4)$$

where c , \mathbf{M}_i and V_i^{ext} are the light speed, vector potential (magnetic fields) and external scalar potential (i.e., electron-nuclei attraction, nuclei-nuclei repulsion and applied electric fields), respectively. The momentum \mathbf{p}_i is calculated by:

Relativistic Corrections

$$\mathbf{p}_i = -i\vec{\nabla} \quad (3-5)$$

The two terms $\boldsymbol{\alpha}$ and $\boldsymbol{\beta}$ are defined by the Dirac matrices:

$$\boldsymbol{\alpha} = \left(\left(\begin{array}{cc} \mathbf{0} & \boldsymbol{\sigma}_x \\ \boldsymbol{\sigma}_x & \mathbf{0} \end{array} \right), \left(\begin{array}{cc} \mathbf{0} & \boldsymbol{\sigma}_y \\ \boldsymbol{\sigma}_y & \mathbf{0} \end{array} \right), \left(\begin{array}{cc} \mathbf{0} & \boldsymbol{\sigma}_z \\ \boldsymbol{\sigma}_z & \mathbf{0} \end{array} \right) \right), \quad \boldsymbol{\beta} = \begin{pmatrix} \mathbf{I}_2 & \mathbf{0} \\ \mathbf{0} & -\mathbf{I}_2 \end{pmatrix} \quad (3-6)$$

with the Pauli matrices:

$$\boldsymbol{\sigma}_x = \begin{pmatrix} 0 & 1 \\ 1 & 0 \end{pmatrix}, \boldsymbol{\sigma}_y = \begin{pmatrix} 0 & -i \\ i & 0 \end{pmatrix}, \boldsymbol{\sigma}_z = \begin{pmatrix} 1 & 0 \\ 0 & -1 \end{pmatrix} \quad (3-7)$$

and \mathbf{I}_n is the n-dimensional identical matrix:

$$\mathbf{I}_4 = \begin{pmatrix} \mathbf{I}_2 & \mathbf{0} \\ \mathbf{0} & \mathbf{I}_2 \end{pmatrix} \quad (3-8)$$

The four-component relativistic Schrödinger equation is however not exact, due to the implicit form of the vector potential \mathbf{M}_i describing the magnetic interactions. Several approximated Hamiltonians have been recovered, e.g., the *Dirac-Coulomb Hamiltonian* by entirely neglecting M_i ; the *Dirac-Coulomb-Gaunt Hamiltonian* by using the Gaunt term for electron-electron magnetic interactions, the *Dirac-Coulomb-Breit Hamiltonian* by considering both electron-electron magnetic interactions and the retardation effect setting the speed of the interaction propagation to c , etc.

Calculations performed by solving the four-component relativistic Schrödinger equation (3-3) leads to a *fully-relativistic* description, which is however only feasible for atoms by exploiting the spherical symmetry as well as small molecules. The other serious problem is that the eigenvalues of the four-component relativistic Schrödinger equation are not bounded from below, which could lead to a variational collapse of the desired electronic solution into the positronic states. This problem can be avoided if the small components for positronic states are projected out. Formally, the following exact transformation exists between \mathbf{X} and Φ :

$$\mathbf{X} = \frac{\boldsymbol{\sigma} \cdot \sum_i^N (c\mathbf{p}_i + \mathbf{M}_i)}{2Nc^2 + E - V} \Phi \quad (3-9)$$

which leads to the transformed Schrödinger equation:

$$\left[\boldsymbol{\sigma} \cdot \sum_i^N (c\mathbf{p}_i + \mathbf{M}_i) \frac{1}{2Nc^2 + E - V} \boldsymbol{\sigma} \cdot \sum_i^N (c\mathbf{p}_i + \mathbf{M}_i) + V \right] \Phi = E\Phi \quad (3-10)$$

with the potential:

$$V = \sum_i^N \sum_{i < j}^N \frac{1}{r_{ij}} + \sum_i^N V_i^{ext} \quad (3-11)$$

and the Pauli vector:

Relativistic Corrections

$$\boldsymbol{\sigma} = (\sigma_x, \sigma_y, \sigma_z) \quad (3-12)$$

It is obviously seen from (3-9) that $\mathbf{X} \ll \Phi$ due to the extreme large term of mc^2 in the denominator. Therefore \mathbf{X} is also-called the *small components*, and Φ the *large components*. The application of the exact transformation between the small and large components for practical solutions of relativistic effects is by no means possible. Therefore many efforts have been undertaken on the simplifications of the transformation so that \mathbf{X} is small enough to be negligible. These relativistic electronic structure approaches range from a fully-relativistic four-component over a two-component to a spin-free scalar-relativistic one-component all-electron description. Eliminating the chemically inactive core relativistic effects can also be accounted for by two-component or one-component *scalar-relativistic* ECP (effective core potential) methods.

3.2 All-electron approach

3.2.1 Foldy-Wouthuysen Hamiltonian

A systematic and attractive procedure for decoupling the large and small components was presented by Foldy and Wouthuysen [114]. The resultant FW Hamiltonian is:

$$H^{\text{FW}} = H_{\text{nrel}} + H_{\text{rel}}^{\text{FW}} \quad (3-13)$$

where H_{nrel} is the usual non-relativistic Hamiltonian, and the relativistic effects, truncated at c^{-2} are corrected by H_{rel} :

$$H_{\text{rel}}^{\text{FW}} = -\frac{1}{8c^2} \nabla^4 + \frac{1}{8c^2} \nabla^2 V + \frac{1}{4c^2} (-i\vec{\nabla} V \times \vec{\nabla}) \cdot \mathbf{s} \quad (3-14)$$

The first, second and third contributions are called *mass-velocity* term, *Darwin* term, and the *spin-orbit coupling* term. The contribution from the magnetic fields for the relativistic correction to Zeeman effects is disregarded. Although this expansion has proved to be strongly singular, it is useful to understand the origin of relativistic effects. The mass-velocity effect is negative, which leads to the core orbital contraction and energetic stabilization; the Darwin effect results in the positive relativistic energy shift for s states and is null for other states for a Coulomb potential; the spin-orbit terms deals with the splitting of states and couples the spin- and angular-momenta, which has the most pronounced effect where the potential changes most rapidly, i.e., close to the nuclei.

3.2.2 Douglas-Kroll-Hess Hamiltonian

The *Douglas-Kroll-Hess Hamiltonian* [115, 116] leads to a two-component Schrödinger equation which is bounded from below and variational. Without the magnetic field, the DKH Hamiltonian reads:

Relativistic Corrections

$$\begin{aligned}
 H^{\text{DKH}} = & \sum_i^N \left[E_i - A_i [V_i + R_i V_i^{\text{ext}} R_i] A_i - W_1(i) E_i W_1(i) - \frac{1}{2} \{W_1(i)^2, E_i\} \right] \\
 & + \sum_i^N \sum_{i < j}^N A_i A_j \left[\frac{1}{r_{ij}} + R_i \frac{1}{r_{ij}} R_i + R_j \frac{1}{r_{ij}} R_j + R_i R_j \frac{1}{r_{ij}} R_i R_j \right] A_i A_j
 \end{aligned} \tag{3-15}$$

where

$$E_i = E_{p_i} = c\sqrt{\mathbf{p}_i^2 + c^2}, \quad A_i = A_{p_i} = \sqrt{\frac{E_i + c^2}{2E_i}}, \quad R_i = R_{p_i} = \frac{c\mathbf{s}_i \cdot \mathbf{p}_i}{E_i + c^2} \tag{3-16}$$

$\{\}$ denotes an anti-commutator. $W_1(i)$ is a momentum space integral:

$$W_1(i)\Psi(\mathbf{p}) = \int W_1(\mathbf{p}, \mathbf{p}') d\mathbf{p}', \quad W_1(\mathbf{p}, \mathbf{p}') = A_{p_i} (R_{p_i} - R_{p_i'}) A_{p_i'} \frac{V(\mathbf{p}_i, \mathbf{p}_i')}{E_{p_i} + E_{p_i'}} \tag{3-17}$$

where $V(\mathbf{p}_i, \mathbf{p}_i')$ is the Fourier transform coefficient of the external potential V_i^{ext} .

However, the relativistic effects from the second two-electron term in (3-15) are usually minor and therefore the non-relativistic Coulomb operator is utilized instead for most cases in order to avoid dramatically increasing computational costs. When the DKH Hamiltonian is applied to calculate properties, the corresponding property operators need to be accordingly transformed. The DKH method has been widely implemented in various programs for explicit relativistic all-electron calculations of atoms and molecules.

3.2.3 Wood-Boring Hamiltonian

The *Wood-Boring Hamiltonian* is obtained by directly eliminating the small component in (3-10) without the magnetic field.

$$\begin{aligned}
 H^{\text{WB}} &= \boldsymbol{\sigma} \cdot \sum_{i=1}^N c\mathbf{p}_i \frac{1}{2Nc^2 + E - V} \boldsymbol{\sigma} \cdot \sum_{i=1}^N c\mathbf{p}_i + V \\
 &= \boldsymbol{\sigma} \cdot \sum_{i=1}^N \mathbf{p}_i \frac{1}{2Nc^2 + E - V} \boldsymbol{\sigma} \cdot \sum_{i=1}^N \mathbf{p}_i + V \\
 &= \underbrace{\sum_{i=1}^N \mathbf{p}_i \frac{1}{2Nc^2 + E - V} \sum_{i=1}^N \mathbf{p}_i}_{\text{scalar-relativistic}} + \underbrace{i\boldsymbol{\sigma} \cdot \left\{ \left[\sum_{i=1}^N \mathbf{p}_i \left(1 + \frac{E - V}{2Nc^2} \right)^{-1} \right] \times \sum_{i=1}^N \mathbf{p}_i \right\}}_{\text{spin-orbi coupling}} + V
 \end{aligned} \tag{3-18}$$

It is obvious that the WB Hamiltonian is decomposed into the spin-independent and spin-dependent parts, which in turn explains the scalar-relativistic and spin-orbit coupling effects individually. Unlike the energy-independent FW and DKH Hamiltonians, the WB Hamiltonian provides a set of energy-dependent operators that needs to be solved iteratively. The WB Hamiltonian is mainly applied in atomic finite difference calculations, e.g., to generate the all-electron atomic reference data needed for the adjustment as calibration of ECPs. In the central field approximation for one electron

Relativistic Corrections

atom, the equation (3-18) gives the following energy-dependent operators for the large component radial equation:

$$(H_{nrel}^{WB} + H_{MV}^{WB} + H_D^{WB} + H_{SO}^{WB})R_{n\kappa} = \varepsilon_{n\kappa}R_{n\kappa} \quad (3-19)$$

with the H_{nrel}^{WB} being the non-relativistic Hamiltonian specified in (2-61). The WB mass-velocity, Darwin and spin-orbit coupling terms consist of the relativistic corrections with all being functions of the orbital energy $\varepsilon_{n\kappa}$. The relativistic quantum number κ is defined as:

$$\kappa = \begin{cases} -(l+1) = -(j + \frac{1}{2}) & \text{for } j = l + \frac{1}{2} \\ l = j + \frac{1}{2} & \text{for } j = l - \frac{1}{2} \end{cases} \quad (3-20)$$

3.3 Effective core potential (ECP)

All-electron calculations are not always feasible or necessary. The goal of a reduction of computational costs leads to the restriction of the explicit wavefunction calculation for valence electrons while keeping the valence properties of systems, which after replacement of the core electron system by a potential leads to the *effective core potential* (ECP) methods. ECP methods are in accordance with one of the most fundamental assumptions in chemistry that low lying core electrons are relatively inert and not perturbed by a molecular or crystalline environment (*frozen core approximation*). Thus ECP has been accepted as efficient tools to carry out spin-free and spin-orbit relativistic first-principles calculations for both molecules and crystals. They are especially indicated when heavy elements are involved. Two families of relativistic ECP methods exist: those based on the Huzinaga–Cantu equation [117] which leads to valence orbitals with the same nodal structure as the all-electron orbitals are known as *model potential (MP)* methods, and those relying on the pseudo-orbital transformation [66], which produces radially less nodal or even nodeless valence pseudo-orbitals are known as *pseudopotential (PP)* methods.

3.3.1 Frozen core approximation

If we divide the orbitals into two subgroups of N_c localized core electrons and N_v delocalized valence electrons, we may formally rewrite the relativistic Fock operator (2-9) as follows:

Relativistic Corrections

$$\begin{aligned}
 f(\mathbf{r}) = & \boldsymbol{\alpha} \cdot \sum_i^N c\mathbf{p}_i + (\boldsymbol{\beta} - \mathbf{I}_4)Nc^2 \\
 & - \underbrace{\sum_A^{\text{nuclei}} \frac{Z_A^{\text{eff}}}{|\mathbf{r} - \mathbf{r}_A|} + \sum_v^{N_v} (J_v(\mathbf{r}) - K_v^A(\mathbf{r}))}_{\text{Valence potentials}} + \underbrace{\sum_A^{\text{nuclei}} \left(-\frac{Z_A^{\text{core}}}{|\mathbf{r} - \mathbf{r}_A|} + \sum_c^{N_c} J_c^A(\mathbf{r}) \right)}_{\text{Core Coulomb potentials}} \\
 & - \underbrace{\sum_A^{\text{nuclei}} \sum_c^{N_c} K_c^A(\mathbf{r})}_{\text{Core exchange potentials}}
 \end{aligned} \quad (3-21)$$

with the effective core charge equal to the total nuclei charge minus the number of electrons represented by ECP:

$$Z_A^{\text{eff}} = Z_A - Z_{\text{core}} \quad (3-22)$$

The exact non-local core potentials including Coulomb and exchange parts can be approximated by the sum of approximated frozen core potentials for different atoms in order to make the calculations more affordable:

$$\begin{aligned}
 f_{\text{frozencore}}(\mathbf{r}) = & \boldsymbol{\alpha} \cdot \sum_i^N c\mathbf{p}_i + (\boldsymbol{\beta} - \mathbf{I}_4)Nc^2 \\
 & - \sum_A^{\text{nuclei}} \frac{Z_A^{\text{eff}}}{|\mathbf{r} - \mathbf{r}_A|} + \sum_v^{N_v} (J_v(\mathbf{r}) - K_v^A(\mathbf{r})) + \sum_A^{\text{nuclei}} V_{\text{frozencore}}^A(\mathbf{r})
 \end{aligned} \quad (3-23)$$

Therefore it is obvious that the problem of explicitly treating an N -electron system has been converted to the one of explicitly treating the N_v -system only, which tremendously reduces the computational efforts. Thus the **frozen core approximation** is so-called that the core potentials are fixed to particular forms and not allowed to change upon the formation of molecules or crystals. The relativistic effects can be included by the DKH or WB approach for valence electrons.

However, the simplification of exact core Coulomb and exchange potentials by the frozen core potentials indeed neglects the core-valence and core-core electron correlation interactions in the correlation picture. These introduce tremendous errors for a large core calculation. The short-ranged core-core exchange-correlation effects can be minimized by defining non-overlapping cores. On the other hand, the core-core and core-valence exchange-correlation interactions can be approximately corrected by a classical **core polarization potential (CPP)** with respect to the electric fields generated by electrons and nucleus outside this core (including valence electrons) as follows:

$$V_{\text{CPP}}^A = -\frac{1}{2} \sum_{pq}^3 \alpha_{pq} \sum_{i \notin A} F_p^{i*} F_q^i \quad (3-24)$$

3.3.2 Model potentials (MP)

In the first-principles MP approach, the frozen core potential is represented by:

Relativistic Corrections

$$\begin{aligned}
 V_{frozencore}^A(\mathbf{r}) &= V_{Coulomb}^A(\mathbf{r}) + V_{Exchange}^A(\mathbf{r}) + P_{core}^A(\mathbf{r}) \\
 &= \frac{1}{r} \sum_i^{n_a} c_i^A e^{-a_i^A r^2} - \sum_{c \in A} \sum_{rstu} |\Phi_r(\mathbf{r})\rangle S_{rs}^{-1} \langle \Phi_s(\mathbf{r}) | K_c^A | \Phi_t(\mathbf{r})\rangle S_{rs}^{-1} \langle \Phi_u(\mathbf{r}) | \\
 &\quad + \sum_{c \in A} B_c^A |\Psi_c(\mathbf{r})\rangle \langle \Psi_c(\mathbf{r}) |
 \end{aligned} \quad (3-25)$$

The first term uses the Gaussian functions to expand the local Coulomb potential and to simulate the spherical density within the core sphere, to the arbitrary precision controlled by the number of Gaussian functions n_a . The second term contributes to the non-local exchange potential calculated by the primitive basis functions $\Phi(\mathbf{r})$ for core orbitals. The last term is a projection operator, constructed from an appropriate set of atomic core orbitals, in order to project the atomic core solutions out of the valence wavefunctions orthogonal to the core. All these various frozen core parameters in the MP are then optimized to reproduce the desired valence atomic orbital energies and orbital shapes with comparable accuracies with respect to the relativistic all-electron reference data (e.g., WB finite difference approach), when such a Hamiltonian containing the potential of (3-25) is applied to the atomic system.

One of the most important features of MP approach is probably that the valence orbitals retain the same radial nodal structures as the all-electron orbitals, which advantageously leads to accurate correlation energies relative to the correlation calculations done with all-electron orbitals. However, the nodal structure of valence orbitals demands a relatively large size of the basis sets to expand the valence orbitals and thus makes MP calculations more expensive.

3.3.3 Pseudopotentials (PP)

The pseudopotential method desires to reduce or even remove the original nodes of valence orbitals. To this end, the valence orbitals must be transformed into nodeless *pseudo valence orbitals* along with the necessary transformation of Fock operators. One formal transformation, the Phillips-Kleinman (PK) transformation [66], has been discussed in Chapter 2 for the pseudopotential band structure calculations of solids. The PK projector reads:

$$P(\mathbf{r}) = \sum_{c \in core} (\varepsilon_v - \varepsilon_c) |\Psi_c(\mathbf{r})\rangle \langle \Psi_c(\mathbf{r})| \quad (3-26)$$

For the valence orbital transformation by requiring the core-valence orthogonality:

$$\Psi_v(\mathbf{r}) = \left(1 - \sum_c |\Psi_c(\mathbf{r})\rangle \langle \Psi_c(\mathbf{r})| \right) \Psi_v^P(\mathbf{r}) \quad (3-27)$$

The corresponding pseudo eigenequation follows:

$$[f(\mathbf{r}) + P(\mathbf{r})] \Psi_v^P(\mathbf{r}) = \varepsilon_v \Psi_v^P(\mathbf{r}) \quad (3-28)$$

Therefore PK exhibits that there indeed exists such a transformation for both Fock operator and valence orbitals. However, the PK approach does not practically lead to the

Relativistic Corrections

reduction of computational efforts with respect to all-electron methods since it requires the knowledge of the core orbitals and their orbital energies.

The simplification is available by defining the one-particle frozen core potential $V_{frozencore}^A$ as follows:

$$V_{frozencore}^A(\mathbf{r}) = -\frac{Z_A^{core}}{|\mathbf{r} - \mathbf{r}_A|} + V_L^A(\mathbf{r}) + V_{cv,SO-average}^A(\mathbf{r}) + V_{cv,SO}^A(\mathbf{r}) \quad (3-29)$$

In the above expression, the first term denotes the core-electron attractions. The second term restores the local contribution in the frozen core potential. The third term specifies the SO-averaged semi-local core-valence potential:

$$V_{cv,SO-average}^A(\mathbf{r}) = \sum_{l=0}^{L-1} V_l^A(\mathbf{r}) \sum_{m_l=-l}^{m_l=l} |\Psi_{lm_l}\rangle \langle \Psi_{lm_l}| \quad (3-30)$$

The last term includes the SO correction:

$$V_{cv,SO}^A(\mathbf{r}) = \sum_{l=1}^{L-1} \frac{2\Delta V_l^A(\mathbf{r})}{2l+1} \sum_{m_l=-l}^{m_l=l} \sum_{m'_l=-l}^{m'_l=l} |\Psi_{lm_l}\rangle \langle \Psi_{lm_l}| \mathbf{l} \cdot \mathbf{s} |\Psi_{lm'_l}\rangle \langle \Psi_{lm'_l}| \quad (3-31)$$

The potential $V_l^A(\mathbf{r})$ and difference potential $\Delta V_l^A(\mathbf{r})$ are usually expanded in terms of Gaussian functions:

$$V_l^A(\mathbf{r}) = \sum_i^{n_\alpha} r^{n_{il}} c_{il}^A e^{-\alpha_{il}^A r^2} \quad (3-32)$$

$$\Delta V_l^A(\mathbf{r}) = \sum_i^{n_\alpha} r^{n_{il}} \Delta c_{il}^A e^{-\alpha_{il}^A r^2} \quad (3-33)$$

These pseudopotentials are determined via a fitting procedure with respect to the atomic reference data. They take care of the Coulomb and exchange interactions as well as core-valence orthogonality. There are two types of PPs according to the type of pseudo valence orbitals, namely the *shape-consistent* PP, which takes all-electron valence orbitals and orbital energies as the reference data, and *energy-consistent* PP, which takes all-electron total valence energies or other quantum mechanical observable quantities (e.g., ionization energies, atomic spectrum, etc.) as the reference data.

3.3.3.1 Shape-consistent PPs

The shape-consistent PP is connected with the pseudo valence orbital which keeps the true nodal valence orbitals in the bonding region and removes only the nodes of valence orbitals in the chemically inactive inner region by a smooth polynomial expansion. The radial parts of pseudo valence orbitals can be thus expressed as:

Relativistic Corrections

$$R_{\Psi_l^P(\mathbf{r})} = \begin{cases} R_{\Psi_v(\mathbf{r})} & \text{for } |\mathbf{r}| \geq R_{\max}[\Psi_v(\mathbf{r})] \\ \sum_{i=0}^4 c_i r^{i+l+2} & \text{for } |\mathbf{r}| < R_{\max}[\Psi_v(\mathbf{r})] \end{cases} \quad (3-34)$$

where R_{\max} is the cut-off radius at which the true valence orbital experiences its outmost maximum. Therefore the shape-consistent PPs provide valence orbitals with reduced nodes. The free parameters are determined by normalization and continuity conditions, i.e., matching of the orbitals as well as their derivatives at the sphere surface at R_{\max} .

3.3.3.2 Energy-consistent PPs

For the energy-consistent PPs, the valence orbitals are transformed into completely nodeless pseudo valence orbital. Such PPs are generated by minimizing with respect to the free parameters in the PP the following functional to reproduce the low-energy atomic spectrum.

$$\min \left[\sum_I^{\text{lowlying states}} w_I (E_I^{PP} - E_I^{\text{all-electron}})^2 \right] \quad (3-35)$$

with the total valence energy for the low-lying state I from the PP method E_I^{PP} and the all-electron $E_I^{\text{all-electron}}$. The sum runs over a multitude of chemically possible electronic states so as to guarantee the transferability of generated PPs from one chemical environment to another. This formalism can be used to generate one-, two- and also four-component PPs at any desired level of relativity (non-relativistic Schrödinger, or relativistic WB, DKH, Dirac-Coulomb or Dirac-Coulomb-Breit Hamiltonian; implicit or explicit treatment of relativity in the valence shell) [118]. The reference data $E_I^{\text{all-electron}}$ is usually derived from finite difference state-averaged multi-configuration Dirac-Hartree-Fock calculations based on the Dirac-Coulomb or Dirac-Coulomb-Breit Hamiltonian or corresponding HF-like calculations using the WB Hamiltonian.

Chapter 4 Bonds and Bands in Crystals

Chemical bonds are important for crystals. They determine not only the band structure, but also the crystal stability in the sense that bonding and antibonding interactions are competitively balanced in a stable crystal. In this chapter, we discuss how chemical bonds in crystals are formed based on atomic orbital interactions and their consequences on energy bands and state distributions. As one example, the simplest one-dimensional mono-atomic chain in the CO-LCAO approach is presented. We will see that, unlike molecules, a specific type of bond in a crystal is always connected with a specific \mathbf{k} point and thus may change its property when moving to another \mathbf{k} point. An overall bond within a crystal results from all contributions from all \mathbf{k} points. Although in the one-dimensional case \mathbf{k} is not a vector, we keep the bold face notation for consistency with other chapters of this thesis.

4.1 Bonding and antibonding interactions

We assume that in a one-dimensional crystal there is only one atom in each cell with the lattice constant a , and all atoms are equivalent in all cells (cf. Figure 4-1). The atomic orbitals are denoted as χ_j . The first Brillouin zone is thereby located at $-\frac{\pi}{a} < \mathbf{k} \leq \frac{\pi}{a}$.

4.1.1 s orbitals

We first need to construct the crystal Bloch orbitals by using occupied s orbitals following the equation (2-26) for three special \mathbf{k} points, i.e., $\mathbf{k} = 0, \mathbf{k} = \frac{\pi}{2a}, \mathbf{k} = \frac{\pi}{a}$. These Bloch orbitals are presented in Figure 4-2, Figure 4-3 and Figure 4-4. Clearly, at $\mathbf{k} = 0$, the s-type Bloch orbital shows a complete occupied σ -bonding interaction with no nodes throughout the entire crystal at the lowest band level, while at $\mathbf{k} = \frac{\pi}{a}$, a complete occupied σ -antibonding interaction is manifested with the maximum number of nodes at the highest band level. The $\mathbf{k} = \frac{\pi}{2a}$ point leads to an occupied complex Bloch orbital with both real and imaginary components, each of which has weaker antibonding overlappings due to the farther orbital distances of $2a$, intermediated by nonbonding s orbitals, than those at $\mathbf{k} = \frac{\pi}{a}$.

The same bond patterns can be identically achieved if the two neighbor cells are joined into one supercell by the translation of $a' = 2a$. In this case, within each supercell, two s orbitals can form both bonding and antibonding interactions, each of which is thus repeated along the chain. This produces directly the Figure 4-2 and Figure 4-4, yet corresponding to the point $\mathbf{k}' = 0$ for the supercell. The Figure 4-3 can be equally

Bonds and Bands in Crystals

generated either at the point $\mathbf{k}' = \frac{\pi}{a'}$ for the $a' = 2a$ supercell, or at the point $\mathbf{k}' = 0$ for the $a' = 4a$ supercell.

4.1.2 p orbitals

We look at another topologically different type of occupied orbitals, i.e., the p orbitals. In the same way as has been done for s orbitals, we generated the p_z -type Bloch orbitals shown in Figure 4-5, Figure 4-6 and Figure 4-7. The p_z -type Bloch orbitals show an entirely reverse consequence for bonding with respect to the s-type Bloch orbitals. The most σ -antibonding and most σ -bonding interactions take place at $\mathbf{k} = 0$ and $\mathbf{k} = \frac{\pi}{a}$, respectively, which stay at the highest and lowest occupied band level, respectively. At $\mathbf{k} = \frac{\pi}{2a}$, the Bloch orbital contains a reduced σ -bonding interaction intermediated by the nonbonding p_z orbitals.

The p_x - and p_y -type Bloch orbitals show equivalent bond properties in the sense that the same pattern of orbital interactions is resulting as for s-type Bloch orbitals, except that p_x (p_y) orbitals tend to form π -bonds rather than σ -bonds for this mono-atomic array.

4.1.3 s- p_z orbital interactions

Based on the above discussion, we are able to describe how s and p_z orbitals couple with each other. Due to the symmetry mismatch, the s- p_x , s- p_y , p_z - p_x and p_z - p_y interactions are not allowed. The resultant one-electron crystal orbitals in g symmetry are formed as:

$$\Psi_{s+p_z}(\mathbf{k}) = C_{s+p_z}(\mathbf{k})[\Phi_s(\mathbf{k}) + \Phi_{p_z}(\mathbf{k})] \quad (4-1)$$

$$\Psi_{s-p_z}(\mathbf{k}) = C_{s-p_z}(\mathbf{k})[\Phi_s(\mathbf{k}) - \Phi_{p_z}(\mathbf{k})] \quad (4-2)$$

By simply superposing the corresponding s- and p_z -type Bloch orbitals, we find (cf. Figure 4-8) that the resulting Ψ_{s+p_z} (Ψ_{s-p_z}) orbitals are bonding and antibonding states at the points $\mathbf{k} = \frac{\pi}{a}$ and $\mathbf{k} = 0$, respectively.

4.2 Energy band

Following the above discussion, we can plot the energy band of the mono-atomic chain along the \mathbf{k} -path $0 \rightarrow \frac{\pi}{2a} \rightarrow \frac{\pi}{a}$, qualitatively in Figure 4-9. For the s-band, the curve should go up in energy along the path, since the chain experiences from the complete s-s bonding at $\mathbf{k} = 0$, through a weak antibonding at $\mathbf{k} = \frac{\pi}{2a}$ to the complete antibonding

Bonds and Bands in Crystals

at $\mathbf{k} = \frac{\pi}{a}$, and thus $E(\mathbf{k} = 0) < E(\mathbf{k} = \frac{\pi}{a})$. For the p_z -band, the curve is developed the other way round with $E(\mathbf{k} = 0) > E(\mathbf{k} = \frac{\pi}{a})$. In general, it is the topology of local orbital interactions (i.e., atomic orbitals for a mono-atomic cell or molecular orbitals for a multi-atomic cell) which determines whether the relevant band should go up or down.

Another important feature of a band is its dispersion, or band width, i.e., the difference between the highest and lowest energy levels within a band. Once the mono-atomic chain is prolonged, the local orbital overlappings between cells are thereby reduced and either bonding interactions or antibonding interactions are accordingly weakened, which pushes up the energy of bonding orbitals and down that of antibonding orbitals, respectively. Thus as a result the band width is reduced. In other words, those orbitals, e.g. the core orbitals, which are chemically inactive and couple little with each other, should present a flat band with a small width, whereas those orbitals, e.g., the valence orbitals, which are chemically active and strongly couple with each other, should present a relatively steep or even oscillating band with a large width.

4.3 Density of states (DOS)

In molecules we are able in principle to single out every orbital including the core and frontier orbitals responsible for molecular electronic structure. However, there is no way even theoretically to do so when the number of orbitals is infinite and jammed into a small energy interval. The crystal orbitals unfortunately fall in the latter case. The strategy invented for the solid state community is to group a bunch of crystal orbitals instead of considering a single one. There are many ways for this grouping. For example, the energy band is one approach, which essentially counts the relevant \mathbf{k} points at the small orbital energy interval $E + dE$. An alternative way is to count how many crystal orbitals there are at the small energy interval $E + dE$. This quantity is called **density of states (DOS)**, defined as the sum over all possible electronic energy bands in the complete first Brillouin zone:

$$D(E) = \left| \frac{dN(E)}{dE} \right| = \frac{1}{V_{BZ}} \sum_n \int_{BZ} \delta[E - \varepsilon_n(\mathbf{k})] d\mathbf{k} \quad (4-3)$$

where N is the total number of energy levels in a crystal at the energy interval $E + dE$. In order to find out how much a given fragment A (an orbital, an atom, a group of orbitals, or a group of atoms) contributes to the DOS at a certain energy E , one can define a **projected density of states (PDOS)** by using a projector $\Omega_{A,n}(\mathbf{k})$:

$$PD_A(E) = \left| \frac{dN_A(E)}{dE} \right| = \frac{1}{V_{BZ}} \sum_n \int_{BZ} \Omega_{A,n}(\mathbf{k}) \delta[E - \varepsilon_n(\mathbf{k})] d\mathbf{k} \quad (4-4)$$

Here the projector $\Omega_{A,n}(\mathbf{k})$, say in the CO-LCAO approach, reads:

Bonds and Bands in Crystals

$$\begin{aligned}
 \Omega_{A,n}(\mathbf{k}) &= \sum_{\mathbf{R}} \int \rho_{A,n}(\mathbf{r} + \mathbf{R}; \mathbf{k}) d\mathbf{r} \\
 &= \sum_{\mathbf{R}} \sum_{\mu \in A} \langle \Psi_n(\mathbf{r}; \mathbf{k}) | \Phi_{\mu}(\mathbf{r}; \mathbf{k}) \rangle \langle \Phi_{\mu}(\mathbf{r}; \mathbf{k}) | \Psi_n(\mathbf{r} + \mathbf{R}; \mathbf{k}) \rangle \\
 &= \sum_{\mathbf{R}} \sum_{\mu \in A} \sum_{\nu} S_{\mu\nu}(\mathbf{k}) c_{\mu}^*(\mathbf{k}) c_{\nu}(\mathbf{k}) e^{i\mathbf{k} \cdot \mathbf{R}}
 \end{aligned} \tag{4-5}$$

where $S_{\mu\nu}(\mathbf{k})$ is the overlap matrix element (cf. (2-16)). Thereby the PDOS for the fragment A is written as:

$$PDOS_A(E) = \frac{1}{V_{BZ}} \sum_n \sum_{\mathbf{R}} \sum_{\mu \in A} \sum_{\nu} \int_{BZ} S_{\mu\nu}(\mathbf{k}) c_{\mu}^*(\mathbf{k}) c_{\nu}(\mathbf{k}) e^{i\mathbf{k} \cdot \mathbf{R}} \delta[E - \varepsilon_n(\mathbf{k})] d\mathbf{k} \tag{4-6}$$

It can be derived that generally the DOS is related to the band structure by the surface integral for α and β spins:

$$D(E) = \frac{1}{V_{BZ}} \sum_n \int_{S_n(E)} \frac{1}{|\nabla_{\mathbf{k}} \varepsilon_n(\mathbf{k})|} d\mathbf{S} \Big|_{\alpha} + \frac{1}{V_{BZ}} \sum_n \int_{S_n(E)} \frac{1}{|\nabla_{\mathbf{k}} \varepsilon_n(\mathbf{k})|} d\mathbf{S} \Big|_{\beta} \tag{4-7}$$

where \mathbf{S} is the surface at energy E in the reciprocal space, and n is the band index. $\nabla_{\mathbf{k}} \varepsilon_n(\mathbf{k})$ is a gradient vector normal to that surface whose magnitude is equal to the rate of change of the band energy $\varepsilon_n(\mathbf{k})$ in the normal direction. For a closed shell system, the DOS becomes:

$$D(E) = \frac{2}{V_{BZ}} \sum_n \int_{S_n(E)} \frac{1}{|\nabla_{\mathbf{k}} \varepsilon_n(\mathbf{k})|} d\mathbf{S} \tag{4-8}$$

The DOS is proportional to the reciprocal of the energy derivative with respect to the vector \mathbf{k} . One direct consequence is that a flat band results in a sharp DOS peak with atomic orbital-like shapes, e.g., for core orbitals. On the other hand, a flat and broad DOS implies that certain orbital interactions take place, e.g., for valence orbitals. The DOS of the mono-atomic chain can be thus schematically plotted, as presented in Figure 4-10.

One may raise the question concerning the singularity of the integrand in (4-8) if $\nabla_{\mathbf{k}} \varepsilon_n(\mathbf{k}) = 0$. Fortunately, it can be shown that for a three-dimensional lattice such singularities are integrable, yielding finite values for the DOS. However, these singularities do result in the divergence of the slope, e.g., $\frac{dD(E)}{dE}$. These singularities are called *van Hove singularities*. The DOS for the mono-atomic chain in Figure 4-10 is an example.

Bonds and Bands in Crystals

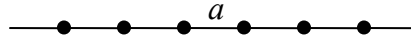


Figure 4-1 The mono-atomic array.

$$\Phi_s(\mathbf{k} = 0) = \sum_{n=0} e^{ik \cdot (na)} \chi_n = \chi_0 + \chi_1 + \chi_2 + \chi_3 + \dots$$

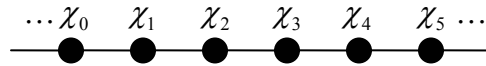


Figure 4-2 The real s-type Bloch orbital at $\mathbf{k} = 0$.

$$\Phi_s(\mathbf{k} = \frac{\pi}{2a}) = \sum_{n=0} e^{ik \cdot (na)} \chi_n = (\chi_0 - \chi_2 + \chi_4 - \chi_6 + \dots) + i(\chi_1 - \chi_3 + \chi_5 - \chi_7 + \dots)$$

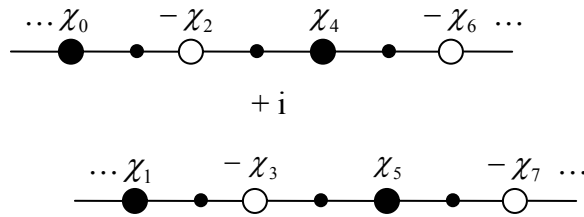


Figure 4-3 The complex s-type Bloch orbital at $\mathbf{k} = \frac{\pi}{2a}$.

$$\Phi_s(\mathbf{k} = \frac{\pi}{a}) = \sum_{n=0} e^{ik \cdot (na)} \chi_n = \chi_0 - \chi_1 + \chi_2 - \chi_3 + \dots$$

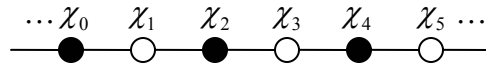


Figure 4-4 The real s-type Bloch orbital at $\mathbf{k} = \frac{\pi}{a}$.

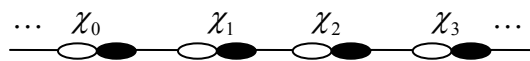


Figure 4-5 The real p_z -type Bloch orbital at $\mathbf{k} = 0$.

Bonds and Bands in Crystals

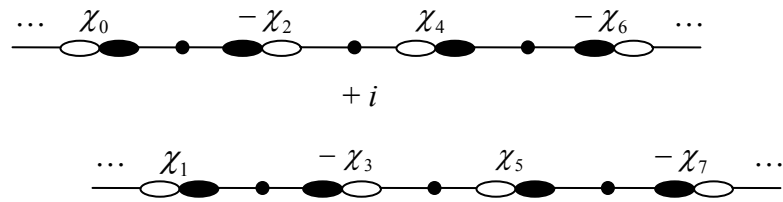


Figure 4-6 The complex p_z -type Bloch orbital at $\mathbf{k} = \frac{\pi}{2a}$.

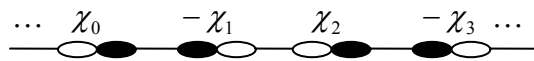


Figure 4-7 The real p_z -type Bloch orbital at $\mathbf{k} = \frac{\pi}{a}$.

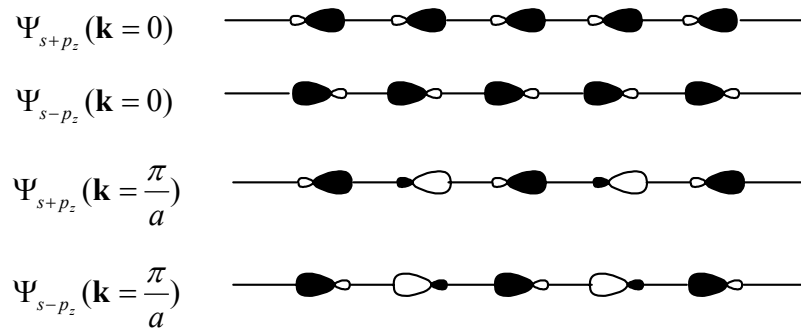


Figure 4-8 The real s - p_z -type Bloch orbitals at both $\mathbf{k} = 0$ and $\mathbf{k} = \frac{\pi}{a}$.

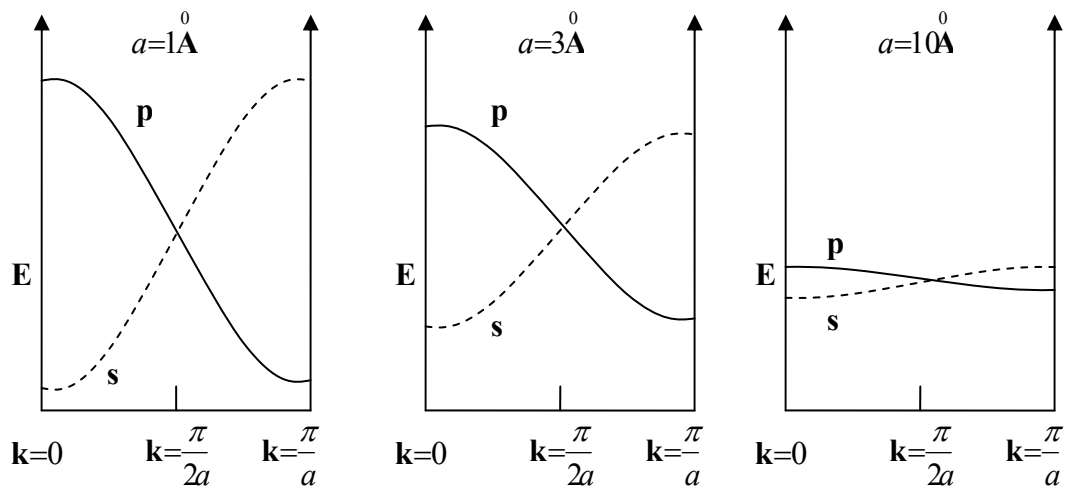


Figure 4-9 The energy bands of the mono-atomic chain with respect to different lattice constants.

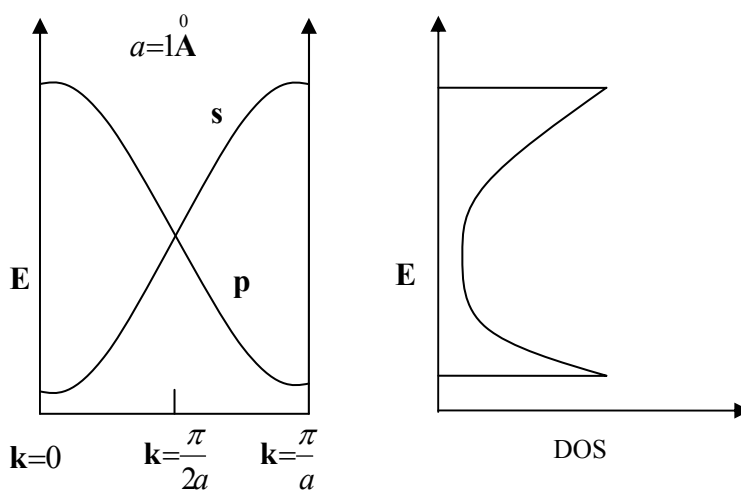


Figure 4-10 The energy band (left) and DOS (right) for the s and p states of the mono-atomic chain.

Chapter 5 Harmonic Phonon Frequencies

5.1 Harmonic approximations

The calculation of vibrational spectra for molecular systems is well-known and implemented into many successful quantum chemistry program systems. The method is based on the calculation of the Hessian matrix, either numerically or analytically. The situation is much more complicated for crystals due to the constraint of translational symmetry. We begin the analysis for solids by defining the Cartesian displacement of each atom in the crystal:

$$\mathbf{u}_\alpha^{\mathbf{R},i} = \mathbf{r}_\alpha^{\mathbf{R},i} - \bar{\mathbf{r}}_\alpha^{\mathbf{R},i} \quad (\alpha = x, y, z) \quad (5-1)$$

where $\mathbf{r}_\alpha^{\mathbf{R},i}$ is the α -th component of a position vector for the atom i in the \mathbf{R} unit cell. $\bar{\mathbf{r}}_\alpha^{\mathbf{R},i}$ is the corresponding equilibrium position.

We consider a perfect crystal containing an infinite number of unit cells each of which includes a number of M atoms. Therefore there are $3M$ independent displacements per unit cell. For crystals, since no rotational motions are possible, there should be, unlike in the molecular case, $3M-3$ vibrational degrees of freedom, which are referred to as *the optical modes*, by excluding 3 translational movements, i.e., the *acoustic modes*, along the x , y and z directions.

In terms of the Cartesian displacement, the total crystal potential energy E can be expanded in a Taylor series around the equilibrium geometrical configuration as:

$$\begin{aligned} E = E_0 + \sum_{\mathbf{R}} \sum_{i \in \mathbf{R}} \sum_{\alpha}^3 \left(\frac{\partial E}{\partial u_\alpha^{\mathbf{R},i}} \right)_0 u_\alpha^{\mathbf{R},i} + \frac{1}{2!} \sum_{\mathbf{R}, \mathbf{G}} \sum_{i \in \mathbf{R}} \sum_{\alpha, \beta}^3 \left(\frac{\partial^2 E}{\partial u_\alpha^{\mathbf{R},i} \partial u_\beta^{\mathbf{G},j}} \right)_0 u_\alpha^{\mathbf{R},i} u_\beta^{\mathbf{G},j} \\ + \frac{1}{3!} \sum_{\mathbf{R}, \mathbf{G}, \mathbf{H}} \sum_{i \in \mathbf{R}} \sum_{\alpha, \beta, \gamma}^3 \left(\frac{\partial^3 E}{\partial u_\alpha^{\mathbf{R},i} \partial u_\beta^{\mathbf{G},j} \partial u_\gamma^{\mathbf{H},k}} \right)_0 u_\alpha^{\mathbf{R},i} u_\beta^{\mathbf{G},j} u_\gamma^{\mathbf{H},k} + \dots \end{aligned} \quad (5-2)$$

where E_0 is a constant potential at the equilibrium structure and can be eliminated in the following discussion, owing to the fact that this simply amounts to a shift of the origin of the energy scale. The second term maps to the total equilibrium field and should be zero. The *harmonic approximation* is so defined that the series is truncated after the third term in (5-2). These higher order terms provide *anharmonic effects* and are significant for the fine details of vibrational spectra. They can be corrected by semi-empirical models since the strict first-principles anharmonic corrections are only feasible for systems containing a few atoms. Thus (5-2) is reduced to the contribution from the second order term only:

Harmonic Phonon Frequencies

$$\begin{aligned}
 E &= \frac{1}{2!} \sum_{\mathbf{R}, \mathbf{G}}^M \sum_{i \in \mathbf{R}} \sum_{\substack{\alpha, \beta \\ j \in \mathbf{G}}}^3 \left(\frac{\partial^2 E}{\partial u_{\alpha}^{\mathbf{R}, i} \partial u_{\beta}^{\mathbf{G}, j}} \right)_0 u_{\alpha}^{\mathbf{R}, i} u_{\beta}^{\mathbf{G}, j} \\
 &= \frac{1}{2!} \sum_{\mathbf{R}, \mathbf{G}}^M \sum_{i \in \mathbf{R}} \sum_{\substack{\alpha, \beta \\ j \in \mathbf{G}}}^3 f_{\alpha\beta}^{\mathbf{R}\mathbf{G}, ij} u_{\alpha}^{\mathbf{R}, i} u_{\beta}^{\mathbf{G}, j}
 \end{aligned} \tag{5-3}$$

Here $f_{\alpha\beta}^{\mathbf{R}\mathbf{G}, ij}$ denotes the force constant. It is noted that, according to the translational invariance for crystals, the force constants cannot depend on the absolute position of unit cells but only upon their relative positions, i.e.:

$$f_{\alpha\beta}^{\mathbf{R}\mathbf{G}, ij} = f_{\alpha\beta}^{\mathbf{R}+\mathbf{t}, \mathbf{G}+\mathbf{t}, ij} \tag{5-4}$$

Here $\mathbf{R} + \mathbf{t}$ and $\mathbf{G} + \mathbf{t}$ identify the unit cells translated by the same lattice vector \mathbf{t} . Consequently we immediately have by letting $\mathbf{t} = \mathbf{R}$ or $\mathbf{t} = \mathbf{G}$:

$$f_{\alpha\beta}^{\mathbf{R}\mathbf{G}, ij} = f_{\alpha\beta}^{\mathbf{0}\mathbf{G}-\mathbf{R}, ij} = f_{\alpha\beta}^{\mathbf{R}-\mathbf{G}, \mathbf{0}, ij} \tag{5-5}$$

Additionally we have the commuting index symmetry:

$$f_{\alpha\beta}^{\mathbf{R}\mathbf{G}, ij} = f_{\beta\alpha}^{\mathbf{G}\mathbf{R}, ji} \tag{5-6}$$

The Newton equation of motion for the atom i in the \mathbf{R} unit cell is expressed as:

$$\sum_{\mathbf{G}}^M \sum_{j \in \mathbf{G}} \sum_{\beta}^3 f_{\alpha\beta}^{\mathbf{R}\mathbf{G}, ij} u_{\beta}^{\mathbf{G}, j} = m_i \frac{d^2 u_{\alpha}^{\mathbf{R}, i}}{dt^2} \tag{5-7}$$

The above linear differential equation has a general plane-wave-like solution:

$$u_{\alpha}^{\mathbf{R}, i}(\mathbf{k}) = \frac{A_{i, \alpha}}{\sqrt{m_i}} e^{i(\mathbf{k} \cdot \mathbf{R} - \bar{\omega} t)} \tag{5-8}$$

This solution describes a general motion of the lattice where all equivalent atoms in different unit cells experience periodic displacements of the same frequency $\frac{\bar{\omega}}{2\pi}$ and

amplitude $\frac{A_{i, \alpha}}{\sqrt{m_i}}$ with a phase difference determined by the vector \mathbf{k} . The \mathbf{k} is a wavevector

and represents a traveling lattice wave of the wavelength $\frac{2\pi}{|\mathbf{k}|}$ propagating towards the

direction of \mathbf{k} , called a *normal mode*, or a *phonon*. Although the \mathbf{k} vector is the same reciprocal lattice vector as has been discussed for the electronic theory of solids, nevertheless, it indicates the wave of atomic collective motions other than the wave of electrons. The equation (5-8) can also be equivalently reformed as:

Harmonic Phonon Frequencies

$$\begin{aligned}
 u_{\alpha}^{\mathbf{R},i}(\mathbf{k}) &= e^{i\mathbf{k}\cdot\mathbf{R}} \left(\frac{A_{i,\alpha}}{\sqrt{m_i}} e^{-i\bar{\omega}t} \right) \\
 &= e^{i\mathbf{k}\cdot\mathbf{R}} u_{\alpha}^{0,i}
 \end{aligned} \tag{5-9}$$

which can be regarded as the Bloch condition for lattice waves, similar to the Bloch theorem in (1-15) for electronic wavefunctions.

Inserting (5-9) into (5-7) and applying the conditions (5-5) and (5-6), we come to:

$$\sum_{j \in \mathbf{R}} \sum_{\beta}^3 f_{\alpha\beta}^{ij}(\mathbf{k}) \frac{A_{j,\beta}}{\sqrt{m_i m_j}} = A_{i,\alpha} \bar{\omega}^2 \tag{5-10}$$

where we use the force constant is transformed to the reciprocal space:

$$f_{\alpha\beta}^{ij}(\mathbf{k}) = \sum_{\mathbf{R}} f_{\alpha\beta}^{0\mathbf{R},ij} e^{i\mathbf{k}\cdot\mathbf{R}} \tag{5-11}$$

If we define a $3M \times 3M$ dimensional matrix $\mathbf{H}(\mathbf{k})$ for each \mathbf{k} point, called *dynamic matrix*¹³, and a $3M$ dimensional vector matrix \mathbf{A} , the following secular eigenequation is obtained:

$$\mathbf{H}(\mathbf{k})\mathbf{A} = \mathbf{A}\mathbf{E}(\mathbf{k}) \tag{5-12}$$

with

$$\mathbf{H}(\mathbf{k}) = \begin{pmatrix} \frac{f_{xx}^{11}(\mathbf{k})}{\sqrt{m_1 m_1}} & \frac{f_{xy}^{11}(\mathbf{k})}{\sqrt{m_1 m_1}} & \dots & \frac{f_{zy}^{1M}(\mathbf{k})}{\sqrt{m_1 m_M}} & \frac{f_{zz}^{1M}(\mathbf{k})}{\sqrt{m_1 m_M}} \\ \frac{f_{xx}^{21}(\mathbf{k})}{\sqrt{m_2 m_1}} & \frac{f_{xy}^{21}(\mathbf{k})}{\sqrt{m_2 m_1}} & \dots & \frac{f_{zy}^{2M}(\mathbf{k})}{\sqrt{m_2 m_M}} & \frac{f_{zz}^{2M}(\mathbf{k})}{\sqrt{m_2 m_M}} \\ \vdots & \vdots & \vdots & \vdots & \vdots \\ \frac{f_{xx}^{(M-1)1}(\mathbf{k})}{\sqrt{m_{M-1} m_1}} & \frac{f_{xy}^{(M-1)1}(\mathbf{k})}{\sqrt{m_{M-1} m_1}} & \dots & \frac{f_{zy}^{(M-1)M}(\mathbf{k})}{\sqrt{m_{M-1} m_M}} & \frac{f_{zz}^{(M-1)M}(\mathbf{k})}{\sqrt{m_{M-1} m_M}} \\ \frac{f_{xx}^{M1}(\mathbf{k})}{\sqrt{m_M m_1}} & \frac{f_{xy}^{M1}(\mathbf{k})}{\sqrt{m_M m_1}} & \dots & \frac{f_{zy}^{MM}(\mathbf{k})}{\sqrt{m_M m_M}} & \frac{f_{zz}^{MM}(\mathbf{k})}{\sqrt{m_M m_M}} \end{pmatrix}_{3M \times 3M} \tag{5-13}$$

and

$$\mathbf{A} = \begin{pmatrix} A_{1,x} \\ A_{1,y} \\ A_{1,z} \\ \vdots \\ A_{M,y} \\ A_{M,z} \end{pmatrix}_{3M}, \quad \mathbf{E}(\mathbf{k}) = \begin{pmatrix} \bar{\omega}_1(\mathbf{k}) & 0 & \dots & 0 \\ 0 & \bar{\omega}_2(\mathbf{k}) & \dots & 0 \\ \vdots & \vdots & \dots & \vdots \\ 0 & 0 & \dots & \bar{\omega}_{3M}(\mathbf{k}) \end{pmatrix}_{3M} \tag{5-14}$$

¹³ The dynamic matrix at the $\mathbf{k}=0$ point corresponds to the Hessian matrix for molecular cases.

Harmonic Phonon Frequencies

Therefore the vibrational frequencies can be solved by diagonalizing the dynamic matrix, and the vibrational eigenvectors for each eigenvalue are given by the corresponding transformation matrix with the normalization constraint:

$$\mathbf{A}^+ \mathbf{A} = \mathbf{I} \quad (5-15)$$

The plot of phonon energies against the coordinates of \mathbf{k} points depicts the phononic states and refers to the *phonon dispersion*, similar to the band structure of electronic states. The statistic state distribution of phonons is continuous and can be described by the *density of phonons*, also similar to the corresponding concept of the electronic density of states.

It is clear from the definition that the dynamic matrix has properties which are quite similar to the case of electronic theory in (1-16), (1-17) and (1-18):

$$\mathbf{H}(\mathbf{k}) = \mathbf{H}(\mathbf{k} + \mathbf{K}) \quad (5-16)$$

$$\mathbf{H}(\mathbf{k}) = \mathbf{H}(\beta\mathbf{k}) \quad (5-17)$$

$$\mathbf{H}^*(\mathbf{k}) = \mathbf{H}(-\mathbf{k}) \quad (5-18)$$

Therefore, similar to the electronic calculation, the phononic calculation is only necessary within the first Brillouin zone. Additionally, due to the commuting index symmetry in (5-6), only the calculations of those unequal elements are necessary.

5.2 Lattice summation and collective displacements

As the equation (5-11) manifests itself, the force constant at \mathbf{k} for atom i in the reference 0-cell is obtained by displacing atoms j running through, in principle, an infinite crystal in all three Cartesian directions and subsequently performing the Fourier transform. Unfortunately, this is not possible without breaking the translation symmetry of the lattice (see Figure 5-1) if the atoms are displaced one by one. What is feasible is to do collective displacements of atoms by exploiting the translation symmetry.

5.2.1 Frozen phonon approach

Let us define a force resulting from the displacement $(u_\beta^{\mathbf{R},j})'$ of atom j in the \mathbf{R} cell proportional to the phase factor $e^{-i\mathbf{k}\cdot\mathbf{R}}$:

$$F_\beta^{\mathbf{R},j} = -\frac{\partial E}{\partial (u_\beta^{\mathbf{R},j})'} \quad (5-19)$$

where the displacement $(u_\beta^{\mathbf{R},j})'$ is:

$$(u_\beta^{\mathbf{R},j})' = u_\beta^{\mathbf{R},j} e^{-i\mathbf{k}\cdot\mathbf{R}} \quad (5-20)$$

The equation (5-11) is simplified as:

Harmonic Phonon Frequencies

$$\begin{aligned}
 f_{\alpha\beta}^{ij}(\mathbf{k}) &= \frac{\partial}{\partial u_{\alpha}^{0,i}} \sum_{\mathbf{R}} (-F_{\beta}^{\mathbf{R},j}) \\
 &= -\frac{\partial F_{\beta}^j}{\partial u_{\alpha}^{0,i}}
 \end{aligned}
 \tag{5-21}$$

Therefore the strategy to solve the infinite lattice summation is available immediately due to (5-21): the j -type atoms are collectively displaced in every cell proportionally to $e^{-i\mathbf{k}\cdot\mathbf{R}}$ (cf. Figure 5-2). This approach is called the **frozen phonon** which virtually creates a static phonon propagating along the wavevector \mathbf{k} . For the special Γ point, the phase factor vanishes and thus all the atoms of the type j are identically displaced in all cells so that a perfect lattice is remaining. Such atomic collective displacements can be automatically generated by making use of any electronic structure calculation code with the consideration of periodic boundary condition. Therefore the Γ -phonon calculations turn out to be the same way, within a unit cell, as molecules.

5.2.2 Supercell approach

An alternative way for the lattice summation is the **supercell approach**, i.e., the individual displacements of atoms take place in the supercell. We consider a two-dimensional lattice. The supercell is assumed to have 2×3 dimensionality in terms of the single cell, which leads to the reciprocal lattice cell reduced by $\frac{1}{2} \times \frac{1}{3}$ compared to that of the single cell. Their direct and reciprocal lattices are shown in Figure 5-3. The \mathbf{k} points in the reciprocal lattice are denoted as $\Gamma(0,0)$, $\mathbf{k}_1(\frac{\mathbf{b}_1}{2}, 0)$, $\mathbf{k}_2(\frac{\mathbf{b}_1}{2}, \frac{\mathbf{b}_2}{3})$ and $\mathbf{k}_3(0, \frac{\mathbf{b}_2}{3})$.

According to the Bloch condition in (5-9) and assuming the real vibration vector at Γ point in the reciprocal lattice, we can arrive at the vibration patterns of these direct lattice points within the supercell, containing both real and imaginary components, at \mathbf{k}_1 , \mathbf{k}_2 and \mathbf{k}_3 points. This is presented in Figure 5-4. For example, the displacements for the $(\mathbf{a}_1, 2\mathbf{a}_2)$ point read at \mathbf{k}_1 , \mathbf{k}_2 and \mathbf{k}_3 , respectively, as:

$$u_{\alpha}^{(\mathbf{a}_1, 2\mathbf{a}_2), i}(\mathbf{k}_1) = e^{i\frac{2\pi}{2}} u_{\alpha}^{0,i} = -u_{\alpha}^{0,i}
 \tag{5-22}$$

$$u_{\alpha}^{(\mathbf{a}_1, 2\mathbf{a}_2), i}(\mathbf{k}_2) = e^{i(\frac{1}{2} + \frac{2}{3})2\pi} u_{\alpha}^{0,i} = (\frac{1}{2} + i\frac{\sqrt{3}}{2})u_{\alpha}^{0,i}
 \tag{5-23}$$

$$u_{\alpha}^{(\mathbf{a}_1, 2\mathbf{a}_2), i}(\mathbf{k}_3) = e^{i\frac{2}{3}2\pi} u_{\alpha}^{0,i} = (-\frac{1}{2} - i\frac{\sqrt{3}}{2})u_{\alpha}^{0,i}
 \tag{5-24}$$

It is evidently seen from Figure 5-4 that for these \mathbf{k} points, the periodically repeated units associated with the vibrational vectors are not the original single cell any more but the supercells framed in the dashed rectangles, except for the central Γ point where the original single cell is the repeated unit.

Harmonic Phonon Frequencies

Let us generalize the supercell approach as follows for a three-dimensional crystal containing $N_1 \times N_2 \times N_3$ single cells. We consider the equation (5-11) again, for a particular \mathbf{k}_0 point.

$$f_{\alpha\beta}^{ij}(\mathbf{k}) = \sum_{\mathbf{R}} (f_{\alpha\beta}^{0\mathbf{R},ij} e^{i\mathbf{k}_0 \cdot \mathbf{R}}) e^{i(\mathbf{k}-\mathbf{k}_0) \cdot \mathbf{R}} \quad (5-25)$$

The lattice summation is performed over single cells associated with the direct lattice vector $(\mathbf{a}_1, \mathbf{a}_2, \mathbf{a}_3)$. Let $\mathbf{k}' = \mathbf{k} - \mathbf{k}_0$,

$$f_{\alpha\beta}^{ij}(\mathbf{k}'+\mathbf{k}_0) = \sum_{\mathbf{R}} (f_{\alpha\beta}^{0\mathbf{R},ij} e^{i\mathbf{k}_0 \cdot \mathbf{R}}) e^{i\mathbf{k}' \cdot \mathbf{R}} \quad (5-26)$$

For this particular \mathbf{k}_0 point in terms of the reciprocal lattice vector $(\mathbf{b}_1, \mathbf{b}_2, \mathbf{b}_3)$,

$$\mathbf{k}_0 = \frac{k_1^0}{N_1} \mathbf{b}_1 + \frac{k_2^0}{N_2} \mathbf{b}_2 + \frac{k_3^0}{N_3} \mathbf{b}_3 \quad (5-27)$$

one can always find a position vector $\mathbf{R}_0 = m_1^0 \mathbf{a}_1 + m_2^0 \mathbf{a}_2 + m_3^0 \mathbf{a}_3$ that meets the periodic condition:

$$e^{i\mathbf{k}_0 \cdot \mathbf{R}_0} = 1 \quad (5-28)$$

$$\frac{k_1^0}{N_1} m_1^0 + \frac{k_2^0}{N_2} m_2^0 + \frac{k_3^0}{N_3} m_3^0 = n_{\min} \quad (5-29)$$

where n_{\min} is the minimum possible integer. If we define a new lattice vector $(\mathbf{a}'_1, \mathbf{a}'_2, \mathbf{a}'_3)$, namely for a particular supercell, by:

$$\mathbf{a}'_1 = m_1^0 \mathbf{a}_1, \quad \mathbf{a}'_2 = m_2^0 \mathbf{a}_2, \quad \mathbf{a}'_3 = m_3^0 \mathbf{a}_3 \quad (5-30)$$

There are $N'_1 \times N'_2 \times N'_3$ supercells in a crystal:

$$N'_1 \times N'_2 \times N'_3 = \left(\frac{N_1}{m_1^0}\right) \times \left(\frac{N_2}{m_2^0}\right) \times \left(\frac{N_3}{m_3^0}\right) \quad (5-31)$$

The equation (5-26) is converted to the lattice summation with respect to the position vector $\mathbf{S} = s_1 \mathbf{a}'_1 + s_2 \mathbf{a}'_2 + s_3 \mathbf{a}'_3$ of this particular supercell:

$$\begin{aligned} f_{\alpha\beta}^{ij}(\mathbf{k}'+\mathbf{k}_0) &= \sum_{\mathbf{S}} (f_{\alpha\beta}^{0\mathbf{S},ij} e^{i\mathbf{k}_0 \cdot \mathbf{S}}) e^{i\mathbf{k}' \cdot \mathbf{S}} \\ &= \sum_{\mathbf{S}} f_{\alpha\beta}^{0\mathbf{S},ij} e^{i\mathbf{k}' \cdot \mathbf{S}} \end{aligned} \quad (5-32)$$

where the second equality is due to the fact $e^{i\mathbf{k}_0 \cdot \mathbf{S}} = 1$.

The new reciprocal lattice vectors due to (5-30) are:

$$\mathbf{b}'_1 = \frac{\mathbf{b}_1}{m_1^0}, \quad \mathbf{b}'_2 = \frac{\mathbf{b}_2}{m_2^0}, \quad \mathbf{b}'_3 = \frac{\mathbf{b}_3}{m_3^0} \quad (5-33)$$

Harmonic Phonon Frequencies

The point \mathbf{k}' can be actually represented in terms of $(\mathbf{b}'_1, \mathbf{b}'_2, \mathbf{b}'_3)$:

$$\begin{aligned}\mathbf{k}' &= \mathbf{k} - \mathbf{k}_0 \\ &= \frac{k_1 - k_1^0}{N_1} \mathbf{b}_1 + \frac{k_2 - k_2^0}{N_2} \mathbf{b}_2 + \frac{k_3 - k_3^0}{N_3} \mathbf{b}_3 \\ &= \frac{k'_1}{N'_1} \mathbf{b}'_1 + \frac{k'_2}{N'_2} \mathbf{b}'_2 + \frac{k'_3}{N'_3} \mathbf{b}'_3\end{aligned}\tag{5-34}$$

Evidently, the origin of this new reciprocal lattice is shifted from Γ to Γ' , i.e., from $\Gamma = 0$ to $\Gamma' = \mathbf{k}_0$. Therefore the force constant at the \mathbf{k}_0 point in the original reciprocal lattice $(\mathbf{b}_1, \mathbf{b}_2, \mathbf{b}_3)$ is achieved at Γ' in the new reciprocal lattice $(\mathbf{b}'_1, \mathbf{b}'_2, \mathbf{b}'_3)$:

$$f_{\alpha\beta}^{ij}(\mathbf{k}_0) = f_{\alpha\beta}^{ij}(\Gamma') = \sum_{\mathbf{s}} f_{\alpha\beta}^{\text{OS},ij}\tag{5-35}$$

It turns out that the calculation of \mathbf{k}_0 phonons for a single cell $(\mathbf{a}_1, \mathbf{a}_2, \mathbf{a}_3)$ is converted to the problem of calculating the Γ' phonons for a supercell $(\mathbf{a}'_1, \mathbf{a}'_2, \mathbf{a}'_3)$, which can in turn be calculated by using the frozen phonon approach. That is to say, in practice of a supercell approach, all atoms within this supercell corresponding to a particular \mathbf{k}_0 point are independently displaced and the displacements are essentially equivalent to those of equivalent atoms in another supercell (cf. Figure 5-5).

5.3 Implementing the Γ frequencies in the CO-LCAO approach

According to the above frozen-phonon scheme, we have implemented the computation of harmonic vibrational modes at the Γ point for periodic compounds in the framework of CO-LCAO approach, since the computation of vibrational frequencies is not yet available in the released version of the CRYSTAL03 package. We have created a bsh-script to generate the atom-displaced structures, and thus the dynamic matrix at the Γ point is obtained by using a numerical derivative of the total energies with respect to the displacements. A C-language code has been written to diagonalize the dynamic matrix. The vibrating eigenvectors can be subsequently evaluated with the normalization condition for each mode. The detailed information of the implementation can be found in the section 9.2.

Harmonic Phonon Frequencies

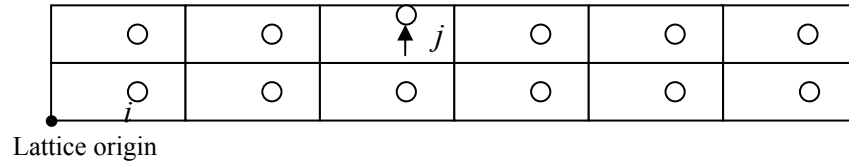


Figure 5-1 The broken translation symmetry by displacing one atom in a cell.

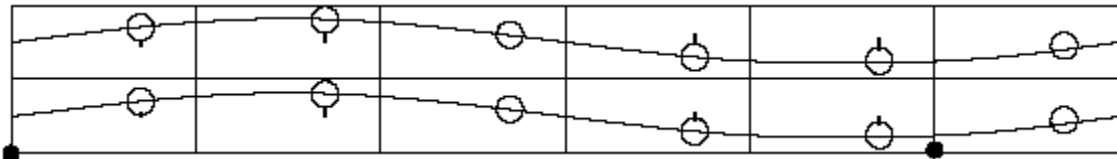


Figure 5-2 The frozen phonon approach for the lattice summation.

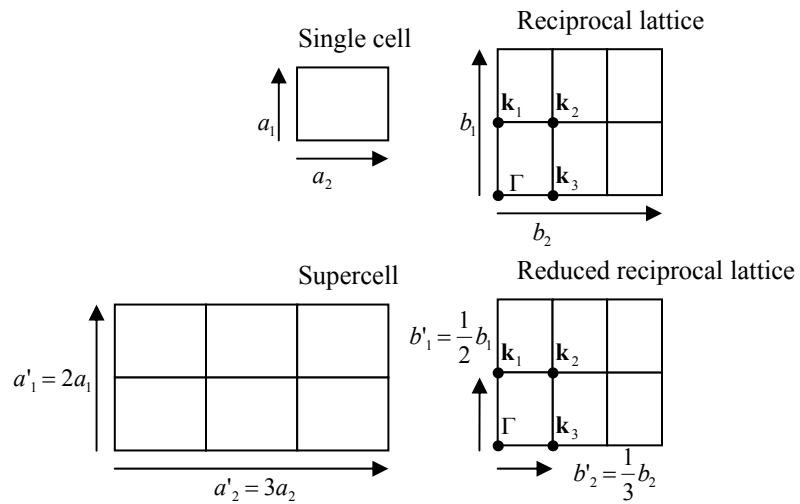


Figure 5-3 Two dimensional lattices for the single cell and the supercell.

Harmonic Phonon Frequencies

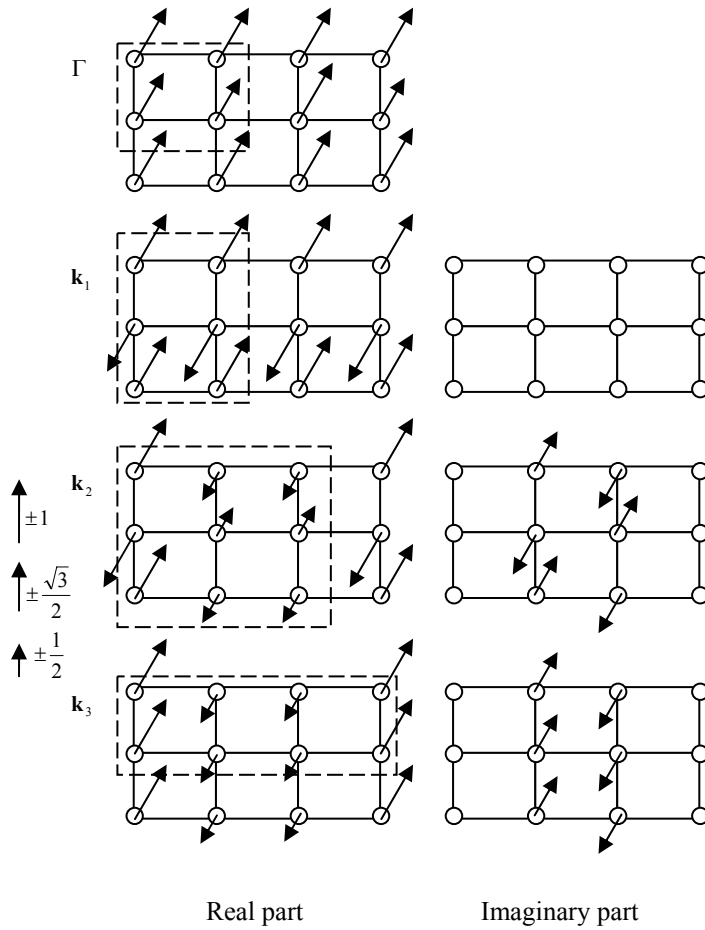


Figure 5-4 The displacement patterns for a two-dimensional lattice at the k_1 , k_2 and k_3 points.

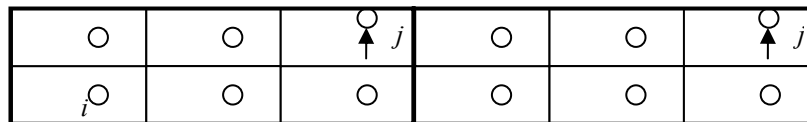


Figure 5-5 The collective displacements of atoms in two supercells containing 2×3 single cells each.

Part II

Applications

Chapter 6 Electronic Structure of BiBO

Insightful information contained in electronic bands of crystals can be used to project what roles the electronic crystal states play in determining the structure and basic properties, an information which is unavailable through mere experiments. In this chapter, we calculate and discuss the energy bands, the density of states and spin-orbit effects.

6.1 Computational details

Different first-principles methods (i.e., HF, LDA, GGA and hybrid functionals) were used to optimize the atomic coordinates of BiBO and the accuracies were compared with the experimental bond lengths and angles by running the CO-LCAO-based package CRYSTAL03 [64]. The optimizations were performed by using a modified conjugate gradient algorithm [119]. Analytical gradients were evaluated for both HF and DFT and the optimization convergence was achieved by fulfilling three criteria, i.e., between optimization steps the root mean square (RMS) of energy change, gradient change and displacement change should stay less than 10^{-7} a.u., 0.0003 a.u. and 0.0012 a.u., respectively. The following tolerances were employed in the evaluation of infinite Coulomb and HF exchange series: 10^{-7} for the Coulomb overlap, HF exchange overlap, Coulomb penetration and the first exchange pseudo-overlap; 10^{-14} for the second exchange pseudo-overlap. The Fock matrix has been diagonalized at 24 **k**-points within the irreducible Brillouin zone corresponding to a shrinking factor of 4 in the Monkhorst net [63]. The larger number of 150 **k**-points reduces the energy by only 6.4×10^{-6} a.u. In order to improve the convergence, a negative energy shift of 1.0 a.u. to the diagonal Fock/KS matrix elements of the occupied orbitals was added to reduce their coupling to the unoccupied set and maintained after the diagonalization. A very accurate extra-large grid consisting of 75 radial points and 974 angular points was employed in the DFT calculations, where Becke grid point weights [120] were chosen.

In order to investigate the relativistic effects resulting from the heavy Bi cations, we have used an energy-consistent scalar-relativistic as well as a corresponding non-relativistic first-principles ECP of the Stuttgart-Köln variety for Bi [121]. The 1s-5d shells were included in the ECP core and others (i.e., 6s6p ...shells) were left in the valence. The explicit quantum chemical treatment is restricted to the valence electrons and scalar-relativistic effects are usually implicitly accounted for by a proper adjustment of free parameters in the valence model Hamiltonian. The reference data used to determine the spin-orbit averaged relativistic potential have been taken from relativistic all-electron calculations using the so-called Wood-Boring scalar-relativistic HF approach. Both AE WB and ECP calculations have been performed with an atomic finite-difference HF scheme in order to avoid basis set effects in the determination of the ECP parameters. A (4s4p1d)/[2s2p1d] double-zeta valence basis set [121, 122] was applied to the Bi atoms in all calculations with energy-optimized outmost orbital exponents of 0.09 (p orbital) for

Electronic Structure of BiBO

the scalar-relativistic ECP as well as 0.1063 (s orbital) and 0.0944 (p orbital) for the non-relativistic ECP.

The basis sets of boron and oxygen atoms were originally taken from the public EMSL database [123]. Modifications of the exponents of uncontracted outmost orbitals are necessary if they are too diffuse. The triple-zeta Dunning contraction (11s, 6p)/[5s, 3p] [124] and 6-311G* basis sets were employed for oxygens and borons, respectively. One additional d polarization function with the optimized exponent of 0.8700 and 0.8268 was added to the (11s, 6p)/[5s, 3p] contractions of the oxygens for scalar-relativistic and non-relativistic calculations, respectively.

The following process was executed for the basis set optimization: Each exponent was varied with a step size of 0.05 and a single point calculation was completed with CRYSTAL03. At every single optimization iterative stage, each optimal exponent was obtained by a three-point parabolic fitting. The above step was repeated until the variation of SCF energy stayed below 10^{-6} a.u. All the basis set optimizations were performed at the hybrid B3PW scalar-relativistic level and the optimized orbitals were directly transferred to HF and other DFT calculations. We assume that these optimized sets for B3PW are also quite close to the optimum for other methods. For example, the exponent variation of the oxygen d polarization functions from 0.87 to 0.82 leads to a scalar-relativistic HF energy difference of only 3.5×10^{-5} a.u.

The spin-orbit effects were calculated with the plane-wave code WIEN2K [91] only to correct the scalar-relativistic LDA and GGA calculations for band gaps. The muffin-tin radii of Bi, O and B are 2.36 a.u., 1.26 a.u. and 1.26 a.u., respectively. The cutoff energy is -6.0 Ry separating the core and valence configurations of $5d^{10}6s^26p^3$, $2s^22p^4$ and $2s^22p^1$ for Bi, O and B, respectively. The calculations were performed with 1418 LAPWs and converged with 20 **k**-points due to the twofold convergence criteria of the energy less than 10^{-6} Ry and the charge center distance less than 10^{-4} a.u. The occupied core states were treated with fully relativistic effects (mass-velocity, Darwin and Spin-Orbit (SO) corrections) by solving the relativistic Dirac-Fock equation [125], and the valence states were individually calculated with scalar relativistic corrections and SO perturbations in a second variational procedure [126] by using the scalar-relativistic eigenfunctions as basis. The valence SO corrections were applied only to Bi.

6.2 Accuracies of HF, LDA, GGA and hybrid functionals

Before the discussion of the electronic structure, we present results of scalar-relativistic calculations with different Hamiltonians (i.e., HF, LDA, GGA and hybrid functionals) to establish their accuracies with respect to experimental data. In order to make parallel comparisons between different methods, the lattice constants should stay invariant with respect to different methods. Thus in all our subsequent calculations, only the inner-cell atomic coordinates have been fully optimized while fixing the lattice constants to their experimental values. To be sure of its accuracy by the experimental lattice constants for the electronic structure calculations, we also performed the lattice optimization by

Electronic Structure of BiBO

calculating the fully atom-relaxed energies for B3PW with respect to forty cell volumes corresponding to the lattice constants with the variations from +3% to -3% of the experimental ones. The optimized crystallographic lattice constants deviate from the experimental values by less than 0.6% with an energy reduction of only 0.0076 eV. Therefore we assume that the calculations using the experimental lattice constants are sufficiently accurate to describe the band structure of BiBO if other approximations (ECPs, limited basis sets, etc.) are taken into account.

The calculated average absolute deviations $|\Delta_d|^{\text{Bi-O}}$ for Bi-O bond lengths, $|\Delta_d|^{\text{B-O}}$ for B-O bond lengths and $|\Delta_\angle|$ for bond angles between the experimental and theoretical values are listed in Table 6-1. We found that $|\Delta_d|^{\text{Bi-O}}$ is considerably greater than $|\Delta_d|^{\text{B-O}}$ for all methods especially for LDA, which may be due to the incomplete error cancellation between the Bi ECP and the functionals. For $|\Delta_d|^{\text{B-O}}$ there seems to be no evident method bias. The hybrid functionals B3LYP and B3PW indeed reduce the deviations $|\Delta_d|^{\text{Bi-O}}$ and $|\Delta_\angle|$ by a factor of two with respect to LDA and GGA. Although HF gives similar $|\Delta_d|^{\text{B-O}}$ and $|\Delta_d|^{\text{Bi-O}}$ values to B3PW and B3LYP with differences of only a few thousandths of an Angstrom, the $|\Delta_\angle|$ value is almost two times larger than for the hybrid functionals. From a theoretical point of view, HF is not suitable for the electronic structure investigation of BiBO due to its exclusion of correlation effects. Moreover, our previous report [127] suggests that, for some cases like hexagonal ionic lanthanide sesquioxides Ln_2O_3 ($\text{Ln}=\text{La}\sim\text{Pm}$), B3PW agrees with the experimental geometry (i.e., both lattice constants and internal atomic coordinates) even notably better than B3LYP. Therefore, the B3PW functional is recommended and utilized for all the subsequent calculations of BiBO. Nevertheless, the small overestimations of some Bi-O bond lengths even at the B3PW level are at least partially caused by the omission of a core-polarization potential [127, 128] in our applied ECPs for Bi, i.e. the neglect of static and dynamic core-valence correlation.

The scalar-relativistic HF, LDA, GGA and hybrid functionals give the indirect band gaps of 12.54 eV, 3.96 eV/3.96 eV, 4.05 eV/4.07 eV and 5.79 eV/5.69 eV (cf. Table 6-1). Whereas HF overestimates the band gap by a factor of three due to the absence of correlation effects, the LDA and GGA routines underestimate the band gap by about 0.34 eV and 0.24 eV, respectively, which is in line with the general observation that band gaps are usually underestimated within the DFT scheme. The B3PW and B3LYP functionals overshoot the band gap by 1.39 eV, which is however not surprising since B3PW and B3LYP are not pure DFT approaches and mix exact HF and pure DFT exchange with empirically determined weights. Accordingly these hybrid approaches should produce the band gaps located between the results of HF and pure DFT methods. The good performance of GGA and LDA compared to the hybrid approaches has to be viewed with great care, however. If we take into account the spin-orbit effects of the Bi cations, as we will discuss in the following, the hybrid functionals would bring the calculated band gaps much closer to the experimental result than the LDA and GGA approaches.

6.3 Energy band

The band structures for BiBO are illustrated in Figure 6-1 for scalar-relativistic B3PW, non-relativistic B3PW and scalar-relativistic HF calculations. The bands below about -2.0 eV refer to the occupied valence states (valence band, VB) and the bands above refer to the virtual states (conduction band, CB). The scalar-relativistic B3PW gives the indirect band gap of 5.69 eV determined between the Z point at the bottom of conduction bands and the E point at the top of valence bands. This suggests the photon-phonon coupling for a non-vertical E-Z transition in order to meet the energy conservation mainly fulfilled by photons and the momentum conservation mainly fulfilled by phonons. The band dispersions are significant along the specified \mathbf{k} -point paths. As pointed out by Hoffmann [129], band dispersions are determined by the inter-unit-cell overlapping of atomic orbitals, i.e., the overlapping degree sets the band width and the topology of that overlapping provides the way that the bands run up or down. Therefore, the band dispersions along B-D and Z- Γ (i.e., the inter-cell orbital overlapping towards the direction of the c lattice vector) imply additional notable interactions besides the electrostatic attraction between Bi cations and coordinating oxygens anions, since the layers of $[\text{B}_3\text{O}_6]^{3-}$ polyanions are alternating along the c lattice direction connecting the Bi cations in between (Figure 1 (a)). Other \mathbf{k} -point paths in Figure 6-1 correspond to the strong B-O covalent bonds in both $[\text{BO}_3]^{3-}$ and $[\text{BO}_4]^{5-}$ units and thus their bands are much more dispersive than the bands for the Bi-O interactions.

6.4 Electronic state distribution

We explore the electronic state distribution with the density of states projected out for the atomic valence orbitals of bismuths and oxygens in the $[\text{BiO}_4]^{5-}$ units (Figure 6-2) as well as for the triangular $[\text{BO}_3]^{3-}$ and tetrahedral $[\text{BO}_4]^{5-}$ units (Figure 6-3). For the scalar-relativistic B3PW calculation, the lower part of the valence states below -24 eV mainly correspond to the occupied O 2s states, which are well separated by about 7.7 eV from the occupied O 2p states dominating the upper part of the valence states until the top of the valence states at about -5.6 eV. The valence states have contributions also from the admixture of Bi 6s and 6p orbitals contrary to the separation of O 2s and 2p orbitals. Although Bi 6s6p states appear relatively weak, they can be neglected by no means because of their important overlapping with the occupied O 2p states widely spreading over the same region. This indicates that the covalent interactions between the central Bi cations and the coordinating oxygens may take place from the energy matching point of view, which is consistent with the band structure feature. The theoretical measurement of this Bi-O covalent degree will be quantified in Chapter 7.

The lower parts of the conduction states between 0 eV and 3 eV result from the strong origin of the unoccupied Bi 6p orbitals with only small contributions from other orbitals. The region above 3 eV can be divided into two sectors (Figure 6-3), i.e., from ~ 3 eV to ~ 7 eV consisting of the states of $[\text{BO}_3]^{3-}$ units and above about 7 eV consisting of the states of both $[\text{BO}_3]^{3-}$ and $[\text{BO}_4]^{5-}$ units. These unoccupied states result mainly from the

boron empty orbitals since the oxygen 2s2p states show little contributions to the conduction bands (Figure 6-2).

6.5 Spin-orbit coupling

We examine the spin-orbit coupling for Bi cations on the energy band of BiBO. The non-relativistic B3PW calculation gives an indirect band gap of 4.92 eV. The scalar-relativistic effect enlarges the gap to 5.69 eV. One may note that the scalar-relativistic band gap is considerably larger than the experimental value of 4.3 eV, while the non-relativistic band gap appears to agree quite well with only half of the deviation from the experimental value. In Table 6-2, it also seems that the LDA and GGA approaches give band gaps closer to the experimental value than B3PW and B3LYP. We explain this result as the consequence of neglecting the spin-orbit splitting of the Bi 6p states due to the averaged SO potential in the applied ECP of Bi, whereas SO effects originating from Bi have been theoretically found to significantly reduce the band gaps of some Bi-containing crystals like CsBi₄Te₆ [130] and Bi₂Te₃ [131]. The SO effects were therefore explored by recalculating the band gaps of BiBO without and with SO correction using the plane-wave code WIEN2K. The calculated band gaps without SO corrections are 3.90 eV (PW-LDA), 4.08 eV (PBE), 4.08 eV (PW91) (Table 6-2), which are quite close to the corresponding results obtained with the CO-LCAO code CRYSTAL03. It can further be seen from Table 6-2 that SO interactions considerably lower the band gaps by about 0.7 eV to 3.21 eV (PW-LDA), 3.37 eV (PBE) and 3.36 eV (PW91), which are left about 1.0 eV lower than the experimental result and thus are not sufficiently accurate. Although the plane-wave method cannot derive a SO correction for hybrid functionals, it is reasonable to infer that the reduction of the gap for B3PW due to SO couplings would be similar to that for LDA and GGA. On the other hand, at the all-electron state-averaged multi-configuration Dirac-HF level using the Dirac-Coulomb Hamiltonian (GRASP) [132], the Bi 6p_{1/2}-6p_{3/2} atomic spinor splitting is 2.10 eV, i.e., 6p_{1/2} is lowered by 1.40 eV compared to the scalar relativistic 6p. We therefore conclude that around 50% of the atomic SO effect is transferred to the solid BiBO. Although without SO corrections the B3PW functional overrates the band gap significantly, a SO lowering of the conduction band by this magnitude (about between 0.70 eV and 1.40 eV) would bring the B3PW estimate (about between 4.29 eV and 4.99 eV) into much better agreement with the experimental value of 4.3 eV than the LDA and GGA results.

Electronic Structure of BiBO

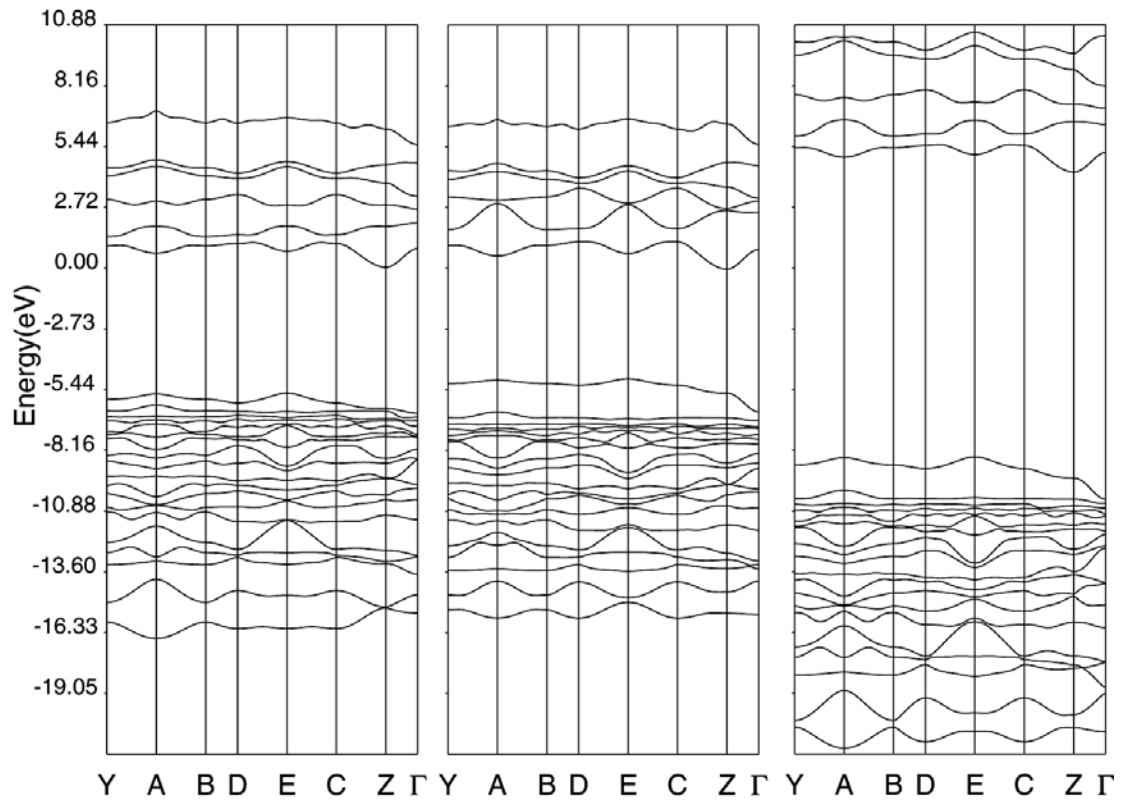


Figure 6-1 The energy bands of BiBO over the valence band region obtained from scalar-relativistic B3PW (left), non-relativistic B3PW (middle) and scalar-relativistic HF (right) calculations.

Electronic Structure of BiBO

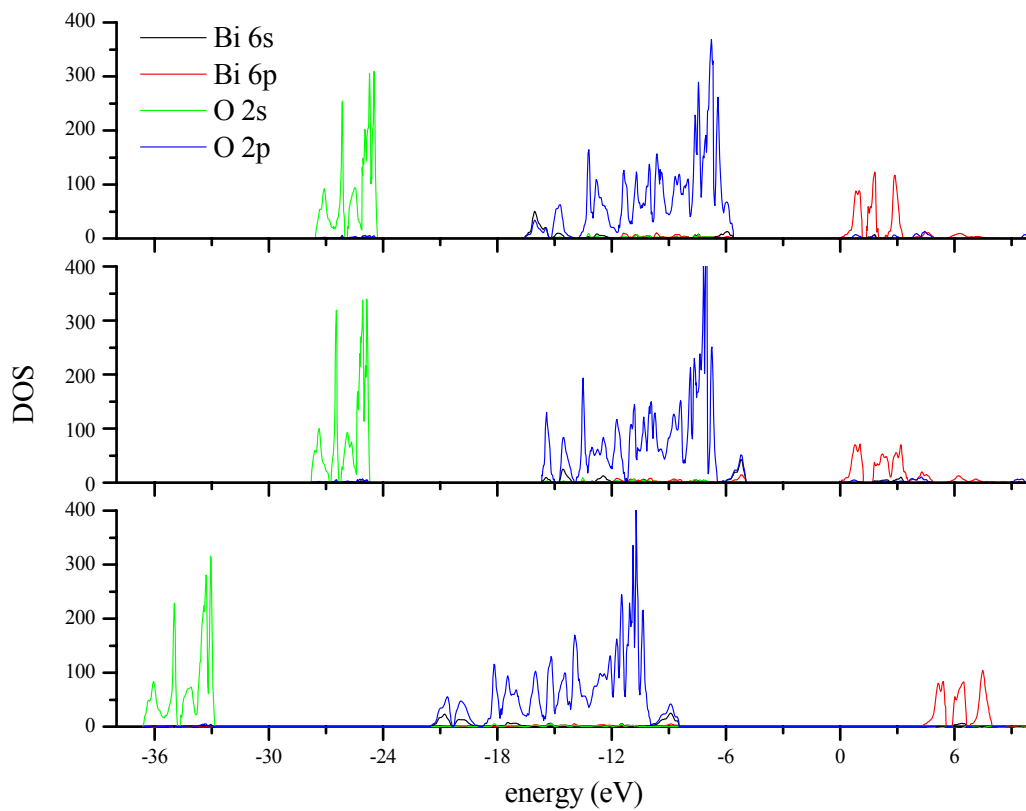


Figure 6-2 The l-momentum-projected density of states for the valence orbitals of bismuths and oxygens of $[\text{BiO}_4]^{5-}$ units of BiBO for scalar-relativistic B3PW (top), non-relativistic B3PW (middle) and scalar-relativistic HF (bottom) calculation.

Electronic Structure of BiBO

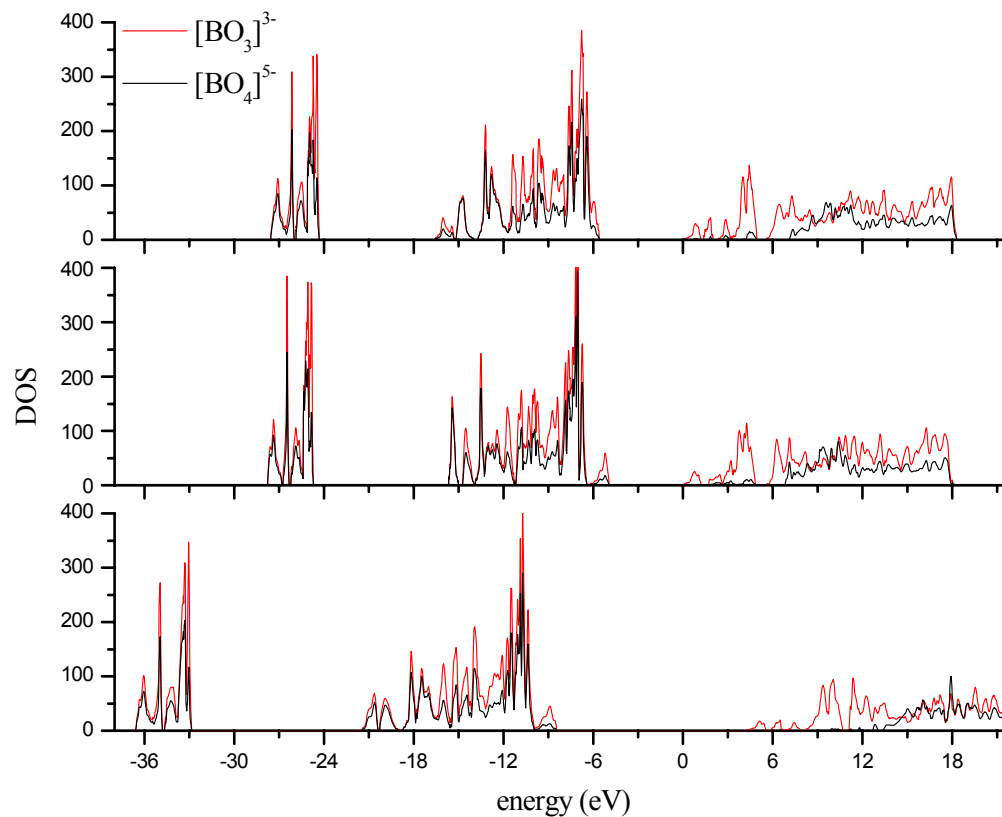


Figure 6-3 The atom-projected density of states for the triangular $[\text{BO}_3]^{3-}$ and tetrahedral $[\text{BO}_4]^{5-}$ units of BiBO for scalar-relativistic B3PW (top), non-relativistic B3PW (middle) and scalar-relativistic HF (bottom) calculations.

Table 6-1 The dependence of the geometry and band gap of BiBO on HF, LDA, GGA and hybrid functionals for scalar-relativistic calculations. The lattice constants were fixed to their experimental values.

	Exp. [33]	HF	VWN-LDA	PW-LDA	PBE	PW91	B3LYP	B3PW
[BiO ₄] ⁵⁻ (Å)	2.390	2.380	2.405	2.404	2.394	2.394	2.389	2.388
	2.086	2.061	2.140	2.140	2.135	2.133	2.105	2.109
[BO ₃] ³⁻ (Å)	1.411	1.394	1.404	1.404	1.412	1.411	1.404	1.405
	1.365	1.354	1.368	1.368	1.376	1.375	1.367	1.367
[BO ₄] ⁵⁻ (Å)	1.339	1.336	1.345	1.345	1.352	1.350	1.344	1.344
	1.487	1.489	1.490	1.490	1.505	1.504	1.500	1.498
	1.436	1.446	1.444	1.443	1.451	1.450	1.446	1.446
∠O6'-Bi-O7' (°)	102.15	103.18	100.79	100.89	99.85	100.02	101.17	101.40
∠O4-Bi-O5 (°)	152.20	154.66	149.69	149.75	148.80	149.03	151.20	151.32
∠O6-Bi-O7 (°)	90.58	89.92	89.18	89.22	90.04	90.01	90.15	89.88
Δ _d ^{Bi-O} (Å)		0.018	0.034	0.034	0.026	0.026	0.010	0.012
Δ _d ^{B-O} (Å)		0.009	0.005	0.005	0.011	0.010	0.007	0.007
Δ _∠ (°)		1.38	1.63	1.70	2.08	1.96	0.80	0.78
Band gap (eV)	4.3	12.54	3.96	3.96	4.05	4.07	5.79	5.69

Table 6-2 The spin-orbit effect on band gaps of BiBO.

Band gap (ev)	HF	VWN-LDA	PW-LDA	PBE	PW91	B3LYP	B3PW
no SO							
CRYSTAL03	12.54	3.96	3.96	4.05	4.07	5.79	5.69
Δ _{gap} (eV) ^a	+8.24	-0.34	-0.34	-0.25	-0.23	+1.49	+1.39
no SO							
WIEN2K	no ^c	no	3.90	4.08	4.08	no	no
Δ _{gap} (eV) ^a	no	no	-0.40	-0.23	-0.22	no	no
SO							
WIEN2K	no	no	3.21 (-0.69) ^b	3.37 (-0.71) ^b	3.36 (-0.72) ^b	no	no
Δ _{gap} (eV) ^a	no	no	-1.09	-0.93	-0.94	no	no

a: The deviations Δ_{gap} compared with the experimental value (4.30 eV).

b: The numbers in the parenthesis are the SO corrections calculated by WIEN2K.

c: No HF, B3PW and B3LYP calculations available for the plane-wave code WIEN2K

Chapter 7 Orbital Interactions and Bonds in BiBO

The energy band of crystals can be essentially viewed in various ways. Solid state physicists would like to basically explain a band by invoking electronic wave motions through crystals. For example, the forbidden band (i.e., the area between the highest occupied and lowest unoccupied bands with a band gap) is often regarded as the region where the destructive electronic interference takes place for scattered electronic waves. However, a chemical picture for describing a band is closely related to orbital interactions and resultant chemical bonds, as we have discussed in Chapter 4 for an atomic chain. For the crystal BiBO, we will demonstrate that these orbital interactions between central Bi cations and surrounding oxygen anions result in various consequences to interpret corresponding properties of BiBO, e.g., the chemical stability, the optical response, the unusual relativistic effect as well as the asymmetric Bi lone-pair electrons.

7.1 Origin of chemical stabilities

7.1.1 Crystal orbital overlap population

We have applied the crystal orbital overlap population (COOP) scheme following the classic introduction by Hughbanks and Hoffmann [133] in order to analyze the chemical bonds in BiBO. We note that several other methods such as COHP [134] (crystal orbital Hamilton population) and BCOOP [135] (balanced crystal orbital overlap population) are alternative options. COOP describes the density of bonding and antibonding interactions between specific orbitals at a given energy in solids, while its integral intensity for a certain energy interval denotes the relative bond strength within this energy interval. Regions with positive COOP contributions are bonding, regions with negative COOP contributions are antibonding, and zero COOP contributions are nonbonding. The Mulliken overlap population $O_{\alpha\beta}^s(\varepsilon)$ at the energy ε between two atom-centered orbital sets α in the reference cell $(0, 0, 0)$ and β in the cell \mathbf{G} reads:

$$O_{\alpha\beta}^{\mathbf{G}}(\varepsilon) = \frac{1}{V_{BZ}} \sum_{u \in \alpha} \sum_{v \in \beta} S_{uv}^{\mathbf{G}} \int_{BZ} e^{i\mathbf{k} \cdot \mathbf{G}} \sum_i a_{u,i}^*(\mathbf{k}) a_{v,i}(\mathbf{k}) \delta[\varepsilon - \varepsilon_i(\mathbf{k})] d\mathbf{k} \quad (7-1)$$

$(i \in \text{all crystal orbitals})$

If we define the Heaviside step function $H(\varepsilon - \varepsilon_i(\mathbf{k}))$, it yields:

$$\begin{aligned}
 O_{\alpha\beta}^G(\varepsilon) &= \sum_{u \in \alpha} \sum_{v \in \beta} S_{uv}^G \frac{d \left[\frac{1}{V_{BZ}} \int_{BZ} e^{i\mathbf{k} \cdot \mathbf{G}} \sum_i a_{u,i}^*(\mathbf{k}) a_{v,i}(\mathbf{k}) H[\varepsilon - \varepsilon_i(\mathbf{k})] d\mathbf{k} \right]}{d\varepsilon} \\
 &= \sum_{u \in \alpha} \sum_{v \in \beta} S_{uv}^G \frac{dP_{uv}^G(\varepsilon)}{d\varepsilon} \quad (7-2) \\
 &\quad (i \in \text{all crystal orbitals})
 \end{aligned}$$

where S_{uv}^G is the element of the overlap matrix for the atomic orbital u in the reference cell $(0, 0, 0)$ and v in the cell g , and $P_{uv}^G(\varepsilon)$ is the element of the density matrix projected out up to the energy level ε . COOP between the Bi 6s (6p) and O 2p was computed by overlapping corresponding orbitals at Bi1 with those at O4, O5, O6 and O7 in the cell $(0, 0, 0)$, COOP for the triangular $[\text{BO}_3]^{3-}$ units at B9 with O5 in the cell $(0, 0, 0)$ and O2', O6' in the cell $(1, 0, 0)$, and COOP for the tetrahedral $[\text{BO}_4]^{5-}$ units at B8 with O4, O3 in the cell $(0, 0, 0)$ and O2', O5' in the cell $(0, 0, 1)$.

7.1.2 Quantifying chemical bonds in BiBO

The strength and dispersion of Bi-O covalent bonds are quantitatively manifested by scalar-relativistic B3PW COOP in Table 7-1. Bi 6s and O 2p orbitals form both separate bonding and antibonding 6s-2p interactions, while only Bi 6p-O 2p bonding interactions spread continuously below the top of the valence band. Therefore it turns out that the Bi 6s orbitals do host active lone-pair electrons instead of “inert” ones. The Bi 6s-O 2p bonding should contain dominant Bi 6s components and the Bi 6s-O 2p antibonding should contain dominant O 2p components, according to the density of states in Figure 6-2. The Bi-O bonding and antibonding are located over different energy intervals. For example, for O6 and O7, 6s-2p bonding stays within a narrow energy range from -16.6 eV to -14.5 eV; 6s-2p antibondings spread from -13.5 eV to the top of valence bands at about -5.6 eV. For the nearest O6 and O7 atoms around the central Bi, the 6s-2p and 6p-2p bond intensities are remarkably larger than those for the more distant O4 and O5 atoms because of the fast decay of orbital overlapping with increasing Bi-O distance. This is consistent with the classic chemical concept of short-range covalent bonds. From

Figure 7-1, the 6p-2p bonding is found to be significantly important to the stabilization of the $[\text{BiO}_4]^{5-}$ units in the way that it compensates to a great extent the 6s-2p antibondings. However, since the 6p-2p compensation is not complete by leaving the relative net antibonding strength of the negative -0.14 eV below the Fermi level in $[\text{BiO}_4]^{5-}$, it is reasonable to conclude that the electrostatic attraction between Bi cations and O anions is still indispensably necessary to assemble together the two layers of $[\text{B}_3\text{O}_6]^{3-}$ rings at both sides of Bi (Figure 1 (a)). We will point out in the next section that this unstable net antibonding in $[\text{BiO}_4]^{5-}$ is caused by the scalar-relativistic effect of the Bi cations.

The electronic densities in the O6-Bi-O7 and O4-Bi-O5 planes projected within the energy range from -16.6 eV to -14.5 eV are visualized in Figure 7-2 for Bi 6s-O 2p

Orbital Interactions and Bonds in BiBO

bondings. We do not visualize the electronic densities at higher energy levels in order to avoid ambiguity because this region is contributed by both Bi 6p-O 2p bonding and Bi 6s-O 2p antibonding interactions. It is clearly observed that the electrons are concentrated in the middle between Bi and O atoms, which typically represents covalent bonds between Bi 6s and O 2p orbitals.

The covalent bonds in both triangular $[\text{BO}_3]^{3-}$ and tetrahedral $[\text{BO}_4]^{5-}$ units are much stronger than those in $[\text{BiO}_4]^{5-}$ units according to COOP plots in Figure 7-3. It is observed that, the B-O bonds in $[\text{BO}_3]^{3-}$ show a bonding character across the valence band and the antibonding stays in conduction bands, which leaves the strong relative net bonding intensity of 2.90. The B-O bonds in $[\text{BO}_4]^{5-}$ stay bonding from -15.2 eV to -11.0 eV and antibonding from -8.5 eV to -6.3 eV, ending up with the relative net bonding intensity of 0.56 which is much weaker than the B-O bonds in $[\text{BO}_3]^{3-}$ units. Therefore the total relative net bonding for the $[\text{BiO}_4]^{5-}$, $[\text{BO}_3]^{3-}$ and $[\text{BO}_4]^{5-}$ units in BiBO adds up to 3.32 much larger than 0 so that it is sufficient to achieve the stability of BiBO at ambient conditions significantly contributed by the B-O bondings in polyanions. Becker [47] pointed out that according to structure data analysis for numerous anhydrous polyborates the tetrahedral $[\text{BO}_4]^{5-}$ units are not favored units in polyborates at ambient conditions. Most crystallographic structures of anhydrous polyborates contain more triangular $[\text{BO}_3]^{3-}$ units than tetrahedral $[\text{BO}_4]^{5-}$ (cf. Figure 2 in the reference [47]). One reason which can be suggested here due to our calculations for BiBO is that a large ratio of $[\text{BO}_4]^{5-}$ to $[\text{BO}_3]^{3-}$ may greatly intensify the B-O antibonding interactions in $[\text{BO}_4]^{5-}$ close to the Fermi level to such an extent that only the application of external pressure can stabilize the structure.

7.2 Origin of optical effects

Equation (7-3) is formulated to quantitatively describe the density of optical absorptions gauging the contributions from different units in BiBO, which is basically the mathematical convolution at a given energy shift $\hbar\omega$ between the density of states $d_u^{VB}(E)$ for atomic orbital u in VB (valence band) and the density of states $d_v^{CB}(E)$ for atomic orbital v in CB (conduction band).

$$G_{uv}(\omega) = \int_{-\infty}^{+\infty} d_u^{VB}(E) d_v^{CB}(E - \hbar\omega) dE \quad (7-3)$$

Therefore the contributions for optical absorptions from $[\text{BiO}_4]^{5-}$, $[\text{BO}_3]^{3-}$ and $[\text{BO}_4]^{5-}$ units can be calculated by equation (7-4) running over all VB orbitals and those CB orbitals building up $[\text{BiO}_4]^{5-}$, $[\text{BO}_3]^{3-}$ and $[\text{BO}_4]^{5-}$ units, respectively.

$$G_I(\omega) = \sum_u^{VB} \sum_v^{CB} G_{uv}(\omega) \quad (7-4)$$

The plots with respect to the wavelength are presented in Figure 7-4 for the scalar-relativistic B3PW calculation. It is found that the absorption of BiBO begins at about 200 nm. In the long wavelength region from 200 nm to 130 nm, $[\text{BiO}_4]^{5-}$ units dominate the optical absorption mainly due to the electronic transfer from occupied O 2p to virtual Bi

Orbital Interactions and Bonds in BiBO

6p orbitals at the bottom of the conduction bands between 0 eV and 3 eV. The contribution of single Bi cations due to the inner-shell electronic transfer from 6s to 6p is much less than that of the $[\text{BiO}_4]^{5-}$ units since the majority of Bi 6s states stays deep in energy at about -16 eV far away from the top of valence band. The electronic transitions from occupied O orbitals to virtual B orbitals in borate anions, however, have to demand higher photon energies since the virtual B states stay above about 3 eV. For example, the absorption of triangular $[\text{BO}_3]^{3-}$ units becomes fast increasingly important if the wavelength is below 120 nm and reaches the maximum at about 50 nm. In the short wavelength region below 80 nm, the tetrahedral $[\text{BO}_4]^{5-}$ units even become one of the significant absorbers to about 50 nm where the maximum absorption is achieved.

In order to study the effect of optical polarization of BiBO, we define equation (7-5) following the Kramers-Krönig relation. We call this quantity density of optical polarizations since it depicts the number of polarized states per volume at a given energy interval $\omega + d\omega$:

$$P_{uv}(\omega) = \lim_{\delta \rightarrow 0} \left\{ \int_0^{\omega-\delta} \frac{\omega' G_{uv}(\omega')}{\omega'^2 - \omega^2} d\omega' + \int_{\omega+\delta}^{+\infty} \frac{\omega' G_{uv}(\omega')}{\omega'^2 - \omega^2} d\omega' \right\} \quad (7-5)$$

As revealed in the equation (7-5), the density of optical polarization should have a similar trend as the density of optical absorptions against the energy although $P_{uv}(\omega)$ is explicitly calculated. Therefore $[\text{BiO}_4]^{5-}$ units also dominate the optical polarization of BiBO in the long wavelength region. The polarization of $[\text{BO}_3]^{3-}$ and $[\text{BO}_4]^{5-}$ units require higher photon energies than the one of $[\text{BiO}_4]^{5-}$ units. These findings actually explain the calculated SHG coefficients (e.g., $d_{22}^{\text{BiO}_4\text{-only}} = -2.829$ pm/V, $d_{22}^{\text{BO}_3\text{-only}} = -0.233$ pm/V and $d_{22}^{\text{BO}_4\text{-only}} = -0.118$ pm/V) [45] in the static limit based on the wavefunction cutting approximation.

The crystal BiBO shows a quite different electronic origin for optical effects compared to other IA and IIA metal-containing borates such as $\beta\text{-BaB}_2\text{O}_4$ [136], LiB_3O_5 , CsB_3O_5 and $\text{CsLiB}_6\text{O}_{10}$ [137] where the optical effects are mainly accounted for by the contributions of $[\text{BO}_3]^{3-}$ and $[\text{BO}_4]^{5-}$ borate units. This special optical feature of BiBO is, on one hand, due to the presence of the empty 6p orbital at Bi as an electron acceptor; and on the other hand due to the high spatial-overlapping between the atomic orbital on the Bi and O atoms which results in the covalent Bi-O bonds and large optical transition matrix elements. However, the relatively difficult polarization of $[\text{BO}_4]^{5-}$ units is the consequence of the 3-D network of tetrahedral structures which prohibits the electrons from being conjugated in a plane and thus higher photon energies are required.

7.3 Scalar-relativistic and correlation effects

In Figure 6-2, there is an obvious state redistribution in the valence band due to the scalar-relativistic and correlation effects. A large part of Bi 6s states stay at about -5 eV for the non-relativistic calculation. However, the scalar-relativistic effect strongly stabilizes the majority of Bi 6s states at about -16 eV and leaves only small contributions

Orbital Interactions and Bonds in BiBO

at the top of valence band. It is mainly this negative shift of Bi 6s states that increases the band gap from 4.92 eV to 5.69 eV by scalar-relativistic effects. The relativistic stabilization of Bi 6s orbitals on one hand forces more electrons in Bi 6s orbitals (i.e., $6s^{2.17}$) than in the non-relativistic case (i.e., $6s^{1.89}$), but on the other hand impairs the energy level matching between Bi 6s and O 2p orbitals. The scalar-relativistic and correlation effects can be found out in Table 7-1, where the relative bond strength is concerned by the integral COOP intensity. The relative net bonds in $[\text{BiO}_4]^{5-}$ units are 0.41 and -0.52 for the non-relativistic and scalar-relativistic calculations respectively, which obviously indicates that by the scalar-relativistic effect the Bi-O bonds are partially destroyed in the $[\text{BiO}_4]^{5-}$ units and stay antibonding. This bond instability mainly originates from the significantly intensified Bi 6s-O 2p antibonding interactions from -0.82 to -1.19 and reduced Bi 6s-O 2p bonding interaction from 0.41 to 0.25, while the Bi 6p-O 2p bonding states are only slightly affected from 0.82 to 0.80. It is this intensified antibonding repulsion between Bi 6p and O 2p orbitals that results in the elongations of the bond Bi-O4 (O5) and Bi-O6 (O7) by 0.010 Å and 0.032 Å respectively (cf. Table 7-2) compared to the non-relativistic case, which is in contradiction to the expected relativistic effect that seems to always be a bond contraction effect in previous reports [138].

BiBO could not have come into being at ambient conditions if no dynamic electron-electron correlations have been taken into account, since the tetrahedral $[\text{BO}_4]^{5-}$ units connecting the $[\text{BiO}_4]^{5-}$ and $[\text{BO}_3]^{3-}$ units would collapse. This is expected from the HF result given in Table 7-1 that the B-O bonding interactions in $[\text{BO}_4]^{5-}$ are almost compensated by the B-O antibonding ones ending up with almost null strength (0.11). On the other hand, the net Bi-O antibonding intensity in $[\text{BiO}_4]^{5-}$ is much stronger (i.e., -0.52) without electron correlations than the B3PW case (i.e., -0.14). Accordingly, the reason for the occurrence of BiBO, from the chemical bonds point of view, is that the correlation effect fully removes the inner orbital instabilities within both $[\text{BiO}_4]^{5-}$ and $[\text{BO}_4]^{5-}$ units in the way that both B-O and Bi-O antibondings are much weakened from -0.44 to -0.13 and from -1.48 to -1.19, respectively, as well as both B-O and Bi-O bondings are slightly intensified from 0.55 to 0.69 and from 0.96 to 1.05, respectively. In addition, the B-O bond intensity within $[\text{BO}_3]^{3-}$ is only slightly reinforced by the correlation effect from 2.51 to 2.66, which is another important factor that primarily contributes to the stability of BiBO.

Scalar-relativistic and correlation effects are important not only in the aspect of BiBO stability, but also to its optical performance. If one compares the densities of states in Figure 6-2, the absence of either the scalar-relativistic effect or the correlation effect leads to the appearance of Bi 6s states at the high-end of the valence band. In that case only the Bi cations would exhibit a contribution to the optical response of BiBO in the long wavelength region due to the inner-shell electronic transfer from 6s to 6p orbitals (see Figure 7-5 and Figure 7-6).

Orbital Interactions and Bonds in BiBO

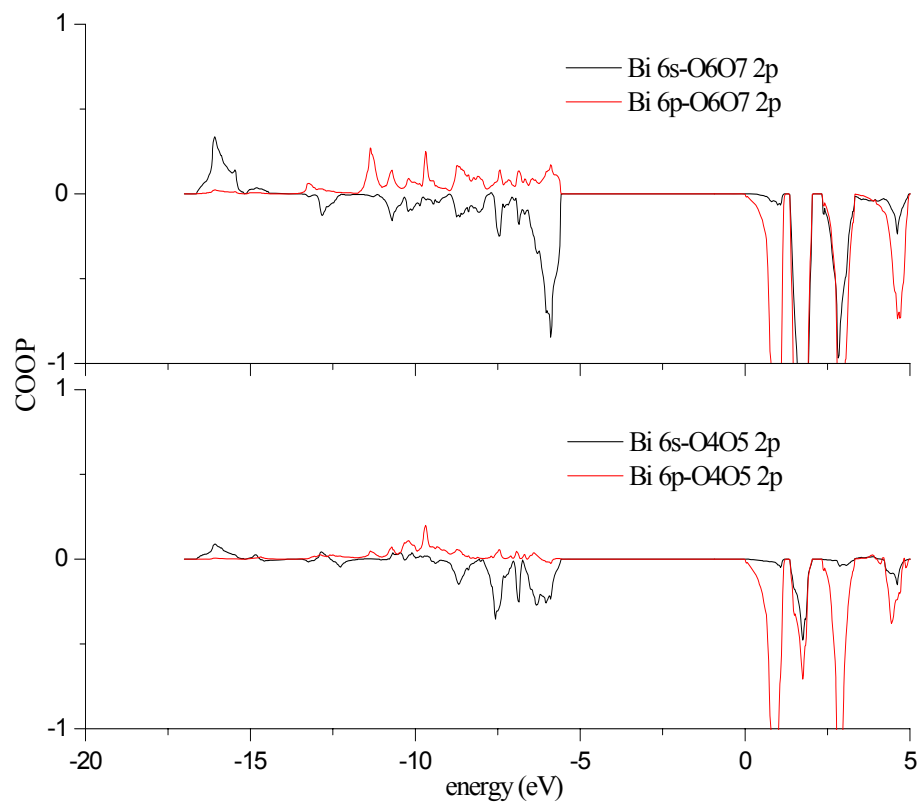


Figure 7-1 COOP plots for the interactions of Bi-O in $[\text{BiO}_4]^{5-}$ units for the scalar-relativistic B3PW calculation.

Orbital Interactions and Bonds in BiBO

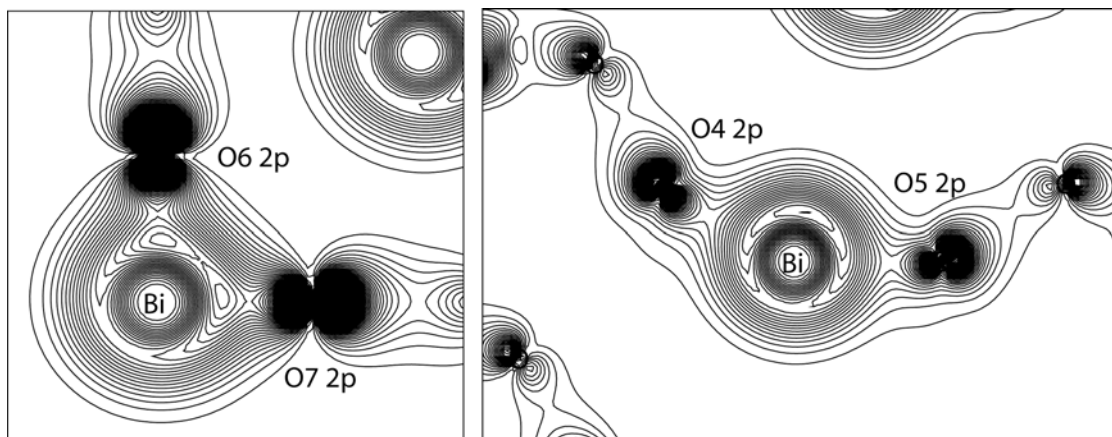


Figure 7-2 The projected electronic densities in the O6-Bi-O7 and O4-Bi-O5 planes for Bi 6s-O 2p bondings. The contour lines are plotted between the minimum of 0.0 and the maximum of 0.1 with the step size of 0.001.

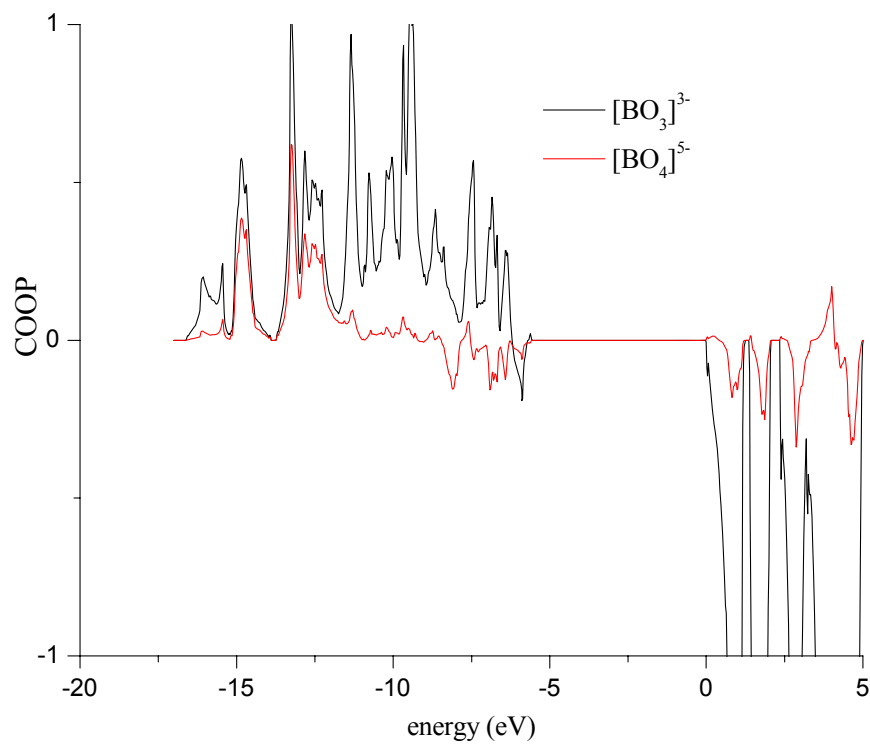


Figure 7-3 COOP plots for the interactions of B-O in $[\text{BO}_3]^{3-}$ triangular and $[\text{BO}_4]^{5-}$ tetrahedral units for the scalar-relativistic B3PW calculation.

Orbital Interactions and Bonds in BiBO

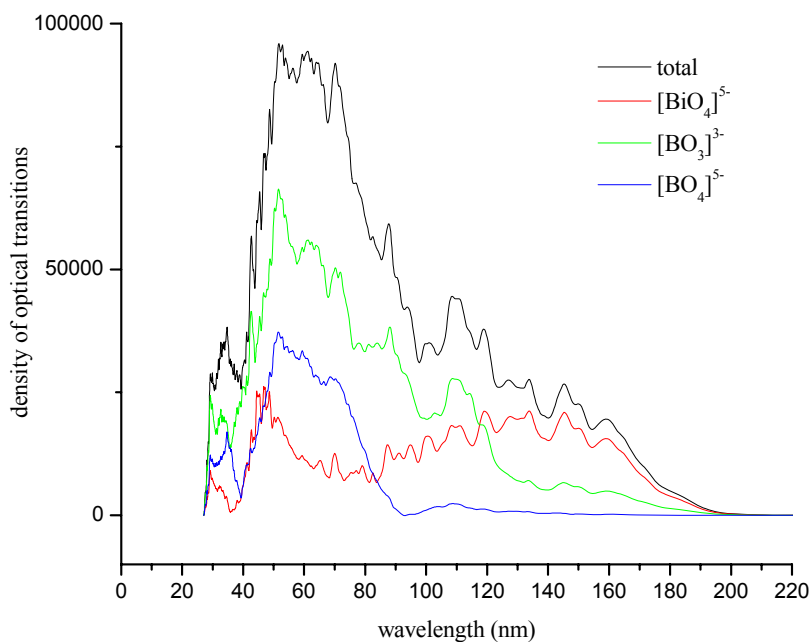


Figure 7-4 The density of optical absorptions for the BiBO (total) crystal as well as the $[\text{BiO}_4]^{5-}$, $[\text{BO}_3]^{3-}$ and $[\text{BO}_4]^{5-}$ subunits at the scalar-relativistic B3PW level.

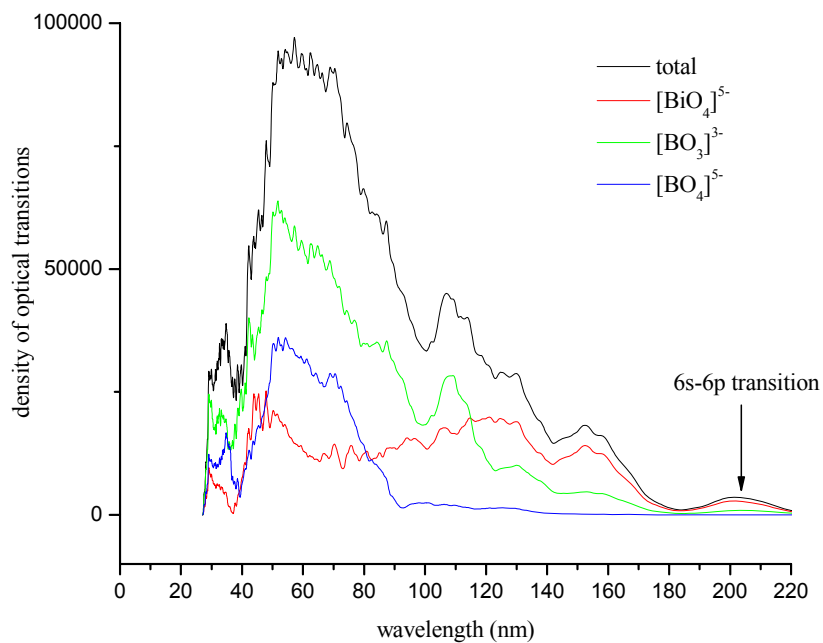


Figure 7-5 The density of optical absorptions for the BiBO (total) crystal as well as the $[\text{BiO}_4]^{5-}$, $[\text{BO}_3]^{3-}$ and $[\text{BO}_4]^{5-}$ subunits at the non-relativistic B3PW level.

Orbital Interactions and Bonds in BiBO

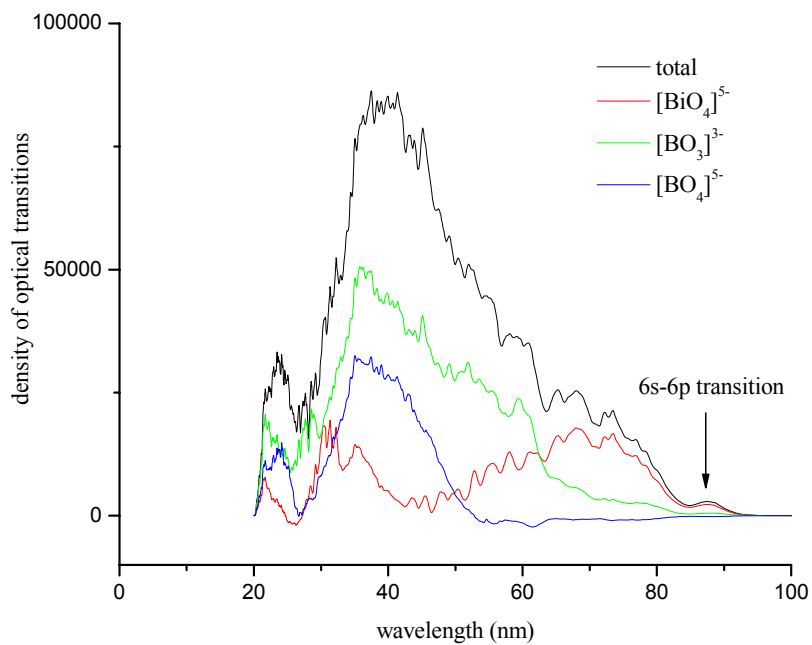


Figure 7-6 The density of optical absorptions for the BiBO (total) crystal as well as the $[\text{BiO}_4]^{5-}$, $[\text{BO}_3]^{3-}$ and $[\text{BO}_4]^{5-}$ subunits at the scalar-relativistic HF level.

Orbital Interactions and Bonds in BiBO

Table 7-1 Scalar-relativistic and correlation effects on the bond densities for the valence states of BiBO.

Bonds	Bonding ^a	Antibonding ^a	Net bonds ^b
Scalar-relativistic B3PW			
6s-2p	0.25	-1.19	-0.94
Bi-O 6p-2p	0.80	conduction band	0.80
total in [BiO ₄] ⁵⁻	1.05	-1.19	-0.14
B-O in [BO ₃] ³⁻	2.90	conduction band	2.90
B-O in [BO ₄] ⁵⁻	0.69	-0.13	0.56
total in BiBO ^c	4.64	-1.32	3.32
Non-relativistic B3PW			
6s-2p	0.41	-0.82	-0.41
Bi-O 6p-2p	0.82	conduction band	0.82
total in [BiO ₄] ⁵⁻	1.23	-0.82	0.41
B-O in [BO ₃] ³⁻	2.66	conduction band	2.66
B-O in [BO ₄] ⁵⁻	0.67	-0.18	0.49
total in BiBO ^c	4.56	-1.00	3.56
Scalar-relativistic HF			
6s-2p	0.31	-1.48	-1.17
Bi-O 6p-2p	0.65	conduction band	0.65
total in [BiO ₄] ⁵⁻	0.96	-1.48	-0.52
B-O in [BO ₃] ³⁻	2.51	conduction band	2.51
B-O in [BO ₄] ⁵⁻	0.55	-0.44	0.11
total in BiBO ^c	4.02	-1.92	2.10

a: Bonding and antibonding were given by corresponding integral intensities of COOP over the valence region.

b: Net bonds were evaluated by the sum of bonding and antibonding.

c: Total in BiBO were evaluated by the sum of the bonding, antibonding and net bonds for Bi6s-O2p, Bi6p-O2p, B-O in [BiO₄]⁵⁻, [BO₃]³⁻ and [BO₄]⁵⁻ units, respectively.

Table 7-2 Scalar-relativistic effects on bond lengths of BiBO.

Bond lengths	Scalar-relativistic	Non-relativistic	Relativistic effects	
[BiO ₄] ⁵⁻ (Å)	Bi-O4 (O5)	2.388	2.378	0.010
	Bi-O6 (O7)	2.109	2.077	0.032
[BO ₃] ³⁻ (Å)	B-O	1.405	1.409	-0.004
	B-O	1.367	1.365	0.002
	B-O	1.344	1.342	0.002
[BO ₄] ⁵⁻ (Å)	B-O	1.498	1.506	-0.008
	B-O	1.446	1.443	0.003

Chapter 8 Asymmetric Bi Lone-Pair Electrons in BiBO

In the last two chapters we have studied the electronic structure of BiBO by first-principles B3PW DFT calculations, where the origins of chemical stabilities and optical effects of BiBO have been clarified in detail along with the correlation and Bi relativistic effects for the $[\text{BiO}_4]^{5-}$, $[\text{BO}_3]^{3-}$ and $[\text{BO}_4]^{5-}$ units. We have found that the Bi-O covalent interactions play critical roles in determining not only the chemical stability of the $[\text{BiO}_4]^{5-}$ units but also the optical response of BiBO in the long wavelength region. In this chapter, we concentrate on the other important consequence of Bi-O covalent couplings, i.e., the determinant mechanism for the origin of the stereochemical activity of the Bi lone-pairs in BiBO.

8.1 Advances for electronic lone-pairs

A lone-pair is a valence-shell orbital containing two electrons which are not involved in covalent bonding. The critical role played by lone-pair electrons in terms of molecular geometries has been examined in the classic valence shell electron pair repulsion theory (VSEPR) proposed by Sidgwick and Powell [139] and later by Gillespie and Nyholm [140]. The lone-pair effect and the remarkable success of VSEPR explaining three-dimensional shapes of many small main group atom-containing molecules such as NH_3 , H_2O , SF_4 , IF_4 , SnCl_2 can be nowadays found in most inorganic chemistry text books. Thanks to recent achievements of computer techniques and quantum chemistry, many interests concerning lone-pair effects have been directed from small molecules to large systems [141, 142, 143] and periodic compounds [144, 145, 146, 147]. The stereochemical activity [148] of lone-pair electrons has been shown to cause, for example, not only Jahn-Teller geometry distortions [148, 149] but also a large optical response in TeO_2 -based materials [150] as well as the ferroelectricity in BiMnO_3 [151].

Metal lone-pair electrons are usually associated with subvalent states (e.g., $5s^2$ or $6s^2$ for the 5th or 6th row p-block elements) of elements near the bottom of groups 13 to 15. The role of relativistic effects in the lone-pair formation, i.e. the relativistic stabilization of the s shell, has been discussed previously [152, 153]. The lone-pair electrons with spherically symmetrical shapes display an “inert pair effect” which does not result in distorted Advances for electronic lone-pairs structures, e.g., cubic NaCl-like PbS [154]. The lone-pairs are considered to be stereochemically active but chemically inactive if the spherical symmetry is lost. Since the stereochemically active lone-pairs cannot be formed by pure symmetric 5s or 6s valence orbitals, less symmetric orbitals have to be mixed in. Numerous reports have explored the detailed mechanisms of lone-pair asymmetrization for various molecules and periodic solids. Several decades ago Orgel [155] invoked the hybridization of the outmost s and p orbitals for the B-subgroup metals to explain both the structural distortion and the large dielectric response of lone-pairs. Verbaere and coworkers [156] invented the electronic lone-pair localization (ELPL) model which

Asymmetric Bi Lone-Pair Electrons in BiBO

attributes the lone-pair formation to the purely electrostatic response of lone-pair electrons to the asymmetric electrostatic field within ionic crystals.

However, if the simple hybridization of valence s and p orbitals within central cations is fully responsible for the stereochemical activity of lone-pairs, one cannot understand why the tetragonal distortion of the cubic NaCl-like structure takes place only for PbO with asymmetric electronic distributions around Pb (II) whereas PbS remains undistorted in a rocksalt phase with symmetric electron distributions around Pb (II). The role played by anionic ligands in determining the structural distortion and shape of lone-pairs was implicitly mentioned by Wheeler and Kumar [148] when reporting extended Hückel calculations for the molecules BiI_6^{3-} and BiCl_6^{3-} as well as the extended solids BiI_3 and SbI_3 . It was concluded that although the hybridization of the cationic s and p_z orbitals predominates trigonal distortions for the molecule BiCl_6^{3-} and solid SbI_3 with the stereochemical activity of the central cations, the s- p_z interaction is partly balanced by mixing the HOMO and a lower energy $1a_1$ orbital with ligand lone-pair orbitals determined by the HOMO- $1a_1$ energy gap. More recent density functional theory (DFT) studies for solids of PbO [157, 158, 159], PbS [160], SnX (X=O, S, Se and Te) [161, 162] further explained the distorted structures and asymmetric electron densities for PbO and SnO by both the covalent interaction between cationic metal s and O 2p orbitals and the subsequent interaction between the cationic metal p and the antibonding part of cationic metal s-O 2p bonds.

Unlike in these NLO materials like LiB_3O_5 and BaB_2O_4 , a $6s^2$ -lone-pair on the metal Bi is believed to contribute to the NLO properties of BiBO. If we take a look at the total electronic densities in the (100) and (001) planes in Figure 8-1, we find at one side of the Bi cations against the oxygen atoms asymmetric lobe-like distributions of the electronic density along the b lattice vector, i.e., the so-called “lone-pairs”. They are somewhat more spherical and expanded in the (100) plane than in the (001) plane. Figure 8-1 reveals that the lone-pair electronic density is highly anisotropically distributed in the 3-dimensional space around the Bi cations.

However, it is important to point out that the distorted coordination around Bi (III) does not necessarily prove a structure determining stereochemical activity of the Bi lone-pairs since the spatial arrangements of the $[\text{BO}_3]^{3-}$ and $[\text{BO}_4]^{5-}$ groups could impose the resulting geometry as well. Nevertheless, the stereochemical activity of the Bi lone-pairs has been widely used to explain the anisotropies of thermal expansion [163], piezoelectric and elastic properties [30] for BiBO.

8.2 Modeling orbital interactions for Bi 6s, Bi 6p and O 2p

It has been clear that both Bi 6s and 6p orbitals have strong covalent interactions with O 2p orbitals following the discussions in Chapter 7. However, it is also important to investigate what detailed mechanism rules these interactions and according to which hierarchy the interactions can be ordered since the Bi lone-pairs are essentially shaped by these interactions.

Asymmetric Bi Lone-Pair Electrons in BiBO

One may imagine that Bi 6s, Bi 6p and O 2p states couple with each other via one of four possible routes: Bi 6s-6p hybridized orbitals are formed first in the primary interaction and subsequently participate in covalent bonding and antibonding with O 2p orbitals in the secondary interaction (Figure 8-3 (a)); or Bi 6s and Bi 6p individually form covalent bonds with O 2p (Figure 8-3 (b)); or Bi 6p-O 2p covalent occupied bonding and unoccupied antibonding orbitals are formed first in the primary interaction, and the former resultant filled bonding orbitals subsequently take the further coupling with Bi 6s orbitals in the secondary interaction (Figure 8-3 (c)); or Bi 6s-O 2p interactions generate covalent occupied bonding and occupied antibonding orbitals in the primary interaction, and the latter resultant filled antibonding orbitals subsequently couple with Bi 6p orbitals in the secondary interaction (Figure 8-3 (d)).

The routes sketched in Figure 8-3 (a-c) are not suitable to describe the interaction of the Bi 6p with the Bi 6s and O 2p orbitals in BiBO if one refers to the distribution of Bi 6s, Bi 6p and O 2p states in Figure 8-2. According to route Figure 8-3 (a), Bi 6s-6p hybridization demands that the Bi 6p states should be mixed with the Bi 6s states over the shared energy region. However, this model is inconsistent to the fact that no Bi 6p states are found in the Bi 6s region from -16.6 eV to -14.5 eV (Figure 8-2). Therefore the classic viewpoint due to VSEPR which demands the hybridization of central atomic s and p orbitals is not correct for BiBO.

According to route Figure 8-3 (b), on one hand, the lowest unoccupied states, i.e., the top states shown in Figure 8-3 (b), should involve only Bi 6p and O 2p states, whereas the small amount of Bi 6s states virtually appear at about 2 eV (Figure 8-2); on the other hand, the highest occupied states, i.e., the middle two states shown in Figure 8-3 (b), should contain some amount of separate Bi 6s states and Bi 6p states, whereas the continuously mixed Bi 6s-6p states virtually stay between -13.5 eV and -5.6 eV (Figure 8-2). In addition, this model may lead to a too small band gap.

According to route Figure 8-3 (c), the lowest unoccupied states should involve only Bi 6p and O 2p states, and the lowest occupied states should contain some components of Bi 6p states mixed with pronounced Bi 6s states. However, it disagrees with the findings that the small amount of Bi 6s states virtually appears at about 2 eV and no Bi 6p orbitals are distributed in the Bi 6s region between -16.6 eV and -14.5 eV (Figure 8-2).

Finally, Figure 8-3 (d) route can qualitatively agree well with the DOS of Bi 6s, Bi 6p and O 2p states shown in Figure 8-2. According to this route, the lowest occupied states originate from Bi 6s-O 2p bondings, which should be composed of pronounced Bi 6s states and some amount of O 2p states; the highest occupied states are caused by the bonding coupling between Bi 6p orbitals and the resultant Bi 6s-O 2p antibonding orbitals, which should contain the majority of O 2p states and less mixed Bi 6s and Bi 6p states; the lowest unoccupied states result from the antibonding coupling between Bi 6p orbitals and the resultant Bi 6s-O 2p bonding orbitals, which should involve strong unoccupied Bi 6p states, much less unoccupied O 2p states and least unoccupied Bi 6s states.

Asymmetric Bi Lone-Pair Electrons in BiBO

If the C_2 axis is taken as the z direction, the Bi 6p orbitals can be decomposed into individual $6p_x$, $6p_y$ and $6p_z$ states. Due to the symmetry compatibility, only atomic orbitals representing the same parity can be mixed with each other. That is to say, the orbital mixture may take place for $6s$ - $6p_z$ pairs having A representation and $6p_x$ - $6p_y$ pairs having B representation under the C_2 constraint. The projected DOS for these states are shown in Figure 8-4, where the unoccupied $6p_z$ states are located in the middle between the $6p_x+6p_y$ states on the left and the $6p_x-6p_y$ states on the right. It can be seen that in the energy region for the occupied Bi 6p states from -13.5 eV to -5.6 eV, only $6p_z$ orbitals most effectively overlap with Bi 6s orbitals, while the Bi $6p_x$ and $6p_y$ orbitals interact only with each other. Similarly, for the unoccupied Bi 6p states, the empty Bi 6s states are mixed only into Bi $6p_z$ states. Therefore, in connection with the model of Figure 8-3 (d), it is mainly the Bi $6p_z$ orbitals that are coupled into the Bi 6s components of occupied Bi 6s-O 2p antibonding states.

8.3 Origin of asymmetric Bi lone-pair electrons

As revealed in the above section, the Bi 6s-6p hybridization model, claimed by VSEPR or earlier reports, cannot be applied to BiBO to explain the origin of Bi lone-pairs. In this section, we further examine which key step of the Bi-O interaction mechanism illustrated in Figure 8-3 (d) significantly determines the Bi lone-pairs. To this end, several hypothetical deformed (isotropically expanded and compressed) unit cells were assumed in addition to the experimental crystallographic unit cell (original cell). For reasons of simplicity, only two cases corresponding to the isotropically expanded ($a=8.539$ Å, $b=5.992$ Å and $c=7.810$ Å) and the original ($a=7.116$ Å, $b=4.993$ Å and $c=6.508$ Å) unit cells are presented in this thesis as typical examples. The atomic coordinates in the original unit cell of BiBO have been fully relaxed with the C_2 symmetry constraint until convergence was achieved. The atomic positions in the expanded cell were generated without further optimizations by using the same fractional coordinates as for the optimized ones in the original cell. The resultant Bi-O6 (Bi-O4) distances are 2.531 Å (2.866 Å) for the expanded cell and 2.109 Å (2.388 Å) for the original cell, respectively. We note that the expanded cell is not corresponding to a real physical state of BiBO but merely a convenient model to investigate the roles played by Bi 6s6p and O 2p orbitals in determining the dependence of Bi lone-pair asymmetry on the intensities of Bi-O interactions.

The electronic densities in the O4-Bi-O5 and O6-Bi-O7 planes are presented in Figure 8-5 for the original and expanded BiBO unit cells. The electronic densities corresponding to O core electrons are truncated by the contour line threshold of 0.100 to remove the map obscurity. From the contrasts of the electronic densities for the two cases, it is obvious that in both O4-Bi-O5 and O6-Bi-O7 planes the Bi non-spherical lone-pairs exhibited for the original cell of BiBO are almost spherically embraced around Bi for elongated Bi-O distances. Let us check how the Bi lone-pairs bring the influence to the distorted O4-Bi-O5 angle. The optimized O4-Bi-O5 angles are 151.32° and 158.82° for the original and expanded unit cell, respectively. Therefore, the Bi lone-pairs indeed have notable effects

Asymmetric Bi Lone-Pair Electrons in BiBO

due to “stereochemical activity” to distort the $[\text{BiO}_4]^{5-}$ units. For the original BiBO cell, more electrons are concentrated at one side of the Bi lone-pair lobes so that the repulsions between Bi lone-pairs and O4O5 electrons are enhanced which lead to smaller O4-Bi-O5 angles. However, the calculated O6-Bi-O7 angles are close to 90° for both the original and the expanded cell with the difference of less than 1° , which suggests that the angle of crossed Bi-O6 and Bi-O7 bonds is not tightly related to the lone-pair effect. Therefore the distortion of $[\text{BiO}_4]^{5-}$ units invokes complicated mechanisms which not only need to reduce the repulsions between lone-pairs and O4O5 electrons but also has to counterpoise the inner tension of triangular $[\text{BO}_3]^{3-}$ and tetrahedral $[\text{BO}_4]^{5-}$ units. These two factors add up to the stable distortion of the $[\text{BiO}_4]^{5-}$ units.

The integrated intensities of COOP for Bi-O bonds are listed in Table 8-1 for the original and expanded BiBO cells. In all cases, Bi 6s-O 2p interactions end up with net antibonding and Bi 6p-O 2p with net bonding. Compared to the original cell, the elongation of Bi-O distances weakens the strength of Bi 6s-O6O7 2p (also for Bi 6s-O4O5 2p) net antibondings as expected from -0.60 (-0.34) to -0.28 (-0.14). However, the Bi 6p-O 2p bonding strength is only slightly variant from 0.56 (0.24) to 0.50 (0.20). Bi lone-pairs are shaped less spherical (see Figure 8-5) when there are stronger Bi 6s-O 2p interactions. The electronic densities in the O6-Bi-O7 and O4-Bi-O5 planes projected from -16.6 eV to -14.5 eV and from -13.5 eV to -5.6 eV are respectively illustrated in Figure 8-6 for the original BiBO cell. The Bi 6s-O 2p covalent bondings are clearly visualized in the left maps and the Bi lone-pair lobes are found at Bi 6s-O 2p antibonding states in the right maps.

Therefore it is reasonable to conclude that Bi 6s-O 2p antibonding states are the origin of non-spherical Bi lone-pairs for BiBO. The reason can be understood if the mechanism in Figure 8-3 (d) is applied here to clarify the origin of non-spherical Bi lone-pairs. As a matter of fact, the Bi lone-pairs would be shaped asymmetric at the first stage where symmetric Bi 6s orbitals take antibonding interactions with asymmetric O 2p orbitals. This antibonding essentially creates nodal surfaces and depletes electrons in the region between Bi and O atoms ending up with the spherical symmetry-broken electronic distributions at the other side of Bi. The Bi 6p orbitals (particularly $6p_z$) would have a joint significance to determine the asymmetry of Bi lone-pairs only if the number of Bi $6p_z$ electrons is competitively large enough to reshape the Bi 6s electronic distribution via Bi 6s electron-Bi $6p_z$ electron interactions once Bi $6p_z$ electrons are merged into Bi 6s-O 2p occupied antibonding states (see Figure 8-3 (d)). However, although there are about 0.90 electrons at Bi 6p orbitals due to Mulliken population, the Bi $6p_z$ electrons are counted by only 0.36 and the majority of Bi $6p_z$ orbitals are evidently unoccupied. We further calculated the electronic densities projected onto O6-Bi-O7 and O4-Bi-O5 planes (Figure 8-7) by removing p basis set functions at Bi centers. The electronic densities without involving Bi 6p orbitals are similar to the left maps in Figure 8-5 where Bi 6p orbitals have been accounted for. By taking these facts into account, we come to the conclusion that the Bi 6s orbitals are much more significant than the Bi 6p in the

Asymmetric Bi Lone-Pair Electrons in BiBO

determination of the asymmetry of non-spherical Bi lone-pairs for BiBO. This finding is however contrary to the Pb lone-pair model for α -PbO proposed recently by Watson and coworkers [162, 164] where the asymmetric electron density around Pb (II) arises predominantly from a mixing of O 2p and Pb 6p orbitals at the top of valence band.

The Bi lone-pairs mainly consist of not only Bi 6s electrons but also some amount of O 2p electrons via the Bi 6s-O 2p antibonding interactions. The following equation is used to calculate how many Bi 6s electrons are distributed into non-spherical Bi lone-pairs.

$$Q_{Bi-lone-pairs}^{6s} = \frac{I_{antibonding}}{I_{bonding} + I_{antibonding}} Q_{Bi6s} \quad (8-1)$$

where $I_{bonding}$ and $I_{antibonding}$ are the integral intensity of projected DOS for Bi 6s-O 2p bonding and Bi 6s-O 2p antibonding states, and Q_{Bi6s} is the total Mulliken electronic population for Bi 6s orbitals. According to equation (8-1), Bi lone-pairs contain 0.92 Bi 6s electrons (*i.e.*, 42% of the total Bi s population of 2.17) which are populated over a broad energy interval of 7.9 eV. Therefore it is hard to believe that the Bi 6s components of lone-pairs have considerable contributions to the excellent optical response of BiBO although this has been suggested previously [44]. If one takes a look at the projected DOS in Figure 8-2, the electronic transition from strong filled O 2p states near the Fermi level to strong empty Bi 6p states can dominantly control the optical effects of BiBO. Therefore the optical effects of BiBO are most likely more determined by the O 2p components of the Bi lone-pairs rather than by the Bi 6s components.

Asymmetric Bi Lone-Pair Electrons in BiBO

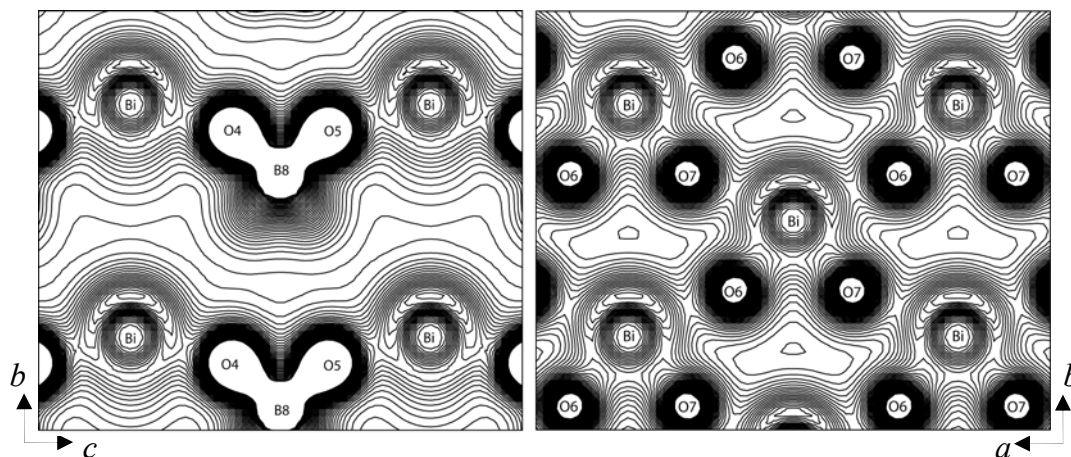


Figure 8-1 The total electronic densities in (100) (left) and (001) (right) planes for BiBO with the original cell. The contour lines are plotted between the minimum of 0.0 and the maximum of 0.1 with the step size of 0.003.

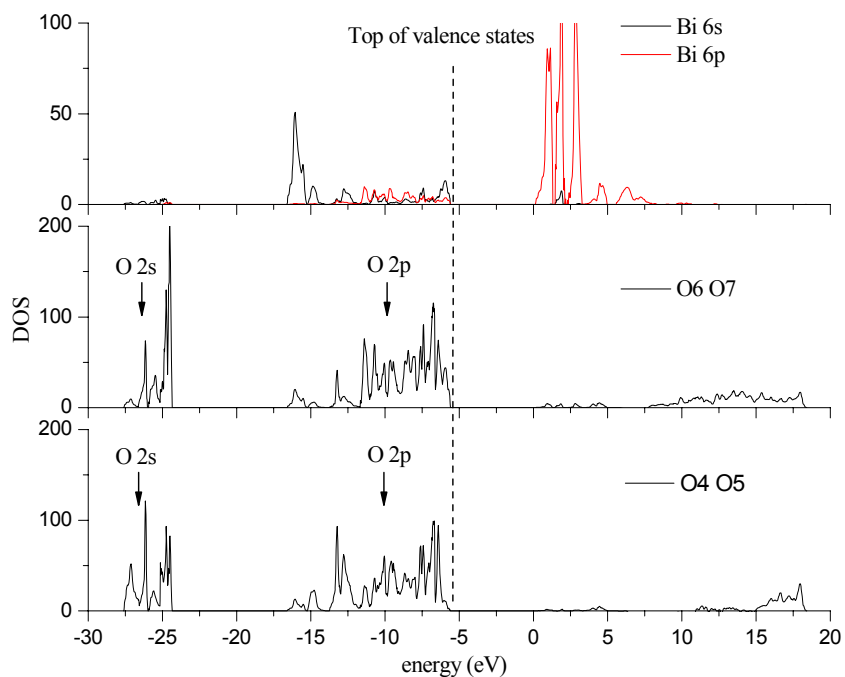


Figure 8-2 The l-momentum projected DOS for Bi 6s, Bi 6p, O6O7 and O4O5 orbitals for BiBO.

Asymmetric Bi Lone-Pair Electrons in BiBO

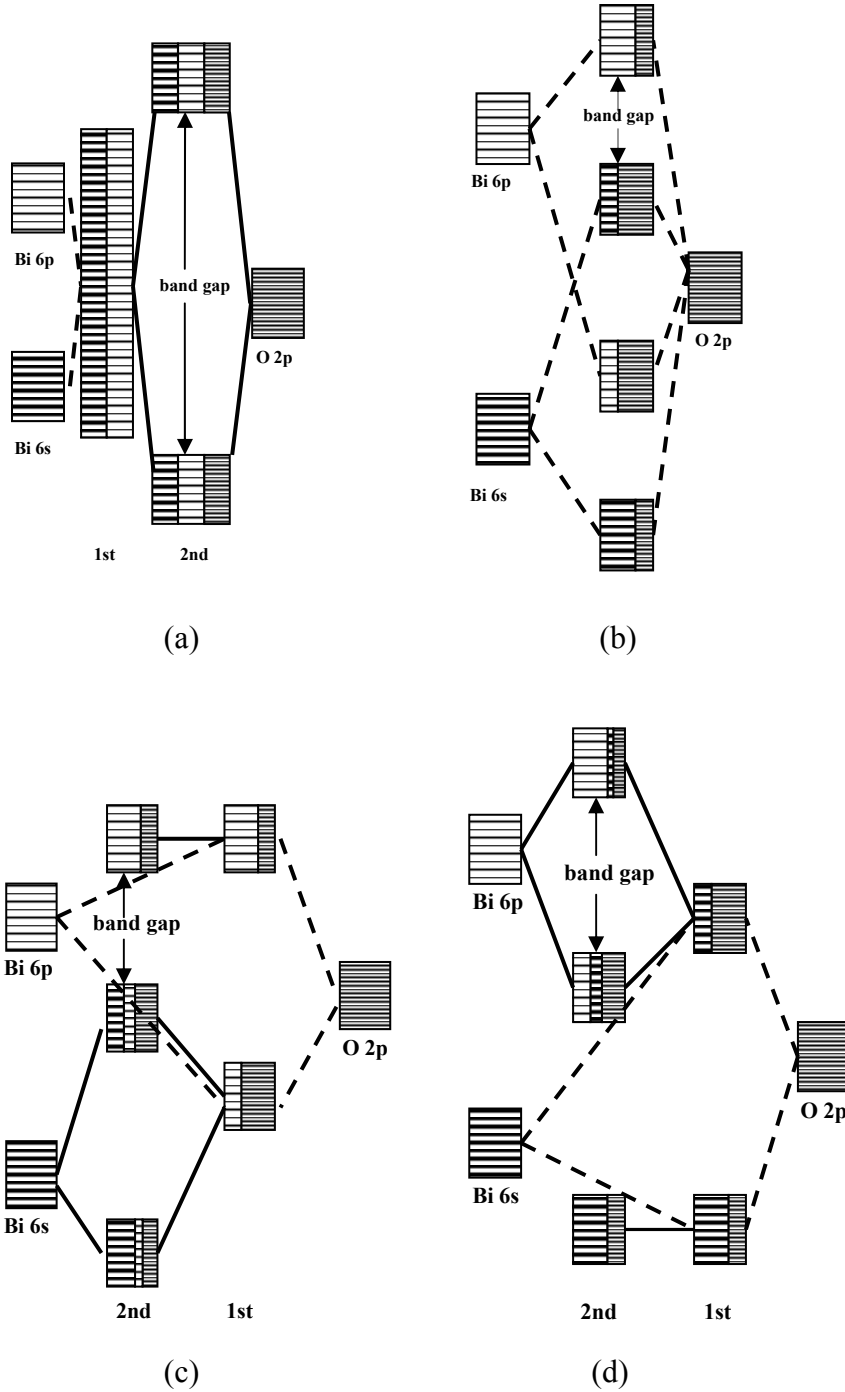


Figure 8-3 Four schematic routes to model the interactions between Bi 6s, Bi 6p and O 2p orbitals from (a) to (d). Bi 6s, Bi 6p and O 2p states are represented by rectangles filled with three different patterns. The content of each of the three states is schematically weighted by the width of the corresponding pattern. The primary interaction is indicated by the dashed lines (1st) and the secondary interaction by the solid lines (2nd).

Asymmetric Bi Lone-Pair Electrons in BiBO

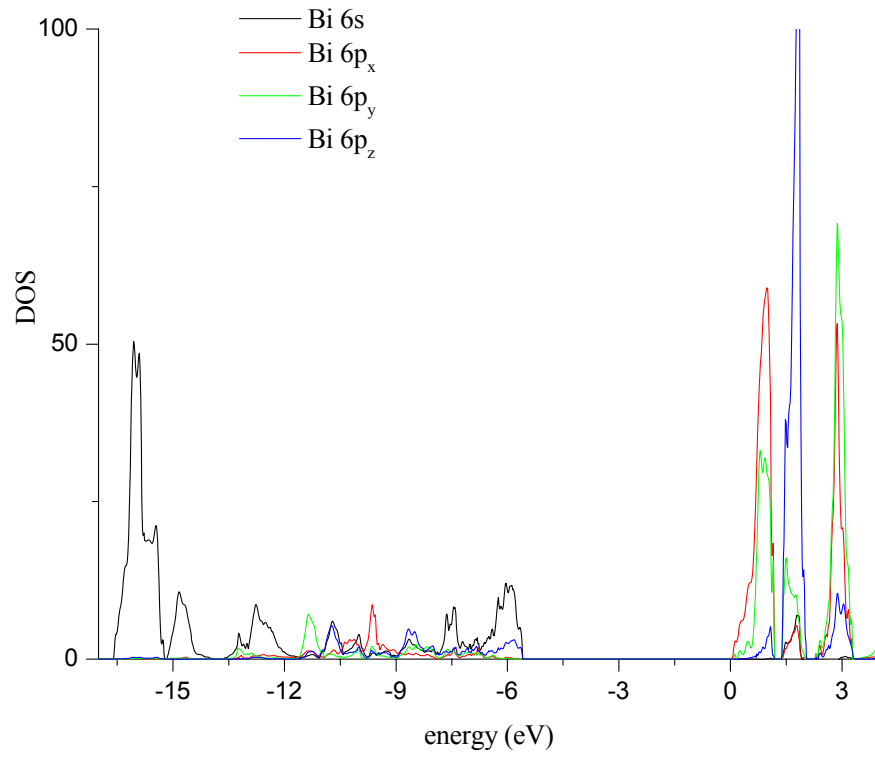


Figure 8-4 The $|m|$ -momentum projected DOS for Bi 6s, Bi 6p_x, Bi 6p_y and Bi 6p_z orbitals for BiBO.

Asymmetric Bi Lone-Pair Electrons in BiBO

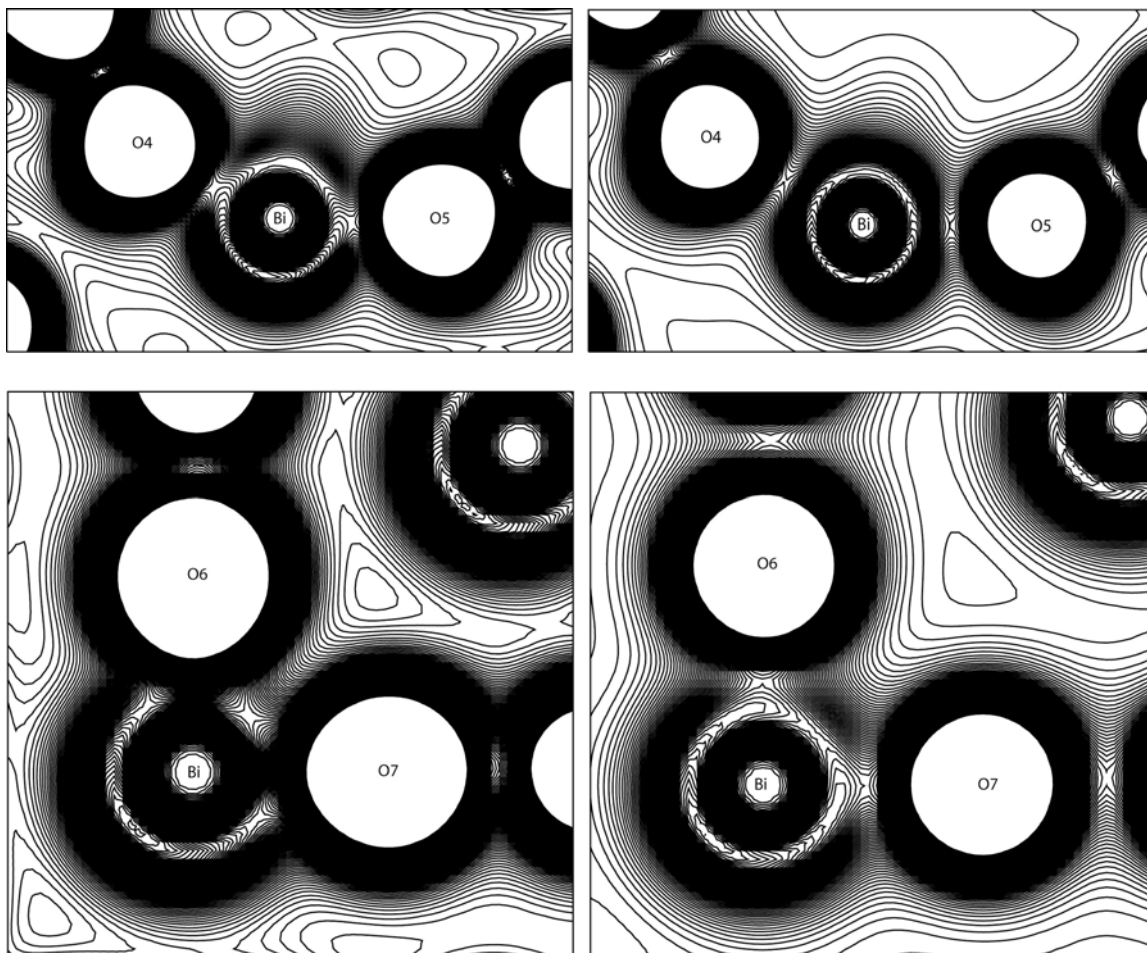


Figure 8-5 The total electronic densities in O4-Bi-O5 (top) and O6-Bi-O7 (bottom) planes for BiBO with the original (left) and expanded cells (right). The contour lines are plotted between the minimum of 0.0 and the maximum of 0.1 with the step size of 0.0008.

Asymmetric Bi Lone-Pair Electrons in BiBO

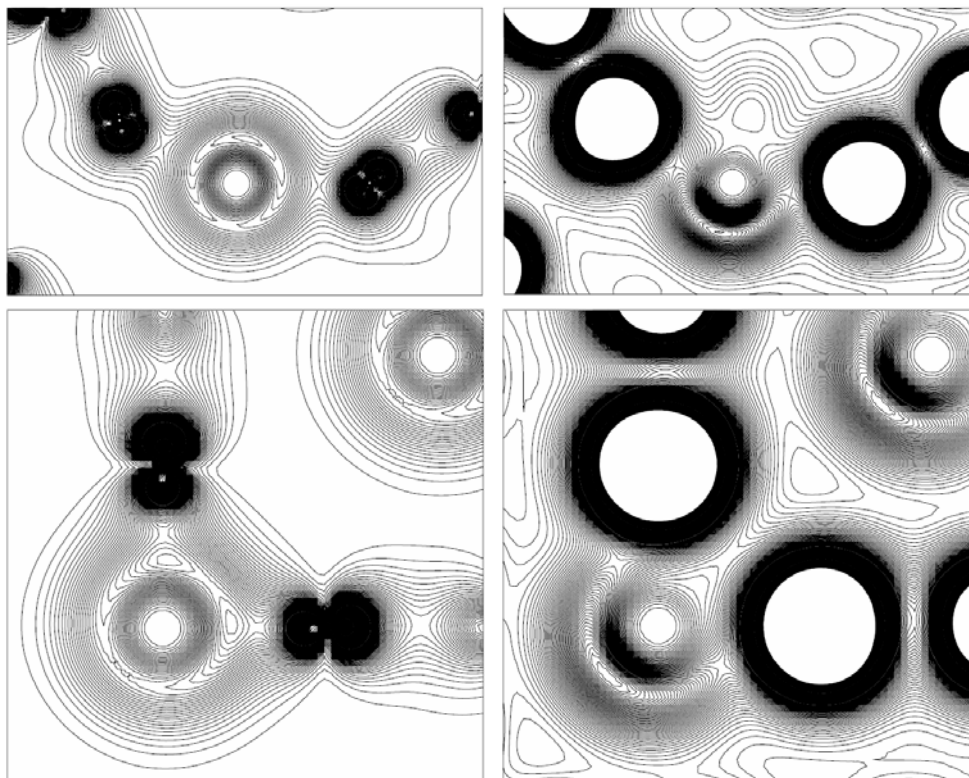


Figure 8-6 The projected electronic densities in O4-Bi-O5 (top) and O6-Bi-O7 (bottom) planes for the original BiBO cell from -16.6 eV to -14.5 eV (left) and from -13.5 eV to -5.6 eV (right). The contour lines are plotted between the minimum of 0.0 and the maximum of 0.1 with the step size of 0.0008.

Asymmetric Bi Lone-Pair Electrons in BiBO

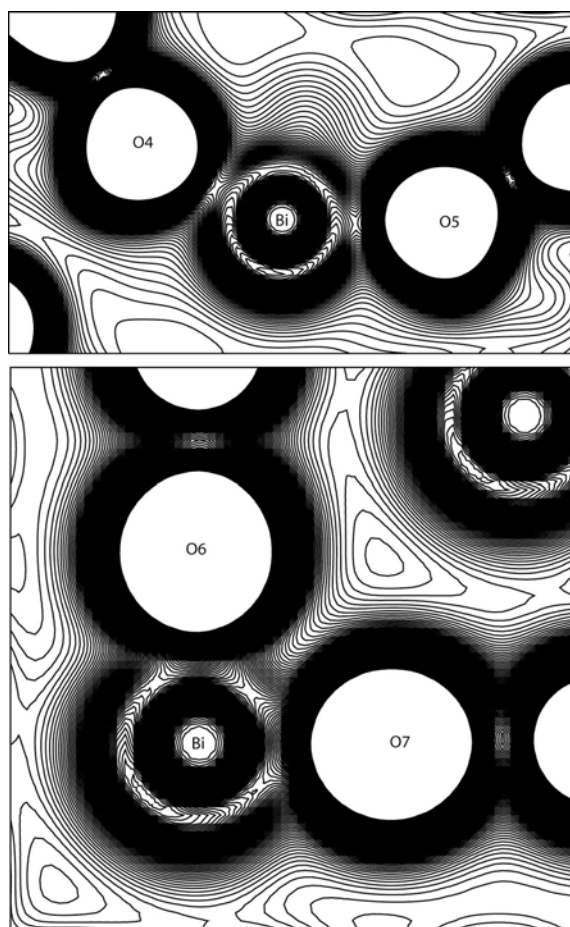


Figure 8-7 The total electronic densities in O4-Bi-O5 (top) and O6-Bi-O7 (bottom) planes for BiBO without Bi 6p basis set functions. The contour lines are plotted between the minimum of 0.0 and the maximum of 0.1 with the step size of 0.0008.

Table 8-1 Integrated intensities of COOP for Bi 6s-O 2p and Bi 6p-O 2p bonds for BiBO with the original and expanded cells.

bonds	Bi-O6O7		Bi-O4O5	
	6s-2p	6p-2p	6s-2p	6p-2p
original cell	-0.60	0.56	-0.34	0.24
expanded cell	-0.28	0.50	-0.14	0.20

Chapter 9 Harmonic Vibrational Modes of BiBO

9.1 Introduction

Although during the last five years several experimental IR and Raman spectra of BiBO were recorded [28, 41, 165, 166, 167] and the phonon modes were also obtained indirectly by modeling the reflectance [40], the analysis and assignment of the modes remain difficult. Correspondingly, the attention was focused instead on the characteristic functional groups and the associated familiar bands, i.e., a considerable amount of the information contained within the spectra have been neglected. For example, the modes related to $[\text{BO}_3]^{3-}$ and $[\text{BO}_4]^{5-}$ units were assigned by empirically comparing them with the corresponding vibrational modes of these units reported in other borate crystals (e.g., rare-earth borates) and glasses. The interpretation of the far-infrared region reflecting the vibrating of Bi-O bonds is however not available so far while it has been attempted to relate the large polarizability of Bi-O bonds in BiBO to its outstanding nonlinear optical properties [166].

First-principles electronic structure methods rooted upon sophisticated codes and powerful computers often provide a solution to such problems and may add valuable information for the interpretation of the experimental observations: by accurately determining the vibrational modes of a system, it is possible to assign unambiguously the spectral features to actual normal mode oscillations, allowing a deeper understanding of the vibrational spectrum as well as the bonding and chemical properties of the system under consideration. In the previous Chapters 6, 7 and 8, we have focused on the first-principles calculation of electronic properties of BiBO, where the origins of chemical stabilities, optical effects as well as Bi non-spherical lone-pairs have been clarified in detail. In these studies both electron correlation effects as well as the major relativistic effects, the latter mainly originating from the heavy Bi centers, have been taken into account. Therefore in this chapter we direct the attention to the first-principles lattice-vibrational properties of BiBO and derive the harmonic modes by performing density functional theory calculations with the gradient-corrected hybrid B3PW functional. The major advantage of theoretical studies as the one presented here is that all vibrational modes can be unambiguously assigned with regard to their symmetry as well as to the motions of individual atoms or groups of atoms, which can be graphically displayed. To the best of our knowledge, no previous quantum chemical computations on this subject have been published.

This chapter is organized as follows. In the next section, the theoretical methods and computational details applied to derive the harmonic vibrational frequencies are presented. In the third section, the method described in the previous section is tested on the simple ionic crystal cubic MgO to exhibit the accuracy which can be actually achieved. In the fourth section, the vibrations in $[\text{BiO}_4]^{5-}$, triangular $[\text{BO}_3]^{3-}$ and

tetrahedral $[\text{BO}_4]^{5-}$ units are illustrated, discussed and compared with the available experimental results. In the last section, the conclusions are briefly summarized.

9.2 Computing dynamic matrix

First-principles DFT applying the hybrid B3PW functional was used to optimize the atomic coordinates of BiBO within the CO-LCAO scheme. The optimizations for atomic coordinates were performed using a modified conjugate gradient algorithm [119]. Analytical gradients were evaluated and the optimization convergence was achieved by fulfilling three criteria, i.e., between optimization steps the root mean square (RMS) of energy change, gradient change and displacement change should stay less than 10^{-7} a.u., 0.0003 a.u. and 0.0012 a.u., respectively. The following tolerances in CRYSTAL03 were employed in the evaluation of infinite Coulomb and HF exchange series: 10^{-7} for the Coulomb overlap, HF exchange overlap, Coulomb penetration and the first exchange pseudo-overlap; 10^{-14} for the second exchange pseudo-overlap. The Fock matrix has been diagonalized at 24 \mathbf{k} -points within the irreducible Brillouin zone corresponding to a shrinking factor of 4 in the Monkhorst net [63]. In order to improve the convergence, a negative energy shift of 1.0 a.u. to the diagonal Fock/KS matrix elements of the occupied orbitals was added to reduce their coupling to the unoccupied set and maintained after the diagonalization. A very accurate extra-large grid consisting of 75 radial points and 974 angular points was employed in the DFT calculations, where Becke grid point weights [120] were chosen.

The reliable and accurate simulation of vibrations for crystals is still at a less developed stage than for molecules [168], and so far, only DFT methods with plane wave basis sets were consistently implemented for frequency calculations by response theory. The major advantage of the CO-LCAO approach over the usual plane-wave schemes is the application of the popular hybrid density functionals such as B3PW and B3LYP, which have not yet been implemented into any of the widely used plane-wave codes so far mainly due to the technical problems related to the integral evaluation. Thus pure LDA and GGA methods prevail in plane-wave schemes. The B3PW and B3LYP functionals have been confirmed in numerous studies of molecules to yield accuracies significantly improved with respect to LDA and GGA in many aspects such as structures, vibrational frequencies, thermochemistry, electronic and magnetic properties [94]. Therefore the CO-LCAO approach has been applied for the frequency evaluation of BiBO, which is also consistent with our previous first-principles B3PW DFT electronic calculations of BiBO. Since the computation of vibrational frequencies is not yet implemented in the released version of the CRYSTAL03 package, we have implemented the numerical evaluation of harmonic vibrational modes. A bsh-script was written to obtain single-point energies of atom-displaced crystalline structures from CRYSTAL03 package computations, and calculated the elements of the dynamic matrix according to the following straightforward numerical formalism based on the harmonic approximation. A C-language code was created to diagonalize the dynamic matrix. The vibrating eigenvectors were subsequently evaluated with the normalization condition for each mode. The elements of the dynamic

Harmonic Vibrational Modes of BiBO

matrix fall into two subsets with respect to the displacements: the diagonal elements $\frac{1}{M_\alpha} \frac{\partial^2 E}{\partial d_{\alpha,i}^2}$ and the nondiagonal elements $\frac{1}{\sqrt{M_\alpha M_\beta}} \frac{\partial^2 E}{\partial d_{\alpha,i} \partial d_{\beta,j}}$ where i must be

different from j . A three-point numerical derivative formula was adopted to compute the diagonal elements,

$$\frac{\partial^2 E}{\partial d_{\alpha,i}^2} = \frac{[E(+\Delta d_{\alpha,i}) - E_0] + [E(-\Delta d_{\alpha,i}) - E_0]}{\Delta d_{\alpha,i}^2} \quad (9-1)$$

where $\Delta d_{\alpha,i}$ is the displacement (0.001 a.u. in our calculations) along the Cartesian i -coordinate of atom α and E_0 is the energy at the non-displaced equilibrium geometry. Accordingly $6N$ single-point calculations have to be performed for the entire $3N$ diagonal elements each of which needs two complete single-point rounds. The nondiagonal elements were computed according to:

$$\frac{\partial^2 E}{\partial d_{\alpha,i} \partial d_{\beta,j}} = \frac{g_{\alpha,i}(\Delta d_{\beta,j}) - g_{\alpha,i}(-\Delta d_{\beta,j})}{2\Delta d_{\beta,j}} \quad (9-2)$$

where $g_{\alpha,i}(\pm\Delta d_{\beta,j})$ is defined as the gradient along the i -coordinate of atom α at the positive and negative displacement along the j -coordinate of atom β :

$$g_{\alpha,i}(\Delta d_{\beta,j}) = \frac{E(\Delta d_{\alpha,i}, \pm\Delta d_{\beta,j}) - E(-\Delta d_{\alpha,i}, \pm\Delta d_{\beta,j})}{2\Delta d_{\alpha,i}} \quad (9-3)$$

Accordingly, $6N(3N-1)$ single-point calculations had to be performed for the entire $3N(3N-1)/2$ nondiagonal elements each of which needs four complete single-point rounds. Therefore, the total number of single-point calculations needed for an evaluation of the frequencies is $18N^2+1$ (e.g. 1801 single-point rounds for BiBO with the number of atoms $N=10$).

The threshold for the single-point energy convergence was set to 10^{-8} a.u. so as to obtain a good compromise between a sufficient numerical accuracy and a not too excessive computational time. All calculations were performed with the same set of orbital-indexed bielectronic integrals for the equilibrium geometry in order to reduce the numerical noise for the dynamic elements. The vibrational frequencies were evaluated at the highest symmetry $\mathbf{k}=0$ point (i.e., the Γ point) in the reciprocal space because Raman and IR experimental data refer to the $\mathbf{k}=0$ point only, where harmonic frequencies of periodic compounds can be calculated in the same way as for molecules. Frequencies at other \mathbf{k} points (i.e. phonon dispersions) can be obtained, as described in Chapter 5, by building up corresponding supercells, which is quite expensive at the current computational level and therefore will not be discussed here.

The basis sets and the corresponding ECP of Bi are described in Chapter 6. The basis sets of boron and oxygen atoms were originally taken from the public EMSL database [123]. Modifications of the exponents of uncontracted outmost orbitals are necessary if they are

too diffuse and cause linear dependence problems in periodic structures. However, since the frequency calculation of BiBO is very time-demanding due to the need to compute numerical differences, the double-zeta 6-31G* basis sets were employed for both boron and oxygen atoms other than the triple-zeta basis sets for electronic structure calculations discussed in Chapters 6, 7 and 8. The outmost sp and d orbitals of the oxygens were energy-reoptimized to be 0.2742 and 0.5380, respectively. In order to perform the basis set optimization at the hybrid B3PW scalar-relativistic level, each exponent was varied with a step size of 0.05 and a single-point calculation was completed with CRYSTAL03. At every single optimization iterative stage, each optimal exponent was obtained by a three-point parabolic fitting. The above cycle was repeated until the variation of the SCF energy stayed below 10^{-8} a.u.

9.3 Method calibration study for cubic MgO

It is necessary to first examine the accuracies of different first-principles methods for frequency evaluations in the CO-LCAO approach for periodic compounds, i.e., HF, Perdew-Wang correlation LDA, Perdew-Wang correlation GGA and Becke three-parameter hybrid B3PW functionals. However, since the evaluation of frequencies for BiBO is highly time-demanding and the experimental data is incomplete, it is neither practical nor helpful to perform these calculations individually on BiBO. Therefore we explored the much simpler but experimentally well investigated crystal of cubic rocksalt-type MgO as test example and determined the deviations of lattice constants and frequencies from available experimental measurements. In all these calculations, the energies were converged by 10^{-8} a.u. (the reasons will be clarified in the following) for 260 **k**-points within the irreducible Brillouin zone. All-electron basis sets 8-61G for Mg and 8-51G for O specifically adjusted to cubic MgO by Causa, et al. [169] were applied. Due to the nuclear site group analysis [170], rocksalt MgO has two triply-degenerate IR-active but Raman-inactive lattice modes both representing the symmetry F_{1u} , one of which is an acoustic branch, whereas the other is an optical branch. The calculated three degenerate optical frequencies are listed in Table 9-1. Pronounced discrepancies of ~ 23 cm^{-1} , ~ 43 cm^{-1} and ~ -13 cm^{-1} compared with the experimental frequencies are found for the HF, PW LDA and PW GGA, respectively, while the B3PW functional only slightly overestimates the frequencies by ~ 6 cm^{-1} . This confirms that the B3PW method is preferable to the HF, LDA and GGA approaches for the evaluation of harmonic frequencies not only for molecules but also probably for periodic compounds.

In addition, the numerical uncertainties with respect to the energy convergence threshold of equation (9-1) and (9-2) need to be examined as well. For example, the accuracy of a dynamic element to 10^{-2} a.u. requires all these energies to meet the severe convergence criteria of 10^{-8} a.u. given the atomic displacement of 0.001 a.u., while the usual energy convergence by 10^{-6} a.u. can enlarge the numerical deviation of dynamic elements by a factor of hundred. Therefore by using equation (9-1) and (9-2) test frequency calculations for the energy convergence thresholds of 10^{-6} , 10^{-8} , 10^{-10} and 10^{-12} a.u. have been performed on MgO with the B3PW functional. The calculated frequencies for the three

Harmonic Vibrational Modes of BiBO

degenerate optical modes of MgO are (414.123 cm⁻¹, 414.126 cm⁻¹, 414.138 cm⁻¹), (445.802 cm⁻¹, 445.820 cm⁻¹, 445.837 cm⁻¹), (446.238 cm⁻¹, 446.248 cm⁻¹, 446.261 cm⁻¹) and (446.151 cm⁻¹, 446.155 cm⁻¹, 446.156 cm⁻¹), respectively. It is obvious that 10⁻⁶ a.u. considerably underestimates the frequencies by about 30 cm⁻¹. The frequencies for 10⁻⁸ a.u. and 10⁻¹⁰ a.u. are converged with respect to that of 10⁻¹² a.u. with differences of only ~0.3 cm⁻¹ and ~0.1 cm⁻¹, respectively, and agree within 6 cm⁻¹ (1.4%) with the experimental value of ~440 cm⁻¹ [171]. It is worthwhile noting that with the energy convergence threshold of 10⁻⁸ a.u., the result is even more numerically accurate for heavy metal-containing systems like BiBO than in the case of MgO, since the heavier mass weight of Bi in the denominator helps to further reduce the numerical error of the

dynamic element $\frac{1}{\sqrt{M_\alpha M_\beta}} \frac{\partial^2 E}{\partial d_{\alpha,i} \partial d_{\beta,j}}$ (e.g., for M_α=M_β=Bi, the numerical error of this

nondiagonal dynamic elements was estimated to be about 4.7 × 10⁻⁵ due to equation (9-1)). The threshold for the single-point energy convergence was therefore set to 10⁻⁸ a.u. for BiBO in the following DFT calculations to obtain a good compromise between a sufficient numerical accuracy and a tolerable computational time.

9.4 Vibrational modes of BiBO

In this section, the calculated vibrational frequencies of BiBO are presented and the vibrational modes are fully assigned based on the analysis of the calculated vibrating vectors. The calculated bond distances and angles are listed in Table 9-2 for double- and triple-zeta basis sets. The double-zeta basis set equilibrium structure exhibits similar deviations from the experimental data as the triple-zeta basis set results, underlining the well-known fast convergence of DFT results with respect to the size of the basis set. Therefore the double-zeta basis sets have been applied for the subsequent frequency calculations in order to reduce the necessary computational time compared to triple-zeta basis set calculations. We assume that the use of a double-zeta basis does not lead to a significant loss of accuracy (cf., the discussion below). The nuclear site group method [170] was applied to decompose the symmetry representation of the Brillouin zone-center vibrational modes. In the crystal structure of BiBO, one Bi and one B atom occupy the C2 sites, and the remaining two B and six O atoms occupy the C1 sites. The lattice modes are represented by 14A+16B, among which there are A+2B acoustic modes. The remaining 13A+14B modes belong to the optical modes and all of them are both IR and Raman active.

The calculated modes are visualized the corresponding frequencies and frequencies are listed together in Figures 9-1 and 9-2. It can be seen that these normal modes are so complex that combined framework motions of all [BiO₄]⁵⁻, [BO₃]³⁻ and [BO₄]⁵⁻ units can be found almost for every mode. One of the reasons is that [BiO₄]⁵⁻, [BO₃]³⁻ and [BO₄]⁵⁻ units share oxygen atoms. Nevertheless, the modes can be basically viewed as belonging to two different types, i.e., Bi-O and B-O vibrations. The first region from 139.38 cm⁻¹ to 309.79 cm⁻¹ is the far-infrared area which is composed of the translational motions of

Harmonic Vibrational Modes of BiBO

central Bi cations as well as the translational and external motions of $[\text{BO}_3]^{3-}$ and $[\text{BO}_4]^{5-}$ borate units (see Figure 9-1 and Table 9-3). It should be stressed that all the external modes are related to the lattice vibration and caused by the collective rolling of both of the entire $[\text{BO}_3]^{3-}$ and $[\text{BO}_4]^{5-}$ backbones with the shared oxygen (e.g., O4) being the supporting pivot and involve little inner movements within the two structural units. However, no simple strict Bi-O bond stretching vibrations are found in this region. Consequently these motions add up to O-Bi-O rocking (in plane, in phase), scissoring (in plane, out of phase), wagging (out of plane, in phase) and twisting (out of plane, out of phase) vibrations. For example, the Bi cation translates along different directions as indicated by the vector arrows in Figure 9-1 for all these eight modes; the borate units translate along the opposite translational direction of the central Bi cations for 139.39 cm^{-1} and 189.68 cm^{-1} . It can be seen from Table 9-3 that all the rocking and wagging vibrations belong to the B antisymmetric representation, all the scissoring vibrations to A symmetric representation and the twisting vibrations to both A and B. Frequencies of the eight normal modes have different distributions for O4-Bi-O5 and O6-Bi-O7 bonds over the four types of O-Bi-O vibrations with the only exceptions for 189.68 cm^{-1} (rocking) and 263.82 cm^{-1} (twisting). There is only one mode for the scissoring vibration for the individual O4-Bi-O5 (139.38 cm^{-1}) and O6-Bi-O7 (260.77 cm^{-1}) bond.

It has been found in our previous first-principles B3PW DFT calculations of BiBO that the covalent interactions between Bi and O lead to the optical response dominantly originating from $[\text{BiO}_4]^{5-}$ units in the long wavelength region mainly due to Bi 6p-O 2p orbital couplings and the asymmetric Bi lone-pair lobe mainly due to Bi 6s-O 2p orbital couplings. Therefore the optical responses of $[\text{BiO}_4]^{5-}$ units and the asymmetry of Bi lone-pairs obviously depend on the Bi-O bond strengths. These are also relevant to the Bi-O vibrational frequencies reflecting the hierarchy of energy distributions of Bi-O motions involving $[\text{BiO}_4]^{5-}$ units. These Bi-O vibrations lead to constantly changing Bi-O distances and O-Bi-O angles which consequently result in the varied Bi-O bond strengths. This is one way how the Bi-O vibrations are combined with the electronic states of BiBO which may bring the significant influence on the optical effects of BiBO and cause as well the vibrating of the Bi lone-pairs.

The second region from 374.46 cm^{-1} to 1516.74 cm^{-1} is responsible for the internal vibrations within the borate units involving the motions with stationary central Bi cations (see Figure 9-2 and Table 9-3). For triangular $[\text{BO}_3]^{3-}$ units, there are five types of motions which contribute to the vibrational modes, i.e., weak external motion, out-of-triangle-plane O-B-O bending motion, in-triangle-plane O-B-O bending motion, symmetric B-O stretching motion and asymmetric B-O stretching motion. It is therefore found that, as presented in Table 3, for $[\text{BO}_3]^{3-}$ units the B-O stretching frequencies are higher than those of the O-B-O bending vibrations, the in-plane O-B-O bending frequencies are higher than those of the out-of-plane O-B-O bending vibrations, and the asymmetric B-O stretching frequencies are higher than those of symmetric B-O vibrations. The external motions (374.46 cm^{-1} , 452.47 cm^{-1} and 563.05 cm^{-1}) are virtually

Harmonic Vibrational Modes of BiBO

weak due to their small amplitudes compared to those of $[\text{BO}_4]^{5-}$ units. The five out-of-plane O-B-O bending motions are distributed over a small frequency interval of $\sim 70 \text{ cm}^{-1}$ (624.77 cm^{-1} , 631.69 cm^{-1} , 651.95 cm^{-1} , 675.27 cm^{-1} and 696.05 cm^{-1}) and the five in-plane O-B-O bending motions over a much larger frequency interval of $\sim 250 \text{ cm}^{-1}$ (743.62 cm^{-1} , 768.15 cm^{-1} , 846.74 cm^{-1} , 979.44 cm^{-1} and 991.22 cm^{-1}). The six highest frequencies refer to the B-O stretching motions at 1090.37 cm^{-1} and 1139.23 cm^{-1} for symmetric vibrations and at 1251.10 cm^{-1} , 1265.56 cm^{-1} , 1433.16 cm^{-1} and 1519.74 cm^{-1} for asymmetric vibrations.

The internal modes of $[\text{BO}_4]^{5-}$ units involve more complex motions than those of $[\text{BO}_3]^{3-}$ units. The coupling of different types of O-B-O motions takes place only between O4-B8-O5' and O3-B8-O2' bonds. The O4-B8-O5' twisting motion combines with the O3-B8-O2' symmetric stretching at 1090.37 cm^{-1} as well as scissoring at both 452.47 cm^{-1} and 1265.56 cm^{-1} , the rocking with the wagging at 631.69 cm^{-1} , the wagging with the asymmetric stretching at 846.74 cm^{-1} and the asymmetric stretching with the wagging at 563.05 cm^{-1} . The tetrahedral B-O asymmetric stretchings (pure stretching of all four B-O bonds in an asymmetric manner) are found at both 991.22 cm^{-1} and 1139.23 cm^{-1} . The modes for pure O-B-O twistings in $[\text{BO}_4]^{5-}$ are located at 374.46 cm^{-1} , 624.77 cm^{-1} , 651.95 cm^{-1} and 675.27 cm^{-1} ; for pure O-B-O rockings at 743.62 cm^{-1} and 1433.16 cm^{-1} ; for pure O-B-O scissorings at 768.15 cm^{-1} , 1251.10 cm^{-1} and 1519.74 cm^{-1} .

Measured vibrational modes are equivocally assigned merely by a specific characteristic functional group, which is however not always possible for BiBO according to the calculated normal modes. The combined B-O movements in both $[\text{BO}_3]^{3-}$ and $[\text{BO}_4]^{5-}$ units due to sharing oxygens are virtually responsible for internal modes. For example, if one takes a look at the six modes with the highest frequencies involving the B-O symmetric and asymmetric stretchings for triangular $[\text{BO}_3]^{3-}$ units (see Table 9-3), these six modes can be grouped into three pairs, i.e., pair I (1090.37 cm^{-1} and 1139.23 cm^{-1}), pair II (1251.10 cm^{-1} and 1265.56 cm^{-1}) as well as pair III (1433.16 cm^{-1} and 1519.74 cm^{-1}), each of which exhibits the same stretching pattern of B-O bonds in triangular $[\text{BO}_3]^{3-}$ units but completely different motions of O-B-O bonds in tetrahedral $[\text{BO}_4]^{5-}$ units (see Figure 9-2). Therefore it is essentially the involvement of these distinct vibrations of O-B-O bonds in tetrahedral $[\text{BO}_4]^{5-}$ units in each pair that causes the frequency splitting within this pair, frequencies which otherwise should stay degenerate as a result of the same B-O stretching pattern in triangular $[\text{BO}_3]^{3-}$ units.

Since 2001 at least five reports on the experimental Raman and IR spectra of BiBO appeared in literature [28, 41, 165, 166, 167]. Moreover, the phonon frequencies have been obtained indirectly by simulating the reflectance of BiBO [40]. Unfortunately, the data provided by these studies is not fully consistent and the combined set of frequencies is larger than the expected 13A and 14B Raman and IR active modes. Only three studies provide a symmetry assignment, which is however also not in agreement for all modes [41, 166, 40]. A comparison to the theoretical results of the present study is thus not straightforward. We decided to compare our data mainly to the most recent experimental

Harmonic Vibrational Modes of BiBO

results of Egorysheva et al. [165], Hu et al. [166] and Kasprowicz et al. [167] as well as the fitting results of Gössling et al. [40] (cf. Table 9-4). In our compilation we group the nearby frequencies obtained in each experimental study for different Raman scattering geometries and only give the interval, i.e. the minimum and maximum value of each group. If available, we add the label A or B for the symmetry assignment made by the authors [166, 167]. If no symmetry assignment is available, we tentatively arrange the values in such a way that they agree best with our calculated results as well as the symmetry assigned data. It is obvious from Table 4 that for the majority of the modes the agreement between theory and experiment is quite good. Deviations exist especially for low frequencies ($<600\text{ cm}^{-1}$) and for high frequencies ($>1200\text{ cm}^{-1}$), as will be discussed below. We note that the agreement between our results and the experimental data is not worse than between any two of the experimental data sets. In the following discussion unless otherwise noted we label the modes according to the calculated frequency in wavenumbers and the symmetry label given as first entry in Table 9-3 and Table 9-4.

Quite good agreement between theory and all experiments is obtained for 190 B, 374 A, 652 A, 696 B, 744 B, 768 A, 847 B, 979 B, 991 A, 1139 B and 1520 A. The modes 625 A, 632 B and 1090 A are missing in the data of Hu et al. [166], those at 238 B, 261 A, 264 A, 310 B, 675 A and 1266 A in the data of Gössling et al. [40] with otherwise good agreement. The modes 1251 B and 1433 B correspond to modes which were related to multi-phonon transitions by Gössling et al. [40] ($1268, 1400$ and 1434 cm^{-1} , B symmetry), whereas their mode at 1363 cm^{-1} in B symmetry has no correspondence in our calculated data set. The same is true for experimental modes of both A and B symmetry in the Vibrational modes of BiBO regions of $1184\sim 1207\text{ cm}^{-1}$ and $1433\sim 1472\text{ cm}^{-1}$. Regarding only the frequencies the modes 452 A and 563 B are in good agreement with the experimental values, however it appears that the symmetry assignments partially disagree. In contrast to all experiments we do not find modes in A symmetry with frequencies near $393\sim 395\text{ cm}^{-1}$ and $202\sim 219\text{ cm}^{-1}$. It remains to be seen if some of the experimental frequencies not corresponding to calculated modes can be explained by multi-phonon transitions. Only modest agreement with experiments is obtained for the lowest modes, 139 A, 142 B and 157 B, e.g. the experimental assignment of the lowest mode is to B rather than A symmetry. Summing up, if we disregard the absence of modes in just one of the four experimental data sets as well as the interpretation as a multi-phonon transition, we obtain good agreement with experiment in 21 out of 27 cases. A revised symmetry assignment for the two modes 452 A and 563 B might even further improve this result.

Some additional information concerning the atomic motions in the modes can be extracted from our calculations. Hu and coworkers attributed the low-frequency band from 136 to 271 cm^{-1} to external vibrations [166], whereas due to our calculated frequencies these modes extend from 139 A to up to 310 B. They also took the bands at $649\sim 675\text{ cm}^{-1}$ and $715\sim 746\text{ cm}^{-1}$ as the $[\text{BO}_3]^{3-}$ in-plane and out-of-plane bending vibrations, respectively. However, our calculated results strongly indicate that the $[\text{BO}_3]^{3-}$ in-plane and out-of-plane bending vibrations actually stay at $744\text{ B}\sim 991\text{ A}$ and 625

Harmonic Vibrational Modes of BiBO

A~696 B, respectively, which on the other hand confirms the rule-of-thumb that the frequencies of in-plane bending vibrations are usually higher than those of out-of-plane bending vibrations. Kasproicz et al. considered the frequencies at 435~862 cm^{-1} and 935~1484 cm^{-1} for bending and stretching vibrations of $[\text{BO}_3]^{3-}$ and $[\text{BO}_4]^{5-}$ groups respectively, which however individually take place at 625 A~991 A and at 1090 A~1520 A according to the present calculations.

Harmonic Vibrational Modes of BiBO

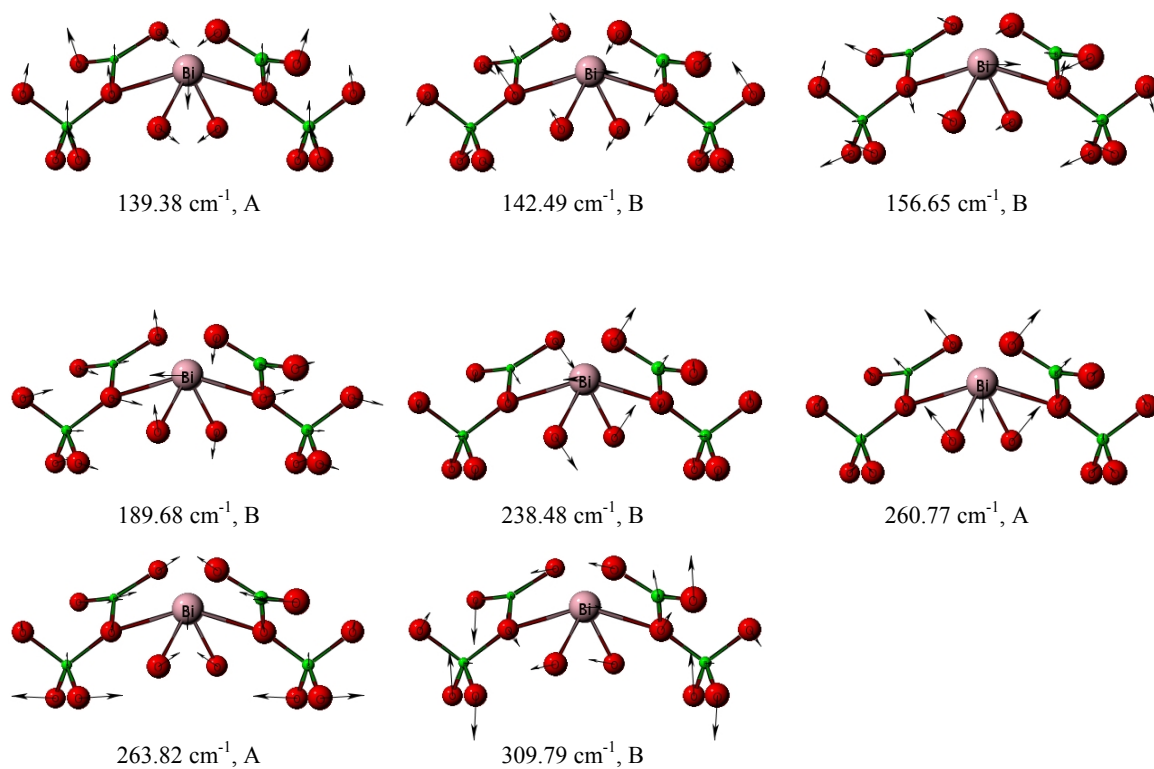


Figure 9-1 The calculated external vibrational modes and frequencies of BiBO. The symmetry types are given following the frequencies. The large light red ball stands for Bi, small green ball for B and medium dark red ball for O.

Harmonic Vibrational Modes of BiBO

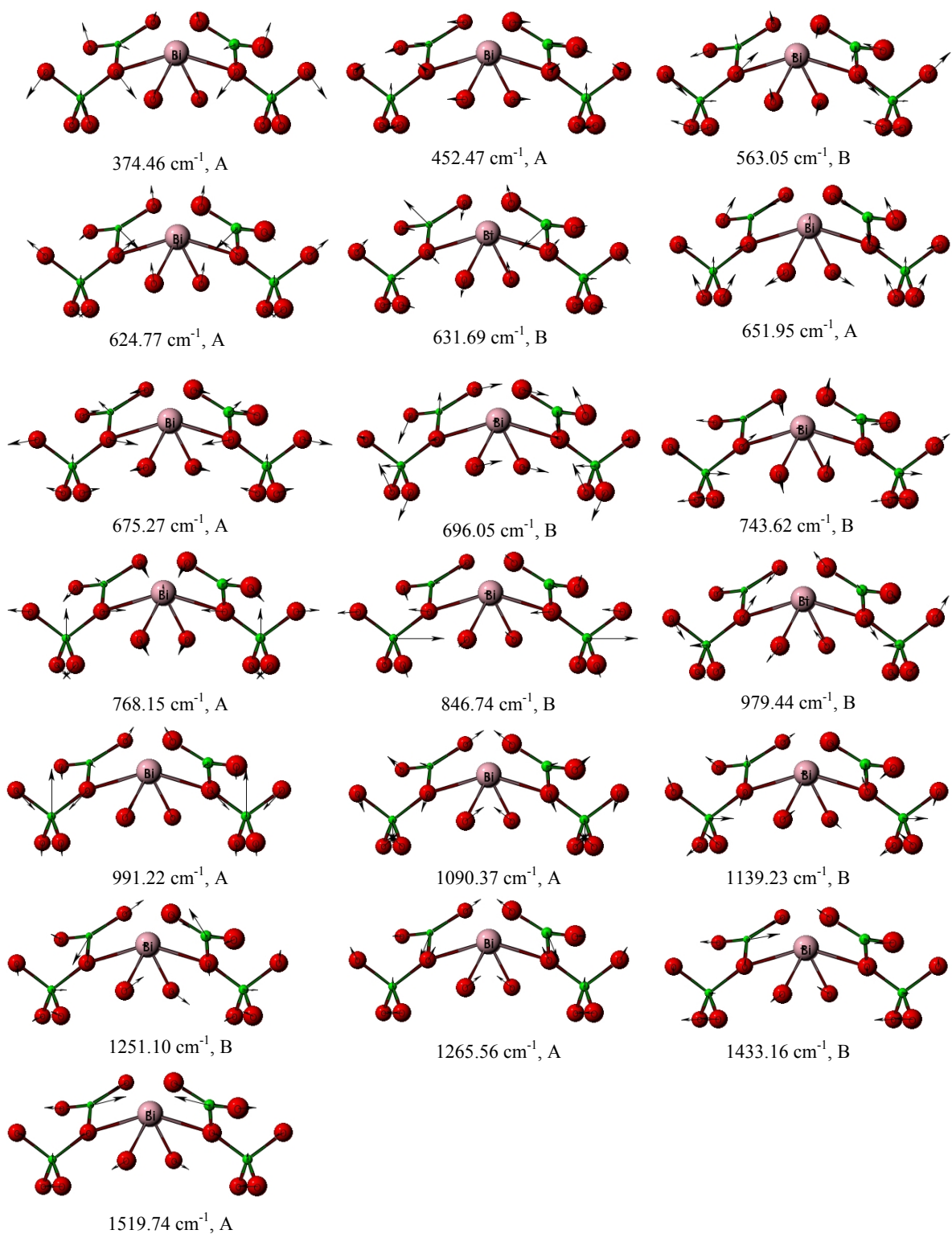


Figure 9-2 The calculated internal vibrational modes and frequencies of BiBO. The symmetry types are given following the frequencies. The large light red ball stands for Bi, small light green ball for B and medium dark red ball for O.

Harmonic Vibrational Modes of BiBO

Table 9-1 Calculated lattice constant and harmonic frequencies of MgO for the calibration of the HF, PW LDA, PW GGA and B3PW methods.

method	lattice constant (Å)	frequencies (cm ⁻¹) (3 degenerate optical modes)
Experiment	4.2198 ^a	~440 ^b
HF	4.192	463.645 463.652 463.652
PW LDA	4.135	483.266 483.266 483.266
PW GGA	4.209	427.609 427.621 427.631
B3PW	4.191	445.802 445.820 445.837

a reference [172]

b peak position, reference [171]

Table 9-2 The optimized B3PW structure of BiBO with respect to different sizes of basis sets.

structural units	Exp. ^a	Double-zeta ^b	Triple-zeta ^c
[BiO ₄] ⁵⁻ (Å)	2.390	2.387	2.388
	2.086	2.102	2.109
[BO ₃] ³⁻ (Å)	1.411	1.404	1.405
	1.365	1.370	1.367
	1.339	1.347	1.344
[BO ₄] ⁵⁻ (Å)	1.487	1.497	1.498
	1.436	1.442	1.446
∠O2-Bi-O3 (°)	102.15	101.57	101.40
∠O4-Bi-O5 (°)	152.20	151.55	151.32
∠O6-Bi-O7 (°)	90.58	89.64	89.88
$ \Delta_d ^{\text{Bi-O}}$ (Å) ^d		0.010	0.012
$ \Delta_d ^{\text{B-O}}$ (Å) ^d		0.007	0.007
$ \Delta_\angle $ (°) ^d		0.72	0.78

a: reference [33]

b: Bi: (4s4p1d)/[2s2p1d]

O/B: 6-31G*

c: Bi: (4s4p1d)/[2s2p1d]

O: Dunning contraction (11s, 6p)/[5s, 3p]

B: 6-311G*

d: $|\Delta_d|^{\text{Bi-O}}$, $|\Delta_d|^{\text{B-O}}$ and $|\Delta_\angle|$ are the calculated average absolute deviations for Bi-O bond lengths, B-O bond lengths and bond angles between the experimental and theoretical values, respectively.

Harmonic Vibrational Modes of BiBO

Table 9-3 Calculated frequencies and theoretical assignments of external and internal modes for BiBO. A symmetry label (A, B) is appended to the frequencies.

External modes		
Freq. (cm ⁻¹)	O4-Bi-O5	O6-Bi-O7
139.38, A	scissoring	twisting
142.49, B	twisting	rocking
156.65, B	twisting	wagging
189.68, B	rocking	rocking
238.48, B	wagging	rocking
260.77, A	twisting	scissoring
263.82, A	twisting	twisting
309.79, B	rocking	wagging
Internal modes		
Freq. (cm ⁻¹)	O-B-O	
374.46, A	weak external motion of [BO ₃] ³⁻ ; O4-B8-O3 and O2'-B8-O5' twistings in [BO ₄] ⁵⁻ ;	
452.47, A	weak external motion of [BO ₃] ³⁻ ; O4-B8-O5' twisting and O3-B8-O2' scissoring in [BO ₄] ⁵⁻ ;	
563.05, B	weak external motion of [BO ₃] ³⁻ ; O4-B8-O5' asymmetric stretching and O3-B8-O2' wagging in [BO ₄] ⁵⁻ ;	
624.77, A	out-of-plane O-B-O bending in [BO ₃] ³⁻ ; O4-B8-O5' and O3-B8-O2' twistings in [BO ₄] ⁵⁻ ;	
631.69, B	out-of-plane O-B-O bending in [BO ₃] ³⁻ ; weak O4-B8-O5' rocking and O3-B8-O2' wagging in [BO ₄] ⁵⁻ ;	
651.95, A	out-of-plane O-B-O bending in [BO ₃] ³⁻ ; O4-B8-O5' and O3-B8-O2' twistings in [BO ₄] ⁵⁻ ;	
675.27, A	out-of-plane O-B-O bending in [BO ₃] ³⁻ ; O4-B8-O5' and O3-B8-O2' twistings in [BO ₄] ⁵⁻ ;	
696.05, B	out-of-plane O-B-O bending in [BO ₃] ³⁻ ; [BO ₄] ⁵⁻ distortion;	
743.62, B	in-plane O-B-O bending in [BO ₃] ³⁻ ; O4-B8-O3 and O2'-B8-O5' rockings in [BO ₄] ⁵⁻ ;	
768.15, A	in-plane O-B-O bending in [BO ₃] ³⁻ ; O4-B8-O5' and O3-B8-O2' scissorings in [BO ₄] ⁵⁻ ;	
846.74, B	in-plane O-B-O bending in [BO ₃] ³⁻ ; O4-B8-O5' wagging and O3-B8-O2' asymmetric stretching in [BO ₄] ⁵⁻ ;	
979.44, B	in-plane O-B-O bending in [BO ₃] ³⁻ ; [BO ₄] ⁵⁻ distortion;	
991.22, A	in-plane O-B-O bending in [BO ₃] ³⁻ ; [BO ₄] ⁵⁻ asymmetric stretching;	
1090.37, A	symmetric B-O stretching in [BO ₃] ³⁻ ; O4-B8-O5' twisting and O3-B8-O2' symmetric stretching in [BO ₄] ⁵⁻ ;	
1139.23, B	symmetric B-O stretching in [BO ₃] ³⁻ ; [BO ₄] ⁵⁻ asymmetric stretching;	
1251.10, B	asymmetric B-O stretching in [BO ₃] ³⁻ ; weak O4-B8-O3 and O2'-B8-O5' scissorings in [BO ₄] ⁵⁻ ;	
1265.56, A	asymmetric B-O stretching in [BO ₃] ³⁻ ; weak O4-B8-O5' twisting and O3-B8-O2' scissoring in [BO ₄] ⁵⁻ ;	
1433.16, B	asymmetric B-O stretching in [BO ₃] ³⁻ ; O3-B8-O2' rocking in [BO ₄] ⁵⁻ ;	
1519.74, A	asymmetric B-O stretching in [BO ₃] ³⁻ ; O3-B8-O2' scissoring in [BO ₄] ⁵⁻ ;	

Table 9-4 Comparisons between the calculated and experimental vibrational frequencies for BiBO (in cm^{-1}). A symmetry label (A, B) is appended if an assignment was made. The frequencies labeled by * is interpreted by the paper authors as multi-phonon transitions.

Calc.	Exp. [165]	Exp. [167]	Exp. [166]	Exp. [40]
139 A	133	134~155	136~167 B	136 B
142 B				146 B
			153~170 A	168 A
157 B	167	168~169		172 B
190 B	192	179, 184	187 B	190 B
	209	199~230	202~219 A	202 A
238 B			212~224 B	
261 A	269	270~271	270~271 A	
264 A				
310 B	315	316~317	316~317 B	
374 A	369	365~370	368~371 A	367 A
	394	394~395	394~395 A	393 A
	453	435~459	439~451 B	441 B
452 A			440~451 A	
	577	570~581	574~581 A	570 A
563 B				
625 A	650	643~647	649~652 A	644 B
632 B				646 A
652 A				
675 A	667, 685	661~680	669, 675 A	
696 B			676~684 B	667 B
744 B	718, 742	711~753	715~758 B	711 B
768 A			736~743 A	731 A
847 B	860	827~862	828~857 B	826 B
979 B	942	935~971	941~967 B	940 B
991 A			940~947 A	947 A
1090 A	1065, 1097	1062~1101	1099~1105 B	1062 A
1139 B				1095 B
	1194	1184~1192	1187~1207 B	1187 B
			1187~1200 A	1199 A
1251 B	1293	1227~1265	1232~1282 B	1268 B *
1266 A			1230~1294 A	
	1380, 1401	1394, 1416	1379~1428 B	1363 B
1433 B				1400 B *
				1434 B *
	1452	1446~1454	1433~1454 A	1448 A
			1454~1472 B	
1520 A	1484	1477~1484	1485~1488 A	1484 A
			1487~1500 B	1486 B *

Chapter 10 Phase Stabilities of Monoclinic LnBO

In this chapter, we turn to investigate another type of triborate, i.e., the monoclinic LnBO containing lanthanide elements. This chapter is divided by two subsections. The first section contributes to generate a set of valence basis sets in connection with the lanthanide scalar-relativistic 4f-in-core pseudopotentials for the first-principles calculations of crystals containing lanthanide metals, which is adapted to their crystal orbitals. With the augmentation of diffuse functions and f/g orbitals, these valence basis sets are also suitable for molecular calculations. The second section presents, with the ease of the generated lanthanide valence basis sets, the first-principles DFT calculations of both symmetric I2/c and assumed asymmetric C2 structures of LaBO and GdBO for their relative stabilities between I2/c and C2 phases.

10.1 Crystal orbital adapted valence basis sets for lanthanide 4f-in-core pseudopotentials

10.1.1 Introduction

Although the quantum chemistry of systems containing lanthanide elements has received much attention in the past two decades [173, 174, 175, 176], at present theoretical chemistry investigations on systems containing f elements are still a considerable challenge [176, 177, 178, 179]. The extremely complex electronic structure of the f-elements (e.g., for lanthanides usually 4f as well as 5d and 6s may be partially occupied in the ground state or rather low-lying excited states), large relativistic effects and strong electron correlations pose considerable difficulties to theoretical work. Traditional wavefunction-based first-principles approaches accounting for relativity at the all-electron Dirac-Coulomb-Breit level and including electron correlation effects by means of coupled-cluster or configuration interaction methods need h- or even i- functions in the one-particle basis sets to yield accurate results [180]. Such highly correlated state-of-the-art all-electron studies are currently feasible only for atoms by exploiting their spherical symmetry and to our knowledge, the method is not applicable to all lanthanide elements, i.e., only calculations for closed-shell systems, one or two electrons outside a closed shell or one or two holes inside a closed shell, are feasible. In order to be able to treat all lanthanide atoms and, more importantly, to be able to deal also with molecules or periodic solid materials, compromises have to be made with respect to the treatment of relativity and electron correlation.

Among the most successful approaches of relativistic first-principles quantum chemistry applicable to these systems is the ECP method [181]. As we have described in Chapter 3, in this approach, the explicit quantum chemical treatment is restricted to the valence electrons and relativistic effects are usually only implicitly accounted for by a proper adjustment of free parameters in the valence model Hamiltonian. Consistent sets of ECP parameters have been published for lanthanide elements, e.g., model potentials [182, 183] as well as energy-consistent [184, 185] and shape-consistent [186, 187] pseudopotentials.

Phase Stabilities of Monoclinic LnBO

Dolg and coworkers developed and thoroughly tested energy-consistent pseudopotentials for lanthanum through lutetium [184, 188, 185, 189], which yielded accurate results in molecular applications. Recently corresponding atomic natural orbital (ANO) Gaussian valence basis sets [190] and segmentedly contracted valence basis sets [191] were derived for the small-core potentials of the entire lanthanide series.

Thanks to recent achievements in describing and predicting properties of bulk materials, electronic structure calculations have become increasingly important in both condensed matter physics and chemistry motivated by designing and preparing materials with controlled properties. The availability of sophisticated codes and powerful computers has made it entirely possible to undertake first-principles computer experiments [192]. Within the CO-LCAO method implemented in the program CRYSTAL03 for the treatment of periodic systems was published more than two decades ago [193, 80, 79, 194], at present no applications to lanthanide or actinide crystals were reported (cited from the website: http://www.crystal.unito.it/Basis_Sets/ptable.html), except for a single study on GdN [195]. For those lanthanide-containing crystalline solids, the ECP method has to be applied mainly in order to eliminate the open 4f shell and many problems related to it. However, the valence basis sets generated for energy-consistent pseudopotentials of lanthanides for molecular applications cannot be transferred directly to periodic compounds without modifications. The reason is that frequently atomic basis sets with diffuse functions give rise to a large overlap between Bloch functions which linearly construct crystal orbitals, and thus not only lead to the wasting of computational resources but also might cause the quasi-linear dependence problems due to numerical limitations. The derivation of systematic lanthanide pseudopotential basis sets for solid state calculations is therefore timely.

In this contribution, HF energy-optimized Gaussian valence basis sets for trivalent lanthanum through lutetium ions were derived and adapted for crystal orbital calculations using Stuttgart-Köln energy-consistent pseudopotentials. In order to eliminate a large part of the difficulties in terms of the partially occupied lanthanide 4f shell, we adopt a 4f-in-core pseudopotential approach [184, 196]. The quality of these basis sets were verified by performing calculations for A-type crystalline lanthanide sesquioxides Ln_2O_3 ($\text{Ln}=\text{La-Pm}$) and comparing the calculated geometries and cohesive energies with experimental results. The calibration investigations for A- Ln_2O_3 were achieved within both HF and DFT schemes using the code CRYSTAL03. We selected the light lanthanides as test cases since molecular calculations revealed that for them the errors of the pseudopotentials are larger than for the heavier lanthanides [175]. To our best knowledge, no previous systematic work was found for the customization of lanthanide valence basis sets adapted for crystal orbitals.

10.1.2 Computational methods

We use energy-consistent scalar-relativistic first-principles pseudopotentials to reduce the computational effort and to incorporate the most important relativistic effects. The

Phase Stabilities of Monoclinic LnBO

method of relativistic energy-consistent first-principles ECPs is described in detail elsewhere [184, 185] and will be outlined here only briefly. The valence-only model Hamiltonian for an atom or ion with n valence electrons is given as

$$H_v = -\frac{1}{2} \sum_i^n \Delta_i + \sum_{i<j}^n \frac{1}{r_{ij}} + V_{av} \quad (10-1)$$

where i and j are electron indices. V_{av} denotes a spin-orbit averaged relativistic ECP in a semi-local form for a core with charge Q

$$V_{av} = -\sum_i^n \frac{Q}{r_i} + \sum_i^n \sum_{lk} A_{lk} \exp(-a_{lk} r_i^2) P_l \quad (10-2)$$

P_l is the projection operator onto the Hilbert subspace of angular momentum l . The free parameters A_{lk} and a_{lk} are adjusted to reproduce the total valence energies of a multitude of low-lying electronic states of the neutral atom and its ions [185]. Most of the lanthanide ions have a trivalent ground state in the condensed phase, i.e., the electronic configuration $[4d^{10}4f^{n-1}]5s^25p^6$ ($n=1\sim 15$ from lanthanum to lutetium; the core is denoted in brackets). Although the 4f-orbitals form an open shell, they are shielded by the more extended and fully occupied 5s and 5p shells from the environment and therefore seem to have a core-like character. Thus mainly the 5d- and 6s-valence orbitals are responsible for the observed chemical behavior of lanthanides [184]. Therefore, the 4f-in-core ECPs for lanthanides were chosen according to the formal oxidation degree of the lanthanide (III) center. Thus, 11 valence electron ECPs were used, i.e., the 1s-4f shells were included in the ECP core, while all others with a main quantum number larger than 4 were treated explicitly (5s5p5d6s ... shells). The reference data used to determine V_{av} have been taken from relativistic AE calculations using the WB (cf. Chapter 3) scalar-relativistic HF approach. Both AE WB and ECP calculations have been performed with an atomic finite-difference HF scheme in order to avoid basis set effects in the determination of the ECP parameters.

The routine to generate the Gaussian valence basis sets for lanthanides is described in the following. In order to compare the basis set effects, we have derived three different sets of primitive Gaussian functions (4s4p3d), (5s5p4d) and (6s6p4d). In order to avoid linear-dependency numerical problems in solid state calculations which are usually caused by too diffuse functions, we simply fixed the most diffuse exponent of each s, p and d set to the value 0.15 in all cases and reoptimized the remaining exponents. According to our experience this choice allows a quite accurate description of the orbital of trivalent lanthanide ions and at the same time does not lead to convergence problems. Lower values should be avoided due to the densely packed nature of many crystalline structures which results in an unpleasant large overlap between basis functions. Firstly the unpolarized Gaussian primitive (4s4p3d) sets of exponents were energy-optimized using the atomic HF program ATMSCF [197] for the energetically lowest LS states of doubly-charged lanthanide cations with the configuration $[4f^{n-1}]5s^25p^65d^1$ (the reason that these cations rather than neutral atoms were selected for basis sets customization will be

Phase Stabilities of Monoclinic LnBO

rationalized in the coming part). Secondly, s, p and d functions were then added to the (4s4p3d) primitives, yielding (5s5p4d) and (6s6p5d) uncontracted basis sets. The quality of the basis sets was verified by a comparison with numerical finite difference HF calculations for the Ln²⁺ ions carried out with the program MCHF [198] (representing the HF basis set limit).

The crystalline calibration calculations of A-type lanthanide oxides were carried out with the CRYSTAL03 program package, using basis sets and methods as indicated in the following. A variety of treatments of exchange and correlation were used: HF, where exchange is computed exactly but correlation is neglected, and DFT within the Kohn-Sham formalism using GGA. Within the DFT scheme, the geometry optimization was performed using the hybrid functional B3LYP and B3PW. It has become a routine approach to use pseudopotentials in connection with DFT in recent years, and the results are often quite accurate [199, 200], although most pseudopotentials and the corresponding basis sets have not been designed for such calculations. The different segmented contraction schemes yield the (4s4p3d)/[2s2p2d], (4s4p3d)/[3s3p2d], (5s5p4d)/[2s2p2d], (5s5p4d)/[3s3p3d], (5s5p4d)/[4s4p3d], (6s6p5d)/[2s2p2d], (6s6p5d)/[3s3p3d] and (6s6p5d)/[4s4p4d] valence basis sets, which were applied in the calculation of A-Pm₂O₃ to investigate the effect of the basis set quality on the final optimized geometry. Uncontracted primitive basis sets (4s4p3d), (5s5p4d) and (6s6p4d) were also tested for the sake of comparison with these contracted basis sets in the case of A-Pm₂O₃. Only the largest basis set (6s6p5d)/[4s4p4d] was chosen to calculate other A-Ln₂O₃ systems based on the work of Pm₂O₃. Due to the present unavailability of f and g functions in the code CRYSTAL03¹⁴, no effort was put to generate polarization basis functions with the angular quantum number larger than two. Sets of one and two f functions possibly also suitable for solid state calculations can be found in a previous publication [184]. For the oxygen atoms, the standard 6-311G* Gaussian function basis set [123] was used without any modification for the all-electron calculation.

The following tolerances were employed in the evaluation of the infinite Coulomb and HF exchange series: 10⁻⁶ for the Coulomb overlap, HF exchange overlap, Coulomb penetration and the first exchange pseudo-overlap; 10⁻¹² for the second exchange pseudo-overlap at DFT level and 10⁻²⁵ at HF level respectively in order to ensure convergence. This is sufficient to converge structures since tests at tighter tolerances for both DFT (10⁻⁷, 10⁻⁷, 10⁻⁷, 10⁻⁷, 10⁻²⁵) and HF (10⁻⁷, 10⁻⁷, 10⁻⁷, 10⁻⁷, 10⁻³⁰) show that the maximum difference of optimized lattice constant is less than 0.005 Å with much more computational time. The Fock matrix has been diagonalized at 116 **k**-points within the irreducible Brillouin zone corresponding to a shrinking factor of 10 in the Monkhorst net. The energy differences with respect to calculations performed with a denser net of **k**-points (288 **k**-points corresponding to a shrinking factor of 14) are smaller than 0.02kJ/cell and

¹⁴ Although the shell types implemented in CRYSTAL03 reach the maximum angular quantum number of 3, our test calculation suggests that the program failed to treat f functions at both HF and DFT level due to the basis set linear dependence even for sufficiently large exponents of f functions. In the newly released CRYSTAL06, the f shell is used only as a polarization function.

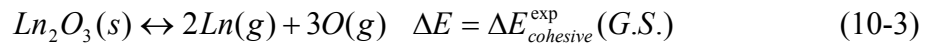
Phase Stabilities of Monoclinic LnBO

0.01kJ/cell at the DFT and HF level, respectively. In order to improve the convergence, a negative energy shift of 1.0 Hartree to the diagonal Fock/KS matrix elements of occupied orbitals was added and maintained after diagonalization thus reducing their coupling to the unoccupied set. A very accurate extra-large grid consisting of 75 radial points and 974 angular points was employed in the DFT calculations, where Becke grid point weights [120] were chosen.

The conjugated gradient (Polak-Ribiere) minimization was applied using a separate ksh-script LoptCG [201] in the full structural optimization with symmetry constraints, and all the calculations were performed with the same set of indexed bielectronic integrals selected from the reference geometry in order to reduce the numerical noise. The total energy tolerance between two subsequent optimization iterations is set to be 10^{-8} Hartree so that the convergence is forced to be achieved by norm criteria instead of energy change for reasons of accuracy.

For the evaluation of cohesive energies from atomic energies, the valence basis sets (6s6p5d) were augmented by adding two s, one p and one d low-exponent Gaussian functions to yield (8s7p6d) primitive sets. The added exponents were optimized using the atomic program ATMSCF [197] for the isolated neutral lanthanide atoms in the $[4f^{n-1}]5s^25p^65d^16s^2$ configuration. These additional functions are needed in order to provide an adequate description of the tails of the isolated atom charge density, especially the diffuse doubly occupied 6s shell [169]. The atomic energy of the oxygen atom was obtained by applying the standard 6-311+G* Gaussian functions with one additional low-exponent function for sp shells. Both Kohn-Sham DFT and the so-called *a posteriori*-HF correlation DFT method implemented in the code CRYSTAL03 were applied to calculate the cohesive energy of lanthanide sesquioxides. The atomic calculations of Ln and O for the evaluation of the cohesive energy within DFT were performed using the program MOLPRO [202], where only the hybrid functional B3LYP was applied for correlation and exchange corrections with Becke grid point weights since the functional B3PW is not available in the present version of this code. In the *a posteriori*-HF correlation scheme, HF calculations were performed for the isolated Ln and O atoms as well as A-Ln₂O₃. The subsequent electron correlation correction was obtained as the integral over the unit cell of a function depending on the crystalline HF charge density. The total energy with this *a posteriori*-HF correlation correction is simply expressed by the sum of the HF energy and the corresponding correlation energy which was evaluated for Wigner-Levy [203], PW-LSD, Perdew86 and PW91 correlation-only functionals in conjunction with exact HF exchange.

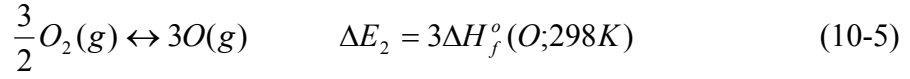
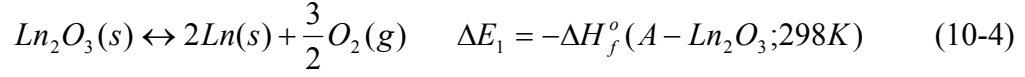
The experimental cohesive energy of Ln₂O₃ was obtained here from available thermochemical data, i.e., the standard enthalpy of formation for A-Ln₂O₃, gaseous neutral lanthanide atom and gaseous oxygen atom, according to the following reactions:



where G.S. is the acronym of ground state, i.e., $[4f^{n-1}]5s^25p^65d^16s^2$ for La (n=1) and Ce

Phase Stabilities of Monoclinic LnBO

($n=2$) as well as $[4f^n]5s^25p^66s^2$ for Pr ($n=3$), Nd ($n=4$) and Pm ($n=5$). The above reaction can be equivalently split into three steps:



Therefore, the experimental cohesive energy is represented as the following expression:

$$\Delta E_{cohesive}^{exp}(G.S.) = 3\Delta H_f^o(O;298K) + 2\Delta H_f^o(Ln;298K) - \Delta H_f^o(A-Ln_2O_3;298K) \quad (10-7)$$

The originally calculated cohesive energy $\Delta E_{cohesive}^{cal}(5s^25p^65d^16s^2)$ of Ln_2O_3 was derived by subtracting the sum of the corresponding energies of the isolated composing atoms from the energy of the bulk lanthanide oxide. However, since the configuration $[4f^{n-1}]5s^25p^65d^16s^2$ was applied in all cases of our theoretical calculations, an energy correction ΔE_{atom}^{exp} of the state separation between $[4f^{n-1}]5s^25p^65d^16s^2$ and $[4f^n]5s^25p^66s^2$ must be supplemented to $\Delta E_{cohesive}^{cal}(5s^25p^65d^16s^2)$ for systems containing Pr, Nd and Pm according to equation (10-8) in order to obtain the real cohesive energy of bulk Pr_2O_3 , Nd_2O_3 and Pm_2O_3 calculated with respect to the experimentally observed atomic ground states:

$$\Delta E_{cohesive}^{cal}(G.S.) = \Delta E_{cohesive}^{cal}(5s^25p^65d^16s^2) + 2\Delta E_{atom}^{exp} \quad (10-8)$$

where the experimental energy correction ΔE_{atom}^{exp} is -0.0404 a.u./atom for Pr and -0.0617 a.u./atom for Nd respectively [184].

Although the experimental values were measured at 298 K while the calculated ones correspond to 0 K, we omit the thermal conversion for the calculated cohesive energies from 0 K to 298 K. A further approximation of the present calculation is the complete neglect of the zero-point energy contribution to the cohesive energy.

The A-type hexagonal structure of lanthanide sesquioxides has been found from La_2O_3 to Pm_2O_3 [204, 205] with the space group $P32/m$ with one formula per unit cell. The metal atoms are in a seven-fold coordination with four oxygens being closer than the other three. The four oxygens are bonded to five and the other three to four metal atoms [206].

10.1.3 Valence basis sets derived from atomic calculations

In this part, let us first state the reason that we prefer ionic $[4f^{n-1}]5s^25p^65d^1$ configurations for doubly-charged lanthanide cations of La through Lu rather than the neutral atoms to newly generate crystal orbital-adapted valence basis sets. In the 11-electron semicore $5s^25p^65d^16s^2$ of neutral lanthanides, the two electrons of 6s shell and one electron of 5d shell are the main sources of chemical properties in condensed matter. However, a

Phase Stabilities of Monoclinic LnBO

substantial deviation from a purely ionic bonding $Ln_2^{3+}O_3^{2-}$ between lanthanide and the surrounding atoms (e.g. oxygen in Ln_2O_3) was confirmed by a Mulliken population analysis (see Table 10-1) following bulk SCF calculations of A- Ln_2O_3 . One can note from Table 10-1, that the Ln-5d population is around 1.0 within the DFT scheme and 0.6 within the HF scheme, and the total atomic charge is about 2.0 instead of the formal oxidation state of 3. In other words, only the two electrons from the diffuse Ln-6s shell are transferred to the oxygen neighbors, whereas the one electron in the more compact Ln-5d shell turns to stay on the lanthanide, thus leading to an occupation close to the one used in our optimizations.

The errors in the total valence energies for La through Lu, which were evaluated by comparing algebraic HF calculations on the doubly-charged cations to corresponding finite difference results, are shown in Figure 10-1. With increasing the size of primitive sets from (4s4p3d) to (6s6p5d) by adding additional s, p and d functions, the maximum error stays below 0.9eV, 0.09eV and 0.05 eV for (4s4p3d), (5s5p4d) and (6s6p5d), respectively. This indicates that only the two larger primitive sets accurately describe the valence orbitals of trivalent lanthanide ions. In addition, the variations of the errors for (6s6p5d) and to a lesser extent also (5s5p4d) along the lanthanide series are much more regular and smooth than for (4s4p3d), so that more reliable comparisons between bulk systems containing different lanthanides are possible. From an analysis of the exponents and coefficients of the (4s4p3d) sets we conclude that three d-functions are not sufficient to describe the 5d pseudo-orbital accurately. The peak in Figure 10-1 is related to two different sets of solutions, which yield the lowest energy in the beginning and end of the series, respectively. In the case of the sets (6s6p5d), the errors vary only very slightly across the lanthanide series and exhibit a local minimum for Tb. However, the opposite and much stronger variation is observed for the basis sets (4s4p3d) where a pronounced local maximum occurs at Sm. This opposite variation in the total energy for (4s4p3d) is in line with that in the 5d orbital energy (not illustrated here), which indicates that an additional d function is necessary to provide an adequate description of the 5d orbital.

The evaluation of cohesive energies needs valence basis sets with diffuse functions which describe the tails of the charge density on the isolated atoms, e.g., especially the diffuse doubly occupied 6s shell. The errors in the total energy for neutral La through Lu, as illustrated in Figure 10-2, were obtained in the same way as for the case of doubly-charged cations without diffuse functions. As one can see from Figure 10-2, the basis sets (8s7p5d) with two additional s and one additional p functions lead to similar errors compared with the basis sets (8s6p5d). Although the diffuse p function has almost no effect for the atomic HF energy, it is indispensable for the description of the $6s^2 \rightarrow 6p^2$ near-degeneracy. An additional diffuse d function dramatically reduces the errors to less than 0.03 eV nearly by a factor of 10. Furthermore, the variation of errors for (8s7p6d) is much more regular.

Phase Stabilities of Monoclinic LnBO

When augmenting the contracted (6s6p5d)/[4s4p4d] and (6s6p5d)/[3s3p3d] sets by 2s1p1d diffuse sets, a lower valence energy and a more regular variation of the error in the total valence energies of the $[4f^{m-1}]5s^25p^65d^16s^2 \ ^2D$ valence state is obtained than with the original (7s6p5d)/[5s4p3d] valence basis sets [184], cf. Figure 10-3. A similar behaviour is observed for the (5s5p4d)/[4s4p3d] and (5s5p4d)/[3s3p3d] sets, although the errors are slightly larger. The corresponding (8s7p6d)/[6s5p5d], (8s7p6d)/[5s4p4d] and (7s6p5d)/[6s5p4d], (7s6p5d)/[5s4p4d] sets are most likely also suitable for molecular calculations and supplement the original (7s6p5d)/[5s4p3d] sets. We do not offer diffuse sets for the basis sets based on the (4s4p3d) primitive sets, due to the too large errors observed in the doubly-charged cations valence energies (cf. above), which also affect the total energies of the neutral atoms at a similar magnitude despite the added diffuse functions. Moreover, due to the poor performance for crystal geometry data (cf. below) we do not offer diffuse sets for the [2s2p2d] contractions in case of all primitive sets.

10.1.4 Calibration calculations of crystalline A-Ln₂O₃

10.1.4.1 Geometry

HF scheme

The crystalline calibration calculations for A-type lanthanide sesquioxides Ln₂O₃ were performed using the newly generated valence basis sets at both HF and DFT level in order to verify the transferability of the basis sets from atoms to bulk materials. First, we applied these basis sets at the HF level combined with different contractions to the arbitrarily selected Pm₂O₃, since the other lanthanide sesquioxides are isostructural. The optimized geometry within the HF framework is listed in Table 10-2. The deviations of lattice constants and bond lengths from the experimental results are, for the largest uncontracted set (6s6p5d), 0.067 Å for a, 0.200 Å for c, 0.074 Å for Pm1-O1 and -0.014 Å for Pm2-O1. Quite similar results were obtained for the smaller uncontracted sets (5s5p4d) and (4s4p3d). This implies that the lattice constants and the bond length Pm1-O1 are substantially overestimated but the bond length Pm2-O1 is slightly underestimated. These relatively large discrepancies between calculated and experimental values are not surprising and partially due to the lack of electron correlation within the HF treatment. For coordinatively saturated molecular close-shell systems including transition metals, the corresponding deviations were found to even exceed ± 0.1 Å for bond distances involving the metal centers [207].

All derived contracted sets, except the [2s2p2d] sets, yield results in good agreement with those of the underlying uncontracted sets. We note here in passing that the seemingly good performance of the [2s2p2d] contraction (e.g. for the lattice constant c) is mostly due to an error cancellation, i.e., basis set incompleteness and neglect of core polarization effects, cf. below. For each case of primitive basis set in Table 10-2, i.e., (4s4p3d), (5s5p4d) or (6s6p5d) individually, the tightest contraction [2s2p2d] leads to the largest deviation with the differences of 0.043 Å, 0.056 Å and 0.055 Å, respectively, at its

Phase Stabilities of Monoclinic LnBO

maximum among the lattice constants and bond lengths, compared to the results obtained for uncontracted basis sets. But when loosening the contraction from [2s2p2d] to [3s3p2d] (or [3s3p3d] for (5s5p4d) and (6s6p5d)) as well as to [4s4p3d] (or [4s4p4d] for (6s6p5d)), the geometry is converged within much smaller maximum-differences of only 0.005 Å, 0.008 Å and 0.007 Å. Therefore, it is clear that although the contraction [2s2p2d] requires less CPU time in condensed matter calculations, this advantage is overthrown by the poor performance in predicting the geometries due to its lower flexibility to properly describe the change of electron density from an isolated ion to the ion in bulk materials.

On the other hand, very similar geometrical parameters are observed for the same basis set contraction among different primitive sizes. For example, for the tightest contraction [2s2p2d], the lattice constants a , c and the bond lengths Pm1-O1, Pm2-O1 are respectively 3.851 Å, 6.101 Å, 2.412 Å and 2.312 Å at its average with the maximum differences of 0.002 Å, 0.008 Å, 0.005 Å, and 0.001 Å for all primitive sets, i.e., (4s4p3d), (5s5p4d) and (6s6p5d). This is originally caused by the nature of the crystal orbital in periodic systems, where the real basis sets are ultimately Bloch functions. When the contraction scheme is maintained, the variational freedom stays constant, and Bloch functions are not so sensitive to the increasing size of primitive Gaussian functions from (4s4p3d) to (6s6p5d) due to the plane-wave term $e^{ik \cdot R}$, although more primitives provide the better description of atomic orbitals.

As it is pointed out above, the primitives (6s6p5d) result in a more regular and smooth variation of the calculated energy for free doubly-charged lanthanide cations along the lanthanide series. Therefore we further applied only the valence basis set (6s6p5d)/[4s4p4d] to the other A-Ln₂O₃ crystalline compounds for geometry optimizations. The obtained geometrical parameters and the available experimental results are listed and compared in Table 10-3. We note that the bond angles agree very well with both the plane-wave pseudopotential calculations and the experimental results, whereas somewhat larger deviations of lattice constants and bond lengths are found.

DFT scheme

Let us now turn to discuss the results obtained within the framework of DFT. First we tested the valence basis sets with different contractions only for A-Pm₂O₃, where the currently popular hybrid functionals B3LYP and B3PW were applied as recommended for geometry optimizations by Koch and Holthausen [94]. We compare the calculated geometries in Table 10-1 in the same way as for HF calculations in Table 10-2. Compared with the experimental results, the deviations of lattice constants and bond lengths are, for the largest uncontracted sets (6s6p5d), 0.064 Å for a , 0.080 Å for c , 0.066 Å for Pm1-O1 and -0.014 Å for Pm2-O1 in B3LYP as well as 0.042 Å for a , 0.097 Å for c , 0.044 Å for Pm1-O1 and -0.028 Å for Pm2-O1 in B3PW. Both functionals perform better than the HF method.

Similar to the HF case, the tightest contraction [2s2p2d] yield results closest to the experimental values, e.g., for (6s6p5d)/[2s2p2d] the derivations are 0.039 Å (a), 0.112 Å

Phase Stabilities of Monoclinic LnBO

(c), 0.045 Å (Pm1-O1), and -0.029 Å (Pm2-O1) for B3LYP as well as 0.020 Å (a), 0.032 Å (c), 0.022 Å (Pm1-O1), and -0.041 Å (Pm2-O1) for B3PW. However, for each case of primitive basis set in Table 10-4, i.e., (4s4p3d), (5s5p4d) or (6s6p5d) individually, the tightest contraction [2s2p2d] leads to the largest deviations with the differences of 0.061 Å, 0.065 Å and 0.078 Å for B3LYP as well as 0.066 Å, 0.061 Å and 0.071 Å for B3PW at its maximum among the lattice constants and bond lengths, compared with the results from the uncontracted sets. But when loosening the contraction from [2s2p2d] to [3s3p2d] ([3s3p3d] for (5s5p4d) and (6s6p5d)) as well as to [4s4p3d] ([4s4p4d] for (6s6p5d)), the geometry is converged within much smaller maximum differences of only 0.008 Å, 0.007 Å and 0.012 Å for B3LYP and 0.002 Å, 0.004 Å and 0.009 Å for B3PW. In addition, for example, for the tightest contraction [2s2p2d] of all primitive sets, i.e. (4s4p3d), (5s5p4d) and (6s6p5d), the lattice constant a, c and the bond length Pm1-O1, Pm2-O1 are respectively 3.841 Å, 6.070 Å and 2.398 Å, 2.309 Å at its average with the maximum differences of 0.003 Å, 0.01 Å and 0.002 Å, 0.001 Å for B3LYP as well as 3.821 Å, 5.986 Å and 2.375 Å, 2.297 Å at its average with the maximum differences of 0.002 Å, 0.003 Å and 0.002 Å, 0.001 Å for B3PW. Therefore, similar valence basis set effects on geometries, as we already pointed out for HF calculations, were observed at DFT level for both B3LYP and B3PW functionals: the calculated geometrical parameters are converged for the [3s3p2d] and other less contracted basis sets and the increasing size of primitive sets from (4s4p3d) to (6s6p5d) results in no apparent variation of final optimized structures. The use of the [2s2p2d] contractions is not recommended. Besides this, as one can see clearly in Table 10-4, the B3PW results agree much better than those of the B3LYP and HF method with the experimental values and the plane-wave pseudopotential results. In the subsequent calculations, only the valence basis set (6s6p5d)/[4s4p4d] and the hybrid functional B3PW were applied to the other A-Ln₂O₃ crystalline compounds.

The calculated geometries for A-Ln₂O₃ (Ln=La-Pm) at the DFT level are listed in Table 10-5. The average deviations of geometrical parameters for the five compounds compared with the experimental results are 0.041 Å (a), 0.092 Å (c), 0.020 Å (Ln1-O1), 0.028 Å (Ln2-O1) and 1.11 degree (Ln1-O1-Ln2), which are smaller than the corresponding deviations at the HF level, i.e., 0.067 Å (a), 0.198 Å (c), 0.040 Å (Ln1-O1), 0.036 Å (Ln2-O1) and 1.14 degree (Ln1-O1-Ln2). The lattice constants and bond lengths obtained from experiment, the projector augmented-wave pseudopotential method (PAW) [208], HF and DFT calculations are respectively plotted in Figure 10-4. The DFT results based on the B3PW functional and (6s6p5d)/[4s4p3d] basis sets are closer to the results of the PAW calculations than to the experimental results within the average deviations of 0.017 Å (a), 0.022 Å (c), 0.006 Å (Ln1-O1), 0.009 Å (Ln2-O1) and 0.10 degree (Ln1-O1-Ln2) for the five compounds. Furthermore, as illustrated in Figure 10-4, our calculated results show a linear correlation for both lattice constants and bond lengths along the atomic number at both HF and DFT levels in agreement with experimental findings and at variance with the irregular variations from La₂O₃ over Ce₂O₃ to Pr₂O₃ in the PAW calculations. This consistently smooth correlation found in our results favors the reliable

Phase Stabilities of Monoclinic LnBO

comparison of properties between crystalline compounds containing different lanthanide metals. Finally, it is easy to conclude that, based on the above analysis of deviations, our valence basis sets in conjunction with DFT/B3PW provide more accurate characterizations for bond lengths and angles than for lattice constants.

At this point it is fair to mention that the present calculations do not take into account the full valence model Hamiltonian for the lanthanides, i.e., the core polarization potential (CPP) is missing due to technical reasons. Previous work on molecules revealed that including a CPP to the 4f-in-core ECPs leads to bond length contractions of several hundredths of an Å, thus explaining at least partially the tendency of the current results to overestimate the experimental values [128]. Another reason for the too long bond lengths and lattice constants is certainly the omission of f-functions in the basis sets, as it also has been demonstrated previously for molecules [188]. We expect that once the inclusion of f-functions becomes possible, this would improve especially the results for the systems at the beginning of the lanthanide series.

10.1.4.2 Charge distribution

The Mulliken populations are shown in Table 10-1. Since the shells with a main quantum number smaller than 5 are taken as effective core potential of Ln, the valence shell electron population has a $5s^25p^65d^16s^2$ configuration as reference (11 electrons). It is well-known that the compact 4f-shell shields the nuclear-charge quite efficiently and only small differences are observed in the populations of the outer valence orbitals when comparing neighboring lanthanides. The s-population is about 2.1 no matter what theoretical scheme was applied, which suggests that the 6s orbital acts as main electron donor in these crystalline compounds. There are only slight differences of the p-population between HF and DFT as well, which is about 6.1, while the difference of the d-population is substantial: whereas the valence d-electron is almost completely retained on the lanthanide at the DFT level (d-population around 1.0), it is partially transferred to oxygen in the HF case (d-population around 0.6). As a result, HF calculations favor all lanthanide sesquioxides with more ionic and polar metal centers than the DFT scheme. In all schemes the total charge Q increases slightly along the series, which implies that the ionic character of the lanthanide is increased and covalent bonding becomes less important from La to Pm. We note that the charge increase mainly stems from the decrease of the 5d population, which is at least partly due to their increasing indirect relativistic destabilization along the lanthanide series. As mentioned in the previous part, the evident covalent contribution to the bonding between lanthanide centers and surrounding oxygens is the main reason that the valence basis sets were generated for the doubly-charged lanthanide cations with an occupied 5d orbital rather than for the triply-charged cations.

10.1.4.3 Cohesive energy

The results for the cohesive energies are listed in Table 10-6. HF calculations for free lanthanide atoms show that in accordance with Hund's rule the ground state within a $4f^{n-1}$ -subconfiguration of La through Pm corresponds to the fully polarized atomic configuration with maximum total spin density, i.e., to $5s^25p^65d^16s^2$ for Ln (Ln=La, Ce, Pr, Nd and Pm). When the DFT calculations for free lanthanide atoms are invoked, a slight unphysical orbital mixing happens between s- and d-orbitals, which leads to the fractional occupations, i.e., of $5s^{3.962}5p^65d^{1.038}$ for La, $5s^{3.967}5p^65d^{1.033}$ for Ce, $5s^{3.972}5p^65d^{1.028}$ for Pr, $5s^{3.976}5p^65d^{1.024}$ for Nd and $5s^{3.980}5p^65d^{1.020}$ for Pm. This unclear configuration is not technically unexpected partly because the current version of MOLPRO2002 simply does not support non-Abelian point-groups and O_h is thus out of reach to prevent such a mixing and partly because density functional approaches favor states with more d-electrons since more correlation contributions are found in d- than s-orbitals due to the more compact nature [94]. Although it is difficult to estimate the energy loss for lanthanide atoms resulting from the s- and d-orbital mixing, the atomic energy deviation between the fractional and integral occupations is believed to be small since the maximum deviation from integral occupation numbers is only 0.038 electrons.

We note that at the scalar-relativistic AE WB HF level, all lanthanides La-Pm possess a $[4f^{n-1}]5s^25p^65d^16s^2$ ground state configuration [184]. Experimentally this is only true for La and Ce, whereas Pr, Nd and Pm have a $[4f^n]5s^25p^66s^2$ ground state configuration [209]. For the latter elements, we thus apply the empirical corrections to the observed ground state as outlined in ref. 8 for all results which include correlation effects.

It turns out that the cohesive energy estimated at the HF level represents about 70% of the experimental one derived from thermochemical data. To restore the cohesive energy theoretically to an acceptable level, correlation contributions are taken into account in two different ways, i.e., the *a posteriori*-HF scheme and the conventional KS DFT. The *a posteriori*-HF correction is very effective in reducing the error in the binding energy to a few per cent according to previous reports on solid calculations [210, 211, 212]. Nevertheless, no previous work was found reporting the calculation of cohesive energies for periodic systems containing lanthanide elements using such a correlation correction. However, similar *a posteriori*-HF correlation corrections were successfully applied to lanthanide atoms using the 4f-in-core pseudopotentials [184]. As one can see in Table 10-6, the calculated cohesive energies account for ≈ 81 -82% (PW-LSD), ≈ 88 -89% (PW-GGA), ≈ 89 -90% (P86) and ≈ 95 -97% (Wigner-Levy) of the experimental values for the four compounds. Once again, the fact is confirmed in this work that the performance of the local spin-density approximation for correlation PW-LSD is considerably improved by the gradient-corrected functional PW-GGA and P86 in calculating the cohesive energy. In the conventional DFT scheme using B3LYP, ≈ 90 -92% of the experimental values were restored.

Phase Stabilities of Monoclinic LnBO

Based on these pleasing results, our approach with respect to 4f-in-core pseudopotentials connected with crystal orbital-adapted valence basis sets for lanthanide elements is successful in evaluating cohesive energies of bulk materials and promising for further applications in this area. As one example, we predicted, by means of the method described below, the theoretical value of cohesive energy for the bulk A-type Pm_2O_3 (see the last column in Table 10-6). This calculation is meaningful since the experimental cohesive energy of Pm_2O_3 is not available up to now due to the radioactive nature of Pm which decays too fast to be thermochemically measured for Pm_2O_3 . It is easy to write the following equations by taking $\Delta E_{\text{cohesive}}^{\text{cal}}(5s^2 5p^6 5d^1 6s^2)$, $\Delta E_{\text{cohesive}}^{\text{cal}}(G.S.)$, $\Delta E_{\text{cohesive}}^{\text{exp}}(G.S.)$, $\Delta E_{\text{corr}}^{\text{exp}}$ and the average deviation \bar{D} as parameters. The physical meanings of these parameters in equations (10-9) and (10-10) have been introduced in the part of computational methods.

$$\Delta E_{\text{cohesive}}^{\text{cal}}(G.S.) = \Delta E_{\text{cohesive}}^{\text{cal}}(5s^2 5p^6 5d^1 6s^2) + 2\Delta E_{\text{corr}}^{\text{exp}} \quad (10-9)$$

$$\Delta E_{\text{cohesive}}^{\text{cal}}(G.S.) = \Delta E_{\text{cohesive}}^{\text{exp}}(G.S.) \cdot \bar{D} \quad (10-10)$$

According to equation (10-9) and (10-10), the correlation is derived in equation (10-11):

$$\Delta E_{\text{cohesive}}^{\text{cal}}(5s^2 5p^6 5d^1 6s^2) = \Delta E_{\text{cohesive}}^{\text{exp}}(G.S.) \cdot \bar{D} - 2\Delta E_{\text{corr}}^{\text{exp}} \quad (10-11)$$

As a result, since $\Delta E_{\text{cohesive}}^{\text{exp}}(G.S.)$ and $\Delta E_{\text{corr}}^{\text{exp}}$ are constants for Pm_2O_3 and Pm, respectively, the linear correlation between $\Delta E_{\text{cohesive}}^{\text{cal}}(5s^2 5p^6 5d^1 6s^2)$ and \bar{D} yields thus as the slope and half of the intercept of this straight line the experimental cohesive energy for the bulk Pm_2O_3 and the atomic energy correction of state separation for neutral atomic Pm, respectively. The theoretical cohesive energy $\Delta E_{\text{cohesive}}^{\text{cal}}(5s^2 5p^6 5d^1 6s^2)$ of Pm_2O_3 for the configuration $[4f^{n-1}]5s^2 5p^6 5d^1 6s^2$ is calculated in the same way as for La_2O_3 through Nd_2O_3 . The deviation \bar{D} is evaluated by averaging the values in parentheses of each row in Table 6 from La_2O_3 to Nd_2O_3 . The plot of $\Delta E_{\text{cohesive}}^{\text{cal}}(5s^2 5p^6 5d^1 6s^2)$ against \bar{D} is illustrated in Figure 10-5. Therefore, the calculated cohesive energy of bulk Pm_2O_3 with respect to the ground states is found to be 1.2330 a.u./cell with the byproduct of an energy separation of -0.82 eV/atom for atomic Pm between the configurations $[4f^n]5s^2 5p^6 6s^2$ and $[4f^{n-1}]5s^2 5p^6 5d^1 6s^2$. In view of the -0.84eV/atom energy separation found experimentally for the neighbor element Nd and the closeness of the corresponding HF and WB all-electron values of Nd and Pm [184], the latter result seems to be reasonable.

Phase Stabilities of Monoclinic LnBO

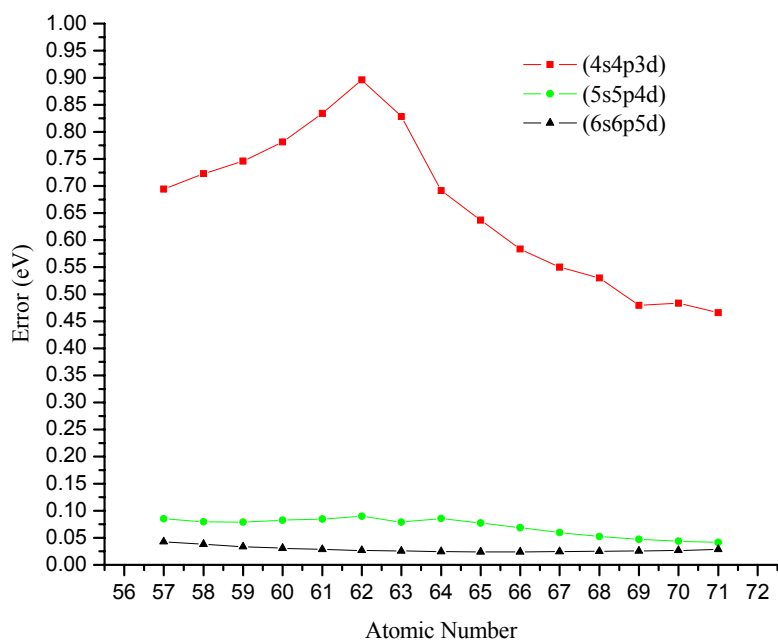


Figure 10-1 The total energy difference between the primitive basis sets result and the HF limit along the lanthanide series for double-charged cations with a $[4f^{n-1}]5s^2 5p^6 5d^1$ valence configuration.

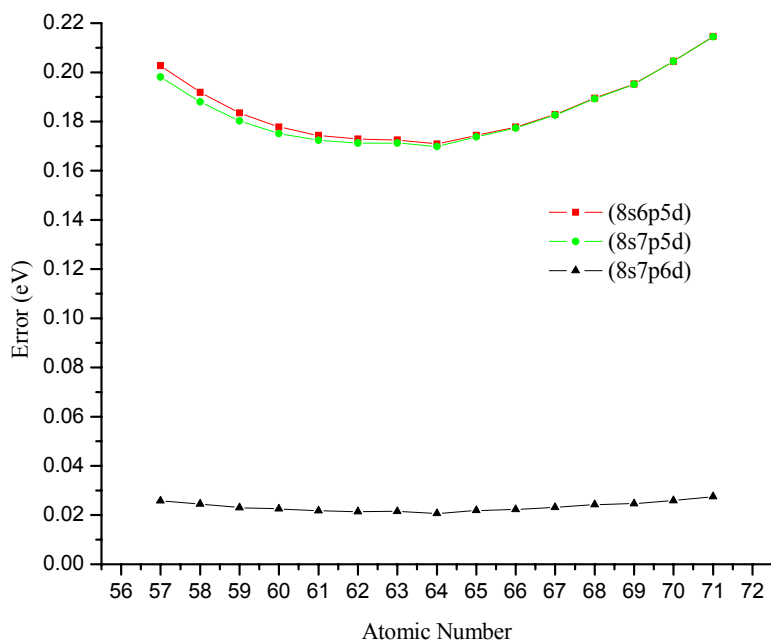


Figure 10-2 The total energy difference between the augmented primitive basis sets result and the HF limit along the lanthanide series for neutral atoms with the $[4f^{n-1}]5s^2 5p^6 5d^1 6s^2$ valence configuration.

Phase Stabilities of Monoclinic LnBO

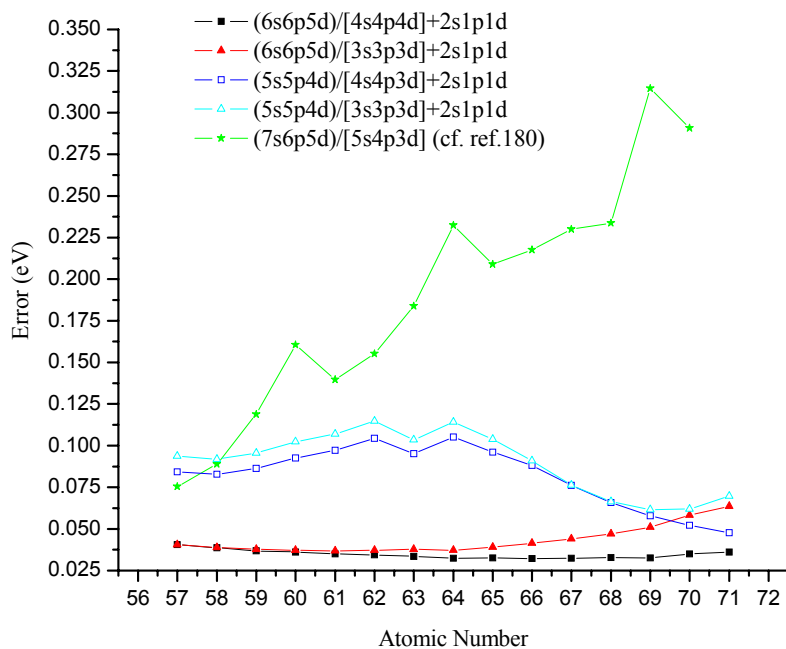


Figure 10-3 The total energy difference between the results of contracted basis sets with the augmentation sets 2s1p1d and the HF limit along the lanthanide series for neutral atoms with the $[4f^{n-1}]5s^25p^65d^16s^2$ valence configuration.

Phase Stabilities of Monoclinic LnBO

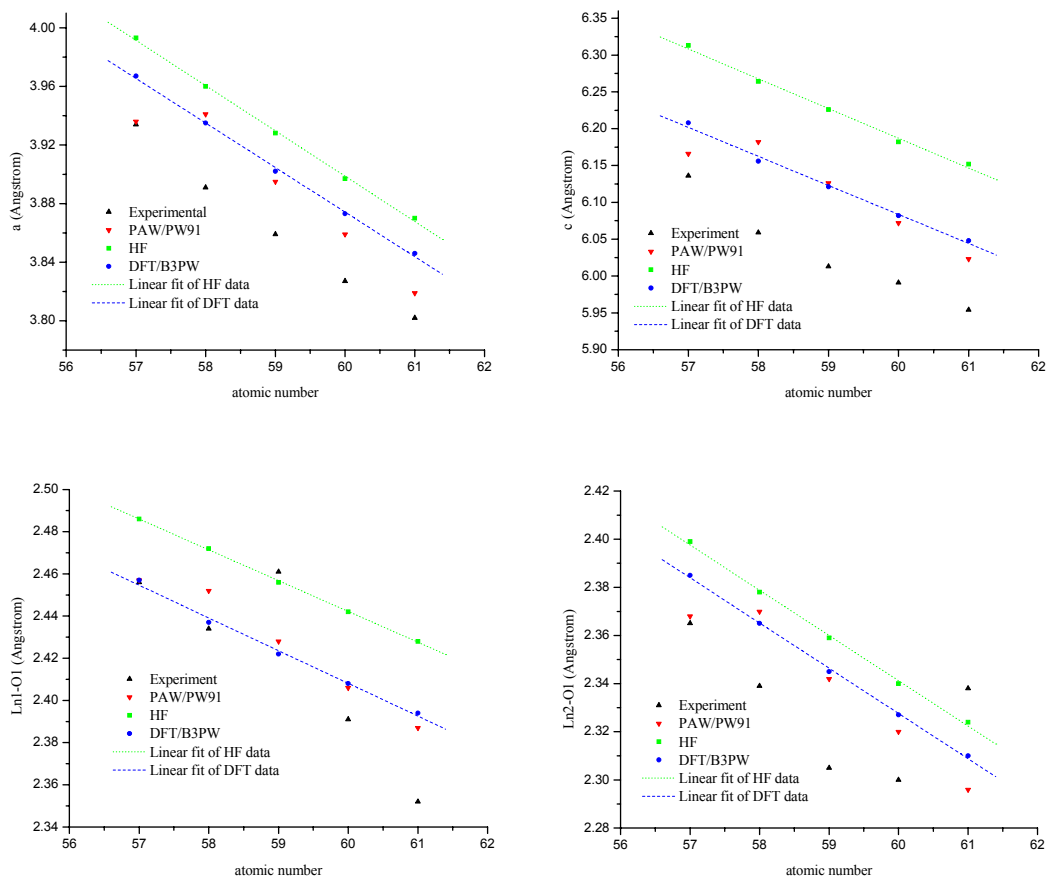


Figure 10-4 The variation of geometrical parameters obtained respectively from experiment, the projector augmented-wave pseudopotential (PAW) method, HF and DFT calculations with respect to atomic numbers of lanthanides from La to Pm. The calculated lattice constants a and c as well as bond lengths Ln1-O1 and Ln2-O1 are linearly fitted by dashed (DFT) and dot (HF) lines, respectively.

Phase Stabilities of Monoclinic LnBO

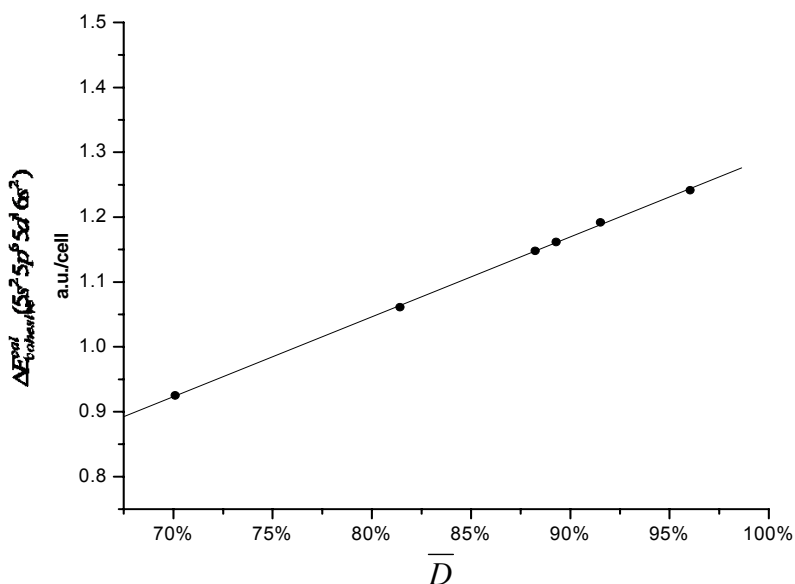


Figure 10-5 The linear correlation between the calculated cohesive energy for the configuration $[4f^{n-1}]5s^2 5p^6 5d^1 6s^2$ of atomic Pm and the average deviation \bar{D} among La_2O_3 through Nd_2O_3 in each scheme. The data is linearly fitted by the equation $\Delta E_{\text{cohesive}}^{\text{cal.}}(5s^2 5p^6 5d^1 6s^2) = 1.23295\bar{D} + 0.05999$, where the slope of 1.23295 a.u./cell stands for the predicted experimental cohesive energy and half of the intercept of 0.0300 a.u./atom stands for the energy correction between the state $[4f^{n-1}]5s^2 5p^6 5d^1 6s^2$ and $[4f^n]5s^2 5p^6 6s^2$ of atomic Pm.

Table 10-1 Mulliken shell populations and atomic charges (Q) on Ln (Ln=La-Pm) in $\text{A-Ln}_2\text{O}_3$ ^a.

	s-shell			p-shell		
	HF	B3LYP	B3PW	HF	B3LYP	B3PW
La_2O_3	2.098	2.136	2.135	6.105	6.129	6.122
Ce_2O_3	2.098	2.140	2.138	6.102	6.128	6.123
Pr_2O_3	2.101	2.144	2.142	6.100	6.129	6.123
Nd_2O_3	2.103	2.146	2.143	6.101	6.130	6.126
Pm_2O_3	2.104	2.149	2.147	6.101	6.131	6.129
	d-shell			Q		
	HF	B3LYP	B3PW	HF	B3LYP	B3PW
La_2O_3	0.641	0.984	1.011	2.156	1.751	1.732
Ce_2O_3	0.644	0.977	1.004	2.157	1.755	1.736
Pr_2O_3	0.636	0.970	0.996	2.164	1.758	1.739
Nd_2O_3	0.629	0.962	0.989	2.169	1.762	1.742
Pm_2O_3	0.619	0.951	0.976	2.176	1.768	1.749

a: A $5s^2 5p^6 5d^1 6s^2$ (ground state/excited state) valence subconfiguration is considered for the lanthanide elements; 0, 1, 2, 3 and 4 electrons in the 4f shell are attributed to the PP core for La, Ce, Pr, Nd and Pm, respectively. The (6s6p5d)/[4s4p4d] valence basis sets were applied for La through Pm elements. For oxygen atoms, the standard 6-311G* all-electron basis set was applied.

Phase Stabilities of Monoclinic LnBO

Table 10-2 Lattice constants a (Å), c (Å), bond lengths Pm1-O1 (Å), Pm2-O1 (Å), bond angles Pm1-O1-Pm2 (degree) and O1-Pm2-O1 (degree) for Pm_2O_3 from HF pseudopotential calculations using valence basis sets (4s4p3d), (5p5s4d) and (6s6p5d) with different contraction schemes ^a.

(4s4p3d)	[2s2p2d]	[3s3p2d]		uncontracted
a	3.852	3.869		3.867
c	6.098	6.148		6.141
Pm1-O1	2.409	2.425		2.424
Pm2-O1	2.313	2.325		2.323
Pm1-O1-Pm2	105.96	106.03		106.05
O1-Pm2-O2	74.04	73.97		73.95
(5s5p4d)	[2s2p2d]	[3s3p3d]	[4s4p3d]	uncontracted
a	3.850	3.871	3.870	3.868
c	6.106	6.157	6.154	6.162
Pm1-O1	2.414	2.427	2.430	2.433
Pm2-O1	2.312	2.325	2.324	2.323
Pm1-O1-Pm2	105.97	106.02	105.97	106.01
O1-Pm2-O2	74.03	73.98	74.03	73.99
(6s6p5d)	[2s2p2d]	[3s3p3d]	[4s4p4d]	uncontracted
a	3.851	3.876	3.870	3.869
c	6.099	6.150	6.152	6.154
Pm1-O1	2.413	2.425	2.428	2.426
Pm2-O1	2.312	2.328	2.324	2.324
Pm1-O1-Pm2	105.95	105.93	105.95	105.96
O1-Pm2-O2	74.05	74.07	74.05	74.04

a: The experimental values are 3.802 Å (a), 5.954 Å (c), 2.352 Å (Pm1-O1), 2.338 Å (Pm2-O1), 110.11 degree (Pm1-O1-Pm2) and 69.89 degree (O1-Pm2-O2) [213].

Phase Stabilities of Monoclinic LnBO

Table 10-3 Lattice constants a (Å), c (Å), bond lengths Ln1-O1 (Å), Ln2-O1 (Å), bond angles Ln1-O1-Ln2 (degree) and O1-Ln2-O1 (degree) for Ln₂O₃ (Ln=La-Pm) from HF pseudopotential calculations using valence basis sets (6s6p5d)/[4s4p4d].

(6s6p5d)/[4s4p4d]		La ₂ O ₃	Ce ₂ O ₃	Pr ₂ O ₃	Nd ₂ O ₃	Pm ₂ O ₃
a	Cal.	3.993	3.960	3.928	3.897	3.870
	PAW. ^a	3.936	3.941	3.895	3.859	3.819
	Exp. ^b	3.934	3.891	3.859	3.827	3.802
c	Cal.	6.313	6.264	6.226	6.189	6.152
	PAW. ^a	6.166	6.182	6.126	6.072	6.023
	Exp. ^b	6.136	6.059	6.013	5.991	5.954
Ln1-O1	Cal.	2.486	2.472	2.456	2.442	2.428
	PAW. ^a	2.457	2.452	2.428	2.406	2.387
	Exp. ^b	2.457	2.434	2.461	2.391	2.352
Ln2-O1	Cal.	2.399	2.378	2.359	2.340	2.324
	PAW. ^a	2.368	2.370	2.342	2.320	2.296
	Exp. ^b	2.365	2.339	2.305	2.300	2.338
Ln1-O1-Ln2	Cal.	106.10	105.99	105.98	105.98	105.95
	PAW. ^a	106.29	106.24	106.24	106.18	106.16
	Exp. ^b	106.20	106.17	104.84	106.08	110.11
O1-Ln2-O2	Cal.	73.90	74.01	74.02	74.02	74.05
	PAW. ^a	73.71	73.76	73.76	73.82	73.84
	Exp. ^b	73.80	73.83	75.16	73.92	74.04

a: The geometry was optimized by Hirosaki et al. [208] performing first-principles calculations based on DFT with PW91 functional using the projector augmented-wave pseudopotential method (PAW), where the localized 4f shell was treated as a core-like shell.

b: The experimental data are cited from the reference [214] for La₂O₃, [215] for Ce₂O₃, [216] for Pr₂O₃, [217] for Nd₂O₃ and [213] for Pm₂O₃.

Phase Stabilities of Monoclinic LnBO

Table 10-4 Lattice constants a (Å), c (Å), bond lengths Pm1-O1 (Å), Pm2-O1 (Å) and bond angles Pm1-O1-Pm2 (degree), O1-Pm2-O1 (degree) for Pm_2O_3 from DFT pseudopotential calculations using valence basis sets (4s4p3d), (5p5s4d) and (6s6p5d) with different contraction schemes. Two calculated geometrical parameters are presented in each box with the first one obtained from B3LYP followed by the second one obtained from B3PW.

(4s4p3d)	[2s2p2d]	[3s3p2d]		uncontracted	Exp. ^a	PAW. ^b
a	3.842	3.864		3.864	3.802	3.819
	3.822	3.844		3.842		
c	6.067	6.136		6.128	5.954	6.023
	5.984	6.052		6.050		
Pm1-O1	2.397	2.418		2.417	2.352	2.387
	2.375	2.394		2.395		
Pm2-O1	2.309	2.324		2.323	2.338	2.296
	2.297	2.311		2.310		
Pm1-O1-Pm2	106.15	106.28		106.20	110.11	106.16
	106.08	106.19		106.18		
O1-Pm2-O2	73.85	73.72		73.80	69.89	73.84
	73.92	73.81		73.82		
(5s5p4d)	[2s2p2d]	[3s3p3d]	[4s4p3d]	uncontracted	Exp. ^a	PAW. ^b
a	3.839	3.869	3.865	3.864	3.802	3.819
	3.820	3.847	3.845	3.844		
c	6.076	6.136	6.138	6.141	5.954	6.023
	5.987	6.050	6.050	6.049		
Pm1-O1	2.399	2.416	2.421	2.423	2.352	2.387
	2.376	2.393	2.397	2.397		
Pm2-O1	2.308	2.326	2.324	2.323	2.338	2.296
	2.296	2.313	2.311	2.310		
Pm1-O1-Pm2	106.20	106.22	106.18	106.19	110.11	106.16
	106.11	106.16	106.11	106.09		
O1-Pm2-O2	73.80	73.78	73.82	73.81	69.89	73.84
	73.89	73.84	73.89	73.91		
(6s6p5d)	[2s2p2d]	[3s3p3d]	[4s4p4d]	uncontracted	Exp. ^a	PAW. ^b
a	3.841	3.869	3.865	3.866	3.802	3.819
	3.822	3.849	3.846	3.844		
c	6.066	6.146	6.148	6.134	5.954	6.023
	5.986	6.054	6.048	6.057		
Pm1-O1	2.397	2.418	2.422	2.418	2.352	2.387
	2.374	2.393	2.394	2.396		
Pm2-O1	2.309	2.326	2.324	2.324	2.338	2.296
	2.297	2.308	2.311	2.310		
Pm1-O1-Pm2	106.16	106.20	106.21	106.15	110.11	106.16
	106.10	106.16	106.06	106.11		
O1-Pm2-O2	73.84	73.80	73.79	73.85	69.89	73.84
	73.90	73.84	73.94	73.89		

a: The experimental values are 3.802 Å (a), 5.954 Å (c), 2.352 Å (Pm1-O1), 2.338 Å (Pm2-O1), 110.11 degree (Pm1-O1-Pm2) and 69.89 degree (O1-Pm2-O2) [213].

b: cf. footnote a in Table 10-3.

Phase Stabilities of Monoclinic LnBO

Table 10-5 Lattice constants a (Å), c (Å), bond lengths Ln1-O1 (Å), Ln2-O1 (Å), bond angles Ln1-O1-Ln2 (degree) and O1-Ln2-O1 (degree) for Ln₂O₃ (Ln=La-Pm) from DFT pseudopotential calculations using valence basis sets (6s6p5d)/[4s4p4d] and the hybrid functional B3PW.

B3PW (6s6p5d)/[4s4p4d]		La ₂ O ₃	Ce ₂ O ₃	Pr ₂ O ₃	Nd ₂ O ₃	Pm ₂ O ₃
a	Cal.	3.967	3.935	3.902	3.873	3.846
	PAW. ^a	3.936	3.941	3.895	3.859	3.819
	Exp. ^b	3.934	3.891	3.859	3.827	3.802
c	Cal.	6.208	6.156	6.121	6.082	6.048
	PAW. ^a	6.166	6.182	6.126	6.072	6.023
	Exp. ^b	6.136	6.059	6.013	5.991	5.954
Ln1-O1	Cal.	2.457	2.437	2.422	2.408	2.394
	PAW. ^a	2.457	2.452	2.428	2.406	2.387
	Exp. ^b	2.457	2.434	2.461	2.391	2.352
Ln2-O1	Cal.	2.385	2.365	2.345	2.327	2.311
	PAW. ^a	2.368	2.370	2.342	2.320	2.296
	Exp. ^b	2.365	2.339	2.305	2.300	2.338
Ln1-O1-Ln2	Cal.	106.16	106.10	106.11	106.10	106.06
	PAW. ^a	106.29	106.24	106.24	106.18	106.16
	Exp. ^b	106.20	106.17	104.84	106.08	110.11
O1-Ln2-O2	Cal.	73.84	73.90	73.89	73.60	73.94
	PAW. ^a	73.71	73.76	73.76	73.82	73.84
	Exp. ^b	73.80	73.83	75.16	73.92	74.04

a: cf. footnote a in Table 10-3.

b: cf. footnote b in Table 10-3.

Table 10-6 Cohesive energy of lanthanide sesquioxides at both HF in combination with the *a posteriori*-HF correlation correction and DFT levels. The comparison with experiment is given in % in brackets. The experimental results for the state $[4f^{n-1}]5s^25p^65d^16s^2$ ($n=1-5$ for La through Pm respectively) were obtained in the way outlined at the end of the section computational methods. The unavailable experimental data for Pm₂O₃ has been substituted by an estimate (cf. text).

(6s6p5d)/[4s4p4d]		La ₂ O ₃	Ce ₂ O ₃	Pr ₂ O ₃	Nd ₂ O ₃	Pm ₂ O ₃
HF (a.u./cell)		0.9048 (69.8%)	0.9114 (70.6%)	0.9154 (73.2%)	0.9195 (75.8%)	0.9250 (75.02%)
	PW-LSD	1.0616 (81.9%)	1.0515 (81.4%)	1.0138 (80.9%)	0.9951 (81.4%)	1.0001 (81.1%)
<i>a posteriori</i> -HF (a.u./cell)	PW-GGA	1.1462 (88.4%)	1.1375 (88.1%)	1.1007 (87.9%)	1.0820 (88.5%)	1.0882 (88.3%)
	P86	1.1508 (89.1%)	1.1592 (89.4%)	1.1142 (88.9%)	1.0955 (89.6%)	1.1017 (89.4%)
	Wigner-Levy	1.2423 (95.8%)	1.2336 (95.5%)	1.2061 (96.3%)	1.1791 (96.5%)	1.1815 (95.8%)
DFT/B3LYP (a.u./cell)		1.1779 (90.9%)	1.1829 (91.6%)	1.1455 (91.4%)	1.1265 (92.2%)	1.1318 (91.8%)
Experiment [218, 216, 217] (a.u./cell)		1.2960 (100%)	1.2914 (100%)	1.2527 (100%)	1.2224 (100%)	1.2330 (100%)

10.2 Phase stabilities of LaBO and GdBO

10.2.1 Computational details

The monoclinic C2 structures of LaBO and GdBO were hypothetically assumed in the way that the Bi cation in BiBO was replaced by La and Gd for LaBO and GdBO, respectively, while the original lattice constants and atomic coordinates of BiBO were retained for LaBO and GdBO. The optimizations of all geometric parameters for LaBO and GdBO were subsequently carried out under the C2 symmetry constraint in the DFT approach for the B3PW hybrid functional. The monoclinic I2/c structures of LaBO and GdBO were taken from the experimental data and fully optimized. The geometry optimizations were performed by using the conjugate gradient code LoptCG [201] modified by us for global optimizations of both lattice constants and atomic coordinates in connection with the package CRYSTAL03. For each displaced lattice constant, the atomic coordinates were relaxed analytically by fulfilling three criteria, i.e., between optimization steps the root mean square (RMS) of energy change, gradient change and displacement change should stay less than 10^{-7} a.u., 0.0003 a.u. and 0.0012 a.u., respectively. The numerical gradients were obtained for lattice constants and the optimization convergence was achieved by meeting the thresholds for the RMS-weighted-norm of 0.001 and maximum-weighted-derivatives of 0.003.

The following tolerances were employed in the evaluation of infinite Coulomb and HF exchange series: 10^{-7} for the Coulomb overlap, HF exchange overlap, Coulomb penetration and the first exchange pseudo-overlap; 10^{-14} for the second exchange pseudo-overlap. The Fock matrix has been diagonalized at 24 **k**-points within the irreducible Brillouin zone corresponding to a shrinking factor of 4 in the Monkhorst net [63]. In order to improve the convergence, a negative energy shift of 1.0 a.u. to the diagonal Fock/KS matrix elements of the occupied orbitals was added to reduce their coupling to the unoccupied set and maintained after the diagonalization. A very accurate extra-large grid consisting of 75 radial points and 974 angular points was employed in the DFT calculations, where Becke grid point weights [120] were chosen.

The basis sets of boron and oxygen atoms were directly taken from BiBO for both LaBO and GdBO in both C2 and I2/c structures. The crystal-orbital-adapted valence basis sets derived in the first section were applied to La and Gd cations in association with the energy-consistent 4f-in-core ECPs of the Stuttgart-Köln variety which leave 11 electrons in the valence configuration of $5s^25p^65d^16s^2$.

We gauge the relative phase stabilities for C2 and I2/c monoclinic phases by the following two means. The first straightforward way is to calculate and compare the enthalpies of C2 and I2/c phases, following the thermodynamics principle, i.e., the lower enthalpy favors the stable structure. To this end, the electronic energies for crystals with fully relaxed atomic positions in isotropically expanded and compressed unit cells along

Phase Stabilities of Monoclinic LnBO

the directions of three fixed lattice constants were calculated and fitted by the Birch-Murnaghan equation [219, 220] (cf. equation (10-12)) with respect to the cell volumes V .

$$E(V) = E_0 + \frac{9}{16} V_0 B_0 \left\{ \left[\left(\frac{V_0}{V} \right)^{\frac{2}{3}} - 1 \right]^3 B_0' + \left[\left(\frac{V_0}{V} \right)^{\frac{2}{3}} - 1 \right]^2 \left[6 - 4 \left(\frac{V_0}{V} \right)^{\frac{2}{3}} \right] \right\} \quad (10-12)$$

where E_0 , V_0 and B_0 refer to the total electronic energy, volume and the bulk modulus at the equilibrium structure, respectively.

The external pressure was calculated according to equation (10-12),

$$P(V) = - \left[\frac{\partial E(V)}{\partial V} \right]_{T=0\text{K}} \quad (10-13)$$

$$= \frac{3}{2} B_0 \left[\left(\frac{V_0}{V} \right)^{\frac{7}{3}} - \left(\frac{V_0}{V} \right)^{\frac{5}{3}} \right] \left\{ 1 + \frac{3}{4} (B_0' - 4) \left[\left(\frac{V_0}{V} \right)^{\frac{2}{3}} - 1 \right] \right\}$$

In our case, the zero-point energy correction was excluded to remain the calculation at the acceptable computational expense. The enthalpy is thereby obtained as:

$$H(V) = E(V) + VP(V) \quad (10-14)$$

The second approach relates the relative structural stability to the chemical bonds. In view of the classic picture of chemistry, a chemically stable compound needs to contain overall more intensive bonding along with overall less antibonding at the equilibrium structure than a chemically less stable compound if no external pressure is applied. The strength of chemical bonds can be measured by COOP in (10-15):

$$O_{\alpha\beta}^G(\varepsilon) = \sum_{u \in \alpha} \sum_{v \in \beta} S_{uv}^G \frac{dP_{uv}^G(\varepsilon)}{d\varepsilon} \quad (10-15)$$

The detailed explanation of (10-15) is available in the section 7.1.1.

10.2.2 Optimized geometric structures

The calculated structural parameters for both C2 and I2/c phases of LaBO and GdBO are given in Table 10-8. For C2 structures, the shrunk lattice constant a as well as expanded lattice constants b and c are observed for LaBO and GdBO compared to those of BiBO. The Ln-O bond lengths stay closer to each other than those of BiBO. The lanthanide contraction effects are found for both C2 and I2/c structures so that the La-O bonds are significantly longer than Gd-O bonds. This also explains the contracted lattice constants of GdBO compared to LaBO with one exception of the lattice constant b in C2 phase.

10.2.3 Electronic structures

The electronic structures are examined by discussing the DOS for C2 and I2/c phases (cf. Figures 10-6, 10-7, 10-8 and 10-9). First of all, both C2 and I2/c phases suggest similar occupied state distributions over the energy level. For example, sharp and strong La s states dominate the energy level at about -39 eV, and Gd s states at about -48 eV. The top of the valence states is contributed by strong O 2p states, weak Ln d states as well as minor O 2s and Ln sp states. The state penetration is found between O 2s and 2p orbitals, which implies that both O 2s and 2p states participate into the orbital interactions with the cations. Second, the split Ln p states shift down the energy level from La to Gd. Consequently the Gd p states have much more significant overlapping with the O 2s states than La p states. The separations of occupied La p states in C2 and I2/c phases are 2.7 eV and 3.1 eV, which are considerably decreased to 0.3 eV and 0.06 eV for Gd p states, respectively. One can imagine that for the heavier lanthanide elements than Gd, their p states would stay below the O 2s energy levels if they are condensed into LnBO crystals.

10.2.4 Energetics and stabilities

The Birch-Murnaghan fittings of the energy points against various ratios of the equilibrium volume to deformed volumes are provided in Figure 10-10 and 10-11. It is clear that at the equilibrium structures with $V_0/V=1.0$, the I2/c phase stands energetically lower than the C2 phase by 0.0198 a.u. (i.e., 12.4 kcal/mol) for LaBO and 0.0099 a.u. (i.e., 6.2 kcal/mol) for GdBO (also cf. Figure 10-7). Therefore, from the energy point of view, LaBO and GdBO seem to preferably crystallize into the I2/c phase rather than the C2 one, which agrees well with the experimental observation that no C2 LnBO phase has yet been confirmed. In the next section, we try to partially explain the reason responsible for such occurrences by manifesting their chemical bonds. The fitted parameters of the Birch-Murnaghan equation (10-12) are given in Table 10-7. The fitted equilibrium volumes and energies differ from the values derived directly from the DFT geometry optimization by only $\sim 0.5 \text{ \AA}^3$, $\sim 0.1 \text{ \AA}^3$, $\sim 0.2 \text{ \AA}^3$ and $\sim 0.1 \text{ \AA}^3$ as well as 6×10^{-5} a.u., 1×10^{-5} a.u., 6×10^{-5} a.u. and 5×10^{-5} a.u. for LaBO (C2, I2/c) and GdBO (C2, I2/c) phases, respectively. The bulk moduli of the realized I2/c phases are over 50% larger than those of hypothetical C2 phases.

Apart from the equilibrium structures, one question remains open to be discussed, i.e., if the application of external pressures favors the stability of C2 phase, or not. The calculated enthalpies corresponding to 0 K are plotted in Figures 10-12 and 10-13 against the various pressures. It is found that the most stable structure for either C2 or I2/c phase takes place at the ambient pressure. The higher pressure would actually further cause the higher instability of the individual structure since the corresponding enthalpy is seen to be increased. On the other hand, it appears in Figures 10-12 and 10-13 that the C2 phases of both LaBO and GdBO are even more instable than I2/c ones at high pressures, and it is highly unlikely to find a converging point at a certain pressure in the enthalpy-pressure

Phase Stabilities of Monoclinic LnBO

curves for C2 and I2/c phases where the former could be viewed to start the transition to the latter phase.

We expect that, due to the similarities of lanthanide elements, the other monoclinic lanthanide borates LnBO (Ln=Ce, Pr, Nd, Sm and Eu) would present the same trend of relative stabilities between C2 and I2/c phases as the cases of LaBO and GdBO, i.e., the monoclinic LnBO would occur with the symmetric I2/c structures rather than the asymmetric C2 ones at the ambient pressure. We have to point out that the current computational investigation on the relative stabilities has not considered any temperature effects, where the thermal vibrations of nuclei may have significant contributions to the crystal stabilities.

10.2.5 Chemical bonds and stabilities

The COOP plots for the Ln-O bonds including the Ln s, p and d orbital contributions in LnBO of C2 and I2/c phases are presented in Figures 10-14, 10-15, 10-16 and 10-17, respectively. In C2 phase, the Ln s-O and Ln p-O bonds form both occupied bonding and antibonding orbitals below the Fermi level. The Ln s-O antibondings are significant at the top of valence states, while the Ln s-O bondings are sharp and weak at the deepest energy level. Both Ln p-O bondings and antibondings are much stronger than Ln s-O counterparts. This is understood as the consequence that, on one hand, Ln 5p orbitals are more spatially extensive than Ln 5s orbitals, and on the other hand, Ln 6s orbitals are left unoccupied in LnBO crystals due to the null Mulliken population at Ln 6s orbitals. The Ln d-O orbital couplings directly result in the occupied Ln d-O bonding orbitals and the corresponding antibonding orbitals are unoccupied. One can further see in Table 10-9 that the Ln d-O bonds are evidently stronger than Ln p-O and Ln s-O bonds, which is in accordance with the fact that the Ln 5d orbitals are more spatially diffuse and thus intend to have more pronounced interactions with the orbitals of oxygen ligands than Ln 5p and Ln 5s orbitals.

The COOP plots for I2/c phases present the tremendously different features from those for C2 phases. First of all, the Ln s-O antibondings are greatly reduced particularly for the parts close to the Fermi level, which almost vanish (cf. Figure 10-15 for LaBO and Figure 10-17 for GdBO). Second, a delicate structural variation of Ln p-O antibondings is found at -12 eV~-15 eV for both LaBO and GdBO. This Ln p-O antibonding COOP becomes almost zero in the I2/c phase (cf. Figure 10-15 for LaBO and Figure 10-17 for GdBO) while a negative peak exists in the C2 phase (cf. Figure 10-14 for LaBO and Figure 10-16 for GdBO). The above two contrasts between the C2 and I2/c indicate the origin of the instabilities of C2 LnBO structures compared to I2/c ones in terms of chemical bonds. One can conclude from Table 10-9 that the I2/c structure is a more favorable phase for LnBO crystals than the C2 structure, since the net Ln-O bonds are intensified from -0.21 (LaBO) and +0.03 (GdBO) in C2 to +0.09 (LaBO) and +0.32 (GdBO) in I2/c due to the greatly reduced overall Ln-O antibonding strengths from -0.81 (LaBO) and -0.65 (GdBO) in C2 to -0.52 and -0.39 in I2/c, although the overall Ln-O

Phase Stabilities of Monoclinic LnBO

bonding strengths seem to remain almost unchanged around +0.61 (LaBO) and +0.70 (GdBO). The weakening of the overall Ln-O antibondings is mainly contributed by the reductions of both Ln s-O and Ln p-O antibondings. The Mulliken population shows that there are 0.7 electrons at the La 5d orbitals. This occupied Ln d-O bonding interaction is particularly important to counteract the considerable unstable Ln s-O and Ln p-O antibonding effects, which in turn stabilizes the I2/c LnBO structure.

We do not discuss the B-O bonds in $[\text{BO}_3]^{3-}$ and $[\text{BO}_4]^{5-}$ units of C2 and I2/c LnBO, since they are similar to what has been pointed out for BiBO crystals.

Conclusively, the LnBO crystals cannot be only viewed as the purely ionic solids, which otherwise cannot explain the relative stabilities of LnBO between C2 and I2/c phases by only the $\text{Ln}^{3+}\text{-O}^{2-}$ electrostatic interactions. The Ln-O covalent bonds are in such a dominant position for LnBO that they bring the significance in determining the structural stability even more remarkable than the $\text{Ln}^{3+}\text{-O}^{2-}$ electrostatic interactions. Nevertheless, as one can find in Table 10-9, the ionicity of I2/c LaBO is much stronger than I2/c GdBO, since the net La-O covalent bond strength is only +0.09 while that of Gd-O is +0.32. This is interpreted as the consequence of the lanthanide contraction effect which leads to the substantially shorter Gd-O distances and more crystal orbital overlapping of I2/c GdBO than I2/c LaBO.

Phase Stabilities of Monoclinic LnBO

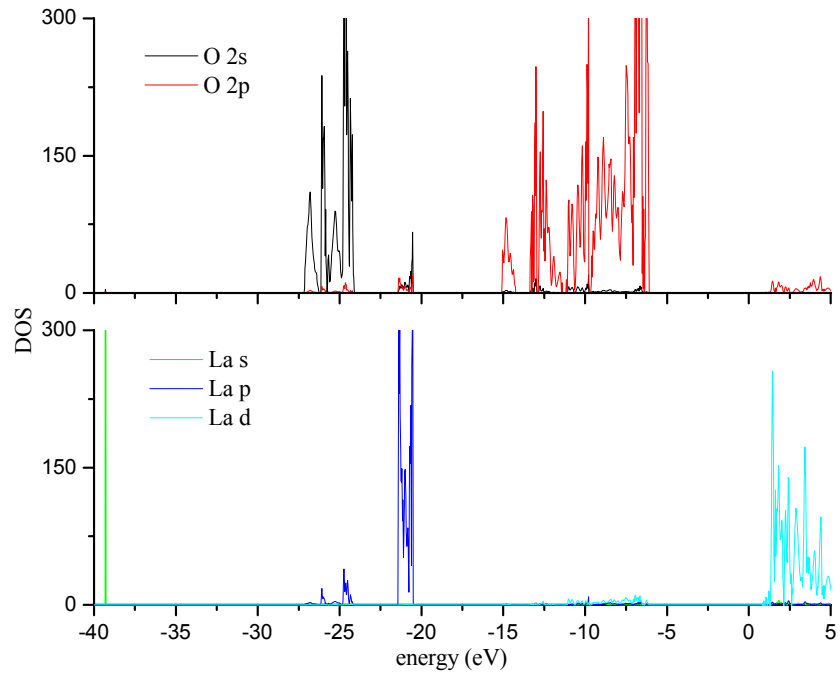


Figure 10-6 The l-momentum projected density of states (DOS) for LaBO C2 phase.

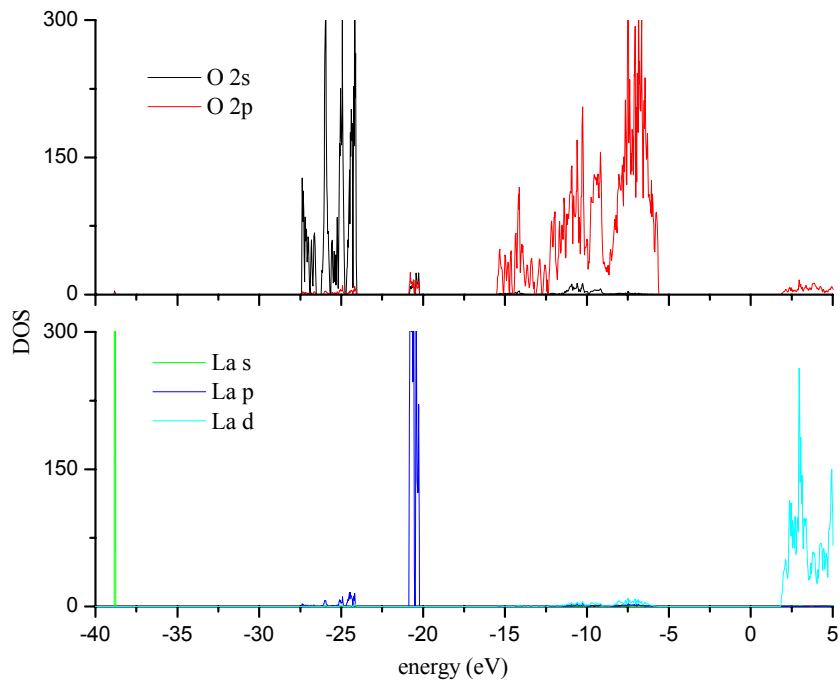


Figure 10-7 The l-momentum projected density of states (DOS) for 12/c LaBO.

Phase Stabilities of Monoclinic LnBO

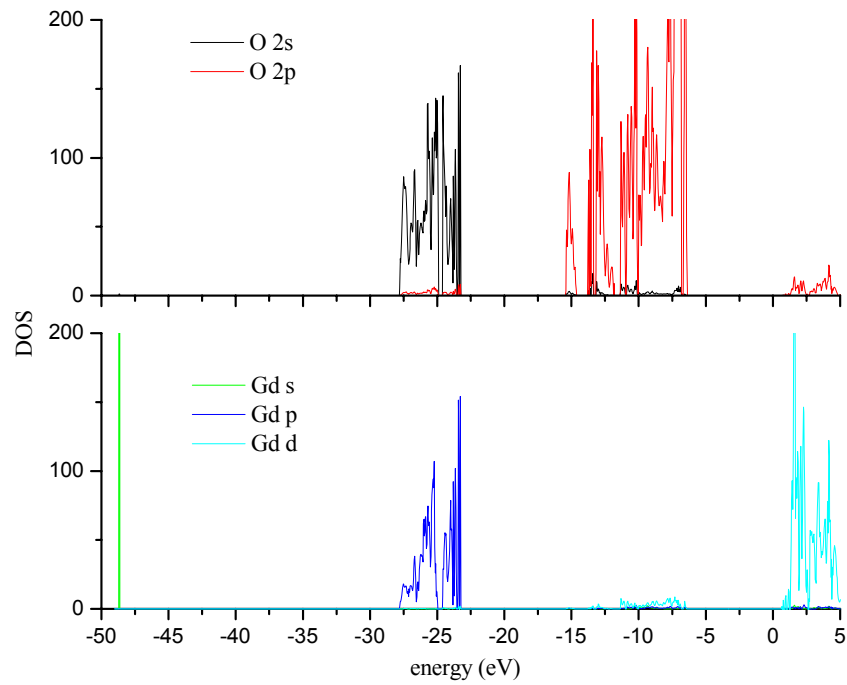


Figure 10-8 The l-momentum projected density of states (DOS) for C2 GdBO.

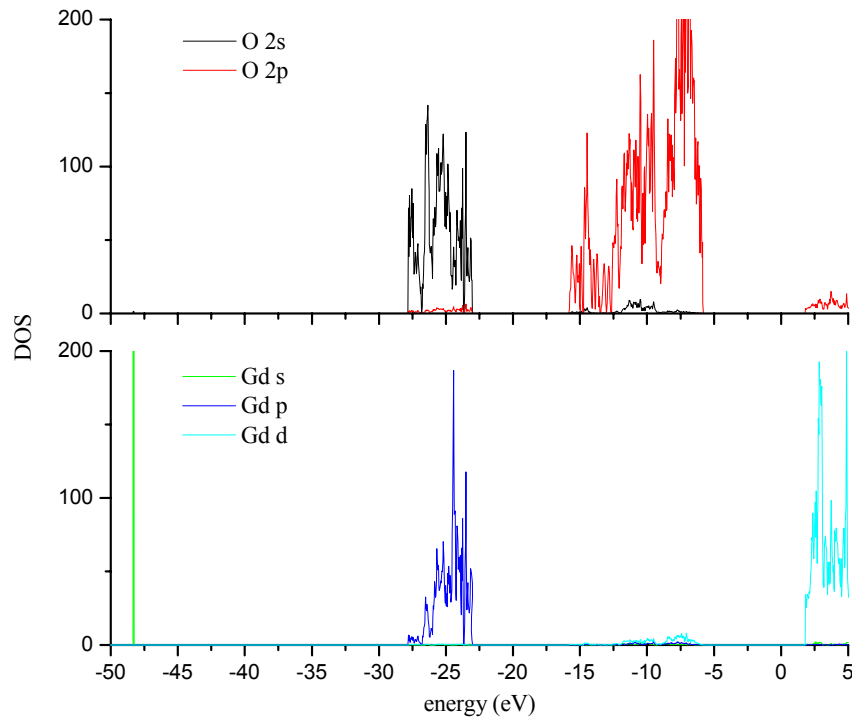


Figure 10-9 The l-momentum projected density of states (DOS) for I2/c GdBO.

Phase Stabilities of Monoclinic LnBO

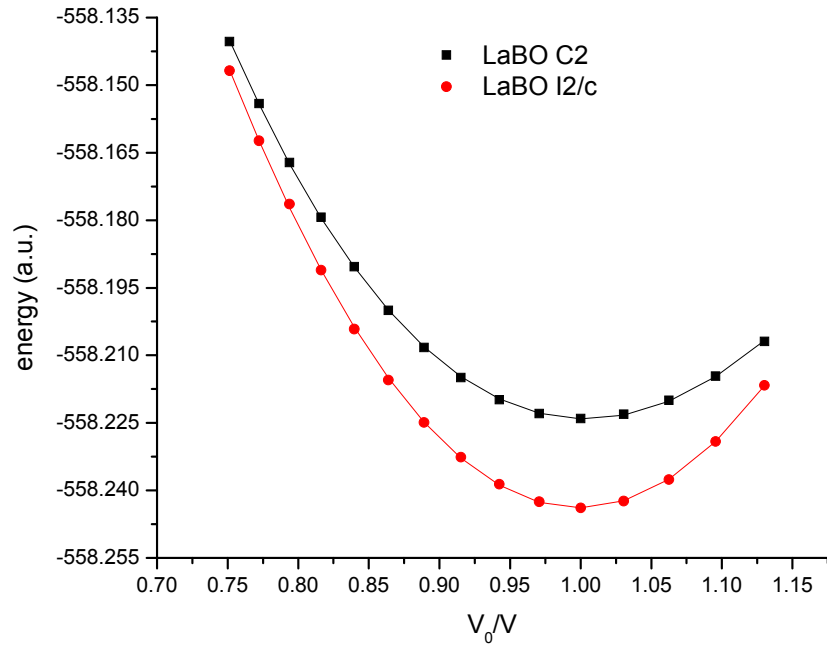


Figure 10-10 The Birch-Murnaghan fitting for the total electronic energies of the LaBO crystal with respect to the volume ratios. V_0 is the volume of a primitive cell at the equilibrium structure.

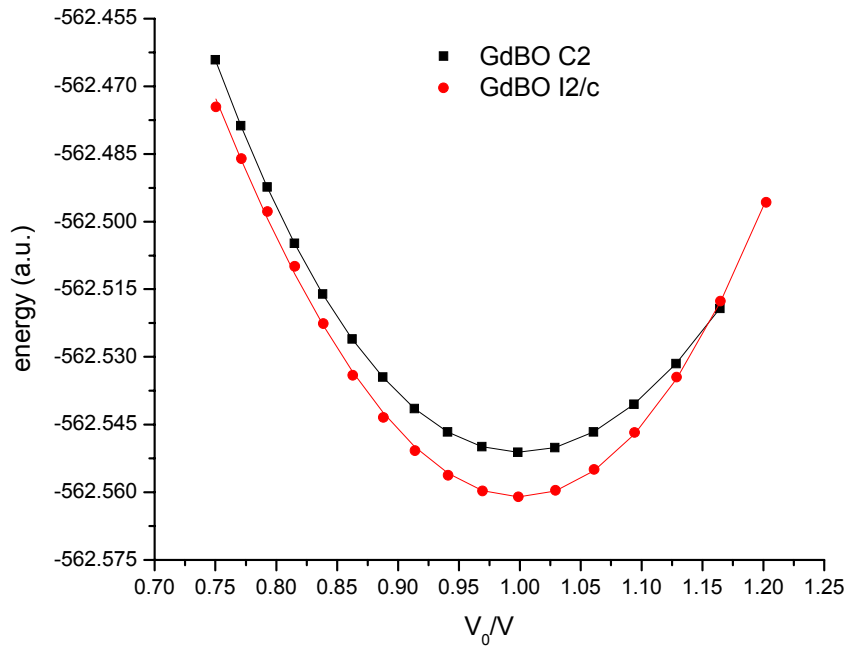


Figure 10-11 The Birch-Murnaghan fitting for the total electronic energies of the GdBO crystal with respect to the volume ratios. V_0 is the volume of a primitive cell at the equilibrium structure.

Phase Stabilities of Monoclinic LnBO

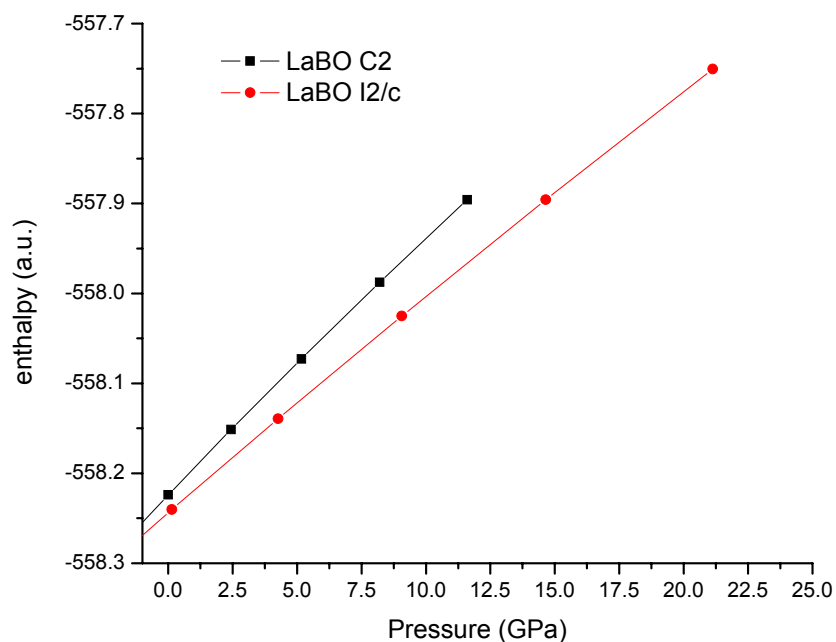


Figure 10-12 The calculated enthalpies against the external pressures derived by the third-order Birch-Murnaghan equation of state for the LaBO crystal.

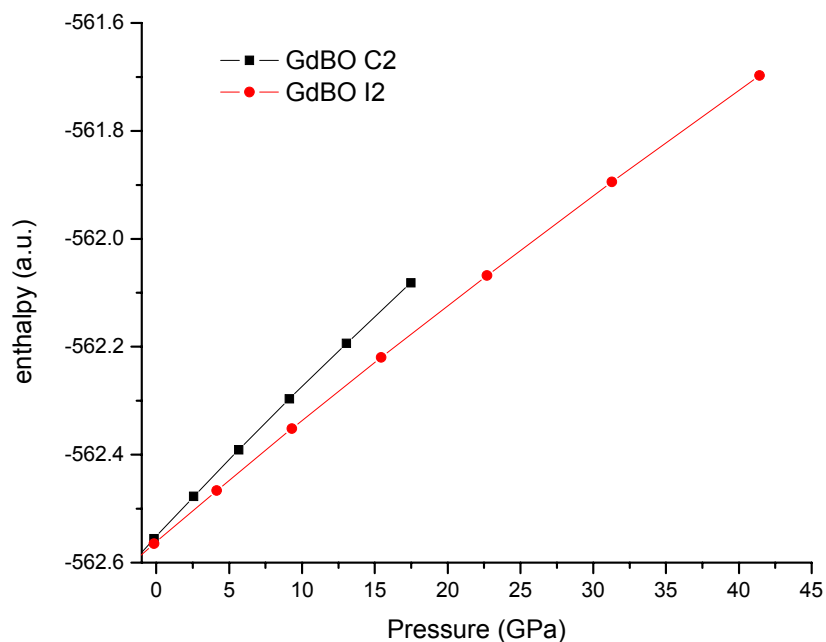


Figure 10-13 The calculated enthalpies against the external pressures derived by the third-order Birch-Murnaghan equation of state for the GdBO crystal.

Phase Stabilities of Monoclinic LnBO

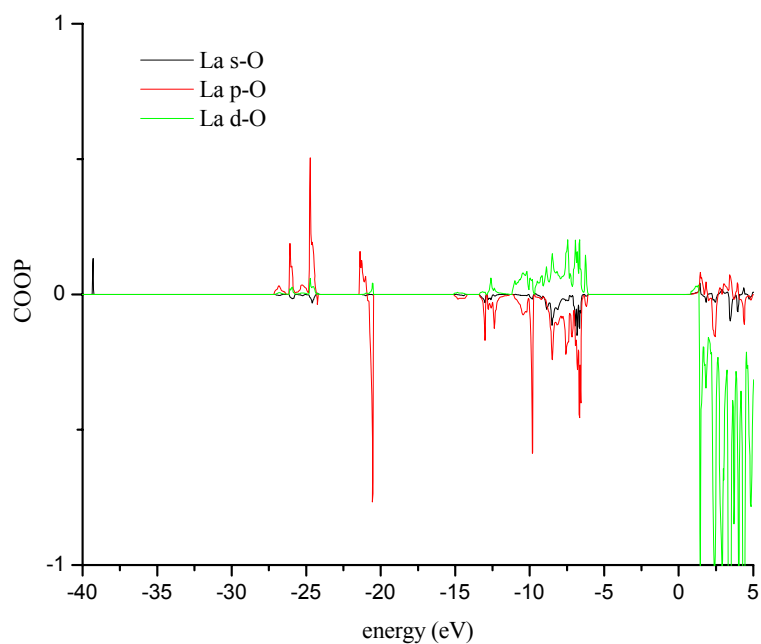


Figure 10-14 The COOP plot of the La-O bonds in C2 LaBO for one La-coordination sphere.

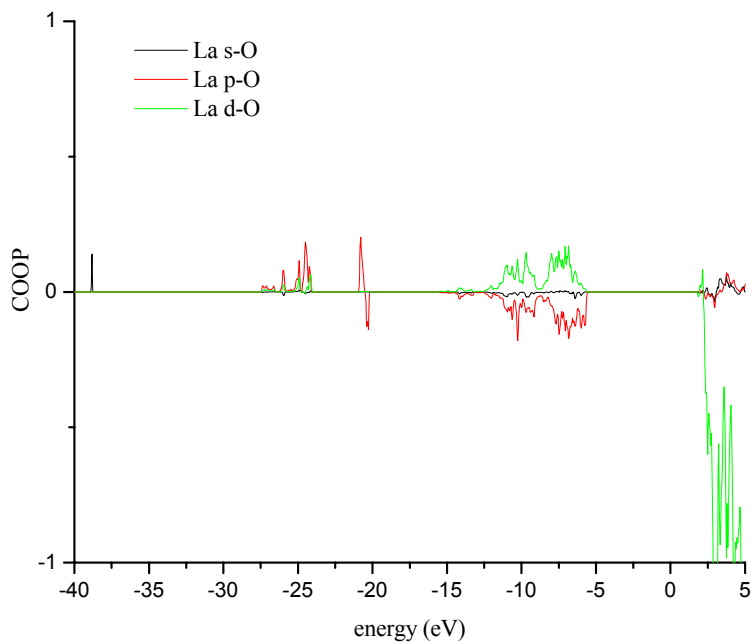


Figure 10-15 The COOP plot of the La-O bonds in I2/c LaBO for one La-coordination sphere.

Phase Stabilities of Monoclinic LnBO

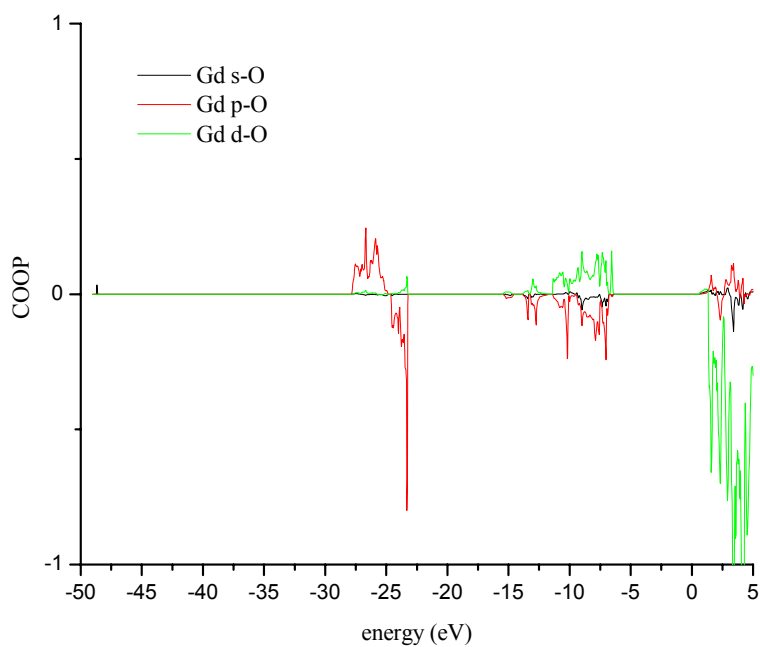


Figure 10-16 The COOP plot of the Gd-O bonds in C2 GdBO for one Gd-coordination sphere.

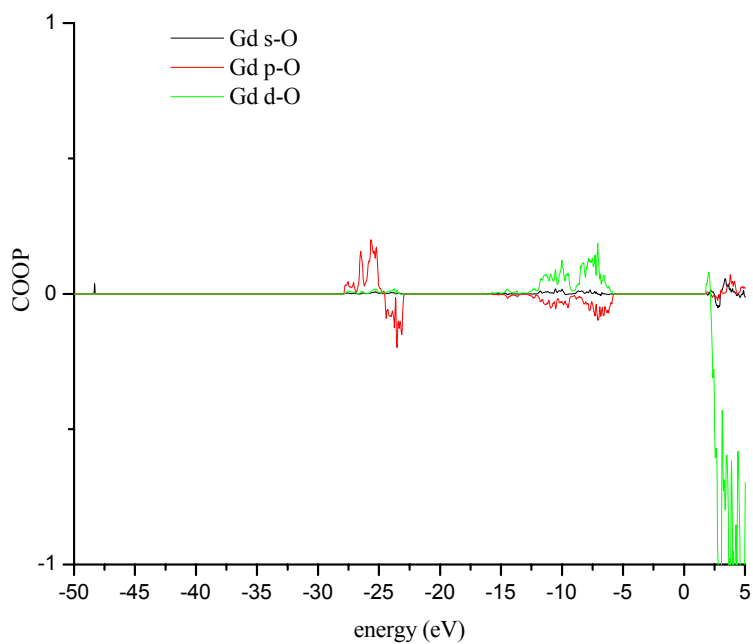


Figure 10-17 The COOP plot of the Gd-O bonds in I2/c GdBO for one Gd-coordination sphere.

Phase Stabilities of Monoclinic LnBO

Table 10-7 The calculated bulk modulus (B_0), its first derivative (B_0'), the equilibrium volume (V_0) and the lowest energy (E_0) in both C2 and I2/c phases for LaB_3O_6 and GdB_3O_6 . The numbers in the brackets denote the values of equilibrium volumes and energies derived from the DFT calculations.

crystals	Parameters	C2	I2/c
LaBO	B_0 (GPa)	76.78	125.95
	B_0'	3.45	4.92
	V_0 (\AA^3)	131.696 (132.133)	108.828 (108.700)
	E_0 (a.u.)	-558.22411 (-558.22405)	-558.24388 (-558.24387)
GdBO	B_0 (GPa)	85.80	130.82
	B_0'	3.85	5.79
	V_0 (\AA^3)	127.262 (127.492)	101.128 (101.257)
	E_0 (a.u.)	-562.55111 (-562.55117)	-562.56105 (-562.56100)

Table 10-8 The comparisons between the experimental and calculated structural parameters for both C2 and I2/c phases of LaBO and GdBO. All the calculated values were derived based on the DFT B3PW results.

C2 phase		Lattice parameters				Ln-O (\AA)			O-Ln-O ($^\circ$)	
		a (\AA)	b (\AA)	c (\AA)	β ($^\circ$)	d_1	d_2	d_3	$\angle 1$	$\angle 2$
LaBO	Cal.	6.530	5.980	6.941	102.81	2.375	2.502	2.483	89.03	159.06
GdBO	Cal.	6.324	6.027	6.803	100.44	2.285	2.350	2.406	92.78	167.96
BiBO	Exp. [31]	7.116	4.993	6.508	105.62	2.086	2.390	2.632	90.58	152.20
I2/c phase		Lattice parameters				Ln-O (\AA)				
		a (\AA)	b (\AA)	c (\AA)	β ($^\circ$)	d_1	d_2	d_3	d_4	d_5
LaBO	Exp. [50]	6.509	8.172	7.983	93.00	2.429	2.563	2.606	2.612	2.846
	Cal.	6.607	8.240	7.999	93.23	2.459	2.560	2.663	2.664	2.874
GdBO	Exp. [54]	6.28	8.02	7.80	93.00	2.282	2.471	2.537	2.638	2.693
	Cal.	6.362	8.106	7.867	93.28	2.358	2.498	2.529	2.549	2.851

$\angle 1$: the O6-Ln-O7 angle (cf. Figure 2)

$\angle 2$: the O4-Ln-O5 angle (cf. Figure 2)

Phase Stabilities of Monoclinic LnBO

Table 10-9 The integral COOP intensities for the strength of Ln-O bonds for one Ln-coordination sphere.

Compounds	Space groups	bonds	bonding	antibonding	net
LaBO	C2	La s-O	+0.01	-0.16	-0.15
		La p-O	+0.18	-0.65	-0.47
		La d-O	+0.41	0.00	+0.41
		overall La-O	+0.60	-0.81	-0.21
	I2/c	La s-O	+0.01	-0.04	-0.03
		La p-O	+0.14	-0.48	-0.34
		La d-O	+0.46	0.00	+0.46
		overall La-O	+0.61	-0.52	+0.09
GdBO	C2	Gd s-O	+0.01	-0.06	-0.05
		Gd p-O	+0.28	-0.59	-0.31
		Gd d-O	+0.40	0.00	+0.40
		overall Gd-O	+0.69	-0.65	+0.04
	I2/c	Gd s-O	+0.04	0.00	+0.04
		Gd p-O	+0.22	-0.39	-0.17
		Gd d-O	+0.45	0.00	+0.45
		overall Gd-O	+0.71	-0.39	+0.32

Chapter 11 Incremental Scheme for Optical Tensors

11.1 Advances of the calculations for crystal NLO coefficients

NLO properties of materials are of exceptional importance in laser science and technology. Obviously, a deep understanding of the mechanism of NLO effects in crystals helps to search for or even design new NLO crystals more efficiently. Several theoretical attempts, including such semi-empirical methods as the bond charge model [221, 222, 223] and the anionic group theory [224, 225] as well as first-principles approaches based on the DFT method [136, 226, 227], have been made to obtain the correlation between NLO responses and microstructures.

The basis assumptions of the bond charge model are: (1) the macroscopic tensor element of the NLO susceptibility of a crystal material is regarded as the appropriate sum of the microscopic tensor element from all constituent chemical bonds; (2) the microscopic tensor element of a single bond can be evaluated with the parameter method of an oscillator model on the basis of the distribution of bond charges. The macroscopic NLO coefficient can be written as:

$$d_{ijk} = \sum_{\mu} \frac{G_{ijk}^{\mu}}{d^{\mu} q^{\mu}} \left(N_b^{\mu} (0.5) \frac{(Z_A^{\mu})^* + n(Z_B^{\mu})^*}{(Z_A^{\mu})^* - n(Z_B^{\mu})^*} f_i^{\mu} (\chi_b^{\mu})^2 + \frac{N_b^{\mu} s(2s-1)(r_0^{\mu})^2}{(r_0^{\mu} - r_c^{\mu})^2} f_c^{\mu} (\chi_b^{\mu})^2 \rho^{\mu} \right) \quad (11-1)$$

where ρ^{μ} is the difference in the atomic size, r_c^{μ} is the core radius, q^{μ} is the bond charge of the μ -th bond, and G_{ijk}^{μ} is the geometrical contribution of chemical bonds of type μ . All of the above parameters can be deduced from the detailed chemical bonding structures of all constituent atoms. This model with the equation (11-1) has been shown to be useful for the NLO effects of A-B type semiconductors with simple σ bonds, however it cannot be extended to other more complex crystals without increasing the number of new parameters with substantial uncertainties. This method has been applied to explain the origin of NLO properties of BiBO [43] with the conclusion that the large NLO tensors arise from the bonds in triangular units $[\text{BO}_3]^{3-}$, a result which obviously completely neglected the remarkable contribution from the $[\text{BiO}_4]^{5-}$ units.

An improved way to connect the microstructure to the bulk NLO effects of material is the anionic group theory, which deals with the microscopic susceptibility of a defined anionic group. The specified anionic group, other than bonds, is considered as the basis structural unit responsible for NLO properties. These assumptions include: (1) the overall NLO coefficient of the crystal is the geometrical superposition of the microscopic susceptibility of the anionic groups, and has nothing to do with the essentially spherical cations; (2) the microscopic susceptibility of the basis anionic group can be calculated from the localized molecular orbitals of this group using molecular first-principles

Incremental Scheme for Optical Tensors

quantum chemistry calculations. For example, the second harmonic generation (SHG) coefficient can be expressed as:

$$\chi_{ijk}^{SHG} = \frac{F}{V} \sum_P N_P \sum_{i'j'k'} \alpha_{i'} \alpha_{j'} \alpha_{kk'} \chi_{i'j'k'}^{(2)}(P) \quad (11-2)$$

where $F = \frac{n^2 + 2}{3}$ is the local field factor, V is the volume of a unit cell, N_P is the number of the P -th groups in this unit cell, and $\alpha_{i'}$, $\alpha_{j'}$, and $\alpha_{kk'}$ are the direction cosines between the macroscopic coordinates of the crystal and the microscopic coordinates for the P -th group. $\chi_{i'j'k'}^{(2)}(P)$ is the microscopic second-order susceptibility of the P -th group, which is available based on the molecular orbital calculation results of this group.

Both the bond charge model and anionic group theory cannot survive those cases where the couplings between bonds or anionic groups are too strong to be neglected, which obviously fails the sum rules for microscopic susceptibilities. The first-principles approach, due to its predictive power and systematic way, has become a more favorable approach to study the NLO properties of materials [225]. The efforts for the first-principles calculations began with the evaluation the SHG coefficients since 1960's [226]. Recently, Chen etc. [136] suggested, based on the previous SHG formalism by Rashkeev etc. [227], the first-principles pseudopotential electronic structure calculation in association with the so-called real-space atom-cutting scheme invented for the quantitative analysis of the individual contributions of the cation and anionic groups to various optical properties. The SHG coefficient is expressed as:

$$\chi_{ijk} = \chi_{ijk}(VE) + \chi_{ijk}(VH) + \chi_{ijk}(two\ bands) \quad (11-3)$$

where $\chi_{ijk}(VE)$ and $\chi_{ijk}(VH)$ denote the contributions from virtual-electron processes and virtual-hole processes, respectively, and $\chi_{ijk}(two\ bands)$ denotes the contribution from two-band processes. They are in turn calculated by:

$$\chi_{ijk}(VE) = \frac{e^3}{8\pi^3 \hbar^2 m^3} \sum_{vc'} \int P(ijk) \text{Im}[p_i^{vc} p_j^{cc'} p_k^{c'v}] \left(\frac{1}{\omega_{cv}^3 \omega_{vc'}^2} + \frac{2}{\omega_{vc}^4 \omega_{c'v}} \right) d\mathbf{k} \quad (11-4)$$

$$\chi_{ijk}(VH) = \frac{e^3}{8\pi^3 \hbar^2 m^3} \sum_{vv'} \int P(ijk) \text{Im}[p_i^{vv'} p_j^{v'c} p_k^{cv}] \left(\frac{1}{\omega_{cv}^3 \omega_{v'c}^2} + \frac{2}{\omega_{vc}^4 \omega_{cv'}} \right) d\mathbf{k} \quad (11-5)$$

$$\chi_{ijk}(two\ bands) = \frac{e^3}{4\pi^3 \hbar^2 m^3} \sum_{vc} \int P(ijk) \frac{\text{Im}[p_i^{vc} p_j^{cv} (p_k^{vv} - p_k^{cc})]}{\omega_{vc}^5} d\mathbf{k} \quad (11-6)$$

where v and v' indicate the valence bands, and c and c' indicate the conduction bands. $P(ijk)$ invokes the full permutation of the Cartesian components i, j, k according to the Kleinman symmetry of the SHG coefficients. The band energy difference and momentum matrix elements are denoted as $\hbar\omega_{\alpha\beta}$ and $p_i^{\alpha\beta}$ for the band α and β .

Incremental Scheme for Optical Tensors

However, reliable predictions of optical properties require adequate basis sets and electronic correlations within the first-principles approach. The correlation effects are usually accounted for by DFT, particularly LDA and GGA schemes for plane-waves, for large and periodic systems. It is well known that in most cases, LDA and GGA usually greatly underestimate the band gap and therefore lead to significantly overestimated optical coefficients, whereas a systematic improvement over DFT band structures is however not available so far.

The direct implementation of some highly correlating methods such as CI (configuration interaction) and CC (coupled cluster) to achieve accurate crystal band structures is by no means effortless, and these wavefunction-based correlation methods are only feasible for atomic and molecular systems. However, thanks to the recent development of the so-called incremental scheme [111, 112, 113], the indirect calculation of correlation energies for large and periodic systems has been made possible by using wavefunction-based correlation methods. The detailed introduction of this method can be found in Chapter 2.7. Generally, the incremental scheme expands the correlation energy into the many-body series with finite (molecules) or infinite (crystals) number of increments and in principle accomplishes no additional approximations if this series is completed. The entire system is thus divided into several domains which can be individually calculated at a low computational cost by using wavefunction-based correlation approaches like CCSD (coupled cluster single and double excitations). The incremental scheme has been successfully applied to derive the cohesive properties (e.g., lattice constant, cohesive energy, bulk modulus) of various periodic compounds including Van der Waals systems (e.g., rare-gas, hydrogen-bond system), ionic systems (e.g., LiF, MgO), covalent systems (e.g., group-III, V, IV cubic semiconductors) and even the delocalized systems (e.g., Li_8 , C_{60} , Hg) with strong correlations [3, 228]. However, to our best knowledge, the incremental scheme has not yet been applied to evaluate non-cohesive properties.

In this thesis, we further extend the incremental scheme beyond the ground state correlation energy to the optical properties. The idea behind this method is that macroscopic optical properties of a bulk crystal can be calculated as the explicit sum of the respective microscopic increments of domains which, in our case, are the localized bond orbitals. This method is in principle exact within the single-reference wavefunction approach, which is evidently different from the approximated microscopic sum in the semi-empirical bond charge model and anionic group theory. In the following part, we present our formalism and a test calculation of polarizabilities and hyperpolarizabilities carried out for a model system $\text{Ga}_4\text{As}_4\text{H}_{18}$.

11.2 Exact incremental expansion of optical tensors

We begin with the Taylor expansion of the i -th component vector of dipole moment P_i in terms of the external perturbative electric field \mathbf{F} :

Incremental Scheme for Optical Tensors

$$\begin{aligned}
 P_i &= P_i^0 + \sum_j^3 \left[\frac{\partial P_i}{\partial F_j} \right]_0 F_j + \frac{1}{2!} \sum_{jk}^3 \left[\frac{\partial^2 P_i}{\partial F_j \partial F_k} \right]_0 F_j F_k \\
 &+ \frac{1}{3!} \sum_{jkl}^3 \left[\frac{\partial^3 P_i}{\partial F_j \partial F_k \partial F_l} \right]_0 F_j F_k F_l + \dots
 \end{aligned} \tag{11-7}$$

where i, j and k denote the Cartesian components of the field, and P_i^0 is the initial dipole moment free of the electric field. The total energy of the system perturbed by the field \mathbf{F} can also be expressed as the Taylor series:

$$\begin{aligned}
 E &= E_0 + \sum_i^3 \left[\frac{\partial E}{\partial F_i} \right]_0 F_i + \frac{1}{2!} \sum_{ij}^3 \left[\frac{\partial^2 E}{\partial F_i \partial F_j} \right]_0 F_i F_j \\
 &+ \frac{1}{3!} \sum_{ijk}^3 \left[\frac{\partial^3 E}{\partial F_i \partial F_j \partial F_k} \right]_0 F_i F_j F_k + \dots
 \end{aligned} \tag{11-8}$$

where E_0 is the total energy free of the electric field.

Due to the external field, the energy gain ΔE reads:

$$\begin{aligned}
 \Delta E &= -\mathbf{P} \cdot \mathbf{F} = -P_i F_i - P_j F_j - P_k F_k \\
 &= -\sum_i^3 P_i^0 F_i - \frac{1}{2!} \sum_{ij}^3 \left[\frac{\partial P_i}{\partial F_j} \right]_0 F_i F_j \\
 &\quad - \frac{1}{3!} \sum_{ijk}^3 \left[\frac{\partial^2 P_i}{\partial F_j \partial F_k} \right]_0 F_i F_j F_k - \dots
 \end{aligned} \tag{11-9}$$

On the other hand, the energy difference is available due to (11-8):

$$\begin{aligned}
 \Delta E &= E - E^0 \\
 &= \sum_i^3 \left[\frac{\partial E}{\partial F_i} \right]_0 F_i + \frac{1}{2!} \sum_{ij}^3 \left[\frac{\partial^2 E}{\partial F_i \partial F_j} \right]_0 F_i F_j \\
 &\quad + \frac{1}{3!} \sum_{ijk}^3 \left[\frac{\partial^3 E}{\partial F_i \partial F_j \partial F_k} \right]_0 F_i F_j F_k + \dots
 \end{aligned} \tag{11-10}$$

Comparing the equation (11-9) and (11-10), one finds the following equalities for any arbitrary field:

$$\begin{aligned}
 P_i^0 &= -\left[\frac{\partial E}{\partial F_i} \right]_0 \\
 \left[\frac{\partial P_i}{\partial F_j} \right]_0 &= -\left[\frac{\partial^2 E}{\partial F_i \partial F_j} \right]_0 \\
 \left[\frac{\partial^2 P_i}{\partial F_j \partial F_k} \right]_0 &= -\left[\frac{\partial^3 E}{\partial F_i \partial F_j \partial F_k} \right]_0 \\
 &\dots
 \end{aligned} \tag{11-11}$$

Incremental Scheme for Optical Tensors

A macroscopic vector, called polarization $\tilde{\mathbf{P}}$ of a material, is defined in the way that each of its Cartesian components \tilde{P}_i comes as the difference between the perturbed and unperturbed dipole moments per unit cell volume, and can be expressed as the power series in the external electric field:

$$\begin{aligned}\tilde{P}_i &= \frac{P_i - P_i^0}{V} \\ &= \sum_j \chi_{ij}^{(1)} F_j + \frac{1}{2!} \sum_{jk} \chi_{ijk}^{(2)} F_j F_k + \frac{1}{3!} \sum_{jkl} \chi_{ijkl}^{(3)} F_j F_k F_l + \dots\end{aligned}\quad (11-12)$$

where $\chi_{ij}^{(1)}$ is known as the first-order macroscopic optical susceptibility, or equivalently the linear-optical susceptibility; $\chi_{ijk}^{(2)}$ and $\chi_{ijkl}^{(3)}$ are second-order and third-order macroscopic optical susceptibility, or equivalently the first-order and second-order nonlinear-optical susceptibility.

Comparing (11-12) with (11-7) and applying (11-11), we come to:

$$\begin{aligned}\chi_{ij}^{(1)} &= -\frac{1}{V} \left[\frac{\partial^2 E}{\partial F_i \partial F_j} \right]_0 \\ \chi_{ijk}^{(2)} &= -\frac{1}{V} \left[\frac{\partial^3 E}{\partial F_i \partial F_j \partial F_k} \right]_0 \\ \chi_{ijkl}^{(3)} &= -\frac{1}{V} \left[\frac{\partial^4 E}{\partial F_i \partial F_j \partial F_k \partial F_l} \right]_0 \\ &\vdots\end{aligned}\quad (11-13)$$

The total energy is the total contribution from HF and correlation energies:

$$E = E_{HF} + E_{corr} \quad (11-14)$$

The equation (11-13) is accordingly simplified as:

$$\begin{aligned}\chi_{ij}^{(1)} &= \chi_{ij, HF}^{(1)} + \chi_{ij, corr}^{(1)} \\ \chi_{ijk}^{(2)} &= \chi_{ijk, HF}^{(2)} + \chi_{ijk, corr}^{(2)} \\ \chi_{ijkl}^{(3)} &= \chi_{ijkl, HF}^{(3)} + \chi_{ijkl, corr}^{(3)} \\ &\vdots\end{aligned}\quad (11-15)$$

where the correlation contributions for optical tensors are thereby obtained in the incremental many-body expansions:

Incremental Scheme for Optical Tensors

$$\begin{aligned}
\chi_{ij,corr}^{(1)} &= \sum_m \chi_{ij,m}^{(1)} + \sum_{m<n} \Delta\chi_{ij,mn}^{(1)} + \sum_{m<n<o} \Delta\chi_{ij,mno}^{(1)} + \dots \\
\chi_{ijk,corr}^{(2)} &= \sum_m \chi_{ijk,m}^{(2)} + \sum_{m<n} \Delta\chi_{ijk,mn}^{(2)} + \sum_{m<n<o} \Delta\chi_{ijk,mno}^{(2)} + \dots \\
\chi_{ijkl,corr}^{(3)} &= \sum_m \chi_{ijkl,m}^{(3)} + \sum_{m<n} \Delta\chi_{ijkl,mn}^{(3)} + \sum_{m<n<o} \Delta\chi_{ijkl,mno}^{(3)} + \dots \\
&\vdots
\end{aligned} \tag{11-16}$$

where for the N -th order susceptibility $\chi_{ijk\dots,corr}^{(N)}$, each increment can be in turn calculated by:

$$\begin{aligned}
\Delta\chi_{ijk\dots,mn}^{(N)} &= \chi_{ijk\dots,mn}^{(N)} - \chi_{ijk\dots,m}^{(N)} - \chi_{ijk\dots,n}^{(N)} \\
\Delta\chi_{ijk\dots,mno}^{(N)} &= \chi_{ijk\dots,mno}^{(N)} - \Delta\chi_{ijk\dots,mn}^{(N)} - \Delta\chi_{ijk\dots,no}^{(N)} - \Delta\chi_{ijk\dots,om}^{(N)} - \chi_{ijk\dots,m}^{(N)} - \chi_{ijk\dots,n}^{(N)} - \chi_{ijk\dots,o}^{(N)} \\
\Delta\chi_{ijk\dots,mnop}^{(N)} &= \chi_{ijk\dots,mnop}^{(N)} - \Delta\chi_{ijk\dots,mno}^{(N)} - \Delta\chi_{ijk\dots,nop}^{(N)} - \Delta\chi_{ijk\dots,opm}^{(N)} - \Delta\chi_{ijk\dots,pmn}^{(N)} \\
&\quad - \Delta\chi_{ijk\dots,mn}^{(N)} - \Delta\chi_{ijk\dots,no}^{(N)} - \Delta\chi_{ijk\dots,op}^{(N)} - \Delta\chi_{ijk\dots,pm}^{(N)} - \Delta\chi_{ijk\dots,mo}^{(N)} - \Delta\chi_{ijk\dots,np}^{(N)} \\
&\quad - \chi_{ijk\dots,m}^{(N)} - \chi_{ijk\dots,n}^{(N)} - \chi_{ijk\dots,o}^{(N)} - \chi_{ijk\dots,p}^{(N)} \\
&\vdots
\end{aligned} \tag{11-17}$$

The one-body increment tensor $\chi_{ijk\dots,m}^{(N)}$ is calculated by allowing the orbital excitation within each local domain m but entirely freezing others at the correlation level; the two-body increment tensor $\Delta\chi_{ijk\dots,mn}^{(N)}$ can be understood as the correction to the one-body increment tensor due to the two-body coupling effect between the local domain m and n ; the three-body increment tensor $\Delta\chi_{ijk\dots,mno}^{(N)}$ is essentially the correction due to the three-body coupling effect among the local domain m , n and o . This interpretation can be generalized for higher-order increment tensors. By taking into account all corrections for the entire coupling effects, the sum rule in (11-16) gives the exact value of optical tensors with no approximations made for the incremental expansion within the first-principles approach. The semi-empirical methods, i.e., bond-charge model in (11-1) and anionic group theory in (11-2), actually correspond to the first-order sum of only one-body increments, whereas the interactions between different bonds or anionic groups are totally ignored.

Generally, the number of terms which need to be evaluated for a system with a number of D local domains is:

$$C_D^1 + C_D^2 + C_D^3 + \dots + C_D^D = 2^D - 1 \tag{11-18}$$

For a periodic compound, D goes to infinity and the incremental expansion becomes an infinite series. That is to say, although the incremental series (11-16) offers us the explicitly exact result of optical tensors, the complete inclusion of the coupling effects among all local domains is only possible for small finite systems. Two approximations are introduced in order to make the expansion (11-16) for optical tensors work practically. First of all, this series has to be truncated at a certain expansion order; second, the

Incremental Scheme for Optical Tensors

sum $\sum_{m < n < \dots}$ is carried out only for the nearby local domains so that the coupling effect for those local domains which are spatially distant to each other can be neglected. The above approximations have been already shown to ensure the fast convergence of this series for correlation energies of various systems [3, 228] by using the localized-orbital-centered domains. In this thesis, we examine the behavior of the two approximations for the calculation of optical first- and second-order susceptibilities and how the accuracy can be controlled by the series truncation.

Although the finite-field approach has been used to derive the incremental expansions of optical tensors, the equations (11-15) and (11-16) are generally held beyond the finite-field approach and therefore other analytical methods (e.g., linear- and non-linear response function, time-dependent perturbation treatment, second-order polarization propagator approximation or random phase approximation) can all be applied to calculate the increments of optical properties.

11.3 Tentative application for Ga₄As₄H₁₈ model system

In this section, the above formalism is applied to the Ga₄As₄H₁₈ model system. At the present stage, we are not aiming at seeking the accurate solutions of optical tensors for crystals. Rather, we explore this simple system to demonstrate how the convergence of the incremental expansion can be achieved by truncating the series, and what problems we have to handle for the calculation of optical tensors within this approach. On the other hand, this entire simple system can be easily handled at the CCSD correlation level, which can be used to gauge the accuracy of incremental expansion.

Ga₄As₄H₁₈ is truncated from the cubic GaAs crystal with the hydrogen atoms to saturate the dangling bonds. The calculation is performed at the CCSD correlation level. The ECP-28MWB [122] is applied to both Ga with 4s²4p¹ valence configuration and As with 4s²4p³ valence configuration in association with (4s4p)/[2s2p] basis sets augmented with the d-orbitals exponents of 0.1867 for Ga and 0.2851 for As, respectively. The library 6-31G basis set [123] is used for hydrogen atoms. We have noted that the size of these basis sets is too small to sufficiently restore the correlation effect for the optical susceptibilities, which does not, however, concern our goal in this thesis.

We have defined two types of local domain spaces, i.e., the space A with five local domains (cf. Figure 11-1) and the space B with seven local domains (cf. Figure 11-2). The five local domains in space A are all As-H bonds label as *a*, all Ga-H bonds label as *e*, all side As-Ga1 bonds labeled as *b*, one central Ga1-As5 bond labeled as *c* and all side Ga-As5 bonds labeled as *d*. The seven local domains in space B are those seven individual Ga-As bond orbitals labeled from *a* to *g* and all orbitals of hydrogen-bonds are frozen.

These calculated results are listed in Tables 11-1 and 11-2. It can be seen that, for either A or B, the linear susceptibilities achieve much faster convergence against the expansion order than the nonlinear ones. For example, in the domain space A, at the 2-body

Incremental Scheme for Optical Tensors

increment correction, the deviation for the linear susceptibilities is within 2% compared to the CCSD value, whereas that for the nonlinear susceptibilities stays about 10%. At the 3-body increment correction, the deviation for the linear susceptibilities further drops to less than 0.6%, whereas the maximum deviation of almost 11% takes place to the nonlinear χ_{yyy} . At the 4-body increment correction, the linear susceptibilities deviate from the CCSD value within 0.05%, and the nonlinear ones also differ from the CCSD value below 1%.

The second feature is that the convergence behavior of these numbers depends on how the domain space is defined. In this case, it seems that the space A is more appropriate to obtain faster convergence of optical tensors, particular of the nonlinear susceptibilities, with respect to the expansion order than the space B, as one can compare between Figures 11-3 and 11-4. Strong oscillatory structures are found for the nonlinear susceptibilities especially the χ_{yyy} component in the domain space B (cf. Figure 11-4). In the domain space A, the tensors χ_{xxx} , χ_{xyy} and χ_{yyy} are restored within 10% at the 3-body increment correction, while in the domain space B, one need to go to the 5-body incremental correction for χ_{xxx} and χ_{xyy} , and even the 6-body for χ_{yyy} . This unpleasing result done in the domain space B implies that these individual bonds indeed undergo strong couplings with each other which slows down the convergence of the series. It is also interesting to see that the correlation energy converges within 1% at the incremental corrections of 2-body (cf. Table 11-1) for the domain space A and 3-body (cf. Table 11-2) for the domain space B, respectively. From this point of view, the problem seems much more severe in terms of how to define suitable domains for the evaluation of optical tensors, especially for the nonlinear components, than the correlation energy, since these susceptibilities are basically the quantities of energy derivatives. Just as Lin has commented in his paper [224], “... *the second-order susceptibility of most NLO crystals arises from basic structural units with delocalized regions of valence electron orbitals belonging to more than two atoms, rather than from regions localized around two atoms connected by a simple σ -type bond.*”, these “basic structural units” need to be grouped into the local domain so that although these susceptibilities are nonlocal within these “basic structural units”, they can be still regarded as fairly good local quantities that the contribution of the coupling between these domains is small.

Incremental Scheme for Optical Tensors

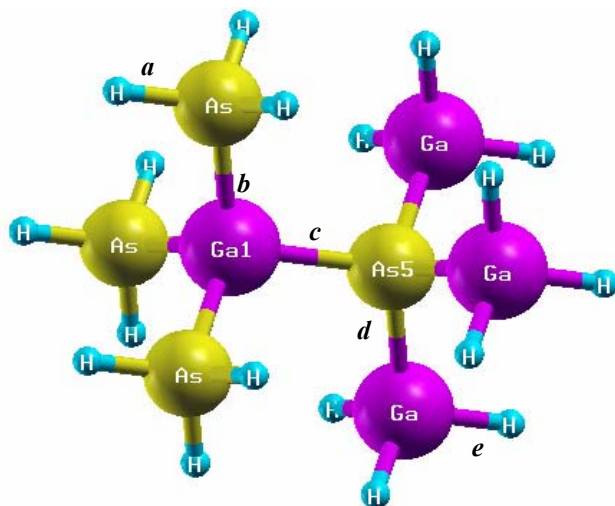


Figure 11-1 The structure of Ga₄As₄H₁₈ with the domain space A.

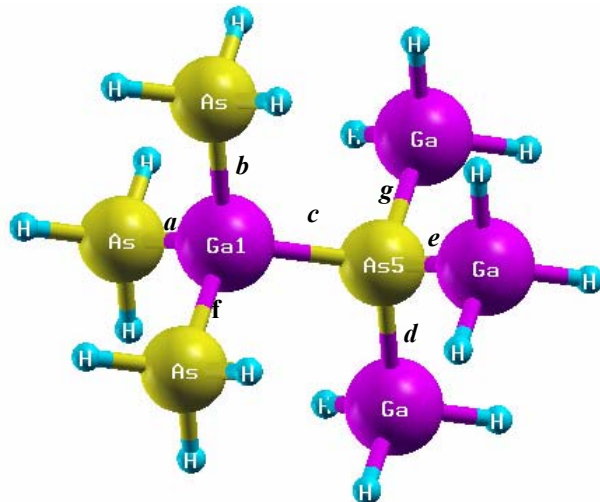


Figure 11-2 The structure of Ga₄As₄H₁₈ with the domain space B.

Incremental Scheme for Optical Tensors

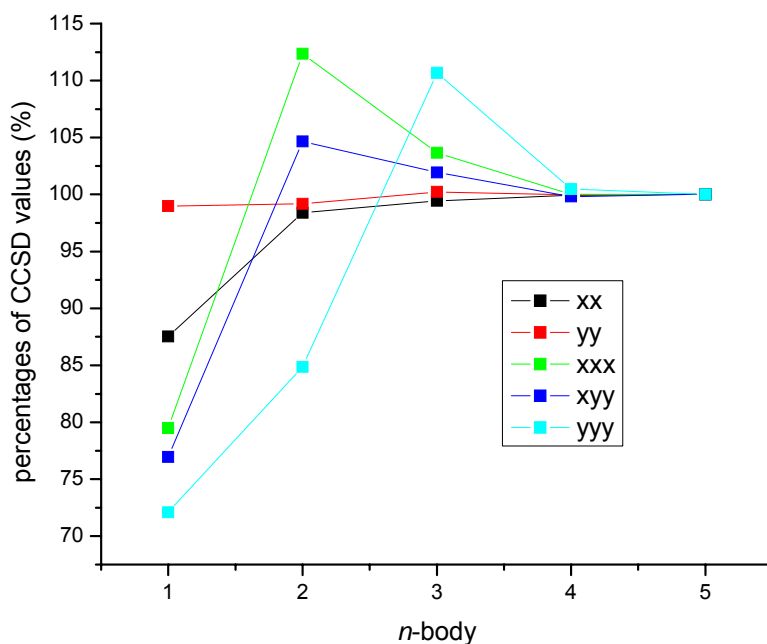


Figure 11-3 The deviation of the optical tensor values at the n -body increment contribution from the CCSD value within the domain space A.

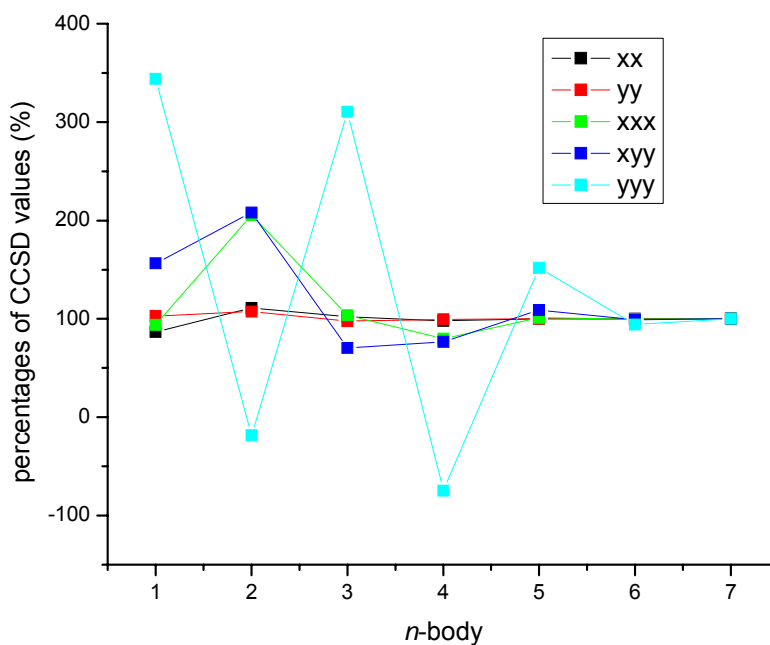


Figure 11-4 The deviation of the optical tensor values at the n -body increment contribution from the CCSD value within the domain space B.

Table 11-1 The incremental expansion for the correlation energy, first- and second-order susceptibilities within the local domain space A. The percentage number indicates the deviation at the n-body increment from the CCSD value.

<i>n</i> -body (A domain)	correlation energy	χ_{xx}	$\chi_{yy} (\chi_{zz})$	χ_{xxx}	$\chi_{xyy} (\chi_{xzz})$	χ_{yyv}
1	-0.62218 78.90%	249.706 87.55%	238.562 98.98%	2462.00 79.50%	526.55 76.94%	83.37 72.08%
2	-0.17122 100.62%	30.864 98.38%	0.490 99.18%	1017.46 112.4%	189.76 104.7%	14.79 84.87%
3	0.00509 99.98%	3.037 99.44%	2.502 100.2%	-269.88 103.7%	-18.79 101.9%	29.84 110.7%
4	-0.00016 99.99%	1.443 99.94%	-0.587 99.97%	-111.93 100.0%	-14.34 99.82%	-11.78 100.5%
5	0.00001 100.00%	0.153 100.0%	0.064 100.0%	-1.02 100.0%	1.19 100.0%	-0.55 100.0%
CCSD	-0.78850	285.203	241.031	3096.66	684.38	115.66

Table 11-2 The incremental expansion for the correlation energy, first- and second-order susceptibilities within the local domain space B. The percentage number indicates the deviation at the n-body increment from the CCSD value.

<i>n</i> -body (B domain)	correlation energy	χ_{xx}	$\chi_{yy} (\chi_{zz})$	χ_{xxx}	$\chi_{xyy} (\chi_{xzz})$	χ_{yyv}
1	-0.12314 58.49%	105.579 86.72%	95.473 103.0%	753.67 93.84%	179.86 156.5%	26.50 344.2%
2	-0.09477 103.50%	29.494 111.0%	4.038 107.4%	896.89 205.5%	59.11 208.0%	-27.92 -18.44%
3	0.00706 100.01%	-10.736 102.1%	-8.915 97.76%	-817.91 103.7%	-158.18 70.31%	25.34 310.7%
4	0.00058 100.42%	-5.008 98.02%	1.775 99.67%	-191.61 79.81%	7.26 76.63%	-29.67 -74.68%
5	-0.00036 100.59%	2.519 100.1%	0.469 100.2%	170.27 101.0%	36.94 108.8%	17.44 151.8%
6	0.00010 100.55%	-0.108 99.99%	-0.184 99.98%	-8.38 99.97%	-11.16 99.07%	-4.44 94.16%
7	-0.00001 100.00%	0.001 100.0%	0.018 100.0%	0.24 100.0%	1.07 100.0%	0.45 100.0%
CCSD	-0.21054	121.741	92.674	803.16	114.90	7.70

Conclusions

This thesis presents the first first-principles quantum chemical simulations of triborates containing bismuth and lanthanides. BiB_3O_6 is a crystal in the acentric monoclinic $C2$ space group with excellent non-linear and linear optical properties due to its large effective second harmonic generation coefficient. One major parts of calculations are devoted to derive the electronic structure, explore the relativistic (at Bi) and correlation effects, find the origins of chemical stability, optical responses and asymmetric Bi lone-pair electrons of BiB_3O_6 as well as its lattice dynamics at the central \mathbf{k} -space point.

First of all, the accuracies for different methods (HF, LDA, GGA and hybrid functionals) have been established for BiB_3O_6 based on the comparisons between the theoretical and experimental results for the geometry and the band gap. The hybrid functionals, especially B3PW, are recommended for all the subsequent calculations, which give the closest geometric parameters and the band gap (if the spin-orbit effect is accounted for) of BiB_3O_6 to the experimental values. The scalar-relativistic band structure indicates that BiB_3O_6 is an insulator with the calculated band gap of 4.29~4.99 eV. The band structure of BiB_3O_6 also suggests that there could be significant couplings between the electronic states and phononic states. The distributions of Bi 6s6p and O 2s2p orbitals over the energy level are studied by calculating the l-momentum projected density of states. It is found that the valence band of BiB_3O_6 is divided into two separate states. Strong occupied O 2s states dominate the energetically lower part, whereas the higher part in energy is contributed by the occupied Bi 6s6p states and intensive O 2p states. The conduction band is mainly composed of unoccupied Bi 6p and B states. The Bi-O interactions in $[\text{BiO}_4]^{5-}$ units have been analyzed using the crystal orbital overlap analysis. The majority of Bi 6s states are intensively populated in the occupied Bi 6s-O 2p bonding region from -16.6 eV to -14.5 eV, and the weak diffuse Bi 6s states are found in the occupied Bi 6s-O 2p antibonding region from -13.5 eV to -5.6 eV. The scalar-relativistic effect results in a Bi-O net antibonding repulsion and the Bi-O bond lengths are therefore elongated opposite to the typical relativistic bond contraction effect. The occurrence of BiB_3O_6 at ambient conditions is due to the correlation effect which significantly stabilizes tetrahedral $[\text{BO}_4]^{5-}$ units from unstable B-O net antibondings to stable B-O net bondings. The covalent B-O bonds in $[\text{BO}_3]^{3-}$ and Bi-O bonds in $[\text{BiO}_4]^{5-}$ are enhanced as well due to the correlation effect.

Two important consequences are found to own to the covalent orbital interactions between Bi and O. Firstly Bi 6p-O 2p bonding interactions promote the spatial-overlapping and electronic densities in the middle of the Bi-O bond, which accordingly favors the O 2p-Bi 6p electronic transitions and leads to the dominant contribution from $[\text{BiO}_4]^{5-}$ units to optical effects of BiB_3O_6 in the long wavelength region. The single Bi cations themselves according to our calculations do not play a critical role in determining the optical properties of BiB_3O_6 in contrast to explanations given in some experimental reports. Additionally, BiB_3O_6 shows quite a different electronic origin for optical effects

Conclusions

from other IA and IIA metal-containing borates such as β -BaB₂O₄, LiB₃O₅, CsB₃O₅ and CsLiB₆O₁₀ where the [BO₃]³⁻ and [BO₄]⁵⁻ units contribute most.

Secondly, the Bi-O covalent interactions bring more asymmetric O 2p orbitals into originally symmetric Bi 6s orbitals and thus partly explain the formation of the Bi lone-pair lobe, supported by our computational results. The non-spherical Bi lone-pairs have been visualized and were found to be anisotropically distributed in the 3-dimensional space since Bi lone-pairs appear relatively more symmetric and expanded in the (100) plane than in the (001) plane. Non-spherical Bi lone-pairs originate from the occupied Bi 6s-O 2p antibonding covalent interactions. Although Bi 6p_z orbitals were found to indirectly couple with both Bi 6s and O 2p states by bonding to the Bi 6s-O 2p occupied antibonding states, unlike the lone-pair model for α -PbO, Bi 6p orbitals are not significantly important to shape Bi lone-pairs as can be concluded from the similarity of Bi lone-pair shapes in the calculated electronic densities with and without Bi p basis set functions. The underlying reason is that the population of electrons at Bi 6p_z is not large enough to intensively change the electronic distribution of the Bi 6s components in the Bi 6s-O 2p antibonding states. Since the calculated number of Bi 6s electrons which contribute to Bi lone-pairs is only 0.92 and the occupied Bi 6s states are weak over the Bi 6s-O2p antibonding region from -13.5 eV to -5.6 eV, it may happen that the Bi 6s components of lone-pairs have not too large contributions to the optical responses of BiB₃O₆. Nevertheless, the lone-pair effect for optical responses of BiB₃O₆ can be partly attributed to the electronic transfer from the O 2p components of Bi lone-pairs near the Fermi level to empty Bi 6p orbitals.

A harmonic frequency calculation for periodic compounds is implemented by applying a numerical-difference method in connection with the CO-LCAO package CRYSTAL03. The complete 13 A and 14 B vibrational modes of BiB₃O₆ were presented at the DFT B3PW level and grouped on the basis of Bi-O and B-O bond motions according to the analyses of the calculated vibrating vectors. The external modes stay at lower frequencies ranging from 139.38 cm⁻¹ to 309.79 cm⁻¹ and are responsible for the rocking, scissoring, wagging and twisting O-Bi-O motions with the moving of central Bi cations and collective movements of borate units. The internal B-O motions in tetrahedral [BO₄]⁵⁻ units range from 374.46 cm⁻¹ to 1516.74 cm⁻¹. Those in triangular [BO₃]³⁻ units start from the higher frequency at 624.77 cm⁻¹, which leaves the three frequencies at 374.46 cm⁻¹, 452.47 cm⁻¹ and 563.05 cm⁻¹ almost purely contributed by B-O bonds in tetrahedral [BO₄]⁵⁻ units since the triangular [BO₃]³⁻ units for the three modes show weak external collective motions. Both agreements and discrepancies have been discussed by comparing the calculated modes and previous experimental reports.

The LnB₃O₆ with Ln=La~Gd is condensed into only the centric monoclinic I2/c space group rather than the acentric C2 symmetry for the BiB₃O₆-like structure. In order to investigate the relative stability between two monoclinic (i.e., C2 and I2/c) phases of LnB₃O₆, the crystal orbital adapted valence basis sets for lanthanide 4f-in-core energy-consistent pseudopotentials describing the configuration [4d¹⁰4fⁿ⁻¹]5s²5p⁶5d¹6s² of

Conclusions

trivalent lanthanides in periodic systems have been generated and tested in bulk calibration calculations for some selected model crystalline A-type lanthanide sesquioxides. The mean absolute errors in the HF energy of $\text{Ln}^{2+}\text{-}5s^25p^65d^1$ for (4s4p3d), (5s5p4d) and (6s6p5d) primitives are 0.66eV, 0.070eV and 0.028eV, respectively. The mean absolute errors are slightly decreased to 0.023eV by extending (6s6p5d) to (8s7p6d) with additional diffuse functions necessary to describe the neutral atoms. Our calculations using the newly generated basis sets (6s6p5d)/[4s4p4d] for geometrical parameters of crystalline Ln_2O_3 (Ln=La, Ce, Pr, Nd and Pm) overshoot the experimental ones by less than 1.5% for lattice constants and 1.2% for bond lengths at the DFT/B3PW level, and achieve the average deviation of about 0.4% for lattice constants and 0.2% for bond lengths when compared with the previously reported PAW calculation. The valence basis sets customized for crystalline calculations restore the calculated cohesive energy of Ln_2O_3 (Ln=La-Nd) to more than 88% of the experimental data within the *a posteriori*-HF correlation scheme in combination with gradient-corrected functionals. Good agreement has also been found between the conventional DFT results and the experimental cohesive energy with the deviation of only few per cent. The cohesive energy of bulk A-type Pm_2O_3 is also calculated to be 773.72kcal/mol to fill the gap in experimental data.

Following the derived valence Gaussian basis sets of lanthanide elements for ECP treatments, the computational study of the relative stabilities between two monoclinic phases, i.e., C2 and I2 space symmetry, of LaB_3O_6 and GdB_3O_6 , was subsequently carried out. The enthalpies were calculated for the two crystals under a set of isotropic external pressures. The enthalpy-pressure relation shows that the lowest enthalpies of both C2 and I2/c phases are achieved at the zero pressure. The C2 phase always stays at the higher enthalpy than the I2/c phase, which indicates that the I2 structure is more stable than C2 one. This agrees with the up-to-date experimental fact that I2 series of LnB_3O_6 with Ln=La~Gd have been already synthesized but no C2 phases are currently available for lanthanide triborates. The underlying reason has been explored in terms of the Ln-O chemical bonds based on the crystal orbital overlap analysis. It is the strong antibonding orbital repulsions between the sp orbitals of lanthanides and the oxygen ligands that lead to the instabilities of C2 LnB_3O_6 structures.

Conclusively, both BiB_3O_6 and LnB_3O_6 can never be regarded as the purely ionic crystals. Those interesting properties belonging to BiB_3O_6 and LnB_3O_6 that have been discussed so far arise from the intensive Bi-O and Ln-O covalent bonds, which cannot be understood within only the electrostatic Bi-O and Ln-O interactions.

Nonlinear optical properties of materials are of exceptional importance in laser science and technology. The bond charged model and anion group theory reported in references include only the first-order approximation, which cannot be held any more for some types of crystals. The incremental scheme has been further developed to calculate the optical properties beyond the ground state correlation energy. The resultant formalism shows that the macroscopic optical properties of a bulk crystal can be calculated as the sum of the respective microscopic increments of domains. A test calculation of the simple model

Conclusions

system $\text{Ga}_4\text{As}_4\text{H}_{18}$ suggests that the fast convergence of the expansion series for both susceptibilities and first-order hypersusceptibilities can be achieved, provided that the local domains are defined in the way that the coupling corrections between the individual domains are small enough.

Index of Figures

Introduction

Figure 1	7
Figure 2	8
Figure 3	8
Figure 4	9

Chapter 1

Figure 1-1	18
------------------	----

Chapter 2

Figure 2-1	46
Figure 2-2	46
Figure 2-3	46
Figure 2-4	47
Figure 2-5	48

Chapter 4

Figure 4-1	62
Figure 4-2	62
Figure 4-3	62
Figure 4-4	62
Figure 4-5	62
Figure 4-6	63
Figure 4-7	63
Figure 4-8	63
Figure 4-9	64
Figure 4-10	64

Chapter 5

Figure 5-1	72
Figure 5-2	72
Figure 5-3	72
Figure 5-4	73
Figure 5-5	73

Chapter 6

Figure 6-1	80
Figure 6-2	81
Figure 6-3	82

Chapter 7

Figure 7-1	89
Figure 7-2	90
Figure 7-3	90
Figure 7-4	91
Figure 7-5	91
Figure 7-6	92

Chapter 8

Figure 8-1	101
------------------	-----

Index of Figures

Figure 8-2	101
Figure 8-3	102
Figure 8-4	103
Figure 8-5	104
Figure 8-6	105
Figure 8-7	106

Chapter 9

Figure 9-1	116
Figure 9-2	117

Chapter 10

Figure 10-1	134
Figure 10-2	134
Figure 10-3	135
Figure 10-4	136
Figure 10-5	137
Figure 10-6	147
Figure 10-7	147
Figure 10-8	148
Figure 10-9	148
Figure 10-10	149
Figure 10-11	149
Figure 10-12	150
Figure 10-13	150
Figure 10-14	151
Figure 10-15	151
Figure 10-16	152
Figure 10-17	152

Chapter 11

Figure 11-1	163
Figure 11-2	163
Figure 11-3	164
Figure 11-4	164

Index of Tables

Introduction

Table 1	9
---------------	---

Chapter 6

Table 6-1	83
Table 6-2	83

Chapter 7

Table 7-1	93
Table 7-2	93

Chapter 8

Table 8-1	106
-----------------	-----

Chapter 9

Table 9-1	118
Table 9-2	118
Table 9-3	119
Table 9-4	120

Chapter 10

Table 10-1	137
Table 10-2	138
Table 10-3	139
Table 10-4	140
Table 10-5	141
Table 10-6	141
Table 10-7	153
Table 10-8	153
Table 10-9	154

Chapter 11

Table 11-1	165
Table 11-2	165

Curriculum Vitae

Personal Data

Name: Jun Yang
Born: November 11, 1977, Chongqing, China
Nationality: Chinese

Schools

09. 1984~07. 1990 Nankai Primary School
Chongqing, China
09. 1990~07. 1993 Nankai Middle School
Chongqing, China
09. 1993~07. 1996 Nankai High School
Chongqing, China

Universities

09. 1996~07. 2000 Bachelor of Science (Bsc., 2000~)
Department of Technical Physics
Peking University
Beijing, China
09. 2000~06. 2003 Master of Science (Msc., 2003~)
College of Chemistry and Molecular Engineering
Peking University
Beijing, China
12. 2003~09. 2006 Doctor of Philosophy (Ph.D., 2007~)
Graduiertenkolleg Fellowship Institut für Theoretische Chemie
10. 2006~04. 2007 Universität zu Köln
Wissenschaftlicher Mitarbeiter Cologne, Germany

Bibliography

- [1] C. Pisani, M. Busso, G. Capecechi, S. Casassa, R. Dovesi, L. Maschio, W. C. Zicovich, M. Schütz, *J. Chem. Phys.* **122**, 094113 (2005)
- [2] A. Shukla, M. Dolg, P. Fulde, H. Stoll, *Phys. Rev. B* **60**, 5211 (1999)
- [3] H. Stoll, B. Paulus, P. Fulde, *J. Chem. Phys.* **123**, 144108 (2005)
- [4] A. B. Mukhopadhyay, M. Dolg, C. Oligschleger, *J. Chem. Phys.* **120**, 8734 (2004)
- [5] S. K. Filatov, R. S. Bubnova, *Phys. Chem. Glasses* **41**, 216 (2000)
- [6] P. H. Hermans, *Z. Anorg. Allgem. Chem.* **142**, 83 (1925)
- [7] H. Menzel, *Z. Anorg. Allgem. Chem.* **164**, 22 (1927)
- [8] W. H. Zachariasen, *Z. Kristallogr.* **76**, 289 (1931)
- [9] V. M. Goldschmidt, H. Hauptmann, *Nachr. Ges. Wiss. Gettingen. Math. Phys.* **K1**, 53 (1932)
- [10] S. M. Fang, *Z. Kristallogr.* **99**, 1 (1938)
- [11] W. H. Zachariasen, *Z. Kristallogr.* **98**, 266 (1937)
- [12] P. C. Burns, J. D. Grice, F. C. Hawthorne, *The Cana. Mine.* **33**, 1131 (1995)
- [13] Dewey C. F., W. R. Cook, R. T. Hodgson, J. J. Wynne, *Appl. Phys. Lett.* **26**, 714 (1975)
- [14] P. Becker, *Adv. Mater.* **10**, 979 (1998)
- [15] J. Liebertz, S. Stähr, *Z. Kristallogr.* **165**, 91 (1983)
- [16] C. Chen, B. Wu, A. Jiang, G. You, *Sci. Sin. B* **28**, 235 (1985)
- [17] C. Chen, Y. Wu, A. Jiang, B. Wu, G. Zou, R. Li, S. Lin, *J. Opt. Soc. Am. B* **6**, 616 (1989)
- [18] Y. C. Wu, T. Sasaki, S. Nakai, A. Yokotami, H. Tang, C. T. Chen, *Appl. Phys. Lett.* **62**, 2614 (1995)
- [19] Y. Mori, I. Kuroda, S. Nakajima, T. Sasaki, S. Nakai, *Appl. Phys. Lett.* **67**, 1818 (1995)
- [20] J. M. Tu, D. A. Keszler, *Mater. Res. Bull.* **30**, 209 (1995)
- [21] T. K. Kwon, J. J. Ju, J. W. Cha, J. N. Kim, S. I. Yun, *Mater. Lett.* **20**, 211 (1994)
- [22] L. F. Mei, C. T. Chen, B. C. Wu, *J. Appl. Phys.* **74**, 7014 (1993)
- [23] C. T. Chen, Y. B. Wang, Y. N. Xia, B. C. Wu, O. Y. Tang, K. Wu, W. Zeng, L. H. Yu, *J. Appl. Phys.* **77**, 2268 (1995)
- [24] C. T. Chen, Y. B. Wang, B. C. Wu, K. Wu, W. Zeng, L. H. Yu, *Nature* **373**, 322 (1995)
- [25] G. Aka, A. Kahn-Harari, F. Mougél, D. Vivien, F. Salin, P. Coquelin, P. Colin, D. Pelenc., J. P. Damelet, *J. Opt. Soc. Am. B* **14**, 2238 (1997)
- [26] M. Iwai, T. Kobayashi, H. Furry, H. Mori, T. Sasaki, *Jpn. J. Appl. Phys.* **36**, L276 (1997)
- [27] R. Norrestam, M. Nygren, J. O. Bovin, *Chem. Mater.* **4**, 737 (1992)
- [28] P. Becker, C. Wickleder, *Cryst. Res. Technol.* **36**, 2737 (2001)
- [29] B. Teng, Z. P. Wang, H. D. Jiang, X. F. Cheng, H. Liu, X. B. Hu, S. M. Dong, J. Y. Wang, Z. S. Shao, *J. Appl. Phys.* **91**, 3618 (2001)
- [30] S. Haussühl, L. Bohatý, P. Becker, *Appl. Phys. A* **82**, 495 (2006)
- [31] R. Fröhlich, L. Bohatý, J. Liebertz, *Acta Crystal. C* **40**, 343 (1984)
- [32] L. Bohatý, J. Liebertz, *Z. Kristallogr.* **170**, 18 (1985)
- [33] P. Becker, J. Liebertz, L. Bohatý, *J. Cryst. Growth* **203**, 149 (1999)
- [34] B. Teng, J. Y. Wang, Z. P. Wang, X. B. Hu, H. D. Jiang, H. Liu, X. F. Cheng, S. M. Dong, Y. G. Liu, Z. S. Shao, *J. Cryst. Growth* **240**, 331 (2002)
- [35] H. Hellwig, J. Liebertz, L. Bohatý, *Solid State Commun.* **109**, 249 (1998)
- [36] H. Hellwig, J. Liebertz, L. Bohatý, *J. Appl. Phys.* **88**, 240 (2000)
- [37] C. Du, Z. Wang, Z. J. Liu, X. Xu, B. Teng, K. Fu, J. Wang, Y. Liu, Z. Shao, *Appl. Phys. B* **73**, 215 (2001)
- [38] Z. P. Wang, B. Teng, K. Fu, X. G. Xu, R. B. Song, C. L. Du, H. D. Jiang, J. Y. Wang, Y. G. Liu, Z. S. Shao, *Opt. Commun.* **202**, 217 (2002)
- [39] I. V. Kityk, A. Majchrowski, *Opt. Mater.* **25**, 33 (2004)
- [40] A. Gössling, T. Möller, W. D. Stein, P. Becker, L. Bohatý, M. Grüninger, *Phys. Stat. Solid B* **242**, R85 (2005)
- [41] H. R. Xia, L. X. Li, B. Teng, W. Q. Zheng, G. W. Lu, H. D. Jiang, J. Y. Wang, *J. Raman Spect.* **33**, 278 (2002)
- [42] M. Ghotbi, M. Ebrahim-Zadeh, *Opt. Exp.* **12**, 6002 (2004)
- [43] D. Xue, K. Betzler, H. Hesse, D. Lammers, *Phys. Stat. Sol. A* **176**, R1 (1999)

Bibliography

- [44] D. Xue, K. Betzler, H. Hesse, D. Lammers, *Solid State Commun.* **114**, 21 (2000)
- [45] Z. S. Lin, Z. Z. Wang, C. T. Chen, M. H. Lee, *J. Appl. Phys.* **90**, 5585 (2001)
- [46] P. C. Burns, J. D. Grice, F. C. Hawthorne, *Can. Mine.* **33**, 1131 (1995)
- [47] P. Becker, *Z. Kristallogr.* **216**, 523 (2001)
- [48] E. Parthe, *Z. Kristallogr.* **217**, 179 (2002)
- [49] M. J. Barber, P. Becker, *Z. Kristallogr.* **217**, 205 (2002)
- [50] J. S. Ysker, W. Hoffmann, *Naturwissenschaften* **57** 129 (1970); G. K. Abdullaev, K. S. Mamedov, G. G. Dzhafarov, *Kristallografiya* **26**, 837 (1981)
- [51] A. Gorionova, A., P. Held, P. Becker, L. Bohatý, *Acta Crystal.* **E59**, i83 (2003)
- [52] C. Sieke, T. Nikelski, T. Schleid, T., *Z. Anorg. Allgem. Chem.* **628**, 819 (2002)
- [53] V. I. Pakhomov, G. B. Sil'nitskaya, A. V. Medvedev, B. F. Dzhurinskii, *Neorg. Mater.* **8**, 1259 (1972); H. Müller-Bunz, T. Nikelski, T. Schleid, *Z. Nat. B. Anorg. Chem. Organ. Chem.* **58**, 375 (2003)
- [54] G. K. Abdullaev, K. S. Mamedov, G. G. Dzhafarov, *Kristallografiya* **20**, 265 (1975)
- [55] H. Müller-Bunz, T. Nikeski, Th. Schleid, *Z. Naturforsch.* **58b**, 375 (2003)
- [56] H. Emme, T. Nikelski, T. Schleid, R. Pöttgen, M. H. Möller, H. Huppertz, *Z. Naturforsch.* **59b**, 202 (2004)
- [57] M. F. C. Ladd, *Symmetry in Molecules and Crystals*, Ellis Horwood, New York (1989)
- [58] E. Wigner, F. Seitz, *Phys. Rev.* **43**, 804 (1933)
- [59] N. W. Ashcroft, N. D. Mermin, *Solid State Physics*, Saunders College, Philadelphia (1976)
- [60] W. Jones, N. H. March, *Theoretical Solid State Physics*, Volume 1, Dover Publications, New York (1973)
- [61] H. Jones, *The theory of Brillouin Zones and Electronic States in Crystals*, 2nd revised edition, North-Holland, Amsterdam (1975)
- [62] F. Bloch, *Z. Phys.* **52**, 555 (1928)
- [63] H. J. Monkhorst, J. D. Pack, *Phys. Rev. B* **13**, 5188 (1976)
- [64] V. R. Saunders, R. Dovesi, C. Roetti, R. Orlando, C. M. Z. Wilson, N. M. Harrison, K. Doll, B. Civalleri, I. J. Bush, P. D. Arco, M. Llunell, *CRYSTAL2003 1.0 User's Manual*, 2003, **Aug.** 7
- [65] C. Herring, *Phys. Rev.* **57**, 1169 (1940)
- [66] J. C. Phillips, L. Kleinman, *Phys. Rev.* **116**, 287 (1959)
- [67] J. C. Slater, *Phys. Rev.* **51**, 846 (1937)
- [68] J. C. Slater, *Phys. Rev.* **92**, 603 (1953)
- [69] M. M. Saffren, J. C. Slater, *Phys. Rev.* **92**, 1126 (1953)
- [70] J. Koringa, *Physica* **13**, 392 (1947)
- [71] W. Kohn, N. Rostoker, *Phys. Rev.* **94**, 1111 (1954)
- [72] G. K. H. Madsen, P. Blaha, K. Schwarz, E. Sjöstedt, L. Nordström, *Phys. Rev. B* **64**, 195134 (2001)
- [73] O. K. Anderson, *Phys. Rev. B* **12**, 3060 (1975)
- [74] D. D. Koelling, G. O. Arbman, *J. Phys. F: Metal Phys.* **5**, 2041 (1975)
- [75] M. Springborg, *Methods of Electronic, Structure Calculations from Molecules to Solids*, pp. 123-132, Wiley-VCH Verlag, GmbH, Weinheim (2000)
- [76] D. Feller, E. R. Davidson, *Chem. Rev.* **86**, 681 (1986)
- [77] D. Feller, E. R. Davidson, *Basis Sets for Ab Initio Molecular Orbital Calculations and Intermolecular Interactions*, pp. 1-43, in "Reviews in Computational Chemistry", VCH, New York (1990)
- [78] A. Szabo, N. S. Ostlund, *Modern Quantum Chemistry, Introduction to Advanced Electronic Structure Theory*, Dover Publications, New York (1996)
- [79] R. Dovesi, *Int. J. Quantum Chem.* **29**, 1755 (1986)
- [80] R. Dovesi, C. Pisani, C. Roetti, V. R. Saunders, *Phys. Rev. B* **28**, 5781 (1983)
- [81] M. Causà, R. Dovesi, R. Orlando, C. Pisani, V. R. Saunders, *J. Phys. Chem.*, **92**, 909 (1988)
- [82] C. Pisani, R. Dovesi, C. Roetti, *Hartree-Fock first-principles Treatment of Crystalline Systems, Lecture notes in Chemistry*, Springer Verlag, Heidelberg (1988)
- [83] D. Turnbull, F. Seitz, *Solid State Physics*, Vol. 23, Academic, New York (1970)
- [84] T. H. Dupree, *Ann. Phys.* **15**, 63 (1961)
- [85] J. L. Beeby, *Proc. Roy. Soc. London Ser.* **A302**, 1113 (1967)
- [86] G. J. Morgan, *Proc. Phys. Soc.* **89**, 365 (1966)
- [87] R. Zeller, P. H. Dederichs, *Phys. Rev. Lett.* **42**, 1713 (1979)
- [88] A. Gonis, *Theoretical Materials Science*, Materials Research Society (2000)

Bibliography

- [89] D. Singh, *Phys. Rev. B* **43**, 6388 (1991)
- [90] E. Sjöstedt, L. Nordström, D. J. Singh, *Solid State Comm.* **114**, 15 (2000)
- [91] P. Blaha, K. Schwarz, G. K. H. Madsen, D. Kvasnicka, J. Luitz, *WIEN2k An Augmented Plane-wave + Local Orbitals Program for Calculating Crystal Properties* (Karlheinz Schwarz, Techn. Universität Wien). ISBN 3-9501031-1-2. (2001)
- [92] R. G. Parr, W. T. Yang, *Density-Functional Theory of Atoms and Molecules*, Oxford University Press, New York (1989)
- [93] P. Hohenberg, W. Kohn, *Phys. Rev.* **136**, B864 (1964)
- [94] W. Koch, M. C. Holthausen, *A Chemist's Guide to Density Functional Theory (second edition)*, Wiley-VCH Verlag GmbH (2001)
- [95] W. Kohn, L. J. Sham, *Phys. Rev.* **140**, A1133 (1965)
- [96] J. C. Slater, *Phys. Rev.* **81**, 385 (1951)
- [97] P. A. M. Dirac, *Proc. Cambridge Phil. Soc.* **26**, 376 (1930)
- [98] U. V. Barth, L. Hedin, *J. Phys. C: Solid State Phys.* **5**, 1629 (1972)
- [99] D. M. Ceperley, B. J. Alder, *Phys. Rev. Lett.* **45**, 566 (1980)
- [100] S. H. Vosko, L. Wilk, M. Nusair, *Can. J. Phys.* **58**, 1200 (1980)
- [101] J. P. Perdew, A. Zunger, *Phys. Rev. B* **23**, 5048 (1981)
- [102] J. P. Perdew, Y. Wang, *Phys. Rev. B* **45**, 13244 (1992)
- [103] A. D. Becke, *Phys. Rev. A* **38**, 3098 (1988)
- [104] J. P. Perdew, Y. Wang, *Phys. Rev. B* **33**, 8800 (1986)
- [105] J. P. Perdew, K. Burke, M. Ernzerhof, *Phys. Rev. Lett.* **77**, 3865 (1996)
- [106] J. P. Perdew, *Phys. Rev. B* **33**, 8822 (1986)
- [107] J. P. Perdew, Y. Wang, *Phys. Rev. B* **40**, 3399 (1989)
- [108] J. P. Perdew, *Electronic Structure of Solids 1991*, Akademie Verlag, Berlin (1991)
- [109] C. Lee, W. T. Yang, R. G. Parr, *Phys. Rev. B* **37**, 785 (1988)
- [110] A. D. Becke, *J. Chem. Phys.* **98**, 5648 (1993)
- [111] H. Stoll, *Phys. Rev. B* **46**, 6700 (1992)
- [112] H. Stoll, *J. Chem. Phys.* **97**, 8449 (1992)
- [113] H. Stoll, *Chem. Phys. Lett.* **191**, 548 (1992)
- [114] L. L. Foldy, S. A. Wouthuysen, *Phys. Rev.* **78**, 29 (1950)
- [115] M. Douglas, N. M. Kroll, *Ann. Phys.* **82**, 89 (1974)
- [116] B. A. Hess, *Phys. Rev. A* **33**, 3742 (1986)
- [117] S. Huzinaga, A. A. Cantu, *J. Chem. Phys.* **55**, 5543 (1971)
- [118] B. A. Hess, *Relativistic effects in heavy-element chemistry and physics*, John Wiley & Sons, Ltd. (2002)
- [119] H. B. Schlegel, *J. Comp. Chem.* **3**, 214 (1982)
- [120] A. D. Becke, *J. Chem. Phys.* **88**, 1053 (1988)
- [121] W. Küchle, D. Dolg, H. Stoll, H. Preuss, *Mol. Phys.* **74**, 1245 (1991)
- [122] Energy-Consistent Pseudopotentials of the Stuttgart/Cologne Group: <http://www.theochem.uni-stuttgart.de/pseudopotentiale/clickpse.en.html>
- [123] EMSL Gaussian Basis Set Order Form: <http://www.emsl.pnl.gov/forms/basisform.html>
- [124] T. H. Dunning, *J. Chem. Phys.* **55**, 716 (1971)
- [125] J. P. Desclaux, *Comp. Phys. Comm.* **9**, 31 (1975)
- [126] D. D. Kölling, B. Harmon, *J. Phys. C* **13**, 6147 (1980)
- [127] J. Yang, M. Dolg, *Theor. Chem. Acc.* **113**, 212 (2005)
- [128] Y. X. Wang, M. Dolg, *Theor. Chem. Acc.* **100**, 124 (1998)
- [129] R. Hoffmann, *Angew. Chem. Int. Ed. Engl.* **26**, 846 (1987)
- [130] P. Larson, S. D. Mahanti, D. Y. Chung, M. G. Kanatzidis, *Phys. Rev. B* **65**, 045205 (2002)
- [131] P. Larson, S. D. Mahanti, M. G. Kanatzidis, *Phys. Rev. B* **61**, 8162 (2000)
- [132] K. G. Dyall, I. P. Grant, C. T. Johnson, F. A. Parpia, E. P. Plummer, *Comput. Phys. Commun.* **55**, 425 (1989) GRASP is a relativistic atomic electronic structure code.
- [133] T. Hughbanks, R. Hoffmann, *J. Am. Chem. Soc.* **105**, 3528 (1983)
- [134] R. Dronskowski, P. E. Blöchl, *J. Phys. Chem.* **97**, 8617 (1993)
- [135] A. Grechnev, R. Ahuja, O. Eriksson, *J. Phys.: Condens. Matter* **15**, 7751 (2003)
- [136] J. Lin, M. H. Lee, Z. P. Liu, C. T. Chen, C. J. Pickard, *Phys. Rev. B* **60**, 13380 (1999)

Bibliography

- [137] Z. S. Lin, Z. Z. Wang, C. T. Chen, M. H. Lee, *Phys. Rev. B* **62**, 1757 (2000)
- [138] P. Pyykkö, *Chem. Rev.* **88**, 563 (1988)
- [139] N. V. Sidgwick, H. M. Powell, *Proc. R. Soc. London, Ser. A* **176**, 153 (1940)
- [140] R. J. Gillespie, R. S. Nyholm, *Q. Rev., Chem. Soc.* **11**, 339 (1957)
- [141] F. Cloran, Y. P. Zhu, J. Osborn, I. Carmichael, A. S. Serianni, *J. Am. Chem. Soc.* **122**, 6435 (2000)
- [142] A. K. Chandra, M. T. Nguyen, T. Zeegers-Huyskens, *Chem. Phys.* **255**, 149 (2000)
- [143] F. Kraus, T. Hanauer, N. Korber, *Inorg. Chem.* **45**, 1117 (2006)
- [144] P. Bennich, T. Wiell, O. Karis, M. Weinelt, N. Wassdahl, A. Nilsson, M. Nyberg, L. G. M. Pettersson, J. Stohr, M. Samant, *Phys. Rev. B* **57**, 9274 (1998)
- [145] A. H. Nicola, M. R. Kartin, *Phys. Rev. B* **59**, 8759 (1999)
- [146] U. V. Waghmare, N. A. Spaldin, H. C. Kandpal, R. Seshadri, *Phys. Rev. B* **67**, 125111 (2003)
- [147] N. E. Christensen, A. Svane, E. L. P. Y. Blanca, *Phys. Rev. B* **72**, 014109 (2005)
- [148] R. A. Wheeler, P. N. V. P. Kumar, *J. Am. Chem. Soc.* **114**, 4776 (1992)
- [149] X. Wang, Q. L. Cui, Y. W. Pan, W. Gao, J. Zhang, G. T. Zou, *J. Alloys Comp.* **321**, 72 (2001)
- [150] S. Suehara, P. Thomas, A. P. Mirgorodsky, T. M. Mejean, J. C. C. Mesjard, T. Aizawa, S. Hishita, S. Todoroki, T. Konishi, S. Inoue, *Phys. Rev. B* **70**, 205121 (2004)
- [151] R. Seshadri, A. H. Nicola, *Chem. Mater.* **13**, 2892 (2001)
- [152] P. Schwerdtfeger, G. A. Heath, M. Dolg, M. A. Bennett, *J. Am. Chem. Soc.* **114**, 7518 (1992)
- [153] M. Dolg, W. Kuchle, H. Stoll, H. Preuss, P. Schwerdtfeger, *Mol. Phys.* **74**, 1265 (1991)
- [154] A. R. H. F. Ettema, C. Haas, P. Moriarty, G. Hughes, *Surf. Sci.* **287**, 1106 (1993)
- [155] L. E. Orgel, *J. Chem. Soc. Dec.*, 3815 (1959)
- [156] A. Verbaere, R. Marchand, M. Tournoux, *J. Solid State Chem.* **23**, 383 (1978)
- [157] H. J. Terpstra H. J., R. A. D. Groot, C. Haas, *Phys. Rev. B* **52**, 11690 (1995)
- [158] G. W. Watson, S. C. Parker, G. Kresse, *Phys. Rev. B* **59**, 8481 (1999)
- [159] G. W. Watson, S. C. Parker, *J. Phys. Chem. B* **103**, 1258 (1999)
- [160] A. Walsh, G. W. Watson, *J. Solid State Chem.* **178**, 1422 (2005)
- [161] G. W. Watson, *J. Chem. Phys.* **114**, 758 (2001)
- [162] A. Walsh, G. W. Watson, *J. Phys. Chem. B* **109**, 18868 (2005)
- [163] P. Becker, L. Bohatý L. *Cryst. Res. Technol.* **36**, 1175 (2001)
- [164] D. J. Payne, R. G. Egdell, A. Walsh, G. W. Watson, J. Guo, P. A. Glans, T. Learmonth, K. E. Smith, *Phys. Rev. Lett.* **96**, 157403 (2006)
- [165] A. V. Egorysheva, V. I. Burkov, Y. F. Kargin, V. G. Plotnichenko, V. V. Koltashev, *Cryst. Rep.* **50**, 127 (2005)
- [166] X. B. Hu, J. Y. Wang, B. Teng, C. K. Loong, M. Grimsditch, *J. Appl. Phys.* **97**, 033501 (2005)
- [167] D. Kasproicz, T. Runka, M. Szybowicz, P. Ziobrowski, A. Majchrowski, E. Michalski, M. Drozdowski, *Cryst. Res. Technol.* **40**, 459 (2005)
- [168] F. Pascale, C. M. Z. Wilson, F. L. Gejo, B. Civalleri, R. Orlando, R. Dovesi, *J. Comp. Chem.* **25**, 888 (2003)
- [169] M. Causà, R. Dovesi, C. Pisani, C. Roetti, *Phys. Rev. B* **33**, 1308 (1986)
- [170] D. L. Rousseau, R. P. Bauman, S. P. S. Porto, *J. Raman. Spectr.* **10**, 253 (1981)
- [171] F. F. Bentley, L. D. Smithson, A. L. Rozek, *Infrared and Raman characteristic group frequencies*, John Wiley & Sons Inc. (1968)
- [172] P. Karen, A. Kjekshus, Q. Huang, V. L. Karen, *J. Alloys Compd.* **282**, 72 (1999)
- [173] P. Pyykkö, *Inorg. Chim. Acta* **139**, 243 (1987)
- [174] K. Balasubramanian, *Handbook on the physics and chemistry of rare earths*, K. A. Gschneidner, Jr., L. Eyring (Eds.), Elsevier, Amsterdam, **Vol. 18**, p.29 (1994)
- [175] M. Dolg, H. Stoll, *Handbook on the physics and chemistry of rare earths*, K. A. Gschneidner, Jr., L. Eyring (Eds.), Elsevier, Amsterdam, **Vol. 22**, p.607 (1996)
- [176] M. Dolg, *Encyclopedia of computational chemistry*, P. V. R. Schleyer, N. L. Allinger, T. Clark, J. Gasteiger, P. A. Kollman, H. F. Schäfer III, P. R. Schreiner (Eds.), Wiley, Chichester, p.1478 (1998)
- [177] M. Pepper, B. Bursten, *Chem. Rev.* **91**, 719 (1991)
- [178] G. Schreckenbach, P. J. Hay, R. L. Martin, *J. Comput. Chem.* **20**, 70 (1999)
- [179] M. Dolg, X. Y. Cao, *Recent advances in computational chemistry*, K. Hirao, Y. Ishikawa (Eds), World Scientific Publishing, New Jersey, vol,5, p.1 (2004)
- [180] E. Eliav, U. Kaldor, *Phys. Rev. A* **52**, 291 (1995)

Bibliography

- [181] W. Kutzelnigg, *Phys. Scr.* **36**, 416 (1987)
- [182] Y. Sakai, E. Miyoshi, H. Tatewaki, *J. Mol. Struct. (Theochem)* **451**, 143 (1998)
- [183] L. Seijo, Z. Barandiaran, E. Harguindey, *J. Chem. Phys.* **114**, 118 (2000)
- [184] M. Dolg, H. Stoll, A. Savin, H. Preuss, *Theor. Chim. Acta* **75**, 173 (1989)
- [185] M. Dolg, H. Stoll, H. Preuss, *J. Chem. Phys.* **90**, 1730 (1989)
- [186] T. R. Cundari, W. J. Stevens, *J. Chem. Phys.* **98**, 5555 (1993)
- [187] R. B. Ross, S. Gayen, W. C. Ermler, *J. Chem. Phys.* **100**, 8145 (1994)
- [188] M. Dolg, H. Stoll, *Theor. Chim. Acta* **75**, 369 (1989)
- [189] M. Dolg, P. Fulde, W. Küchle, C. S. Neumann, H. Stoll, *J. Chem. Phys.* **94**, 3011 (1991)
- [190] X. Y. Cao, M. Dolg, *J. Chem. Phys.* **115**, 7348 (2001)
- [191] X. Y. Cao, M. Dolg, *J. Mol. Struct. (Theochem)* **581**, 139 (2002)
- [192] C. A. Perottoni, A. S. Pereira, J. A. H. da Jornada, *J. Phys.: Condensed Matter* **12**, 7205 (2000)
- [193] C. Pisani, R. Dovesi, *Int. J. Quantum Chem.* **17**, 501 (1980)
- [194] C. Pisani, R. Dovesi, C. Roetti, *Hartree-Fock Ab-initio Treatment of Crystalline Systems, Lecture Notes in Chemistry*, Springer, Heidelberg (1996)
- [195] S. Kalvoda, M. Dolg, H. J. Flad, P. Fulde, H. Stoll, *Phys. Rev. B* **57**, 2127 (1998)
- [196] M. Dolg, H. Stoll, H. Preuss, *Theor. Chim. Acta* **85**, 441 (1993)
- [197] R. M. Pitzer, *Atomic electronic structure code ATMSCF*, The Ohio State University, Columbus (1979)
- [198] C. F. Fischer, *The Hartree-Fock Method for Atoms program MCHF*, Wiley, New York, (1977), modified version for pseudopotential and quasirelativistic calculations by M. Dolg (1987)
- [199] Y. K. Han, K. Hirao, *Chem. Phys. Lett.* **318**, 453 (2000)
- [200] A. G. Petukhov, W. R. L. Lambrecht, B. Segall, *Phys. Rev. B* **53**, 4324 (1996)
- [201] C. M. Zicovich-Wilson, Departamento de Fisica, Universidad Autonoma del Estado de Morelos, <http://www.crystal.unito.it/LoptCG/LoptCG.html>
- [202] MOLPRO is a package of first-principles programs written by Werner HJ and Knowles PJ, with contributions from Amos RD, Berning A, Cooper DL, Deegan MJO, Dobbyn AJ, Eckert F, Hampel C, Hetzer G, Leininger T, Lindh R, Lloyd AW, Meyer W, Mura ME, Nicklass A, Palmieri P, Peterson K, Pitzer R, Pulay P, Rauhut G, Schütz M, Stoll H, Stone AJ, Tarroni R, Thorsteinsson T and Werner HJ.
- [203] L. C. Wilson, M. Levy, *Phys. Rev. B* **41**, 12930 (1990)
- [204] H. Müller-Buschbaum., H. G. Vonschne, *Z. Anorg. Allg. Chem.* **340**, 232 (1965)
- [205] H. Müller-Buschbaum, *Z. Anorg. Allg. Chem.* **343**, 6 (1966)
- [206] L. Eyring, B. Holmberg, *Advanced in Chemistry Series*, American Chemical Society, Washington DC, **Vol. 39**, p.46 (1963)
- [207] G. Frenking, I. Antes, M. Böhme, S. Dapprich, A. W. Ehlers, V. Jonas, A. Neuhaus, M. Otto, R. Stegmann, A. Veldkamp, S. F. Vyboishchikov, *Rev. Comput. Chem.* **8**, 63 (1996)
- [208] N. Hirosaki, S. Ogata, C. Kocer, *J. Alloys Comp.* **351**, 31 (2003)
- [209] W. C. Martin, R. Zalubas, L. Hagan, *Atomic energy levels – the rare earth elements*, NSRDS-NBS-60, National Bureau of Standards, US Dept. of Commerce
- [210] P. D'Arco, G. Sandrone, R. Dovesi, R. Orlando, V. R. Saunders, *Phys. Chem. Minerals* **20**, 407 (1993)
- [211] M. Causà, R. Dovesi, C. Roetti, *Phys. Rev. B* **43**, 11937 (1991)
- [212] E. Aprà, M. Causà, M. Prencipe, R. Dovesi, V. R. Saunders, *J. Phys.: Condensed Matter* **5**, 2969 (1993)
- [213] H. Bärnighausen, G. Schiller, *J. Less-Common Metals* **110**, 385 (1985)
- [214] O. Greis, R. Ziel, B. Breidenstein, A. Haase, T. Petzel, *J. Alloys Compd.* **216**, 255 (1992)
- [215] M. Faucher, J. Pannetier, Y. Charreire, P. Caro, *Acta Crystallographica B* **38**, 344 (1982)
- [216] D. R. Lide (editor-in-chief), *Handbook of Physics and Chemistry*, 9-63, 81st edition (2000-2001)
- [217] M. S. Chandrasekharaiah, K. A. Gingerich, *Handbook on the Physics and Chemistry of Rare Earths*, North-Holland, Amsterdam, **Vol. 12**, 409 (1989)
- [218] *Gmelin Handbuch der Anorganischen Chemie*, Seltenerdelemente; Springer-Verlag, Berlin, Teil **C1**, 119 (1974)
- [219] F. Birch, *Phys. Rev. B* **71**, 809 (1947)
- [220] F. Birch, *J. Geophys. Res.* **83**, 1257 (1978)
- [221] B. F. Levine, *Phys. Rev. Lett.* **22**, 787 (1969)

Bibliography

- [222] B. F. Levine, *Phys. Rev. Lett.* **25**, 440 (1970)
- [223] B. F. Levine, *Phys. Rev. B* **7**, 2600 (1973)
- [224] Z. S. Lin, J. Lin, Z. Z. Wang, Y. C. Wu, N. Ye, C. T. Chen, R. K. Li, *J. Phys.: Condens. Matter* **13**, R369 (2001)
- [225] C. T. Chen, Z. S. Lin, Z. Z. Wang, *Appl. Phys. B* **80**, 1 (2005)
- [226] P. N. Butcher, T. P. McLean, *Proc. Phys. Soc. Lond.* **81**, 219 (1963)
- [227] S. N. Rashkeev, W. R. L. Laambrecht, B. Segall, *Phys. Rev. B* **57**, 3905 (1998)
- [228] B. Paulus, *Phys. Rep.* **428**, 1 (2006)